4. CHEMISTRY OF INORGANIC MATERIALS

4.1. Lectures

L01 SOME NON-TRADITIONAL BINDERS AND COMPOSITES TESTED AT THE STUDENT LABORATORIES OF THE INSTITUTE OF MATERIALS CHEMISTRY, BRNO UNIVERSITY OF TECHNOLOGY

JIŘÍ BRANDŠTETR, JAROMÍR HAVLICA, TOMÁŠ OPRAVIL and FRANTIŠEK ŠOUKAL
Department of Materials Chemistry, Faculty of Chemistry, Brno University of Technology, Purkynova 118, 612 00 Brno, Czech Republic,
brandstetr@fch.vutbr.cz

Introduction

At present, the effort to increase the productivity of materials results a.o. in the utilization of different non-traditional cements and composites based preferably on mineral "wastes" – secondary industrial products/fly ashes, metallurgical slags, energogypsum...) These activities save natural mineral resources and decreas the amount of discharged materials on the dumping sites. Novel chemical and mineral admixtures enable the preparation of "tailored" material of demanded special properties. Very often, lack of information and/or unstable quality of secondary materials is the real reason of their unsufficient use. Therefore, better publicity, adequate education at schools of all types, meetings and and conferences can play very important role. At the University of Technology in Brno, the students in their diploma and postdoctoral theses solve in the laboratories many of these problems mostly from chemical point of view with the final objective to enlarge the assortment of binders and mineral composites. Many projects are solved in the cooperation with the industry, where the increasing interest to use "green" material is stil more emphasized. Very often, these activities are connected with the effort to decrease the carbon dioxide emission, solving ecological and economical problems at the same time.

Long Term Durability Of Concrete?

Portland cement (PC) will be our binder No. 1 for next decades, but we know this material only from the year 1824 and its wider use dates to the end of 19th century. The phase composition of concrete based on PC differs from the natural minerals considerably. In the earth crust, we cannot find hydrates of high-calcium minerals, nature does not like such a relatively unstable compounds. From the Table I, the differences between the content of CaO, SiO_2 and Al_2O_3 are especially remarkable.

The CSH gel, portlandite, ettringite and monosulfate incline to sulfatation and/or carbonatation, the content of pores is high (Fig. 1.), the long-term phase changes can bring about the structure decomposition. Therefore, R&D of concrete based on different chemical and phase composition including non-clinker ones is urgently demanded.

High-Performance Concrete (HPC)

For many years, high-strength concrete was only perceived as a new concrete for the construction of high-rise buildings, bridges, offshore platforms etc. Now, high-performance concrete is viewed as an emerging type of new concrete whose applications are growing both in volume and diversity. It is becoming a high-tech material according to the needs of the users, where the decisive role is played by the mineral and especially chemical additives controlling the tailored properties. As a mineral additive into HPC, microsilica is routinely used, which can be substituted by cheaper micro-ground siliceous fly ash. In the R&D, modern instrumental techniques enables the essential study of the chemical bonds of the constituents and the micro-(nano)structure[1].

Table I
Chemical composition of some mineral materials

	Earth crust	Portland cement	BF slag	Siliceous fly ash
SiO_2	64	16–26	28–38	55
Al_2O_3	17	4–8	8–24	26
Fe_2O_3	7	2–5	1–3	7
CaO	6	59–67	30–50	8
Na_2O	2	1–4	1–20	1
MgO	2	0.5–1.5	0.2–1	0.5
K_2O	2	0.5–1.5	0.5–3	0.6
SO_3	<1	<0.5	1–3	0.6

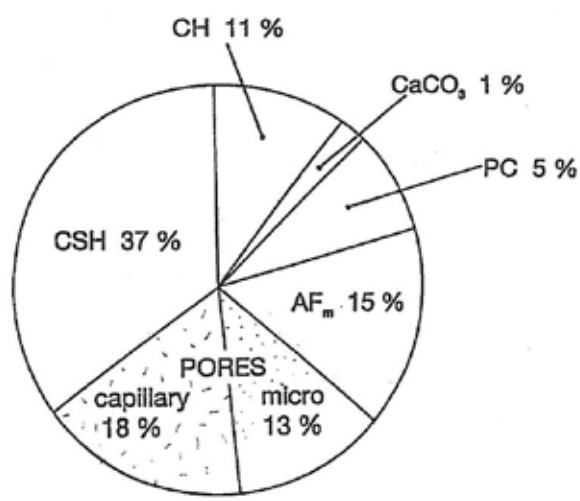

Fig. 1. **Phase composition of the PC paste after 1 year at w/c = 0.5 (Taylor, 1981)**

Chemical Admixtures, Superplasticizers

Very important influence on the production of high-performance concrete exhibit the chemical admixtures of different composition and purpose. Most important, even undispensible, are superplasticizers (SP) enabling to lower considerably the water/cement ratio and thus to increase the strengths or to reduce the cement consumption[2]. At present, broad interest is put on polycarboxylate types SP, which are usually available in solutions, but some newer types of cements (e.g. Danish Secutec) contain the SP in the solid form, which diminish possible mistakes in the preparation of concrete or mortar. Very important is the use of compatible SP in a proper amount, which can be assessed by calorimetric measurement (ref.[3], see next chapters) and slump flow tests.

Self-Compacting Concrete (SCC)

In last decade, self-compacting concrete containing adequate amount of SP are widely used in many different constructions - high-rise buildings, self-leveling floors, in hybrid steel-concrete constructions etc. The viscosity, workability and setting times of superplasticized concrete or mortars are reliably controlled by the slump flow minicone test. By these SCC, steel tubes are filled to reduce the steel consumption at maintaining the total strengths[4]. The use of fine aggregate prevents the segregation.

Reactive Powder Concrete (RPC)

Concrete of ultra-high strengths can be prepared by emitting of coarse aggregate, using only very fine sand under 0.4 mm[5]. This reactive powdered concrete is in fact mortar, RPM. The use of bauxite is recommended, the content of steel microfibers (0.14 × 3 mm) up to 30–50 % to the cement content and thermal treatment enhances the compressive strengths up to 400 MPa[6]. By replacing part of fine sand by steel powder, the strengths can exceed 700 MPa[7]. The first hours of setting under a certain pressure and temperature around 70 °C is recommended.

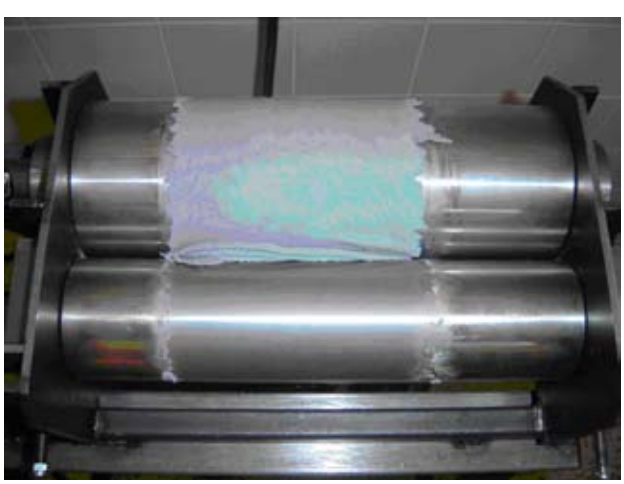

Fig. 2. **Two-cylinder high-shear mixer (mechanochemical activation)**

Gypsum-Free Concrete

Gypsum mixed with the clinker as a retarder of of portland cement setting can be replaced by a higher amount of compatible superplasticizer. Because the start of setting is thus shifted too much, a certain amount of sodium or potassium carbonate must be added[8]. The presence of SP lowers the w/c, the addition of alkalis controls the setting times and the workability of the fresh mixture.

Macro-Defect Free (MDF) Concrete

This composites are in fact inorganic-organic copolymers. The mineral part is cement (portland or aluminate), the organic constituent is polyvinylacohol or certain polyacrylates. MDF materials possess ultra-high flexural strengths up to 150 MPa. Due to very low w/c under 0.15, special high-shear mixing of components is necessary (mechano-chemical activation)[9]. The special two-cylinder mixer (Fig. 2.) will be used also for other composites.

Fig. 3. **Nest of termites (Gambia)**

Green Binders for the Production of Foundry Molds and Cores

The use of water glas as binders in molds for metal casting was introduced in Brno in fifties by prof. Petržela. Some years ago, water glass containing 2 % of sodium aluminate was produced in Poland and introduced on the market under the name Rudal, which can be succesfully used also for the alkali-activation of aluminosilicates in the production of

geopolymers. From organic binders, proteins[13], enzymes and polysaccharides[14,15] can be used. The broad use of these ecologically friendly organic binders enables radical improvement of the hygienic conditions in the casting houses, where due to organic plastics used in the production of cores, toxic emissions are in a high concentration.

Binders for Clayey Materials (Proteins, Polysaccharides, Enzymes)

Clayey materials are usually stabilized by lime or fly ashes (subbases of roads or buildings). Good possibilities show also organic binders on the different bases. In last years, promissing applications show enzymes, decomposing as catalyzers organic constituents in clays forming proteins and saccharides, which act as binders[10,11,12]. This effect is used by the termites - soil eaters building in this way their nests (Fig. 3.) stable against tropical rains. Important is the ratio of siliceous sand to clay. Enzymes used in the construction of roads are available on the market.

Inorganic-Organic Copolymeric Materials

In nature, inorganic – organic copolymers possessing outstanding properties are synthetized succesfully for billions of years and we try in to imitate at least some of them in the R&D by many teams all over the world[16]. To this group of materials, the products of polycondensation of cement with superplasticizers of can be inserted as well as MDF concrete. On the surface of mineral constituents, free cations primarily react with the hydroxyl and/or carboxyl groups of different organic admixtures forming thus copolymers of demanded properties. The mineral admixtures like slag, fly ashes, different aggregate etc. enlarge markedly the assortment of composites possessing tailored properties. The inorganic-organic non-traditional copolymeric materials can be coined without exaggeration as composites for the 21st century.

Geopolymers (Alkali-Activated Alumino-Silicates)

The Activation of Granulated Blast-Furnace Slag (GBFS)

As soon as in seventies, in cooperation with the Research Institute of Building Materials in Kiew, slag-alkaline cements and concrete were prepared[17]. The GBF slag was activated by sodium hydroxide or silicate, forming precursors of zeolites possessing dense amorphous micro(nano)structure and high short-term strengths. Because of efflorescence brought about by sodium carbonate, potassium compounds were succesfully used. These composites of zeolitic character were coined as geopolymers[18], because they are in fact imitation of natural minerals. In the geopolymeric structure silicate and aluminate tetrahedra are connected via oxygen bridges, which can be considered as nanofibers. The calcium compounds present in the slag form preferably CSH gel. Instead of BF slag, other aluminosilicates (fly ashes, metakaolin...) can be successfully used – see next paragraphs. It is possible to prepare on slags high-strength geopolymers possessing the compressive strengths over 150 MPa[19]. The zeolitic character of geopolymers gives to these amorphous materials ion-exchanging properties. According to the nature and concentration of the alkaline compound used, the times of setting and strengths can be controled (see Fig. 5.). These composites are very promissing from ecological as well as economical points of view, because as a base component, industrial by-products ("wastes") are used, saving thus mineral natural resources – limestone and lowering considerably the carbon dioxide emissions. Newer research shows that in many ancient buildings (pyramids), geopolymeric material was used and compacted by tamping, similarly to our concrete[20]. Without any doubts, geopolymers can be considered as material for the 21st century.

Geopolymers From Fly Ashes (FA)

The utilization of siliceous fly ashes from high-temperature coal combustion is prefered, the calcium content is rather small. The reaction rate with alkalis is accelerated at higher temperatures[21]. The production of the geopolymers using fly ashes can have regional character due to the wide occurence of this by-product. The possibility of producing lightweight FA geopolymers introduces very interesting and cheap building material[21] resisting to higher temperatures.

Geopolymers From Metakaolin

By burning kaolin at the temperatures around 750 °C, metaolin is formed, which in the very fine form reacts with alkali hydroxides, carbonates or silicates. These products do not contain calcium oxide and are coined "pure" geopolymers. Preferably, some silica can be added to increase the SiO_2 content. The mutual ratio of the components is aproximately $Na(K)_2O \cdot Al_2O_3 \cdot 4SiO_2 \cdot 10H_2O$. The amorphous character of this zeolite precursor has ion-exchanging properties and can be used for the immobilization of potentially toxic components. The mixture of potassium hydroxide activated metakaolin (10 %) with fine quartz sand (90 %) was succesfully used for the production of sculptures resembling sandstone[22].

The Use of Solid Residues After Fluidized Bed Coal Combustion (FBCC)

Due to lower combustion temperature (around 850 °C) of coal, the solid residues – coarse bed ash and fine fly ash from separators – have different chemical and phase composition in comparison to the high-temperature fly ashes. These residues contain rather high amount of free lime and calcium sulfate (up to 15–20 %) and possess hydraulic properties[23]. The addition of superplasticizers makes it possible to lower the w/c under 0.30, the 28 days compressive strengths are without any further admixtures up to 70 MPa. The possibility to replace gypsum in portland cement production by this material was very succesful, the long-term strengths of the pastes or composites with the addition of FBCC ashes were increased. The presence of solfites in these FA does not interfere. The alkali activation of the FBCC fly ashes can be used for the immobilization of toxic wastes.

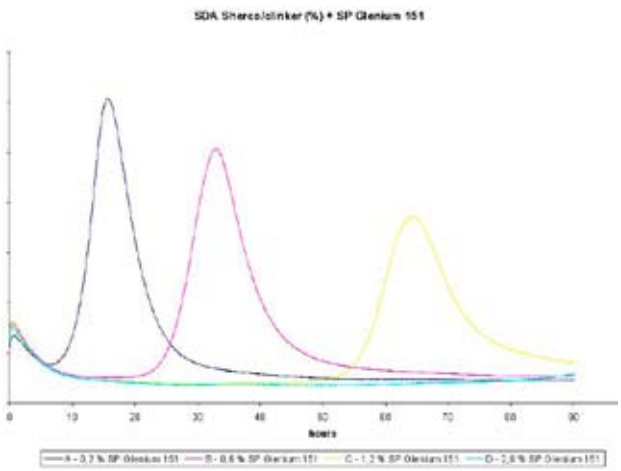

Fig. 4. **Calorimetric measurement of FBCC FA paste containing increasing amount of superplasticizer Glenium 151**

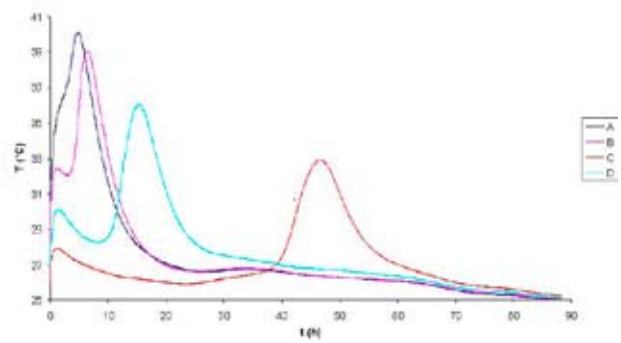

Fig. 5. **Calorimetric measurement of mixtures of BF slag containing decreasing amount of alkali activateing water glass solution (see next Table II)**

Lightweight Composite Based on the Formation and Decomposition of Ettringite, AF_t

Non-traditional composites based on FBCC ashes, energogypsum and lime were developed. According to the chemical composition of the ashes, lime hydrate is added to form CSH gel. At higher temperature, in superplasticized mixture ettringite AF_t is formed, which is due to the consequently enhanced temperature decomposed under the formation of bassanite and monosulfate AF_m. For the compressive strenghts 6–15 MPa, CSH gel is responsible. The volume density is 1,300–1,500 kg m^{-3}.

Application of Calorimetric Methods, Kinetics of Reactions

In optimization of compositions of concrete and mortars, one of the main role sis played by the proper type and amount of admixtures, especially superplasticizer. The use of calorimetery proved to be very suitable metod measuring the hydration heat evolution in time, influenced by the admixtures, w/c, starting temperature etc. The course of reactions enable to assess start and time of setting. The semiadiabatic calorimeter[3] makes it possible to measure series up to 16 samples at the same time. The samples of the fresh mixture (usually 300.0 g) in styrofoam thermoinsulated beakers contain thermoelements connected to the measuring card of the computer enabling to evaluace the results. On next figures, curves ilustrate the influence of the SP content on the start and time of setting (Fig. 4.) and effect of the different amount of sodium component on the activation of blast turnace slag (Fig. 5.).

Table II
Composition of mixtures to the Fig. 5.

	A	B	C	D
BF slag [g]	450	500	460	325
Alkal.activator [ml]	120	90	37.5	50
Water [ml]	30	60	112.5	50

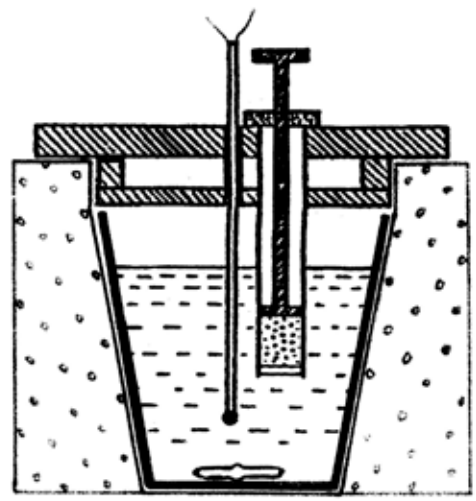

Fig. 6. **Solution calorimeter (enthalpimeter)**

Very useful information can be obtained by the solution calorimetry (enthalpimetry, Fig. 6.), enabling rapid determination of the quality or composition of powdered samples. The thermal impulse of the reaction of the sample with a reagent (e.g. dil. HCl) depends not only on the chemical composition, but also on the fineness of the sample – the specific surface area. This metod enables the rapid determination of some constutuents, which are by other methods time consuming, e.g. determination of the SiO_2 content, sulfates, activity of lime etc.The producers of different binders or metakaolin use enthalpimetric metod for the determination of the effect of grinding.

Discussion and Conclusions

The published papers and different printed matters contain a great amount of novel information, but to find really progressive ones in a given branch is not easy. I tis a pleasure to present, that the effort of increasing the productivity of materials is still more often a main topics of R&D of many

teams all over the world. In the building industry, the utilization of solid by-products of metallurgy and energetic industry ("wastes" like fly ashes, slags, energogypsum etc.) are in fact important raw materials, bringing about marked lowering of carbon dioxide emissions at the same time. These and related problems are solved by our students in diploma and doctoral theses. It is necessary to improve the information activities including the specialized education at all types of schools and thus to contribute to the sustainable development of the society.

REFERENCES

1. Aitcin P. C.: *High-Performance Concrete*. E & FN Spon, Routledge, London, 1998.
2. Brandštetr J., Krátký J., Szklorzová H.: Superplasticizers in concrete and mortars (in Czech). Part I: Silika *13(7–8)*, 214 (2003), Part II: Silika *14(1–2)*, 40 (2004).
3. Brandštetr J., Polcer J., Krátký J., Holešinský R., Havlica J.: Cem. Concr. Res. *31*, 941 (2001).
4. Lukáš J., Brandštetr J., Hela R.: *Proceedings of the International Conference on Bridges*, p. 1032. Dubrovnik, 2006.
5. Brandštetr J.: Minerální suroviny *1*, 23 (1999).
6. Brandštetr J., Havlica J., Opravil T., Frank V.: Silika *17*, 212 (2007), *Proceedings of the III. Conference Non Traditional Cements and Concrete* (V. Bílek and Z. Kyršner, Ed.), p. 119. Brno 2008.
7. Richard P., Cheyrezy M.: *In : Concrete Technology, Past, Present and Future* (Mehta P. K., Ed.). ACI SP p. 144. Detroit 1993.
8. Škvára J., Brandštetr J., Krátký J. : *Plasticizer for the production cement pastes, mortars and concrete.* CZ. pat. No. 297 701 (2007)
9. Šoukal F., Brandštetr J., Havlica J., Odler I.: Silika *17*, 45 (2007).
10. Cagášková L.: Diploma project, FCH BUT, Brno 2006.
11. Horák J. : Diploma project. FCH BUT, Brno 2005.
12. Horák J., Omelková J., Cagášková L., Brandštetr J.: Silika *26*, 146 (2006).
13. Kramářová D., Brandštetr J., Rusín K.: Chem. Listy *99*, 1234 (2008).
14. Laichman L.: Doctoral thesis, FCH BUT, Brno 2008.
15. Laichman L., Brandštetr J., Rusín K. : *Proceedings of the 8th Internat. Foundryman Conference*, p. 1. Zagreb, 2008.
16. Wegner G.: Acta Mater. *48*, 253 (2000).
17. *Proceedings of the conference „Slag-alkaline Cements, Concrete and Constructions*"(Glukhovskiy V.D. and Krivenko P.V., Ed.s.). SRIBM, Kiew 1984.
18. Davidovits J.: J. Thermal Anal. *37*, 1533 (1991).
19. Shi C., Krivenko P. V., Roy D. M.: *Alkali-Activated Cements and Concretes*. Taylor & Francis, 2006.
20. Davidovits J.: *Geopolymer*. Institut Geopolymér, Saint Quentin, 2008. pp. 596.
21. Škvára F., Kopecký L. Němeček J., Bittner J.: Ceramics-Silikáty *50*, 208 (2006).
22. Opravil T., Brandštetr J., Havlica J., Šrámková E.: *Proceedings of the III. Conference Non-Traditional Cements and Concrete* (V. Bílek and Z.Keršner, Ed.), p. 508. Brno 2008.
23. Opravil T., Ptáček P., Šoukal F., Brandštetr J.: *Proceedings of the X. conference "Ecology and New Building Materials"*. p. 99, Brno 2006.

L03 THE EFFICACY OF DEACIDIFICATION BY AEROSOLS OF MgO AND DOLOMITE MICROPARTICLES

SILVIA HOLÚBKOVÁ[a], MICHAL JABLONSKÝ[a], MARTINA BAJZÍKOVÁ[b], JOZEF HANUS[c], JOZEF RYCHLÝ[d], VLADIMÍR BUKOVSKÝ[b] and SVETOZÁR KATUŠČÁK[a]

[a]*Institute of Polymer Materials, Department of Chemical Technology of Wood, Pulp and Paper, Faculty of Chemical and Food Technology, Slovak University of Technology, Radlinského 9, 831 07 Bratislava, Slovak Republic,*
[b]*Slovak National Library, Nám. J. C. Hronského 1, 036 01 Martin, Slovak Republic,*
[c]*Slovak National Archives, Drotárska cesta 42, 81 701 Bratislava, Slovak Republic,*
[d]*Polymer Institute, Slovak Academy of Sciences, Dúbravská cesta 9, 842 36 Bratislava, Slovak Republic,*
silvia.holubkova@stuba.sk

Introduction

It has long been widely acknowledged that paper which is produced in an industrial way is endangered by acid decomposition or oxidation[1]. The degradation process can be stopped effectively by neutralisation and the insertion of an alkaline buffer[2].

Application of mass deacidification process is connected with problems in controlling its efficacy and quality. There are no unified criteria for evaluating particular processes of mass deacidification[3]. Alkaline reserve, pH, their homogenity and effect of deacidification agents are among those used within the scope of evaluation[4,5,6,7]. Nowadays, each organization brings own new parameters to evaluating the deacidification process. Evaluation according to the criteria of 'Library of Congress, Pittsburgh'[4] is one of the options. Another option is evaluation of the process efficacy according to criteria of Swiss National Library, Bern[3,7,8,9].

Deacidification processes produce specific side effects on treated materials, according to their chemistry and method of application. Organic solvents used in, or produced during, liquid-phase processes can cause bleeding of dye stuffs (especially red dyes) in textile book covers, in inks, and stamps. All the deacidification methods using liquid can cause deformation and cockling of paper and binding[8].

Alkaline particles, such as MgO and dolomite micro-particles in the air (SoBu)[10], MgO and CaO in the air (Libertec)[11] and MgO in a perfluoralkanes (Bookkeeper)[4] are also used in deacidification of books and archival documents containing cellulose base. The most significant effect of deacidification methods based on the application of sub-micron particles is a whitish powdery deposit on paper and binding surfaces, obviously the deacidification agent (magnesium oxide, calcium oxide, dolomite microparticles and calcium carbonate). It can be easily removed by brushing, but this creates additional and time-consuming work. If it remains in the book, it can spray out during the use with the risk of health problems for the user[8].

Experimental

Raw Material

Wood containing newsprint paper (grammage 45 g m^{-2}, surface pH: 5.6) containing mechanically bleached, groundwood (55 %), bleached sulphite pulp (20 %), cought trash fibres (15 %) and clay (10 %) was used in experiments. The test books (format A5) were sent for treatment to Sobu (Fürth) company providing commercial mass deacidification.

Accelerated Ageing Procedure

Samples of paper were conditioned according to TAPPI T402 om – 93[12] at 23 ± 1 °C, and at relative humidity of air RH = 50 ± 2 %. Seventy-five sheets of paper (A5 format) were encapsulated inside a PET/Al/PE bag. The samples were aged at 96 ± 2 °C for 0, 2, 5, 10 and 15 days according to ASTM D 6819 – 02: Standard test method for accelerated aging of printing and writing paper by dry oven exposure apparatus, in which sealed glass tubes were replaced by a composite foil made of polyethylene / aluminium / polypropylene (TENOFAN Al / 116S). After ageing, the papers were conditioned for testing according to TAPPI T402 om - 93[12].

Mechanical Properties

Breaking length was determined according to TAPPI T494 om – 88[13] and the folding endurance was determined using the MIT apparatus according to TAPPI T511 om – 96[14] with a tension of 0.3 kg instead of the standard 1 kg.

Evaluation of Treatment Effectiveness

The comparison of treated/modified ($X_{t,m}$) and non-treated/non-modified ($X_{t,n}$) samples after the same period and conditions of ageing is expressed as:

$$S_{X,t} = \frac{X_{t,m}}{X_{t,n}}, \qquad (1)$$

where $S_{X,t}$ stands for permanence coefficient by given treatment, X – examined properties (the breaking length (l_t) and the folding endurance (ω)), t– ageing period

If $S_{X,t} > 1$, the permanence is increased; if $S_{X,t} = 1$, it is not changed; $S_{X,t} < 1$, the permanence is decreased[15].

Linear dependence was obtained after calculating the logarithm of double folds. Time values for $\log \omega = 0$ were calculated from linear equation. Values were used for relative comparison the efficacy of deacidification process to non-treated control sample.

The lifetime of the paper ends when logarithm of the folding endurance becomes zero ($t_{\log \omega} = 0$)

The coefficient of relative increase of the lifetime for folding endurance ($S_{\tau,\omega}$) is to be expressed as eq (2).

$$S_{\tau,\omega} = \frac{t_{\log \omega=0,\, m}}{t_{\log \omega=0,\, n}} \,. \qquad (2)$$

Results

Kinetic dependences of changes in mechanical properties of paper were evaluated. Average values and average divergences that only indicate the variability recorded in measurement, are given for all kinetic dependences.

Stability of paper treated by aerosols of MgO and dolomite microparticles was compared to non-treated paper.

The loss of breaking length under ageing is shown in Fig. 1.

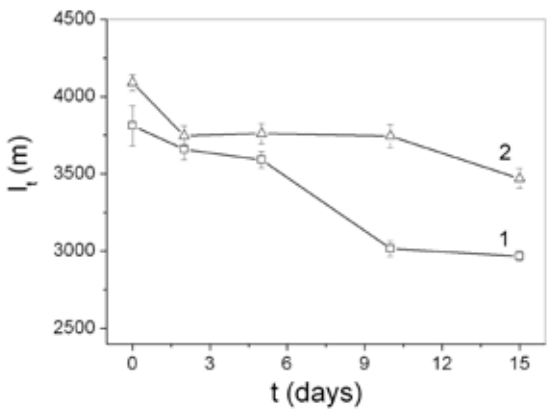

Fig. 1. **Effect of ageing time [days] on breaking length [m]:**
1 – non-treated newsprint paper
2 – newsprint paper treated by aerosols of MgO and dolomite microparticles

The breaking length of unaged non-treated paper was 3,811 m. After 15 days of ageing, the loss of strength decreased by approx. 22 % (2,968 m). After deacidification by aerosols of MgO and dolomite microparticles, the measured breaking length was 4,090 m. After 15 days of ageing, the loss of strength decreased by approx. 15 % (3,470 m). Permanence coefficient of the breaking length for unaged paper was evaluated $S_{lt,0} = 1.1$, the modification caused slight strengthening effect. The permanence of breaking length after 15 days of ageing was $S_{lt,15} = 1.2$, hence the modification caused positive stabilization effect.

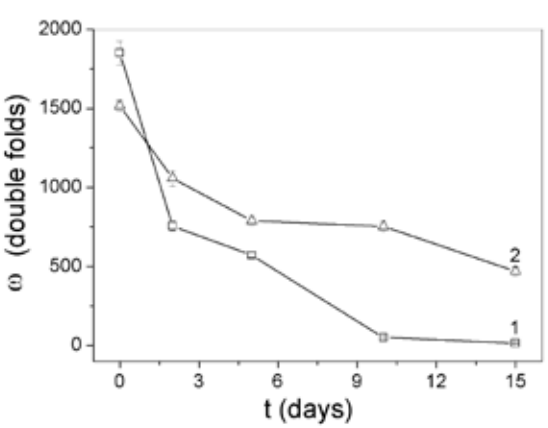

Fig. 2. **Effect of ageing time [days] on folding endurance [double folds]:**
1 – non-treated newsprint paper
2 – newsprint paper treated by aerosols of MgO and dolomite microparticles

The following picture (Fig. 2.) shows folding endurance (ω, double folds, load 0.3 kg) as a function of ageing time.

The number of double folds of untreated paper was 1850. After 2 days of ageing, the number of double folds decreased rapidly (754). After 15 days of ageing, the folding endurance was reduced to 51 double folds. After the deacidification by aerosols of MgO and dolomite microparticles 1515 double folds were determined. The number of double folds kept decreasing during the ageing process, however, the decrease rate was slower comparing to non-treated sample. After 15 days of ageing, the folding endurance was reduced to 470 double folds. The permanence coefficient of folding endurance for unaged paper was evaluated $S_{\omega,0} = 0.8$, which implies that the modification process did not result in strengthening effect, however, stability increased significantly after 15 days of ageing reaching $S_{\omega,15} = 33.6$.

The logarithm of folding endurance related to ageing time is shown in Fig. 3.

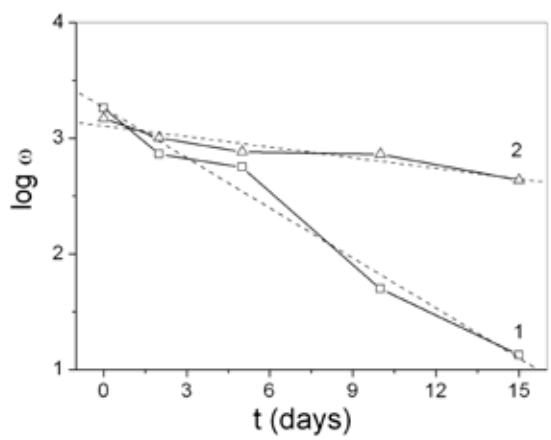

Fig. 3. **Effect of ageing time [days] on logarithm of folding endurance:**
1 – non - treated newsprint paper
2 – newsprint paper treated by aerosols of MgO and dolomite microparticles

Time values for $\log \omega = 0$ were calculated from linear equation. The coefficient of relative increase of the lifetime was calculated from formula (2) $S_{\tau,\omega} = 4.7$; which means that stability of modified paper increased by 470%.

To compare the air–MgO–dolomite microparticles technological platform (TP) to other recent TPs, the following criteria of multifactorial evaluation system of Consortium Kniha[SK] and Library of Congress[4] have been used:

- Innovation potential. Potential of the future development, research, and further education.
- Efficacy in term of increase stability of mechanical properties and life-time prolongation.
  It is the criterion of efficacy of deacidification process according to the Library of Congress[4] on tested paper, which is expressed as the rate at which paper loses strength upon accelerated ageing at 90°C / 50 RH for up to 30 days, shall be decreased by at least a factor of 3.0, when the logarithm of the folding endurance is plotted against time in days ($S_{\tau,\omega}$). The permanence of the treated paper shall be increased by a factor of 300%.
- pH and alkaline reserve,
- Price
- Risk:
  Deterioration of documents, possibility of deacidification of books without their damage, sensorial properties
  Explosion hazard
  Flammability hazard
  Health hazard
  Environmental hazard

On the basis of criteria of multifactorial evaluation system the air–MgO–dolomite TP deacidification fulfills the Consortium Kniha[SK] and Library of Congress[4] requirements for the lifetime increase ($S_{\tau,\omega} = 4.7$), improves the mechanical permanence sufficiently ($S_{\omega,15} = 33.6$; $S_{lt,15} = 1.2$). It is the most advanced, the cheapest and safest one as well (in terms of danger of fire or explosion). Platform HMDO is progressive, however, danger of fire or explosion is significant and is severalfold more expensive. The other TPs are less suitable for deacidification or not suitable for deacidification of books.

The most ecological methods are based on platform water/air regarding the environmental quality, tenability and future prospects. Freons are used in less eco-perspective TPs of which global warming potential is by 320–8,400 times higher than that of CO_2.

Conclusions

The paper was aimed at evaluating the deacidification by aerosols of MgO and dolomite microparticles. The research was based on examination of mechanical properties through multifactorial evaluation according to the requirements of Consortium Kniha[SK] and Library of Congress[4].

The air–MgO–dolomite deacidification TP fulfills requirement for the lifetime increase ($S_{\tau,\omega} = 4.7$), it does improve the mechanical permanence sufficiently ($S_{\omega,15} = 33.6$; $S_{lt,15} = 1.2$). It is most advanced, the cheapest, the most ecological and safest one as well (in terms of danger of fire or explosion or health hazards).

We thank to Project of ME SR No. 2003 SP 200280301 Preservation, Stabilization and Conservation of Traditional Information Carriers in the Slovak Republic for financial support.

REFERENCES

1. Liers, J.: Restaurator *20* (1999).
2. Liers, J.: Restaurierung *2* (2001).
3. Swiss National Library: *International Conference: SAVE PAPER,* p. 94. *Bern, 15–17.Feb. 2006* (Banik, G., Doering, T., Hähner, U.).
4. Buchanan, S., Bennett, W., Domach, M. M.: *An evaluation of the Bookkeeper mass deacidification process*. Pittsburgh 1994.
5. Harris, K., E.: *A paper chase saving the written word at the Library of Congress.* Washington DC 1999.
6. Swiss National Library: *Quality standards for the paper-save Swiss process used for the deacidification of the collections of the Swiss federal archives and the Swiss federal office of culture.* Bern 2004.
7. Swiss National Library: *International Conference: SAVE PAPER,* p. 7. *Bern 15–17. Feb 2006* (Grossenbacher, G).
8. Banik, G.: Restaurator *26*, 1 (2005).
9. Bluher, A.: Papier Restaurierung *4*, 4 (2003).
10. www.sobu.de, 2008 – 05 – 19.
11. www.libertec.de, 2008 – 05 – 19
12. TAPPI T402 om – 93: *Standard conditioning and testing atmospheres for paper, board, pulp handsheets, and related products*.
13. TAPPI T494 om – 88: *Tensile breaking properties of paper and paperboard (using constant rate of elongation apparatus)*.
14. TAPPI T511 om – 96: *Folding endurance of paper (MIT tester)*.
15. Vrška, M., Katuščák, S., Polovka, M., Vizárová, K., Cedzová, M., Hanus, J., Mináriková, J., Bukovský, V.: Wood Res. *49,* (2004).

L04 DISTRIBUTION OF HEAVY METALS IN THE PRODUCTS OF MAGNETIC SEPARATION OF SIDERITE ORE FROM NIŽNÁ SLANÁ

SLAVOMÍR HREDZÁK, MICHAL LOVÁS, ŠTEFAN JAKABSKÝ, DANA GEŠPEROVÁ and MARIÁN BALOG

Institute of Geotechnics of the Slovak Academy of Sciences, Watsonova 45, 043 53 Košice, Slovak Republic, hredzak@saske.sk

Introduction

The mining company Siderite, Ltd. Nižná Slaná is only one producer of iron ore in Slovakia. The mining field of the company is located in the southeast part of the Slovak Ore Mts. and it consists of two near one another placed deposits (their distance is about 2,500 m), namely Manó and Kobeliarovo.

The ore from the first of one contains in the average 33.5 % of Fe, 2.18 % of Mn, 8.5 % of SiO_2, 0.001–0.2 % of As, 0.001–0.03 of Pb, 0.002–0.009 % of Zn and 0.5–1.5 of S. The average quality of ore from the Kobeliarovo deposit is as follows: 33.98 % of Fe, 1.71 % of Mn, 3.71 of SiO_2 and 0.02 % of As[1]. The ores from the both deposit are characterized by fine intergrowth of utility minerals and gangue.

The company exploits siderite ore by underground method, namely sublevel caving. The run-off-mine ore is subjected to crushing and classifying. The coarser classes are pre-treated using a dry high intensity magnetic separation. Only class with a grain size of 0–4 mm is led through bypass and directly added to magnetic product obtained by separation of coarser classes. In such way obtained material is roasted in rotary furnaces with the aim to improve the magnetic properties of main utility Fe-bearing mineral, i.e. siderite. Thus, during magnetizing roasting, siderite is changed into magnetite and/or maghemite with much higher magnetic susceptibility. After cooling the roasted ore is wet ground to a grain size 90 % under 63 μm and subjected to wet low intensity magnetic separation. Magnetic product is filtered and led to pelletizing plant. Final product – blast furnace pellets usually contain 55.4 % of Fe, 3.4 % of Mn and 5 % of SiO_2.

Currently, an annual production of ore is running about 720,000 tons. Subsequently, 320,000 tons of blast furnace pellets are made from the ore[2]. Maximal annual production, i.e. 1,010,365 tons of ore and 447,810 tons of pellets, was attained in 2000[3].

As it was mentioned above, up to now, the ore fraction with a grain size of 0–4 mm is not magnetically pre-treated and it is directly led to rotary furnaces. Its mass yield usually ranges 15–20 %[3], but at some time it can attain up to 45 %, in dependence on grain size quality of run-off-mine ore, resulting from conditions at exploitation. The coarser ore pre-treatment by dry high magnetic separation is aimed at the decreasing of free quartz and accompanying rocks amount in the feed to rotary furnaces. After running-in of this technological line the management of company has begun to pay higher attention to the possibilities of quality improvement of the 0–4 mm class, which can significantly influence the quality of final product especially concerning undesirable components content.

Thus, under laboratory conditions, a dry grain size analysis and tests of dry magnetic separation were performed at the Institute of Geotechnics of the SAS in Košice with the aim to determine the distribution of chemical components as a function of grain size and to verify the possibilities of dry separation of this class.

Experimental

Condition of Dry Magnetic Separation

Dry magnetic separation was carried out using a universal laboratory magnetic separator JONES (Fig. 1.), in a cassette intermediate between of poles separator. The cassette was equipped by two plates, grooved and flat ones, made of carbon-free iron owing to ensuring of required induction and gradient of magnetic field with regard to maximal grain size of a feed (Fig. 2.).

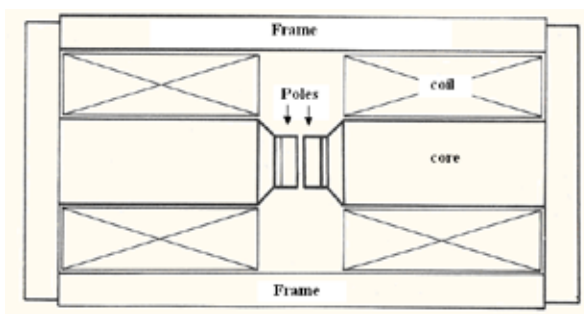

Fig. 1. **Design of the JONES separator**

Fig. 2. **The cassette equipped by plates**

Thus, the conditions of magnetic separation at three values of magnetizing current and appropriate inductions of magnetic field are introduced in Table I.

Methods of Assessment

After determination of mass yields the products of classifying and separation were subjected to chemical analyses and measurements of volume magnetic susceptibility. Loss

Table I
Conditions of magnetic separation

Magnet. current [A]	Induction of magnetic field [T]	
	Top of groove	Flat plate
1.50	0.60	0.47
1.75	0.70	0.54
2.00	0.75	0.60

on ignition (LOI) at 900 ºC and SiO_2 content were assayed gravimetrically. Other elements have been determined by atomic absorption spectroscopy using the device VARIAN with accessories: Fast Sequential AAS AA240FS, Zeeman AAS AA240Z with Programmable Sample Dispenser PSD120, Graphite Tube Atomizer GTA120 and Vapor Generation Accessory VGA-77. Mercury in the products of magnetic separation was assayed using a Trace Mercury Analyser TMA 254.

The volume magnetic susceptibility "κ" measured using the device Kappabridge KLY-2, Geofyzika Brno at the following conditions: a magnetic field intensity of 300 A m^{-1}, a field homogeneity of 0.2 %, an operating frequency of 920 Hz, measurement range of device $-1{,}999 \times 10^{-6}/650{,}000 \times 10^{-6}$ SI units[4].

On the basis of mass yields and chemical analyses the recoveries of observed components into products of classifying and separation were calculated according to the method of classical material balance.

Results

Grain Size Analysis

The results are introduced in Tables II and III, respectively. As to values in Table II, it is clear, that content of Fe is higher in coarser classes. The iron content corresponds with content of manganese, magnesium and LOI. Thus, at increasing of Fe content, the contents of all mentioned components increase too. Conversely, contents of SiO_2 and Al are higher in finer classes. Similarly, the highest values of main undesirable elements such as As, Cu, Zn and Ni were detected in the finest classes. Mercury was determined only in the finest class and its content was of 1.5 ppm. As it implies from Table III, the recoveries of observed components into individual classes are strongly influenced by mass yield values as a result of small differences among contents of given component in various classes. But recoveries of utility components, namely Fe and Mn, into coarser classes (2 mm) are higher than recoveries of SiO_2 and Al. Thus, it can be stated, that main utility mineral, i.e. siderite slightly concentrates in classes 2 mm and free quartz and quartz-bearing rocks in finer classes.

Table II
Chemical composition of grain size classes

Grain size [mm]		Yield [%]	κ	Fe [%]	SiO_2 [%]	Mn [%]	LOI [%]	As [ppm]	Al [%]	Mg [%]	Ca [%]	Cu [ppm]	Zn [ppm]	Pb [ppm]	Ni [ppm]
4.0		15.40	873	29.90	8.32	1.79	29.51	630	0.80	3.84	0.44	115.00	70.00	45.00	14.50
3.0	–4.0	15.15	882	29.28	10.94	1.64	28.78	410	1.07	3.70	0.36	100.00	75.00	20.00	16.80
2.0	–3.0	6.99	894	29.52	10.69	1.75	28.71	820	1.08	3.70	0.35	65.00	100.00	20.00	17.80
1.0	–2.0	23.08	891	28.49	11.89	1.68	28.01	700	1.27	3.59	0.32	145.00	115.00	10.00	19.50
0.5	–1.0	16.80	861	27.83	12.11	1.63	27.72	710	1.35	3.55	0.43	95.00	85.00	20.00	21.90
0.25	–0.5	10.39	865	26.64	13.51	1.59	27.11	770	1.67	3.45	0.59	145.00	100.00	15.00	24.90
0.125	–0.25	6.47	863	25.72	12.74	1.52	26.85	980	2.01	3.36	0.45	300.00	140.00	10.00	32.80
0.063	–0.125	4.06	872	26.46	12.13	1.53	26.59	970	1.72	3.52	0.70	185.00	170.00	25.00	34.50
	–0.063	1.66	862	25.15	13.36	1.38	24.80	1160	2.61	3.25	0.38	150.00	125.00	15.00	34.50
feed		100.00	876	28.28	11.40	1.66	28.08	699	1.30	3.61	0.42	131.30	98.38	20.49	20.88

Table III
Recoveries of observed components into grain size classes

Grain size [mm]		Fe [%]	SiO_2 [%]	Mn [%]	LOI [%]	As [%]	Al [%]	Mg [%]	Ca [%]	Cu [%]	Zn [%]	Pb [%]	Ni [%]
4.0		16.28	11.23	16.65	16.18	13.87	9.49	16.39	16.20	13.48	10.95	33.80	10.69
3.0	–4.0	15.68	14.53	15.04	15.52	8.88	12.49	15.54	13.04	11.54	11.55	14.78	12.18
2.0	–3.0	7.30	6.55	7.37	7.15	8.20	5.82	7.16	5.85	3.46	7.11	6.82	5.96
1.0	–2.0	23.25	24.05	23.41	23.02	23.10	22.59	22.94	17.67	25.49	26.98	11.26	21.55
0.5	–1.0	16.54	17.84	16.49	16.59	17.06	17.49	16.55	17.29	12.16	14.52	16.40	17.62
0.25	–0.5	9.79	12.31	9.98	10.03	11.44	13.38	9.95	14.67	11.48	10.56	7.61	12.39
0.125	–0.25	5.88	7.22	5.93	6.19	9.06	10.02	6.02	6.96	14.78	9.20	3.16	10.16
0.063	–0.125	3.80	4.32	3.75	3.85	5.64	5.39	3.97	6.80	5.72	7.02	4.96	6.71
	–0.063	1.47	1.94	1.39	1.46	2.75	3.34	1.49	1.51	1.89	2.11	1.21	2.74
feed		100.00	100.00	100.00	100.00	100.00	100.00	100.00	100.00	100.00	100.00	100.00	100.00

M a g n e t i c S e p a r a t i o n

The quality of separation products obtained at three values of magnetizing current or more precisely induction of magnetic field is described in Tables IV–VI. Subsequently, the recoveries of observed components into separation products, i.e. magnetic (M) and nonmagnetic (N) ones, are introduced in Tables VII–IX.

An increasing of the value of magnetizing current resulted above all in a rising of mass yield into magnetic product. Understandably, the highest Fe content in magnetic product was achieved at the smallest induction of magnetic field, when grains of liberated siderite with the highest magnetic susceptibility are collected in this product. However, the recovery of iron under such conditions is minimal. Thus, with gradually enhancing of induction, the magnetic product is slightly contaminated by waste components, mainly SiO_2, but the recoveries of iron and manganese significantly rise.

Conclusions

Present results of the research on benefication of the class 0–4 mm of siderite ore can be recapitulated as follows:

Table IV
Properties and quality of products obtained at magnetizing current of 1.5 A

Product	Yield [%]	$\kappa \times 10^6$ [SI unit]	Fe [%]	SiO_2 [%]	Mn [%]	LOI [%]	As [ppm]	Hg [ppm]	Al [%]	Mg [%]	Ca [%]	Cu [ppm]	Zn [ppm]	Pb [ppm]	Ni [ppm]
M	33.36	1011	32.31	5.37	1.64	30.46	370	1.30	0.99	3.24	0.28	110	75	15	15
N	66.64	791	25.12	14.60	1.36	26.62	710	1.60	1.64	3.40	0.35	195	100	10	27
feed	100.00	864	27.52	11.52	1.45	27.90	597	1.50	1.42	3.34	0.33	167	92	12	23

Table V
Properties and quality of products obtained at magnetizing current of 1.75 A

Product	Yield [%]	$\kappa \times 10^6$ [SI unit]	Fe [%]	SiO_2 [%]	Mn [%]	LOI [%]	As [ppm]	Hg [ppm]	Al [%]	Mg [%]	Ca [%]	Cu [ppm]	Zn [ppm]	Pb [ppm]	Ni [ppm]
M	58.01	956	30.62	7.23	1.59	29.70	370	1.00	0.94	3.11	0.29	80	80	15	15
N	41.99	720	23.10	17.96	1.27	25.80	890	1.80	1.57	3.21	0.38	130	105	10	26
feed	100.00	857	27.46	11.74	1.46	28.06	588	1.34	1.20	3.15	0.32	101	91	13	19

Table VI
Properties and quality of products obtained at magnetizing current of 2 A

Product	Yield [%]	$\kappa \times 10^6$ [SI unit]	Fe [%]	SiO_2 [%]	Mn [%]	LOI [%]	As [ppm]	Hg [ppm]	Al [%]	Mg [%]	Ca [%]	Cu [ppm]	Zn [ppm]	Pb [ppm]	Ni [ppm]
M	84.20	1003	29.39	8.53	1.56	29.08	570	1.20	1.15	3.46	0.30	135	87	15	21
N	15.80	549	18.04	27.05	1.00	21.37	1200	3.60	2.34	3.16	0.64	145	110	10	26
feed	100.00	931	27.60	11.45	1.47	27.86	669	1.58	1.34	3.41	0.35	137	91	14	22

Table VII
Recoveries of components into separation products at magnetizing current of 1.5 A

Product	Fe [%]	SiO_2 [%]	Mn [%]	LOI [%]	As [%]	Hg [%]	Al [%]	Mg [%]	Ca [%]	Cu [%]	Zn [%]	Pb [%]	Ni [%]
M	39.16	15.55	37.68	36.42	20.69	28.91	23.21	32.31	28.59	22.02	27.30	42.89	21.50
N	60.84	84.45	62.32	63.58	79.31	71.09	76.79	67.69	71.41	77.98	72.70	57.11	78.50
feed	100.00	100.00	100.00	100.00	100.00	100.00	100.00	100.00	100.00	100.00	100.00	100.00	100.00

Table VIII
Recoveries of components into separation products at magnetizing current of 1.75 A

Product	Fe [%]	SiO_2 [%]	Mn [%]	LOI [%]	As [%]	Hg [%]	Al [%]	Mg [%]	Ca [%]	Cu [%]	Zn [%]	Pb [%]	Ni [%]
M	64.68	35.74	63.35	61.40	36.48	43.42	45.27	57.21	51.32	45.95	51.28	67.45	44.83
N	35.32	64.26	36.65	38.60	63.52	56.58	54.73	42.79	48.68	54.05	48.72	32.55	55.17
feed	100.00	100.00	100.00	100.00	100.00	100.00	100.00	100.00	100.00	100.00	100.00	100.00	100.00

Table IX
Recoveries of components into separation products at magnetizing current of 2 A

Product	Fe [%]	SiO_2 [%]	Mn [%]	LOI [%]	As [%]	Hg [%]	Al [%]	Mg [%]	Ca [%]	Cu [%]	Zn [%]	Pb [%]	Ni [%]
M	89.67	62.68	89.26	87.88	71.68	63.98	72.36	85.35	71.41	83.22	80.82	88.88	81.14
N	10.33	37.32	10.74	12.12	28.32	36.02	27.64	14.65	28.59	16.78	19.18	11.12	18.86
feed	100.00	100.00	100.00	100.00	100.00	100.00	100.00	100.00	100.00	100.00	100.00	100.00	100.00

- utility components of ore, i.e. Fe and Mn, a slightly more concentrate into coarser fractions 2 mm,
- conversely, gangue represented above all by SiO_2 and Al concentrates into finer ones bellow 2 mm,
- a relative high content of As from 980 to 1,160 ppm was detected in fines bellow 0.25 mm,
- similarly, higher contents of other heavy metals such as Cu, Zn and Ni were also determined in fines, while the highest content of Pb was identified in the coarsest fraction,
- an increasing of magnetic field induction at separation resulted in slight reduction of Fe and Mn content in magnetic product, but also in significant enhancement of their recoveries.

Finally, it can be recommended:

- to reject the fraction with a grain size of 0–0.25 mm from technological flowsheet and in such way to prevent the contamination of final product by heavy metals,
- to apply magnetic induction about 0.7–0.8 T at separation process to avoid losses of iron and manganese in nonmagnetic product.

This work has been supported by the Slovak Research and Development Agency on the basis of the contract No. APVV-51-035505 and Slovak Grant Agency for the VEGA projects No. 1/4193/07 and 2/0087/08 as well as the Task of the State Program No. 2004 SP 26 028 0C 01 "High Tech and New Technologies for the field of obtaining and processing of industrial minerals".

REFERENCES

1. Boláček O., Mihók J.: Iron Ore Works, Nižná Slaná, 1994. In: Grecula P. et al.: *Mineral deposits of the Slovak Ore Mountains*, Vol. 1., Geocomplex, Bratislava 1995.
2. Investment project: Innovation of technological process of the Siderit, Ltd. Nižná Slaná and development of reserves of the Nižná Slaná – Manó – Kobeliarovo deposit, Attachment 3.
3. Lukáč S.: Acta Montanistica Slovaca *7*, 227 (2002).
4. Kappabridge KLY-2: Instruction manual for magnetic susceptibility bridge, Geofyzika Brno.

L05 MAGNETICALLY MODIFIED BENTONITE AND STUDY OF ITS IMPROVED SORPTION PROPERTIES

ZUZANA OROLÍNOVÁ and ANNAMÁRIA MOCKOVČIAKOVÁ
Institute of Geotechnics, Slovak Academy of Sciences, Watsonova 45, 043 53, Košice, Slovak Republic, orolinova@saske.sk

Introduction

Clays are naturally occurring aluminosilicates having sheet structure. Natural clays are low-cost and available materials functioning as cation exchangers. They have often been used to adsorb metallic contaminants. Among the three basic classes of clays – kaolinite, micas, smectites, the last mentioned have the largest surface area and the highest cation exchange capacity. If the major mineral in clay is montmorillonite or a member of other smectites, than, it is called bentonite[1]. For evaluation its behaviour against chemical attack, bentonite attracted the researcher's concern for a long time and has been studied extensively[2].

Use of natural bentonite in treating aqueous waste containing heavy metals and organic matter has been previously reported in many works.[3–5] Natural bentonites are usually activated or modified with the aim to improve their sorption properties.[6–7]

It is documented that nano-scaled magnetic particles could be also used for sorption purpouses and they are good sorbents of contaminants from aqueous or gaseous effluents[8].

In this work the natural bentonite was modified by the magnetic particles with the aim to enhance its sorption properties. The structural, surface, porous and sorption properties of composite materials were studied.

Experimental

M a t e r i a l s

The natural bentonite originated from the locality Stará Kremnička – Jelšový potok. It was first treated by sedimentation method to obtain monomineral fraction with the particle size below 20 μm.

The composite materials were prepared from the solutions of ferric and ferrous salts, where bentonite was added before the iron oxide precipitation. The magnetic particles were precipitated by NH_4OH added dropwise. The bentonite dosage was adjusted in order to obtain different bentonite/iron oxide wight ratios 1 : 1, 5 : 1 denoted as A, E respectively. The modification process was realized at two selected temperatures 293 and 358 K.

M e t h o d s

The nitrogen adsorption experiments were realized with Micrometrics ASAP 2400 apparatus (Slovakia). The specific surface area S_{BET} was calculated from the adsorption isotherms according to the BET (Brunauer, Emmett, Teller) method in a range of relative pressure 0.03–0.2 p/p_0. The value of total pore volume V_a was determined from the amount of adsorbed volume at relative pressure close to saturation pressure. The micropore volume V_{micro} and value of external surface S_t were obtained from the *t*-plot analysis. The pore size distribution of studied materials was calculated using the BJH (Barett-Joyner-Halenda) method from the desorption isotherms.

Powder X-ray diffraction (XRD) patterns were collected using a Philips PW1820 (Germany) equipped with a CuKα radiation (40 kV, 40 mA). The JCPDS PDF database was used for the phase identification.

Mössbauer spectroscopy measurements were carried out with a ^{57}Co/Rh γ-ray source (Germany) at the room temperature. The velocity scale was calibrated relative to ^{57}Fe in Rh. Recoil spectral analysis software was used for the quantitative evaluation of the Mössbauer spectra[9].

The value of magnetization of the samples was determined by the superconducting quantum interference device (SQUID) magnetometer measurement (Germany) at the maximum field of 50 kOe.

The scanning electron microscopy (SEM) analyses were made in JEOL JSM-6400 (Germany). Elements present in composites surface were determined using the energy dispersive analyzer of X-rays (EDAX) on the SEM.

The sorption of zinc from model aqueous solutions by the natural and magnetically modified bentonite was carried out using batch-type equilibrium experiments in a rotary shaker for 24 hours at constant ambient temperature. The initial total metal ion concentration range was 10–100 mg dm^{-3}. Sorption experiments were realized at pH = 5 and the sorbent concentration was 2 g.dm^{-3}. The final metal concentration was determined by atomic absorption spectroscopy (AAS using a Varian Spectr AA-30) and the metal uptake was calculated from the difference. Sorption isotherms have been fitted with Langmuir equation. The sorption capacities of the natural and modified bentonite were compared.

Results

The adsorption and desorption isotherms of the natural and modified bentonite, shown in Fig. 1.(a), (b), were obtained from the adsorbed and desorbed gas plotted against the relative pressure. The hysteresis loops are associated with the capillary condensation that is typical for mesoporous materials. The final arising part of the isotherms assigns the occurrence of macropores in the structures[10]. The values of BET surface area calculated from the adsorption isotherm, values of external surface and pore volume are included in Table I. The composite materials showed once more higher values of specific surface area compared to the bentonite. The value of total pore volume has the increasing tendency in dependence of the higher content of iron oxide in the composites. The higher values of the specific surface area and increasing values of total pore volumes should be explained by the secondary pore structure formation caused by the creating of agglomerates on the bentonite surface during the iron oxide precipitation. The *t*-plot method is a transformation of adsorption

isotherm in which relative pressure is replaced by *t* (estimated statistical thickness of adsorbed layer of nitrogen). Plot of *V* (adsorbed gas volume) versus *t* was linearized in the range from 0.354 nm (thickness of adsorbed monolayer) to 0.5 nm (corresponding roughly to the range of relative pressures 0.1–0.2) and the extrapolation of this plot to $t = 0$ gave the values of specific volume of micropores. As follows from the Fig. 2. the contribution of small pores to the total pore volume is not significant because the values of the micropore volume obtained by this method were almost equal to zero.

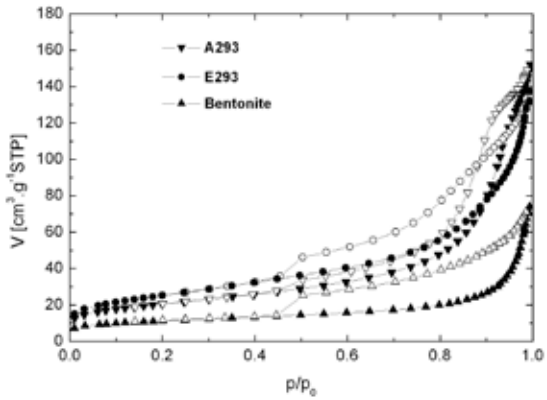

Fig. 1.(a) **Adsorption – desorption isotherms of natural and modified bentonite at 293 K (filled symbols – adsorption isotherms, open symbols – desorption isotherms)**

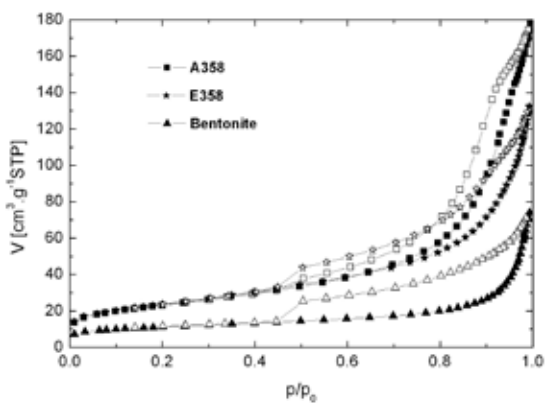

Fig. 1.(b) **Adsorption – desorption isotherms of natural and modified bentonite at 358 K (filled symbols – adsorption isotherms, open symbols – desorption isotherms)**

Distribution of adsorbed volume in the investigated samples was estimated by the BJH method from the desorption isotherms. Fig. 3. shows the dependence of the volume density distribution on the average pore diameter of the natural bentonite and its modified samples.

The curves of the composite materials indicate the increase in the volume in mesopores in comparison to the natural bentonite. The analysis has shown that the porosity of modified samples varied with the different content of magnetic

Table I
Structural parameters of the investigated samples

Sample	S_{BET} [$m_2 g^{-1}$]	V_a [$cm^3 g^{-1}$]	V_{micro} [$cm^3 g^{-1}$]	S_t [$m^2 g^{-1}$]
Bentonite	39.4	0.096	0.005	27.6
A293	73.7	0.216	0.004	64.2
E293	90.7	0.187	0.002	83.9
A358	82.8	0.251	0.004	73.7
E358	84.8	0.183	0.003	77.5

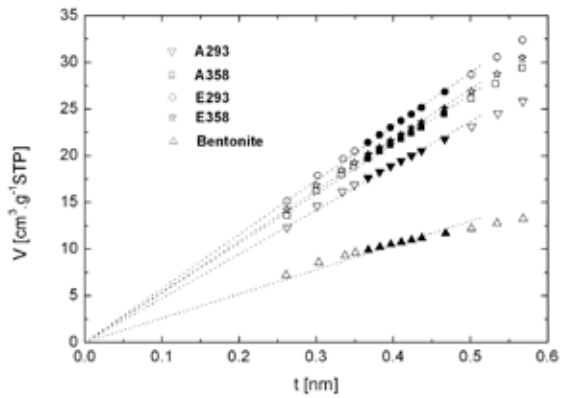

Fig. 2. **t-plot of the investigated samples (filled symbols – linearized parts)**

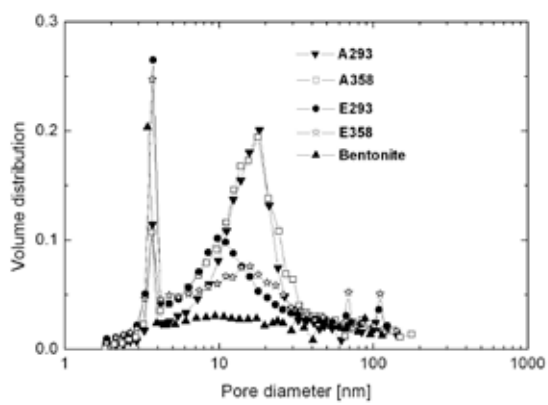

Fig. 3. **Pore size distribution of the investigated samples**

particles in composite. The stronger formation of secondary mesopore structure showed the samples A293 and A358, especially in the range 11–25 nm. The curve of pore size distribution of the E293 sample is shifted left that signifies occurrence of smaller pores in comparison with E358.

The XRD analysis of the composites confirmed the presence of montmorillonite and Fe oxidized phase, but it was not able to determine the iron oxide phase because of strongly overlapping of magnetite and maghemite diffraction lines. Therefore the Mössbauer spectroscopy was used to identify this phase. Except the maghemite, goethite in the samples synthesized at 293 K was observed too, Fig. 4.

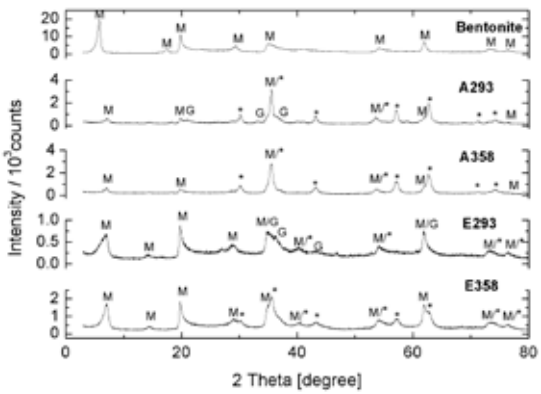

Fig. 4. **X-ray diffraction pattern of natural bentonite and modifiet samples (M – montmorillonite, * - iron oxide diffraction, G – goethite)**

The room temperature Mössbauer spectra of composites A293, A358 and E358 are complexes consisting of paramagnetic doublet and one sextet. The analysis of the A293 sample, Fig. 5.(a), confirmed the presence of γ-Fe_2O_3 (average hyperfine magnetic field for the octahedral site: B^{Oct} = 41.8 T, isomer shift IS = 0.25 mm s^{-1}, relative spectral area RA = 40.15 %; for the tetrahedral site: hyperfine magnetic field B_{hf}^{Tet} = 47.6 T, IS = 0.13 mm s^{-1}, RA = 24.1 %) and small amount of goethite (B_{hf} = 35.8 T, IS = 0.26 mm s^{-1}, quadrupole splitting QS = –0.08 mm s^{-1}, RA = 28.7 %) in composite sample. The Mössbauer spectrum analysis of the samle A358 showed only the presence of maghemite (average hyperfine magnetic field for the octahedral site: B^{Oct} = 38.8 T, isomer shift IS = 0.25 mm s^{-1}, relative spectral area RA = 59.7 %; for the tetrahedral site: hyperfine magnetic field B_{hf}^{Tet} = 47 T, IS = 0.13 mm s^{-1}, RA = 35.8 %) in composite, Fig. 5.(b). The similar results were obtained for the sample E358. The relative spectral area of maghemite was lower that was confirmed by its lower content in composite. More expressive paramagnetic doublet of bentonite was observed for this sample. The Mössbauer spectrum of the E293 sample has shown only a paramagnetic doublet. It was fitted with two paramagnetic doublets, Fig. 5.(c). In the case of very small magnetic particles, they do not show magnetic properties and their sextet structure is bowing into paramagnetic doublet structure.

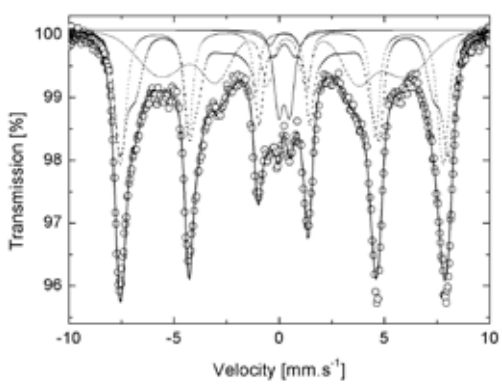

Fig. 5.(a) **Fitted Mössbauer spectrum of the sample A293**

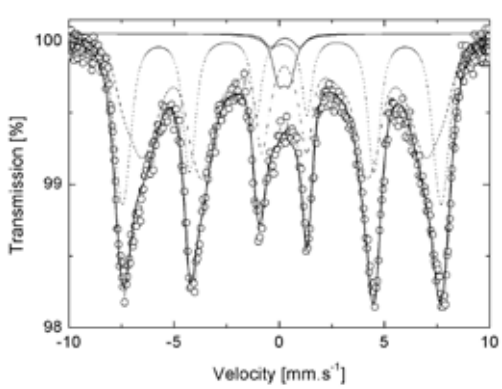

Fig. 5.(b) **Fitted Mössbauer spectrum of the sample A358**

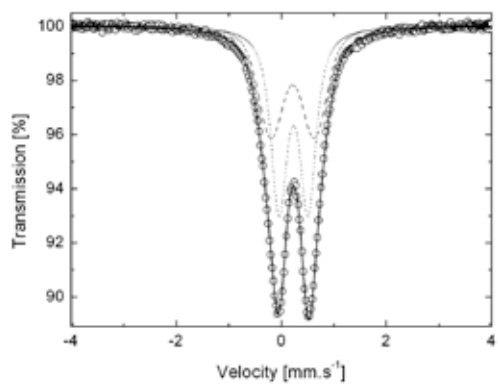

Fig. 5.(c) **Fitted Mössbauer spectrum of the sample E293**

In all investigated composite samples two paramagnetic positions of Fe^{3+} in bentonite were detected.

The magnetization σ of nanosized iron oxide synthesized at 293 K and 358 K without the bearer was measured by SQUID magnetometer. The obtained values were 83.59 emu g^{-1} and 80.95 emu g^{-1} respectively. These measured values were used to calculate the expected theoretical values of magnetization for the modified samples.

The measured magnetization for the composites increases in dependance on the increasing maghemite content in the samples. The measured values do not respond to theoretical. That should be explained by the contribution of measured bentonite magnetization and in the case of samples A293 and E293 also by the presence of goethite in their structures. The value of magnetization of the E293 sample is almost equal to zero. It was confirmed by the Mössbauer spectroscopy that composite E293 contain small particles. The obtained values are listed in Table II.

Fig. 6.(a) shows the morphology of the sample E293 observed by SEM in Compo mode. The white spots belong to maghemite agglomerates on the bentonite surface. It was also confirmed by the EDAX analysis illustrated on Fig. 6(b)

where the presence of Fe and O elements on the bentonite surface was detected.

Table II
Measured and theoretical values of magnetization of the investigated samples

Sample	σ [emu g^{-1}]	Theoretical σ [emu g^{-1}]
Bentonite	4.02	–
A293	37.02	41.80
E293	0.69	13.93
A358	46.22	40.48
E358	15.07	13.49

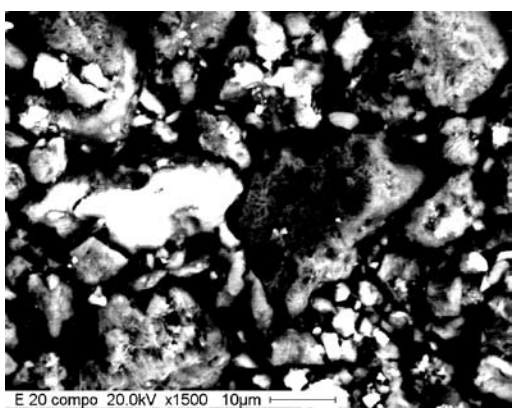

Fig. 6.(a) **SEM Compo mode image of the composite sample E293. White parts signify the presence of iron oxide on the bentonite surface**

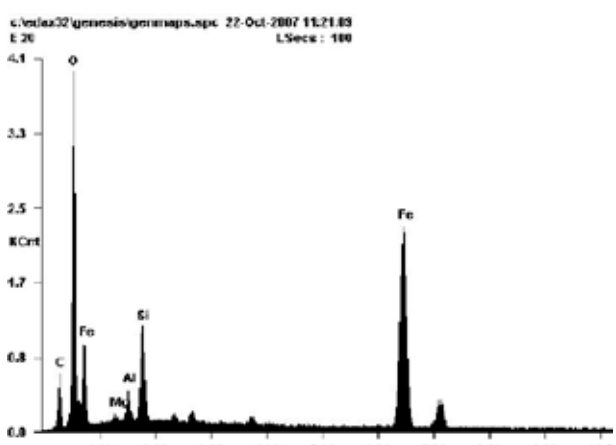

Fig. 6.(b) **EDAX analysis of the composite sample E293**

The sorption experiments of zinc were realized on the natural bentonite and composite material. From all obtained results of previous studies two samples were interesting from the sorption point of view. A358 showed the highest value of pore volume and magnetic property, E293 had the largest specific surface area. On the basis of the result of zeta potential measurement, the last mention sample was used for sorption experiment. The effect of metal ion concentration on zinc adsorption was investigated over the concentration range 10–100 mg dm^{-3} at room temperature. The sorption isotherms obtained at constant temperature are shown in Fig. 7. From this, it is observed that the adsorption capacity q_e increases as a function of metal concentration. The maximum sorption capacity of sorbents has not been reached yet. The experimental data of sorption were fitted with linearized Langmuir type model, Fig. 8.(a), (b), according to the equation (1).

$$\frac{C_e}{q_e} = \frac{1}{Q_m \cdot K} + \frac{C_e}{Q_m}, \qquad (1)$$

where C_e is the equilibrium concentration of metal in solution, q_e is the corresponding amount of metal ions sorbed onto sorbent, Q_m and K are Langmuir constants related to sorption capacity and sorption energy, respectively. Maximum sorption capacity Q_m represents monolayer coverage of sorbent with sorbate and K represents enthalpy of sorption and should vary with temperature.

The maximum sorption capacity of bentonite and E293 calculated from the slope of the plot was 22 mg Zn g^{-1} and 23 mg Zn g^{-1}, respectively.

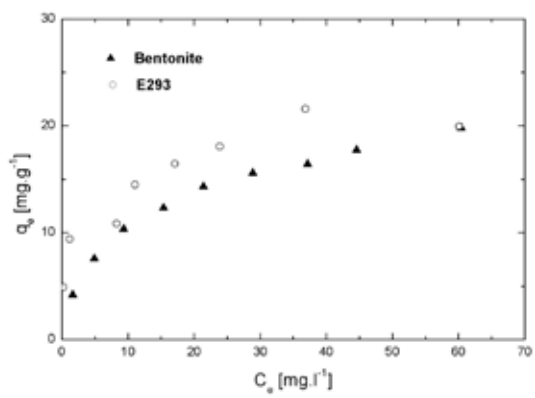

Fig. 7. **Sorption isotherms of Zn^{2+} ions by the natural bentonite and E20 composite sample**

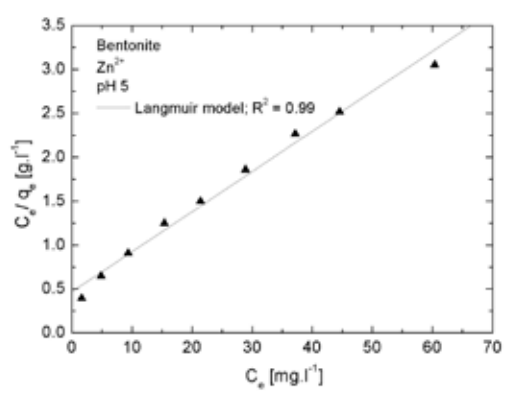

Fig. 8.(a) **Linearized form of Langmuir sorption isotherm of Zn2+ on natural bentonite**

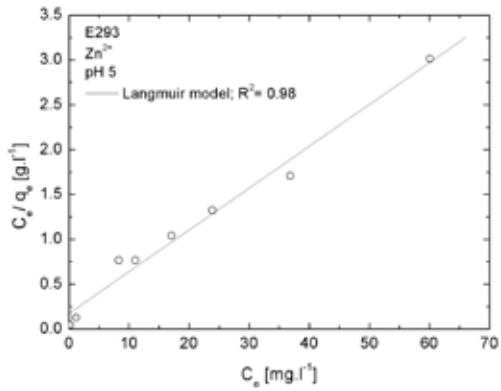

Fig. 8.(b) **Linearized form of Langmuir sorption isotherm of Zn^{2+} on composite E293**

Comparing the efficiency of the natural and modified bentonite towards zinc cations it seems the composite material E293 to be more convenient in removing of this metal from solutions.

Conclusion

Magnetic modification of natural bentonite seems to be a perspective way of enhancing its sorption properties and offers an easy separation and recovery of sorbents[11].

The natural bentonite was modified by iron oxide particles and its improved properties were studied. The natural bentonite as well as composites showed mesoporous structure, the occurrence of macropores was observed from their hysteresis loops. The BET surface area of the composite materials was twice higher in comparison to the natural bentonite. The total pore volume had the increasing tendency in dependance on the higher content of iron oxide in the composite materials because of textural porosity created between the iron oxide particles.

The composite materials exhibited the magnetic properties, which were confirmed by magnetization measurements. The XRD analysis showed the diffractions of Fe oxidized phase in composites materials, in case of the composites synthesized at 293 K, goethite diffractions were observed. Fe oxidized phase was identified by the Mössbauer spectroscopy and it belonged to maghemite. Only the composite sample E293 showed the paramagnetic property that it was caused probably by small iron oxide particles in the composite. The presence of the iron oxide particles on the bentonite surface was observed by SEM and analyzed by EDAX. Maghemite particles were nonhomogenously distributed on the bentonite surface, creating agglomerates.

The sorption properties of the natural bentonite and composite E293 were studied. The composite sample showed the higher adsorption capacity of Zn^{2+} over the whole concentration range in comparison to the natural bentonite. The experimental data were well fitted by the Langmuir type model. Comparing the efficiency of both materials, magnetically modified bentonite seems to be a promise candidate for practical use in heavy metals removal.

The authors are thankful for financial support of VEGA grant G-6189.

REFERENCES

1. Önal, M., Sarikaya, Y., Alemdaroğlu, T.: Turk. J. Chem., *25*, 2412 (2001).
2. Kaya, A., Ören, A.H.: J. Hazard. Mater. *B125,* 183 (2005).
3. Bereket, G., Aroğuz, A. Z., Özel, M. Z.: J. Colloid Interface Sci. *187*, 338 (1997).
4. Tsai, S. Ch., Ouyang S., Hsu, Ch. N.: Appl. Radiat. Isot. *54*, 209 (2001).
5. Tachi, Y., Shibutani, T., Sato, H., Yui, M.: J Contam. Hydrol. *47*, 171 (2001).
6. Volzone, C., Garrido, L. B.: Cerâmica *48*, 153 (2002).
7. Karahan, S., Yurdakoç, M., Seki, Y. Yurdakoç, K.: J Colloid Interface Sci. *36*, 293 (2006).
8. Václavíková, M., Jakabský, Š., Hredzák, S.: Nanoengineered Nanofibrous Materials, NATO Sci. Ser. II. Math. Phys. Chem. *169*, 479 (2004).
9. Lagarec, K., Rancourt, D. G.: *Recoil - Mössbauer Spectral Analysis Software for Windows, version 1.02*, Ottawa, ON 1998.
10. Sing, K. S. W., Everett, D. H., Haul R. A. W., Moscou, L., Pierotti, R. A., Rouquérol, J., Siemieniewska, T.: Pure Appl. Chem. *57*, 603 (1985).
11. Bourlinos, A. B., Zboril, R., Petridis, D., Microporous Mesoporous Mater. *58*, 155 (2003).

L06 REDUCTIVE DISSOLUTION OF SYNTHETIC FERRIC IRON MINERALS BY ACIDOPHILIC BACTERIUM *ACIDIPHILIUM* SJH

ZUZANA PÁLLOVÁ[a], DANIEL KUPKA[a], ALEXANDRA VAŠKOVÁ[a], ZUZANA OROLÍNOVÁ[a], VLADIMÍR ŠEPELÁK[b] and JANA ŠKRLÍKOVÁ[c]

[a]*Department of Biotechnology, Institute of Geotechnics of Slovak Academy of Sciences, Watsonova 45, 043 53 Kosice, Slovak Republic,*

[b]*The Institute of Physical and Theoretical Chemistry, Braunschweig University of Technology, Hans-Sommer-Str. 10, 38106 Braunschweig, Germany,*

[c]*Department of Analytical Chemistry, University of P. J. Šafárik, Moyzesova 16, 041 54 Kosice, Slovak Republic, pallova@saske.sk*

Introduction

Iron oxides are ubiquitous in soils and rocks, lakes and rivers, on the sea floor, in air, and in organisms. They are abundant in soils and aquifers, where they act as a sorbent of heavy metals and of other components. Iron oxides have a substantial impact on the quality of underground waters and porous water in sediments[1].

In an aquatic environment, iron occurs in two oxidative states; Fe^{3+} and Fe^{2+}. Ferric iron is stable in aerobic conditions, especially in neutral and alkaline pH. The concentration of free ferric ions in these conditions is approximately 10^{-17} M. On the other hand, ferrous iron is highly soluble in a wide range of pH and in anoxic conditions[2]. Ferrous iron rapidly oxidizes in the presence of oxygen to ferric iron, which rapidly precipitates above pH 2.5. Below pH 2.5, both iron species are soluble and the oxidation of Fe^{2+} to Fe^{3+} is extremely slow[3].

Dissimilative reduction of ferric iron is an alternative way of respiration of microorganisms in anaerobic conditions. Trivalent iron that could occur in a form of soluble or insoluble compounds can act as a final acceptor of electrons taken during the oxidation of organic matter (heterotrophic organisms) or inorganic matter (autotrophic organisms)[4]. Iron is a redox-active element and it easily transforms from one oxidative state to another. Redoxpotential of the pair Fe^{3+}/Fe^{2+} at pH 2 is 0.77 V. This value (0.84 V) is close to the standard redox potential of the system O_2/H_2O(ref.[5]).

The bacterial reduction of solid state ferric iron causes the dissolution of iron minerals including associated elements[6]. Reductive dissolution of iron can be applied in elimination of undesirable ferric minerals from nonmetalics or in bioremediation of acid mine drainage.

This work presents the behavior of solid as well as liquid ferric iron reduction by bacteria *Acidiphilium* SJH. The bacteria of genus Acidiphilium are heterotrophic, aerobic or facultative anaerobic organisms. These thrive in acidic and neutral range of pH, with an optimum at pH 3 [7]. They oxidize organic substratum to CO_2 and as an oxidant they utilize oxygen or trivalent iron [8]. Acidophilic heterotrophic bacteria have unique properties, therefore they seem to have the possibility for reductive leaching of solid ferric iron compounds[9].

Bacteria Acidiphilium SJH reduce Fe(III) to Fe(II) even at the presence of oxygen[10,5]. The obligatory anoxic environment is not a necessary term in the above mentioned processes of iron reduction. In addition, some strains of the genus Acidiphilium can simultaneously utilize both oxygen and trivalent iron during the oxidation of organic material. The co-respiration of O_2 and Fe^{3+} at acidophilic heterotrophs is an interesting phenomenon. The absence of oxygen is an obligatory requirement for many neutrophilic microorganisms to reduce ferric iron. Iron respiration is inhibited even at a trace amount of oxygen.

Experimental

Iron Oxide Preparation and Characterization

Five pure synthetic iron minerals were prepared as follows:

- Goethite – α-FeO(OH) was prepared from an alkaline system by the hydrolysis of 1M $Fe(NO_3)_3$ with 5M KOH. The synthesis took 60 hours at 70 °C. Yellow-brown colored goethite powder was obtained.
- Lepidocrocite- γ-FeO(OH) was synthesized by oxidizing a Fe^{2+} ($FeCl_2 \cdot 4H_2O$) containing solution at a pH close to neutral. By this method crystalline reddish-yellow lepidocrocite was obtained.
- Magnetite – Fe_3O_4 was prepared from the solution of $FeSO_4 \cdot 7H_2O$ flushed with N_2 gas. The solution of KNO_3 and KOH was used as an oxidizing agent. The oxidation proceeded at 90 °C. The black precipitate occurred after several minutes.
- Maghemite – γ-Fe_2O_3 was prepared by the heating of the sample of synthetic lepidocrocite in a furnace at 250 °C. The thermal transformation was carried out for 2 hours.
- Hematite – α-Fe_2O_3 was being synthesized by acid hydrolysis from the solution of $FeCl_3$ and HCl at 78 °C for ten days.

The resulting products were separated from the liquid phase by centrifugation and then washed with distilled water. The iron oxide powders were finally dried at laboratory temperature and stored in the exicator.

The specific surface area of each iron mineral was measured by the BET (GEMINI 2360, Micromeritics, USA). This method is based on the adsorption of nitrogen molecules on the solid state's surface.

The XRD patterns were collected using a Philips PW 1820 powder diffractometer with CuK_α radiation. The JCPDS PDF database[11] was utilized for phase identification.

Mössbauer spectra of the samples were taken in transmission geometry at temperature T = 293 K. A ^{57}Co/Rh γ-ray source was used. The velocity scale was calibrated relative to ^{57}Fe in Rh. The Recoil spectral analysis software was used for the quantitative evaluation of the Mössbauer spectra[12].

Bacterial Iron-Reduction

Bacterial strain *Acidiphilium* SJH was obtained as a gift from Dr. Barrie Johnson (University of Wales, Bangor, School of Biol. Sci.). It was incubated aerobically in an acidic medium that contained (per liter) 6.25 g $(NH_4)_2SO_4$, 2.5 g $MgSO_4 \cdot 7H_2O$, 0.13 g tryptic soy broth, 0.9 g D-galactose, and 1 ml solution of trace elements. The medium was adjusted at pH 2.5 with 5M H_2SO_4. The bacteria were cultivated in a thermostat at 25 °C under aerobic conditions. The bacterial growth was measured as optical density, recorded at $\lambda = 600$ nm. The grown bacterial cultures were collected by Milipore membrane filters with a pore size 0.22 μm. Cell pellets were suspended in fresh medium and adjusted to final cell concentration equal to $OD_{600} = 1.0$. The cell suspension was poured into special tubes with a screw cap and a septum. Each tube contained m = 0.05 g of iron mineral. The experiments were done in triplicates and each series included one abiotic control. The tubes were closed airtight and incubated statically at 25 °C.

In order to keep anoxic conditions within the tubes and to avoid the contamination, the samples were taken through the cap's septum with sterile needles and syringes. The samples were filtered in order to separate the solid and liquid phases. The leaching solutions were immediately stabilized by sulfuric acid to prevent abiotic oxidation of ferrous iron. The ferrous iron concentration was measured by the o-phenantroline colorimetric method[13], ferric iron by UV- spectrophotometric method at $\lambda = 300$ nm[14].

Bacterial reduction of soluble ferric iron was carried out in a stirred laboratory bioreactor with working volume of 1 dm^3. The innoculum was prepared identical as in the aforesaid experiments. During the incubation, the samples of medium were withdrawn in intervals for the chemical analyses and optical density measurements. Iron speciation and bacterial cell concentration were measured as stated above. The specific iron reduction rates were normalized for cells density equivalent to 1.0 absorbance unit (OD_{600}).

Results

The XRD analyses and Mössbauer spectroscopy confirmed the purity of prepared synthetic minerals. The XRD pattern of the hematite sample is presented in Fig. 1. The positions of all experimental diffraction lines are the same as those for the theoretical diffraction lines of the α-Fe_2O_3 phase. Thus, the as-synthesized sample corresponds to pure α-Fe_2O_3 phase[11].

The room-temperature Mössbauer spectrum of the hematite sample is characterized by symmetric sextet structure (Fig. 2.). The spectrum is well fitted by one sextet component with the hyperfine parameters: isomer shifts IS = 0.24 mm/s, quadrupole splitting $QS_{M1} = -0.10$ mm s^{-1} and hyperfine magnetic field B = 51.2 T. These parameters are characteristic of ferric (Fe^{3+}) ions[15, 16] in octahedral coordination of oxygen ions in α-Fe_2O_3.

Significant differences in specific surface areas were measured for individual iron minerals (Table I).

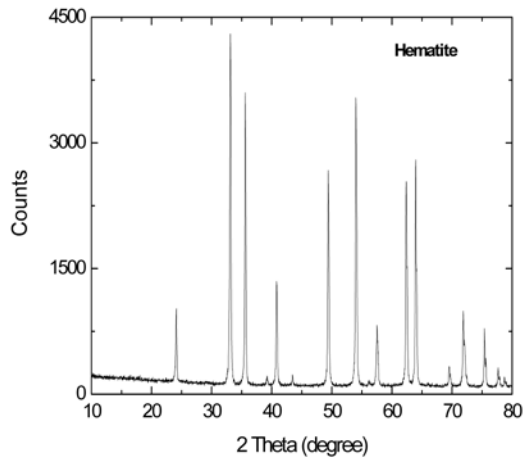

Fig. 1. **XRD patterns of the hematite sample**

Fig. 3 shows the time course of bacterial leaching of goethite and hematite. Non-linear regression was used to calculate initial leaching rate, because the instantaneous rate decreased with time. Goethite and hematite have well ordered crystalline structure and are rather refractory towards leaching. Their stability could also be assumed in natural environment. The samples of lepidocrocite and maghemite possessed the highest specific surfaces. They also proved the highest rates of chemical and bacterial leaching (Fig. 4). The lepidocrocite is a less stable mineral in comparison with goethite and hematite. This was validated by the results of our experiments. The initial rate of iron reduction at lepidocrocite was 3.0 mg dm^{-3} h^{-1}, at maghemite 2.83 mg dm^{-3} h^{-1}. The highest observed concentrations of Fe^{2+} in leaching solutions reached approximately 600 mg dm^{-3}, which corresponds to 20% yield. The rate of the leaching was gradually decreasing. The reason of this decelerating could be the passivation of mineral surface, adsorption of Fe^{2+} ions from solution onto mineral surface or bacterial cells. In addition, the inhibition could be caused by the change of sorption affinity of bacterial cells to mineral surface[17].

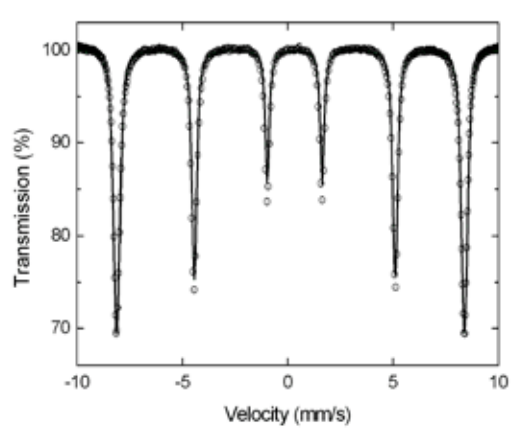

Fig. 2. **Room-temperature ^{57}Fe Mössbauer spectrum of hematite**

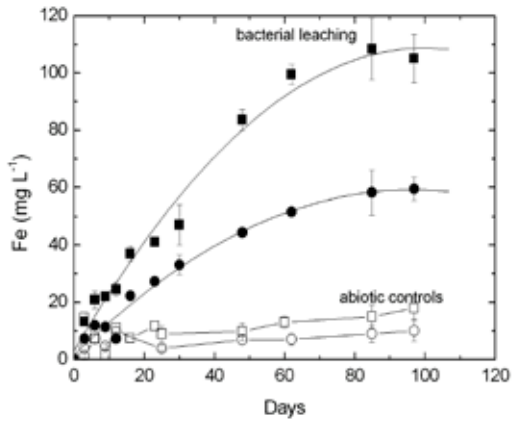

Fig. 3. **Bacterial leaching of goethite (squares) and hematite (circles). Symbols represent the means of triplicate incubations ± standard deviation. Open symbols indicate chemical leaching of minerals in abiotic controls**

Table I
Specific surface area, initial rates of iron reduction and *specific rates of iron reduction normalized for surface area of 1 m^2 and cells density equivalent to 1.0 absorbance unit (OD_{600})

Mineral	S_A [$m^2\,g^{-1}$]	r_0 [$mg\,dm^{-3}\,h^{-1}$]	rsp [$\mu g\,m^{-2}\,h^{-1}$]*
Goethite	30	0.095	0.89
Hematite	5	0.053	3.03
Lepidocrocite	73	3.0	11.64
Maghemite	87	2.83	9.24
Magnetite	13	1.44	31.45

The bacterial activity is limited by the availability of Fe^{3+}. When solid substrates are utilized, the linear bacterial growth is commonly observed. The growth is limited by the rate of iron dissociation from the solid surface. The specific rates of leaching were calculated for a unit of mineral surface and a unit of bacterial cells (Table I). For the quantification of leaching rates for various minerals initial rates were calculated from non-linear regression, using a second-order power function.

In anoxic conditions, bacteria utilized Fe^{3+} cation as an electron acceptor from the oxidation of organic matter (saccharides). The rate of bacterial reduction of Fe^{3+} to Fe^{2+} in the solution highly exceeds the dissociation rate of Fe^{3+} from mineral surface, which is the rate-determining step. Therefore, in the presence of iron reducing bacteria, almost all soluble iron occurs in the form of Fe^{2+} ions.

In solutions without bacteria both iron species were detected (Fig. 5.). The sterile acidic medium (pH 2.2) brought about the chemical leaching of iron from oxihydroxides because of the adsorption H^+ protons to mineral surface followed by the extraction of Fe^{3+} from the crystal lattice[18]. The acid leaching is a reversible process of the hydrolytic reaction connected with the formation of Fe(III) precipitate: $2Fe^{3+} + 3H_2O \leftrightarrow Fe_2O_3 + 6H^+$. The presence of Fe^{2+} in acidic leaching liquors in the absence of Fe-reducing bacteria could be a result of chemical reduction of Fe^{3+} with organic substances obtained in media (D-galactose and tryptic soy broth).

Magnetite contains both Fe^{2+} and Fe^{3+} ions in its crystal structure. Under anoxic conditions, two potential mechanisms exist for aqueous release of iron from magnetite. One is the reaction resulting in maghemite formation and incongruent release of Fe (II) to solution (1)[19].

$$[Fe^{2+}Fe^{3+}{}_2]O_{4(mn)} + 2H^+ \rightarrow \gamma[Fe^{3+}{}_2]O_{3(mh)} + Fe^{2+} + H_2O \quad (1)$$

In addition, in extremely acidic solutions pH < 1 congruent dissolution was observed, which releases both Fe^{2+} and Fe^{3+} from magnetite (2) corresponding to Fe^{3+}/Fe^{2+} ratios of 2 : 1(ref.[20]).

$$[Fe^{2+}Fe^{3+}{}_2]O_{4(mn)} + 8H^+ \rightarrow Fe^{2+} + 2Fe^{3+} + 4H_2O \quad (2)$$

In our experiments, sterile controls containing magnetite proved high concentrations of Fe^{2+} in leaching liquor, according to (1). The presence of trivalent iron points out the possibility of leaching according to (2). Fig. 4. presents the behavior of chemical and bacterial leaching of magnetite. The initial rate of the iron extraction from this mineral was 1.44 $mg\,dm^{-3}\,h^{-1}$. Recounted values to magnetite's specific surface (13 $m^2\,g^{-1}$) showed the highest specific rate of iron extraction.

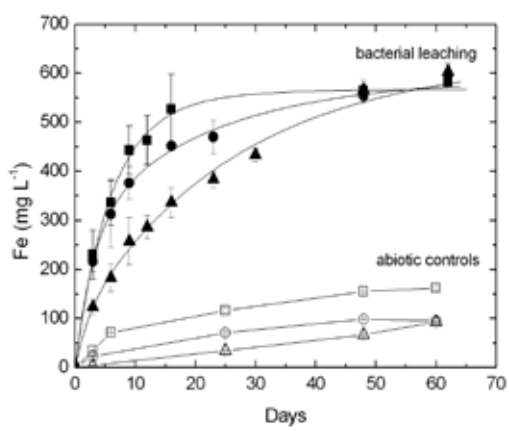

Fig. 4. **Bacterial leaching of lepidocrocite (squares), maghemite (circles) and magnetite (triangles). Symbols represent the means of triplicate incubations ± standard deviation. Curves indicate the fit of a second order power function used to determine initial rates. Open symbols indicate chemical leaching of these minerals in abiotic controls**

Fig. 6. depicts the bacterial reduction of soluble ferric iron in the bioreactor. After the innoculation of bacteria into the fresh medium, the dissolved oxygen was consumed within 2 hours and ferric iron became the only terminal electron acceptor for the bacterial oxidation of organic substratum (3).

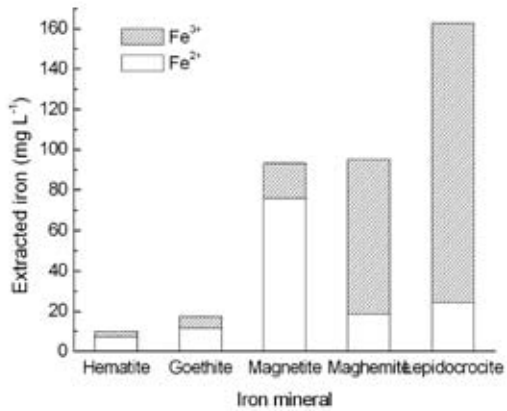

Fig. 5. **Concentration of Fe^{3+} and Fe^{2+} in leaching liquors of sterile controls after 60 days of incubation**

$$C_6H_{12}O_6 + 24\,Fe^{3+} + 6\,H_2O \rightarrow 6\,CO_2 + 24\,Fe^{2+} + 24\,H^+ \quad (3)$$

The bacteria grew exponentialy with a specific growth rate $\mu = 0.024\ h^{-1}$. In this period, the specific rate of iron reduction calculated to an absorbance unit was 250 mg $dm^{-3}\,h^{-1}$. After the exponential growth phase, the specific rate of iron reduction started decreasing. The bacteria completely reduced ferric iron to ferrous iron within 48 hours. After the depletion of Fe^{3+} the bacterial growth has stopped because of the absence of any available electron acceptor in the medium.

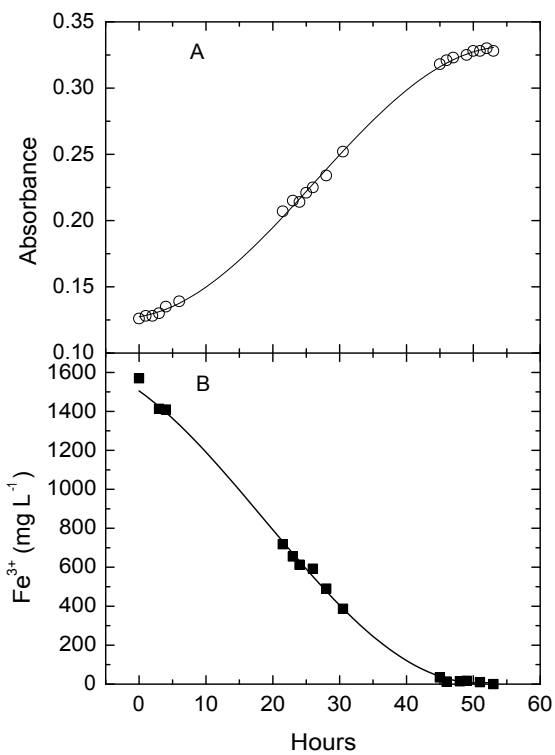

Fig. 6. **Anaerobic incubation of *Acidipjilium* SJH in the medium containing soluble ferric iron. A: The bacterial growth measured as the absorbance. B: The bacterial reduction of soluble ferric iron in the course of incubation**

Conclusions

Iron reduction in natural conditions, in suboxic zones and aquifers, is caused by several abiotic and biotic processes. Iron reducing bacteria make use of Fe(III) as an electron acceptor from the oxidation of organic matter. Solid iron compounds undergo reductive dissolution, which affects the persistence and mobility of metals, phosphates, radionuclides, and organic pollutants[4].

The rate and the extent of bacterial reduction of Fe(III) oxihydroxides could be affected by several factors, mainly by the composition of microbial population, the kind of the iron mineral, and the sorption affinity of bacterial cells to mineral surface[17]. In addition, the rate of iron reducing could be inhibited by adsorption of Fe^{2+} ions from the solution onto the mineral surface or the surface of bacterial cells. This work deals with the kinetics of five synthetic iron minerals´ leaching by acidophilic heterotrophic iron- reducing bacteria. The kinetics of chemical and bacterial leaching depends on the solubility of minerals that follows from the degree of crystal structure's coordination. The initial rates of solid Fe(III) reduction normalized to a biomas and mineral surface unit were in the range from 0.89 to 31.45 $\mu g\,m^{-2}\,h^{-1}$. The leaching rates decreased in the following order: lepidocrocite > maghemite > magnetite > goethite > hematite (Table I). According to these results, hematite presents the most refractory from the studied minerals.

The maximal observed specific rate of solid ferric iron reduction calculated to biomas unit was 4.3 mg $dm^{-3}\,h^{-1}$. The specific rate of bacterial reduction of soluble Fe^{3+} calculated to biomas unit reached 250 mg $dm^{-3}\,h^{-1}$. The rate of soluble iron reduction was incomparably higher than the rates observed at solid ferric compounds rates reduction. In the case of solid phases, the rate determining step is the dissolution of iron ions from the solid phase into the solution.

Acknowledgement This work has been supported by by Slovak Grant Agency, VEGA Project No. 2/0159/08, and No. 2-6189.

REFERENCES

1. Tessier A., Fortin D., Belzile N., DeVitre R., Leppard, G. G.: Geochim. Cosmochim. Acta *60*, 387 (1996).
2. Johnson D. B.: Biodeter. Abstr *9*, 1 (1995).
3. Stumm W., Morgan, J. J.: *Natural Waters*, New York, 1996.
4. Lovley D. R.: FEMS Microbiol. Rev. *20*, 305 (1997).
5. Johnson D. B., Bridge T. A. M.: J. Appl. Microbiol *92*, 315 (2002).
6. Lovley D.R.. Microbiol. Rev *55*, 259 (1991).
7. Johnson D. B., McGinness S.: Appl. Environ Microniol. *57*, 207 (1991).

8. Küsel K., Dorsch T., Acker G., Stackebrandt E: Appl. Environ. Microbiol *65*, 3633 (1999).
9. Bridge T.A.M., Johnson D.B.: Geomicrobiol. J. *17*, 193 (2000).
10. Küsel K., Roth U. Drake H. L. D.: Environ. Microbiol. *4*, 414 (2002).
11. JCPDS PDF, International Centre for Diffraction Data, Newton Square, PA, 2004.
12. Lagarec K., Rancourt D. G.: RECOIL. *Mössbauer Spectral Analysis Software for Windows*. University of Ottawa, Ottawa 1998.
13. Herrera L., Ruiz P., Aguillon J. C., Fehrmann A.: J. Chem. Tech. Biotechnol *44*, 171 (1989).
14. Basaran A. H., Tuovinen O. H.: Appl. Microbiol. Biotechnol *24*, 338 (1986).
15. Menil F. J.: Phys. Chem. Solids *46*, 763 (1985).
16. Goulart A. T., de Jesus Filho F., Fabris J. D. Coey J. M. D.: Hyperfine Interact. *83*, 451 (1994).
17. Caccavo F. Jr.: Appl. Environ. Microbiol. *65*, 5017 (1999).
18. Suter D., Banwart S., Stumm W.: Langmuir, *7* 809 (1991).
19. White A. F., Peterson M. L., Hochella M. F. Jr.: Geochim. Cosmochim. Acta *58*, 1859 (2004).
20. Bruyere V. I. E., Blesa M. A. . J. Electrochem. Soc. *132*, 141 (1985).

L07 THE EFFECT OF HYDROGEN ON COMBUSTION OF NATURAL GAS

ONDŘEJ PROKEŠ, DANIEL TENKRÁT and ALEŠ DOUCEK
Ústav Plynárenství, Koksochemie a Ochrany Ovzduší, VŠCHT Praha, Technická 5; 166 28 Praha 6, prokeso@vscht.cz

Introduction

Due to oncoming fossil fuel depletion, attention is nowadays paid to alternative resources, especially the renewable ones. Their major handicap is a limited possibility of the utilization compared to current resources. Hydrogen, owing to great properties to easy and high-efficient conversion to electricity, is consequently regarded as a universal energy carrier. On this account, R&D of new methods to produce hydrogen, its transport, storage and utilization are the priorities.

Recapitulation of Current State

Production and consumption of hydrogen is gradually increasing nowadays and it is expected to increase by 6 to 10 % annually in next few years. Currently the hydrogen consumption exceeds 50 billion normal cubic meters per year. In connection with changing conditions of world energy market, the structure of particular national energetic conceptions is also changing, leading in an effort to employ the sources with high efficient energy conversion and simultaneously small or even no amount of produced pollutants. It is creditable that these changes are demanded and widely supported also at the politic level. The technology of fuel cells is closely connected with hydrogen utilization and generally works at high efficiency and upon zero emissions of carbon dioxide and also other pollutants. Another hydrogen advantage is high variability of its production. It can be produced from all fossil or regenerative fuels and also nuclear energy. This flexibility and high efficient and clean utilization give hydrogen its giant power and promising future. Concerning distribution of hydrogen, it can be transported as a compressed gas or liquefied. Liquefied hydrogen is preferred for big amounts and for long distances because of higher energy cost for liquefaction. Compressed hydrogen can be transported in pressure flasks or gas pipelines. Co-distribution of hydrogen and natural gas is discussed as a possibility of distribution hydrogen during a transition period to hydrogen economy.

Co-Distribution of Hydrogen with Natural Gas

For a transport of the gaseous hydrogen pipelines can be used similarly to natural gas. However there is not sufficiently wide distribution net nowadays. That is reason why hydrogen and natural gas co-distribution is considered in existing pipelines system. There were several practical experiments, which confirmed possibility to co-distribute up to 5 % vol. hydrogen in natural gas, without any influence on gas industry devices. It means no essential modification on transit pipelines, regulating stations etc. In case of local pipelines it is not necessary to fear of hydrogen addition, since in the past, coal gas, which contains up to 50 % vol., was successfully distributed. Co-distribution of hydrogen with natural gas may be in transition period very advantageous because of several reasons: *(i)* current gas pipelines are able to provide sufficient capacity for hydrogen supply without additional costs, *(ii)* emission of pollutants (CO, NO_x) produced by existing gas appliance can be considerable lowered, causing positive environmental effect especially in bigger agglomerations.

Table I
Composition of used gas mixtures

Component	NG	10 % H_2	20 % H_2	30 % H_2
$\varphi(CH_4)$ [% mol]	97.93	90.58	78.41	69.97
$\varphi(C_2H_6)$ [% mol]	0.777	0.719	0.772	0.684
$\varphi(C_3H_8)$ [% mol]	0.263	0.243	0.262	0.233
$\varphi(i–C_4)$ [% mol]	0.044	0.041	0.044	0.040
$\varphi(n–C_4)$ [% mol]	0.049	0.045	0.049	0.044
$\varphi(i–C_5)$ [% mol]	0.010	0.009	0.010	0.009
$\varphi(n–C_5)$ [% mol]	0.008	0.007	0.008	0.007
$\varphi(C_6)$ [% mol]	0.002	0.002	0.002	0.001
$\varphi(H_2)$ [% mol]	–	7.26	19.52	28.26
$\varphi(CO_2)$ [% mol]	0.059	0.055	0.068	0.061
$\varphi(N_2)$ [% mol]	0.855	0.984	0.81	0.676
$\varphi(O_2)$ [% mol]	–	0.054	0.043	0.024

Table II
Properties of used gas mixtures

Attribute	NG	10 % H_2	20 % H_2	30 % H_2
Hi (15 °C) [MJ m^{-3}]	34.15	32.32	29.48	27.40
Hs (15 °C) [MJ m^{-3}]	37.91	35.93	32.88	30.63
W (15 °C) [MJ m^{-3}]	50.34	49.27	47.85	46.82
d (15 °C) [–]	0.567	0.532	0.472	0.428

Related Legislation

Considering addition of hydrogen to natural gas, safe and trouble-free operation of gas appliances must be ensured. There are two main regulations in the Czech Republic: TPG 902 02 regarding requirements for gas quality and ČSN EN 437 regarding gas appliances testing. TPG 902 02 defines quality grade and testing of gaseous fuels with high methane content. It restricts hydrogen content to 2 % mol. It implies impossibility of distributing hydrogen in natural gas in higher concentrations. According to ČSN EN 437 a gas with hydrogen content 23 % vol. is applied during testing to examine appliance for flame stability or in different word danger of backfiring. Up to 2% difference in Wobbe index is allowed.

Experimental

The main purpose of the research was an evaluation of emission characteristics of various hydrogen–natural gas

mixtures. Furthermore, the determination of optimal volume concentration interval that can be reliable operated under conditions in the Czech Republic were demand. Results should be a basis for evaluation of possibility to co-distribute hydrogen with natural gas. It should be possible also to prove expected lowering of pollutants production. Conclusions should be applicable especially in relation to end user and their gas appliances.

Experimental Arrangement

Measurements were carried out on two standard and one condensing boiler, which should also provide data about benefit of using condensing boilers in respect of specific emission of CO and NO_x. Standard boilers were represented by top supported Therm 12 S with nominal heat output 15 kW and stationary Viadrus G27 ID with nominal heat output 32–37.5 kW. Condensing boilers were represented by Junkers ZSB 16-1 A CERASMART with nominal heat output 16.1 kW. Several model mixtures from 1.5 % vol. up to 40 % vol. of hydrogen in natural gas were examined.

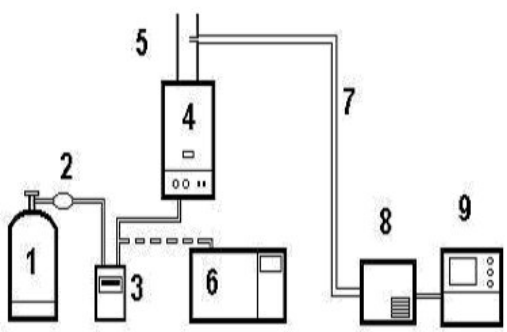

Fig. 1. **Scheme of experimental installation: 1 – pressure cylinder with gas sample, 2 – pressure regulator, 3 – gas meter, 4 – gas boiler, 5 – duct system, 6 – gas chromatograph, 7 – heated sampling track, 8 – sample treatment, 9 – flue gas analyzer**

The Therm boiler was observed in two operational regimes: half and full heat output, the Viadrus boiler was examined at full heat output. Measured quantities were composition of inlet gas (gas chromatography Hewlett-Packard 6890 with TCD and FID), composition of flue gas (analyzer Horiba PG 250, O_2, CO_2, CO, NO_x) and continuous heat output measurement. Flue gas was sampled by portable sample treatment unit PSS-5 with heated inlet filter, heated teflon hose, teflon membrane gas pump and Poltier gas cooler. Experimental arrangement is shown on Fig. 1.

Results

In Table I, compositions of inlet gases are summarized. Also values of lower heat value (H_i), higher heat value (H_s), relative density (d) and Wobbe index (W) calculated according to ISO 6976 are shown.

The results of experiment are average weight concentrations of carbon monoxide $\overline{\rho}_N^{3\%O_2}(\mathrm{CO})$ and nitrogen oxides $\overline{\rho}_N^{3\%O_2}(\mathrm{NO_x})$ (expressed as NO_2) for normal reference state (t = 0 °C, p = 101325 Pa), dry gas and reference oxygen content 3% vol. measured during 15 to 30 minutes intervals of steady state. The Results are summarized in Table III and IV.

Table III
CO emissions: $\overline{\rho}_N^{3\%O_2}(\mathrm{CO})$ [mg m^{-3}]

Boiler	NG	10 % H_2	20 % H_2	30 % H_2
Therm	19.8	15.8	10.8	10.2
Therm (1/2)	44.8	20.8	24.0	30.9
Viadrus	6.4	2.0	0.5	1.7

Table IV
NO_x emissions: $\overline{\rho}_N^{3\%O_2}(\mathrm{NO_x})$ [mg m^{-3}]

Boiler	NG	10 % H_2	20 % H_2	30 % H_2
Therm	175	154	162	142
Therm (1/2)	182	134	139	127
Viadrus	150	126	132	120

Table V
CO specific emissions: $\overline{\xi}(\mathrm{CO})$ [mg kWh^{-1}]

Boiler	NG	10 % H_2	20 % H_2	30 % H_2
Therm	22.1	17.4	11.8	11.0
Therm (1/2)	50.0	23.1	26.2	33.5
Viadrus	7.1	2.2	0.5	1.8

Table VI
NO_x specific emissions: $\overline{\xi}(\mathrm{NO_x})$ [mg kWh^{-1}]

Boiler	NG	10 % H_2	20 % H_2	30 % H_2
Therm	195.7	170.5	177.3	154.0
Therm (1/2)	202.9	147.8	152.5	137.1
Viadrus	167.6	139.6	144.2	130.2

Conclusions

The results prove lowering of weight concentrations of CO by hydrogen addition with an optimum concentration of hydrogen about 20 % vol. Emission of CO was lowered to half for Therm and to less than 10 % for Viadrus in the optimal case (Table III). In all occasions, the highest concentration of CO and NO_x was for natural gas without hydrogen addition, which proves possibility to add hydrogen to natural gas to lower emission of pollutants. Emissions of NO_x showed decreasing tendency with hydrogen addition in the whole interval. Therefore extension of measure interval is desirable in future to at least 40 % vol. of hydrogen. Even more interesting for evaluation of hydrogen effect on emissions are specific emissions per 1 kWh summarized in Table V and VI. It also proved the highest CO and NO_x emission by combustion of natural gas without hydrogen addition.

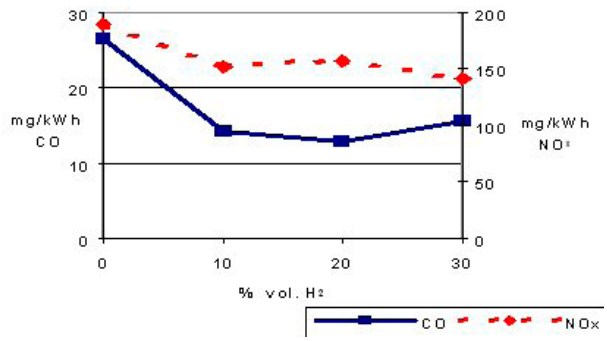

Fig. 2. **Average specific emissions of CO and NO_x**

In the case of NO_x there was lowering up to 30 %, for CO even up to 70 %. Performed experiment showed possibility to combust mixtures of natural gas and hydrogen (up to 30 % vol.) without operational problems i.e. backfiring. Hydrogen addition causes CO and NO_x emission lowering in all observed cases.

This work has been partly supported by MSM 604 613 73 04.

REFERENCES

1. Palmová I., Schöngut J.: Chem. listy *98*, 205 (2004).
2. Čapla L., Buryan P., Prokeš O., Fík J., Žahourek J.: Abhangigkeit der Emission der alten Hauslichen Gasgerate von der Zusammensetzung des Erdgases, 52. Berg- und Huttenmanischen Tag 2001, p.49, Freiberg (2001)
3. Dicks A. L.: J. Power Sources *61*, 113 (1996).
4. Doucek A.: Diploma Thesis, VŠCHT Praha (2007).
5. Prokeš, O., Doucek, A., Tenkrát, D.: Chemické zvesti *61* (2007).
6. Yanga, C., Ogdena, J.: International Journal of Hydrogen Energy *32*, 268 (2007).

L08 EFFECT OF PARTICLE SIZE ON DEHYDROXYLATION OF KAOLIN – AN INFRARED SPECTROSCOPY STUDY

PETR PTÁČEK, DANA KUBÁTOVÁ, JAROMÍR HAVLICA, FRANTIŠEK ŠOUKAL and TOMÁŠ OPRAVIL

Institute of Materials Chemistry, Brno University of Technology, Purkyňova 118, 612 00, Czech Republic, ptacek@fch.vutbr.cz

Introduction

Kaolinite ($Al_2(Si_2O_5)(OH)_4$) dehydroxylation processes have been studied for many years by many ways including thermal analysis[1–8], molecular spectroscopy[1], structural analysis[1,9] and electron microscopy[7,10].

The dehydroxylation of kaolinite is determined by different factor, such as degree of structural ordering, particle size and shape, adsorbed and substituted ions, mineral admixtures, etc. Also the influence of instrumental conditions (especially sample mass, heating rate and sample pre-treatment) on the decomposition is often discussed. Another important experimental factor is the pressure[2,5,6]. It was observed that the temperature of the dehydroxylation effect shifts to lower temperatures as the reduction of particle size takes place[2].

The thermal dehydration of hydroxyl-containing compounds like kaolinite occurs in a formation of water molecules due to an interaction of neighboring OH groups. The water release from the octahedral coordinated Al^{3+} ion could generate isolated OH groups[5]

The reaction path, which gives orthorhombic mullite from kaolinite, can be simplified to following simultaneous reactions[7,11]:

$$Al_2O_3 \cdot 2SiO_2 \cdot 2H_2O \xrightarrow{400-700\,^\circ C} Al_2O_3 \cdot 2SiO_2 + 2H_2O \quad (1)$$

$$2(Al_2O_3 \cdot 2SiO_2) \xrightarrow{925-1{,}050\,^\circ C} 2Al_2O_3 \cdot 3SiO_2 + SiO_2 \quad (2)$$

$$3(2Al_2O_3 \cdot 3SiO_2) \xrightarrow{>1{,}100\,^\circ C} 2(3Al_2O_3 \cdot 2SiO_2) + 5SiO_2 \quad (3)$$

$$SiO_2 \xrightarrow{>1{,}200\,^\circ C} SiO_2\,(\text{cristobalite}) \quad (4)$$

Dehydroxylation is splitting into two separate processes with T_{max} about 550 and 600 °C. The first step was explained due to loss of "structural water" and destruction of the kaolinite sheet structure. The second step was discussed as a kinetically controlled recombination of alumina and silica to the meta-kaolinite structure[5].

The effect of particle size on course of dehydroxylation processes of washed Na-kaolin Sedlec Ia were investigated by mid-infrared spectroscopy via series of isothermal experiment on temperature range from 150 to 650 °C. Ralatioship between particle size and primary spectroscopic variables, i.e. amplitude, peaks wavelength and half-width, of kaolinite spectral bands were evaluated.

Experimental

K a o l i n

Washed Na-kaolin Sedlec Ia from region Karlovy vary (Czech Republic) produced by Sedlecký kaolin a.s. was used in this study. Content of kaolinite is higher than 90 % wt. with equivalent diameter grain median in range 1.2–1.4 μm. The main impurities are mica group minerals and quartz. The colorant oxides content – hematite (α-Fe_2O_3) and tetragonal TiO_2 (rutile), is lower than 0.85 and 0.2 % wt., respectively.

The kaolin grain fraction with particle diameter 90–80 μm (f_{90-80}), 80–71 μm (f_{80-71}), 71–63 μm (f_{71-63}), 63–50 μm (f_{63-50}), 50–40 μm (f_{50-40}) and undersize ($f_{<40}$) were used for FT-IR experiments. This fraction was previously dried for 2 h at 150 °C due to removing of adsorbed water. The specific surface area of sample was 16.6 $m^2 g^{-1}$ (Chembet – 3000). Thermogravimetric weight loss (TG-DTA analyzer Setaram 92–18) of applied kaolin is about 13.15 % wt.

I n f r a r e d S p e c t r o s c o p y

Infrared spectra of samples were recorded in KBr pellets using FT-IR spectrometer Nicolet Impact 400 in the wavelengths range from 4,000 to 400 cm^{-1}. Measurements were done under resolution 8 cm^{-1}.

Heat threaded samples were mixed with KBr with mass ratio 1 : 100. Mixtures were homogenized by grinding in mortar dish. Weighted amount of these mixtures were pressed under 40 kPa for 20 s and next 80 kPa for 30 s.

D a t a P r o c e s s i n g

All correction of spectra (smoothing, subtracting and fitting), mathematic and statistic operations were made with OriginPro 7.0 and Statistica 8.0 software.

Results

The FT-IR spectrum of dray kaolin is shown on Fig. 1. The data from refs.[12–14] were used for interpretation of measured infrared spectra.The quadruplet of IR bands in X-H stretching region (X = O, N, C) are ν_1, ν_2, ν_3 a ν_4 vibration modes of hydroxyl groups in kaolinite structure. The first three bands at 3,697, 3,669 and 3,655 cm^{-1} belong to stretching of so-called outer hydroxyls (ouOH, inner-surface hydroxyls). The rest ν_4(OH) vibration mode is assigned to stretching of inner surface hydroxyl (inOH). These groups are located on the shared plane between the octahedral and tetrahedral sheets of the same kaolinite layer.

The inner-surface hydroxyl groups show a strong in-phase symmetric stretch at 3,697 cm^{-1} (ν_1) with transition moment close to c^* and two weak out of phase vibrations at 3,669 (ν_2) and 3,655 cm^{-1} (ν_3) with transition moment in the (001) plane[12]. The OH groups bending and translation vibrations are located at 935 δ_1(ouOH), 910 δ_2(inOH) and 791, 754 cm^{-1}, respectively.

There are three sharp bands at Si–O stretching region belonging to vibration of Si–O(apical) at 1,115 cm^{-1}, symmetric stretching of Si–O–Si (siloxane bridge) at 1,033 cm^{-1}

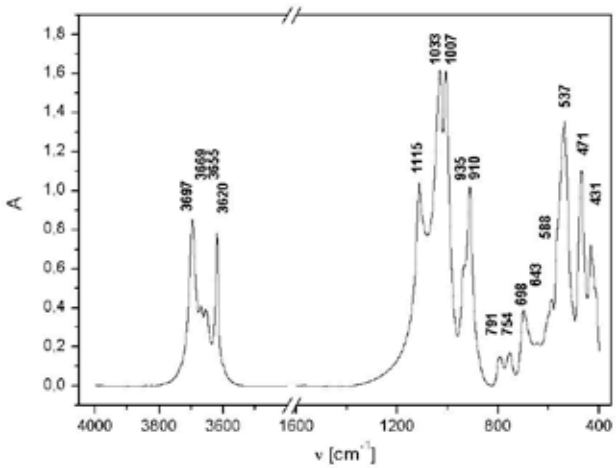

Fig. 1. **Subtracted FT-IR spectrum of kaolin Sedlec Ia for the $f_{50–40}$ fraction**

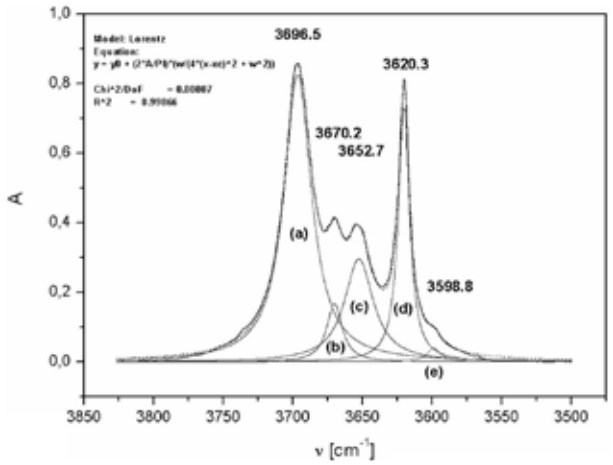

Fig. 2. **Fitted spectrum in the O–H stretching region for the f50-40 fraction of dried kaolin Sedlec Ia: ν_1(ouOH) (a), ν_2(ouOH) (b), ν_3(ouOH) (c), ν_4(inOH) (d) and ν(OH) of admixtures in the**

and asymmetric of Si–O–Si at 1,007 cm^{-1}, respectively. Band of Si–O bending is located at 431 cm^{-1}.

The other kaolinite bands in the spectrum on Fig. 1. are relatet to O–Al–OH (698 cm^{-1}) and Si–O–Al (537 and 470 cm^{-1}) in kaolinite structure. Bands at 643 and 588 cm^{-1} probably belong to admixture of illite.

O H S t r e t c h i n g R e g i o n

IR spectrum fitted over hydroxyl stretching region by Lorentz function is shown on Fig. 2. In addition to fundamental modes of OH groups (a–d) there was found small band at 3,599 cm^{-1} (e), which probably belongs to admixtures in the sample – illite or goethite.

S i – O S t r e t c h i n g a n d O H D e f o r m a t i o n R e g i o n

Loretz function gave no good results over this region thereby the first type Voight function was applied:

$$y = y_0 + A\left[m_u \frac{2}{\pi}\frac{w}{4(x-x_c)^2+w^2} + (1-m_u)\frac{\sqrt{4\ln 2}}{\sqrt{\pi}w} e^{-\frac{4\ln 2}{w^2}(x-x_c)^2}\right] \quad (5)$$

where y_0 is offset, x_c peak center, A amplitude, w width and m_u shape factor of peak. Fitted spectrum is shown on Fig. 3.

D e h y d r o x y l a t i o n o f K a o l i n

The change of the spectra shape during thermal treatment of sample in static oven atmosphere is shown on Fig. 4. for 50–40 μm fraction and on Fig. 5. for 71–63 μm fraction.

Dehydroxylation process is in generally accompanied with decrease OH stretching and bending bands. Stretching and bending modes of Si–O and Al–O bond show loses of their selectivity. The details about kaolinite spectra changes during course of dehydroxylation process we are already described in ref.[15].

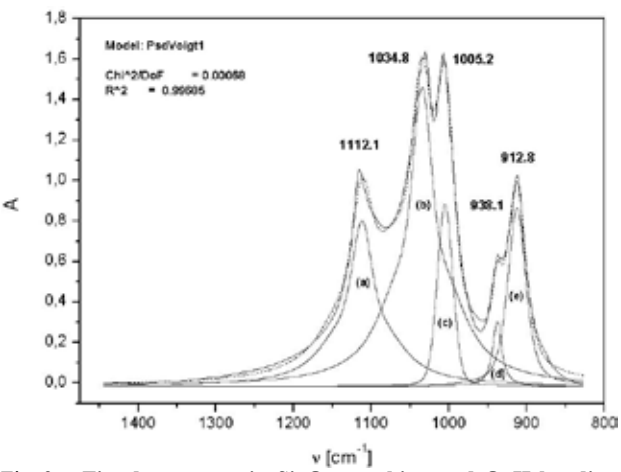

Fig. 3. **Fitted spectrum in Si–O stretching and O–H bending region of kaolin Sedlec Ia ($f_{50–40}$): ν(Si-(apical)O) (a), ν_s(Si–O–Si) (b), ν_{as}(Si–O–Si) (c), δ_1(O–H) (d) and δ_2(O–H) (e)**

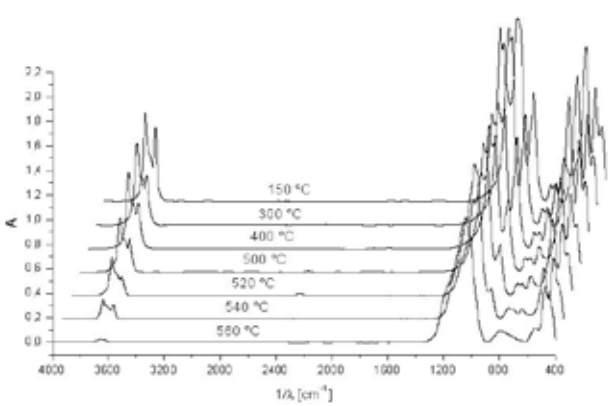

Fig. 4. **Subtracted spectra of burning kaolin Sedlec Ia (fraction $f_{50–40}$)**

Peaks Spectroscopic Variables – The O–H Stretching Region

The progress of the primary spectroscopic parameters, i.e. amplitude, half width and peak's center, of ν_1(ouOH) and ν_4(inOH) IR bands during kaolin thermal were compared. The dependence of peak's amplitude on the temperature and particle size is shown on Figs. 5. and 6.

While peak's amplitude as well as its area is related to amount of hydroxyl groups in sample, the peaks width provides information about level of hydrogen bonds interaction. The width of bands increase together with extends of intermolecular interaction, whereas the peak's center is degreased. Relation of peak's half-width on the temperature and particle size is shown on Figs. 7. and 8.

Peak´s amplitude and half-width show the significant positive correlation on the level $p<0.05$. Value of correlation coefficient was calculated on 0.405.

The dependence of peak's center on the temperature and particle size is shown on Figs. 9. and 10.

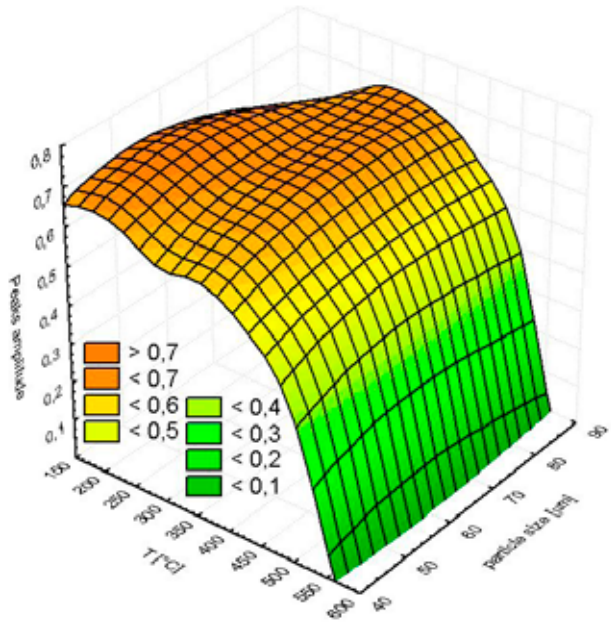

Fig. 5. **Dependence of ν_1(ouOH) peak's amplitude on the temperature and particle size**

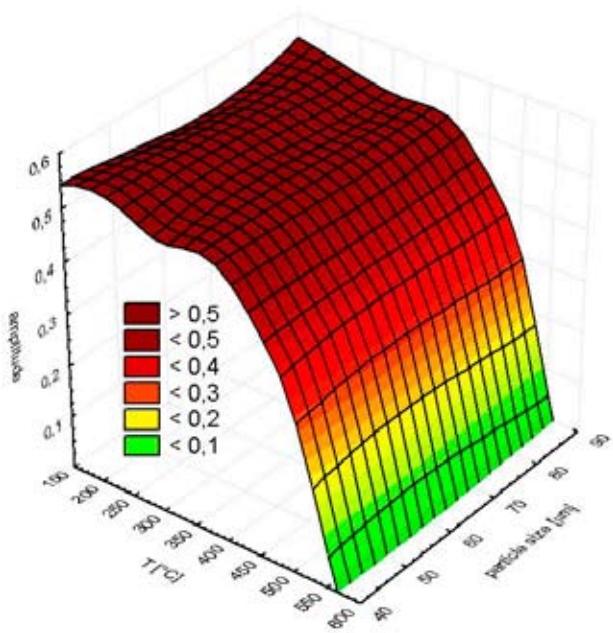

Fig. 6. **Dependence of ν_4(inOH) peak's amplitude on the temperature and particle size**

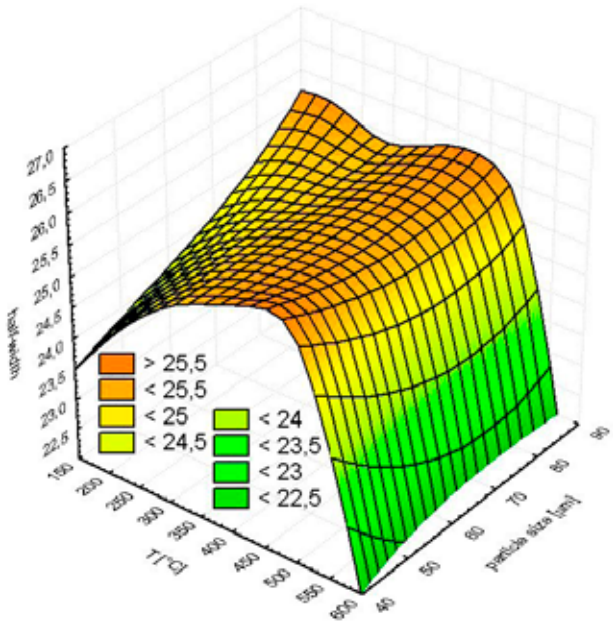

Fig. 7. Dependence of ν_1(ouOH) peak's width on the temperature and particle size

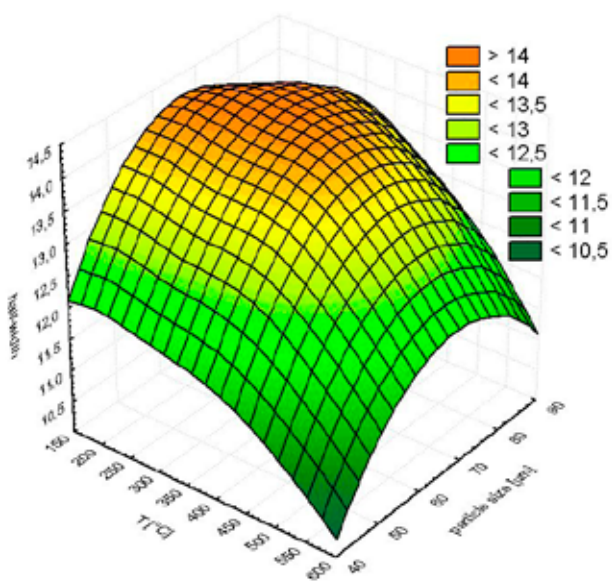

Fig. 8. **Dependence of ν_4(inOH) peak's width on the temperature and particle size**

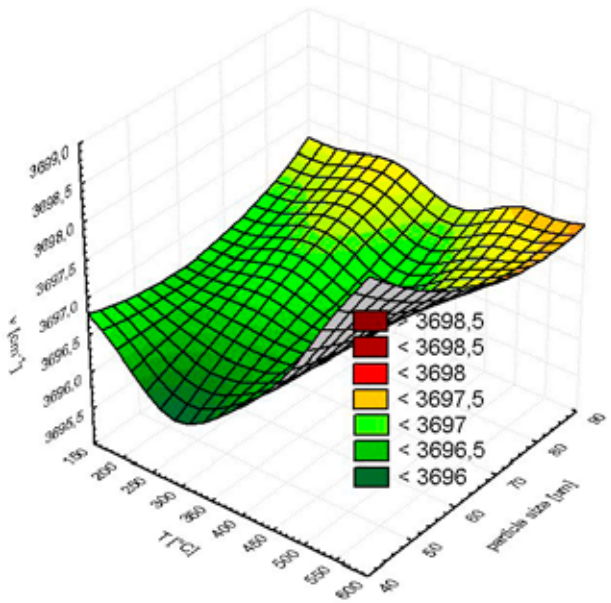

Fig. 9. **Dependence of ν_1(ouOH) peak's wavelength on the temperature and particle size**

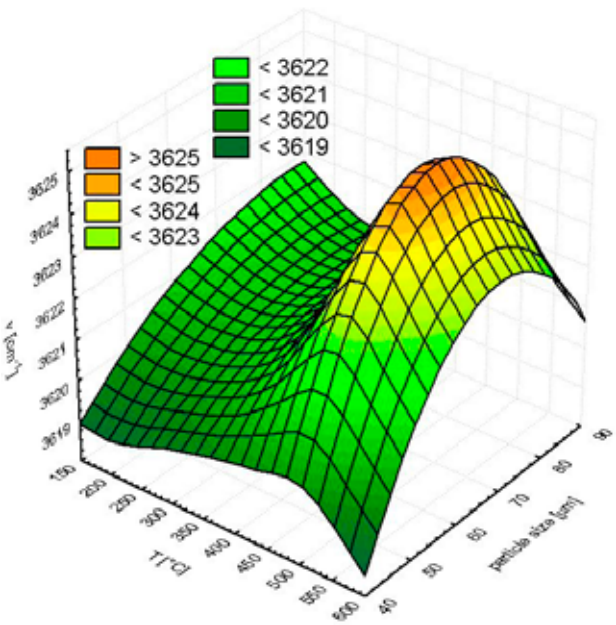

Fig. 10. **Dependence of ν_4(inOH) peak's wavelength on the temperature and particle size**

Peaks Spectroscopic Variables – The Si–O Stretching Region

The band of symmetric stretching of Si–O bond in siloxane bridge (Si–O–Si) at wavelength ~ 1,033 cm^{-1} was pursued. Among other leads the thermal inducted processes during dehydroxylation of kaolinite to increasing of shape factor (m_u) of applied Voight function (1). Further sample heating leads to lose selectivity of ν_s and ν_{as} vibration.

Conclusions

The ν_1(ouOH) and ν_2(inOH) sharp spectral bands were used for dehydroxylation process study, because these stretch band can be fitted with good accuracy and selectivity they isn't lose absorbtion selectivity during dehydroxylation.

The reason for peak's amplitude decrease and its re-entry increase on temperature interval 200–350 °C is pre-dehydroxylation process, which according several authors[8], takes place on the temperature interval from 160 to 360 °C, i.e. this process precluding dehydroxylatin.

For ouOH groups has influence of predehydroxylation process on the shape of spectra decreased with growing particle size (see Fig .5.). This effect is insignificant for inner hydroxyl groups. Smaller particles show more slowly loosing of inOH groups than bigger (see Fig. 6.).

The intensive Van der Wals force for the biggest particles at low temperature is caused by capillary water, while small particles are already exsiccated. There is visible significant influence of pre-dehydroxylation process on the peks half width (see Fig. 7.).

For small particles were interactions between inOH groups decrease with temperature more quickly than bigger particles (see Fig. 8.).

Van der Wals force going to be stronger during pre-dehydroxylation process. The most intensive hydrogen bonds interaction between outer hydroxyls was found for temperature interval from 200 to 300 °C and the particles smaller than 60 µm. The process of pre-dehydroxylation takes place on this temperature interval.

Smaller particles are more sensitive to pre-dehydroxylatin, but dehydroxylation proceeds faster. Isolated OH groups are formed via this process and peak's wavelength during heating increase more rapidly than in the case of bigger particles (see Fig. 9.).

Inner hydroxyl groups show the minimum extent of hydrogen bonds interaction about 500 °C, this correspond to starts of the second dehydroxylation step, i.e. recombination of alumina octahedron and silica tetrahedron (see Fig. 10.).

The influence of dehydroxylation process on the shape of infrared spectrum was also evaluated from shape factor of peak of asymmetric stretching of Si–O bond. Increasing of m_u value with growing temperature means that peak's shape more approaching to Lorentz function profile.

This work has been supported by MŠMT poject NPV – NHV – 1 number 2B08024.

REFERENCES

1. Temuujin J., Okada K., MacKenzie D. J. K., Jadambaa T. J. Eur. Ceram. Soc. *19*, 105 (1988).
2. Pérez-Rodríguez J. L., Pascual J., Franco F., Jiménez de Haro M. C., Duran A., Ramírez del Valle V., Pérez-Maqueda L. A. J. Eur. Ceram. Soc. *26*, 747 (2006).
3. Levy H. J., Hurst J. H. Fuel *72*, 873 (1993).
4. Castelein O., Soulestin B., Bonnet P. J., Blanchart P.: Ceram. Int. *27*, 517 (2001).

5. Heide K., Földvari M.: Thermochim. Acta *446*, 106 (2006).
6. Nahdi K., Llewellyn P., Rouquérol F., Rouquérol J., Ariguib N. K., Ayedi M. T.: Thermochim. Acta *390*, 123 (2002).
7. Traoré K., Gridi-Bennadji F., Blanchart P.: Thermochim. Acta *451*, 99 (2006).
8. Balek V., Murat M.: Thermochim. Acta *282/283*, 385 (1996).
9. Temuujin J., MacKenzie D. J. K., Schmücker M., Schneider H., McManus J., Wimperis S.: J. Eur. Ceram. Soc. *20*, 413 (2000).
10. Santos S. H., Campos W. T., Santos S. P., Kiyohara K. P.: Ceram. Int. *31*, 1077 (2005).
11. Hlaváč J., *Základy technologie silikátů* (trans. name: *The primer of technology of silicates*), chapter II, p. 118, SNTL, Prague 1988.
12. Franco F., Pérez-Maqueda A. L., Pérez-Rodríguez L. J., J. Colloid Interface Sci. *274*, 107 (2004).
13. Deng Y., White N. G., Dixon B. J.: J. Colloid Interface Sci. *250*, 379 (2002).
14. Zhang B., Li Y., Pan X., Jia X., Wnag X.: J. Phys. Chem. Solids *68*, 135 (2007).
15. Ptáček P., Kubátová D., Havlica J., Šoukal F., Opravil T.: Keramický zpravodaj *1*, 5 (2008).

L09 CRITICAL PARTICULATES FINENESS OF THE AIR CLASSIFICATION PROCESSES

TOMÁŠ SVĚRÁK, ONDŘEJ KOZDAS and VÍTĚZSLAV FRANK
Brno University of Technology, Faculty of Chemistry, Institute of Materials Chemistry, Purkynova 118, 612 00 Brno, Czech Republic,
sverak@fch.vutbr.cz

Introduction

Very fine powder materials are used widely in applications of material engineering, chemical industry, industry of building materials, food processing industry, production of pharmaceuticals and in various other areas. In all the here above areas of application, the use of very fine powder materials is conditioned by their granulometry: the contents of particles above the defined limit is usually strictly restricted, respectively the presence of finer particles than defined, i.e. particles below the defined limit – for example the highest acceptable content of pulverous share. In both of the here above cases, for separation of coarse particles from the finer particles, a series of sorting processes are used. Those processes are applied to the given very fine powder material in the form of a dispersion or suspension in the gaseous medium or liquid medium.

One of the basic ways of grain-size classifying of very fine powder materials used in the industry is the "dry" way of sorting of particles of materials dispersed in the flow of gas in the air classifiers. Those air classifiers (often known as "air separators") are based on the principle of competition of centrifugal forces and adrifting forces.

The very often discussed limits defined for working regimes of classification in the air classifiers[1] are the following:

- the required classifying sharpness
- adhesive forces of sorted materials
- the maximal classifying fineness attainable in operation processes
- abrasion

Hereinafter, we will deal with the attainable fineness of classified materials and classifying sharpness of air classifiers.

Experimental

D e f i n i t i o n A r e a

Air classifiers with cylindrical rotor – see Fig. 1. and Fig. 2. – represent the type of classifying equipment that enables us to attain the maximal sorting effectiveness of very fine powder materials under the here above conditions of "dry" industrial classifying.

Functional critical balance of forces causing the movement of sorted materials is established on the level of the radius of the cylindrical turbine in case of uniform motion of particles in a straight line way with a constant speed relative

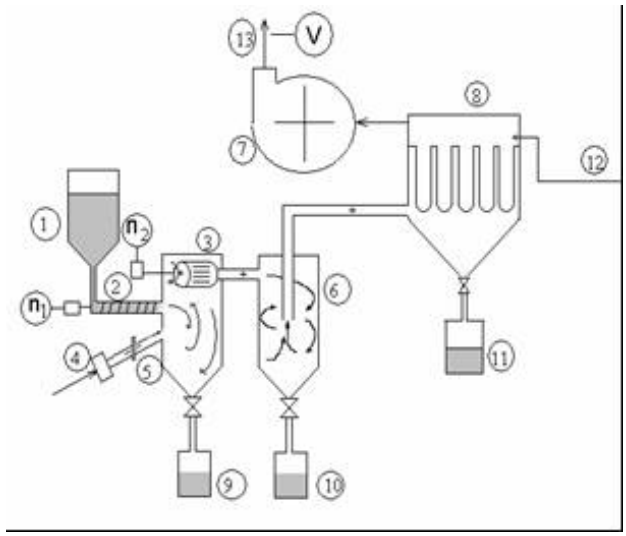

Fig. 1. **Air classifiers function: 1 – Input material hopper, 2 – Feeder, 3 – Classifying chamber, 4 – Suction air filter, 5 – Air flap, 6 – Cyclone clarifier, 7- Centrifugal blower, 8 – Beg dust filter, 9 – Coarse share bin, 10 – Fines bin,11 – Powder fines bin, 12 – Pulsating flick air, 13 – Classification air outlet**

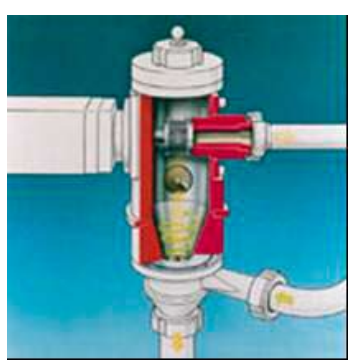

Fig. 2. **Classifying cylindrical turbine of air classifiers**

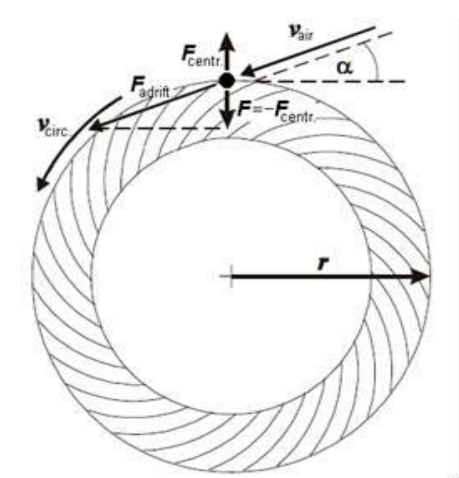

Fig. 3. **The balance of forces in the course of particles classification for dcr**

to the sorting turbine blades. This balance depends on and is given by just and only the centrifugal and adrifting forces then. The adrifting forces are represented by the aerodynamic forces of the resistance of the particle to its relative movement in the centripetal flow of air in the classifying turbine (Fig. 3.).

The balance of forces is defined by the relations[2,3] (1)–(6):

$$F_{adrift} \cdot \sin\alpha = F_{centr} \tag{1}$$

$$F_{adrift} = \frac{1}{2} \cdot C \cdot S \cdot \rho_f \cdot v_{air}^2 \tag{2}$$

$$C = f(\mathrm{Re}) \tag{3}$$

$$\mathrm{Re} = v_{air} \cdot d_{cr} \cdot \rho_f / \mu \tag{4}$$

$$v_{circ} = \pi \cdot D \cdot n \tag{5}$$

$$F_{centr} = 2 \cdot m \cdot v_{circ}^2 / D \tag{6}$$

where:
C [–] – Resistance coefficient taking into account gas flow round the particle,
d_{cr} [m] – Critical particle size,
$d75_F$ [m] – Particle dimension which corresponds to the passed 75% wgt amount of the fine share
D [m] – Effective diameter of classifier turbine,
m [kg] – The particle mass of the critical grain dimension d_{cr},
n [min^{-1}] – Turns of classifier turbine,
q_d [%] – Particle size amount
S [m^2] – Frontal cross-section plane of the critical dimension particle,
v_{air} [m s^{-1}] – Gas flow that drags solid particles into classifier turbine,
v_{circ} [m s^{-1}] – Peripheral velocity of classifier turbine on its effective diameter,
ρ, ρ_f [kg m^{-3}] – Specific mass of classified solid, gas stream density,
μ [Pa s] – Gas stream viskozity
Re [–] – Reynolds number,
T_{mod} [–] – modified Tromp number.

The classification sharpness (7) corresponds to the modified Tromp definition[3] based on the grain-size curves analysis (Fig. 4.).

$$T_{mod} = d75_F / d25_R \tag{7}$$

Experimental Facility and Classified Material

Pilot plant air classifier Hosokawa Alpine ATP-50 (Fig. 5.)

Grain sizer: granulometr LA-500 Horiba (Japonsko).

Classified material : surface treated carbonate filler on the basis 2VA OMYA Vápenná a.s., the specific weight of which equals $\rho = 2.72$ kg m^{-3}; with additional surface treatment by higher fatty acids on the level of 0.3 % wt. (Fig. 6.).

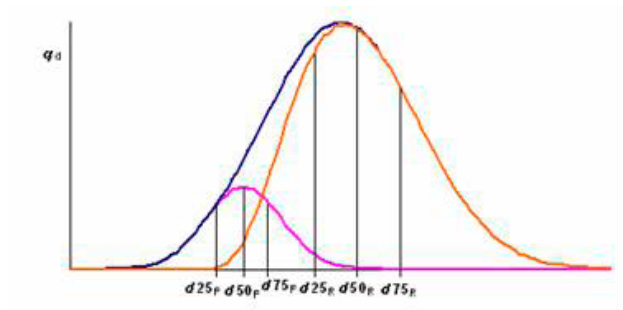

Fig. 4. **Definition of the classification sharpness**

Fig. 5. **Pilot plant air classifier**

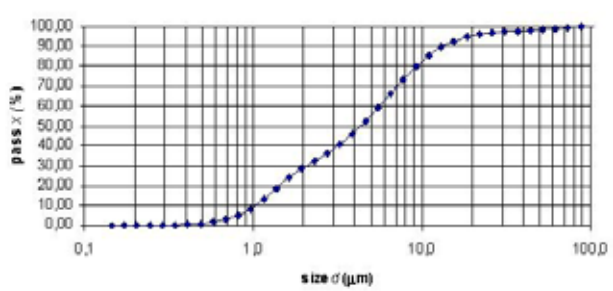

Fig. 6. **Grain sizing curve of the filler at the inlet area of the classifier**

Measurement Procedure

The here above carbonate filler was classified in and by the air classifier. In the course of the process, the following variables were changed[4]: Turns n of the classifying turbine, the input m_{inp} of sorted material incoming into the classifier

as well as the speed *w* of the classifying air incoming into the classifying turbine. The evaluated parameters d_{cr} and T_{mod} were obtained from the grain sizing curves of the coarse and fine shares of the classified material.

We concentrated especially on the classification of the finest particles of material, i.e. on the area with the highest turbine speed attainable in the sorting equipment used.

Results

The iterative calculation of the relations (1)–(6) in Excel® mode provided us the way to establish the classification process area (Fig. 7.). Out of the figure the following is evident: the combinations of the turns range of the classifying turbine *n* and the velocity of the classifying air *w* are needed to attain the required fineness of classifying defined by the size of the coarsest particles d_{cr}

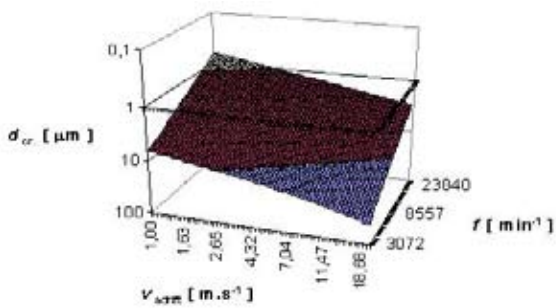

Fig. 7. **Attainable classification fineness as a function of the velocity of the classifying air w and turns of the classifying turbine n**

The analysis of the deviations of the really measured values from calculated values as well as the analysis of the airflow around the particles of material under the conditions of the transition region as well as the changes in the morphology of particles of real material will be specified in a separate publication.

This article deals especially with the limiting conditions under which it is possible to attain the highest fineness of classification. Out of the results we have achieved in the course of the measurements, we show here just the time dependence of the values of classification sharpness T_{mod} in the area of the highest fineness of the classified material and the maximal turns of the classifying turbine with the optimal material input (Fig. 8.). The theoretical (i.e. calculated) fineness of sorting dcr set by regulating the velocity of the classifying air is shown here as a parameter.

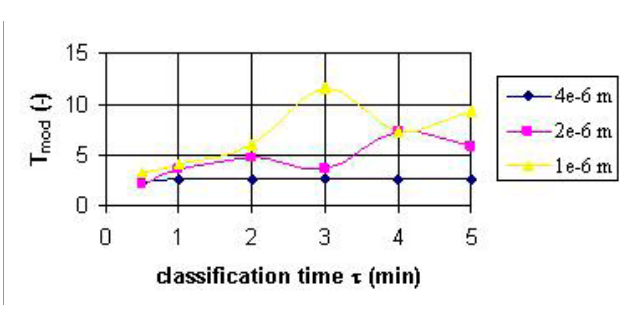

Fig. 8. **Time dependence of the classifying sharpness in the area of the highest fineness of classifying**

Conclusions

The attainable level of the fineness of classification depending on the type of the classified material and the size of the classifiers amounts to several micrometers[5], the paper[6] cites 3µm and the latest catalogue of the products made by the world-renowned company Hosokawa Alpine[7] mentions 2,5 µm. What is the reason for this limitation? Why is it not possible to move the limits of the air classifying towards the higher fineness when attaining higher turns of rotors of the classifiers cannot be a principal problem these days and when the present technologies require particulate solids of higher fineness? The solution to these questions is evidently contained in the analysis relating to Fig. 8.

The chart shows that the classificatio sharpness between the fine and coarse share of the classified material decreases significantly with the set fineness of sorting. As the higher theoretical fineness is set in the classifying system at the given turns of the classifying turbine by the decreasing of the velocity of the classifying air incoming into the classification process, the problem is to keep the regular, relatively very low flow rate of the classifying air in the blades of the classifier at the extremely high turns of the classifying turbine. The measured values of the time dependence (Fig. 8.) show that the conditions for keeping regular conditions are getting worse with the increasing time of classification. Significant change for the worse is evident especially at the initial phase of classifying. On the basis of the computer simulation[4] (Fig. 9.) we assume that in the course of the classification process, at the peripheral area of the classifying turbine, a barrier layer of critical grain of material is created that partially restrains the movement of the finer fractions that have been sorted out into the exhaust of those shares that is located in the axis of the classifying turbine.

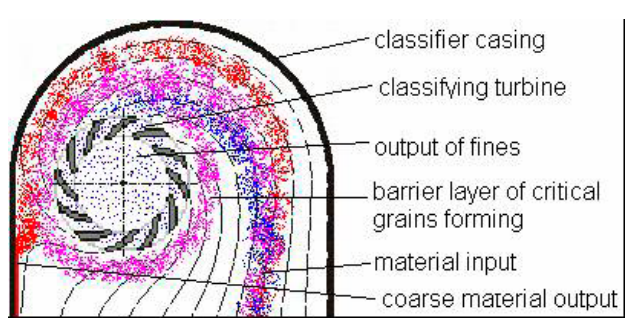

Fig. 9. **Creation of a barrier layer in the classifying process of very fine particulate solids**

As the hypothetical barrier layer of the critical grain of material has to restrain the sorting air flow into this turbine, we anticipate the occurrence of the pressure pulsation (and therefore also a flow rate pulsation) of the classifying air that carries the coarser particles into the finer fractions.

This is the mechanism that we use to explain the irregularities of the conditions under which the classifying air flows into the classifying system. Due to that mechanism, it s no more possible to achieve higher fineness in the processes of air classifying today. We arrived at the following conclusion: Any evidence that would prove occurrence of the hitherto hypothetical barrier layer of the critical sizes of grain of the classified material might result in changes in constructions and processes that could enable us to overcome the fineness classificatio limits of the present air classifiers.

REFERENCES

1. Peukert W.: Production and Handling of Nanoparticles. *Proceedings of the 5th International Conference for Conveying and Handling of Particulate Solids*, Sorento 2006.
2. Himmelblau D. M.: *Basic Principles and Calculations in Chemical Engineering*. 5th Edition, Prentice-Hall International, Inc., Englewood Cliffs, New Jersey 1989.
3. Wills B. A., Napie-Munn T.: *Mineral Processing Technology*. 7th Edition, Elsevier, London 2006.
4. Kozdas O.: Diploma thesis,FCH BUT Brno 2007.
5. Eštoková A., Števulová N.: Chem. Listy *96*, 509 (2002).
6. Sverak T.: Int. J. Miner. Process. Int J Miner Process *74*, 1 (2004).
7. *Handbook Powder and Particle Processing*. 2th Edition, Hosokawa Alpine, Augsburg 2006.

L10 DETERMINATION THE REACTION ORDER FOR FAST FORMATION OF CuS_2O_3

MIHAELA LIGIA UNGUREŞAN[a] and FRANCISC VASILE DULF[b]

[a]*Technical University of Cluj-Napoca, Chemical Department, 103–105 Muncii Bvd., 400641, Cluj-Napoca, Romania*

[b]*University of Agricultural Sciences and Veterinary Medicine, Food Quality Control Department, 3–5 Mănăştur Str., 400372, Cluj-Napoca, Romania,*

Mihaela.Unguresan@chem.utcluj.ro

Introduction

Reactions between thiosulfate and ions of metallic elements in solution have been repeatedly studied, several papers being published, for instance[1,2,3,4,5].

The theory of the method of continuous variations as given by Job is reviewed and extended to cases in which more than one compound is formed from a given pair of components.

The method was applied to the formation of CuS_2O_3. The absorption of the monochromatic light was the property measured in this case. Because only a single compound is formed, the results are independent of the wave length of the light used. Job's method was used to identify the intermediate compound formed by the reaction of the two components.

Cu^{2+} and $S_2O_3^{2-}$ react in a 1 : 1 ratio, consistent with the formation of CuS_2O_3(ref.[6])

The reaction between Cu(II) and thiosulfate ions results from the formation of an intermediary complex, CuS_2O_3, similar with the complex $FeS_2O_3^+$.

It's considered:

$Cu^{2+} + S_2O_3^{2-} \leftrightarrow CuS_2O_3$ $\quad K = k_1/k_2$

$CuS_2O_3 + S_2O_3^{2-} \rightarrow Cu^+ + {}_4O_6^{2-}$ $\quad k$

where the seconds step is determined by speed.

The formation of the reaction intermediate develops fast both ways, which implies the following relation between the speed constants: $k_1, k_2 >> k$.

The concentration of the reactions' intermediate is the one that corresponds to the equilibrium for the first process, just as the first one does not happen.

Due to the fact that the second process takes place, the concentration of the reaction's intermediate is close the equilibrium one, no exactly it, but the approximation of pre-equilibrium is considered the one appropriate to this equilibrium[7].

The formation of this complex can be followed spectrophotometrically, but the time of this reaction is very small (10–50 ms), therefore for the study of the formation of CuS_2O_3 was used the stopped-flow technique.

Experimental

R e a g e n t s

All chemical used were analytical grade, from B&A and were used without further purification. The dilution of $Cu(ClO_4)_2$, $Na_2S_2O_3$ and $HClO_4$ (60%) were made with doubly distilled water.

A p p a r a t u s

A stopped-flow apparatus[7] was used. The essential parts are: two syringes needed to rapidly inject the reactants into the mixing chamber, manually. After leaving the mixing chamber the mixture flows into a third syringe whose piston is suddenly stopped after a predetermined volume of solutions has been injected. At the moment the flow is stopped, a micro switch operated by the third piston triggers the oscilloscope of the detection system.

On the osscillogramme the variation of transmitted light intensity I_t through the solution, depending on time, for known reactant concentrations (Fig. 1.) is followed. The intensity of light at the maximum transparency, I_0, was also recorded.

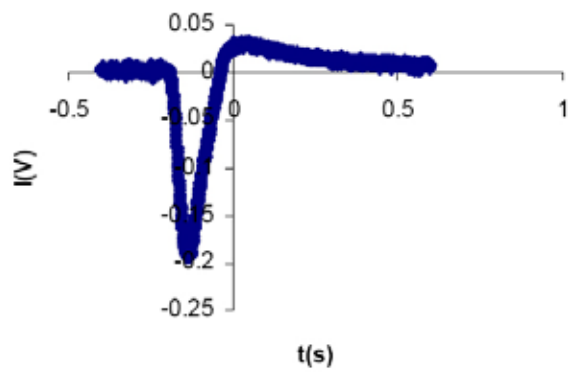

Fig. 1. **The variation of transmitted light intensity I(V) with respect to time t [s] for $[Cu^{2+}] = 5 \times 10^{-3}$ mol dm^{-3}; $[S_2O_3^{2-}] = 5 \times 10^{-3}$ mol dm^{-3}; $\lambda = 430$ nm; T = 21 °C**

For each set of concentrations of the two reactants there have been at least 20 experiments, the reproducibility of the experimental data obtained being very good even for really small concentrations of the reactants. ($[Cu^{2+}] = 5 \times 10^{-4}$ mol dm^{-3}; $[S_2O_3^{2-}] = 5 \times 10^{-4}$ mol dm^{-3}).

Results and Discussion

According to the Lambert-Beer Law, extinctions at different concentrations of the $Cu(ClO_4)_2$, $Na_2S_2O_3$ were computed. Many experimental records were done for concentrations of $[Cu(ClO_4)_2] = [5 \times 10^{-4}, 10^{-1}]$ mol dm^{-3}, $[Na_2S_2O_3] = [5 \times 10^{-4}, 10^{-1}]$ mol dm^{-3}, for wavelength $\lambda = 430$ nm.

The measured absorption at 430 nm, E, is made out of contributions of the colored species, which in our case is just the reaction's intermediate CuS_2O_3:

$E = \varepsilon\, l\, [CuS_2O_3]$

where the optical way is l = 1.2 cm.

The extinction of the solution has been calculated for the mixing period, $E_0 = \log(I_0/I_t)_0$. The initial concentrations of the reactants are identical in all determinations; therefore the

influence of the pre-equilibrium on the experimental reaction order could be fully manifested.

So, for example, with concentrations of $[Cu^{2+}] = 5 \times 10^{-3}$ mol dm^{-3}, $[S_2O_3^{2-}] = 5 \cdot 10^{-3}$ mol dm^{-3} and $[HClO_4] = 2 \times 10^{-2}$ mol dm^{-3}, wavelength $\lambda = 430$ nm and T = 21 °C, I_0 = 1,493.5 mV. The curve of formation the reaction intermediate is given in Fig. 2.

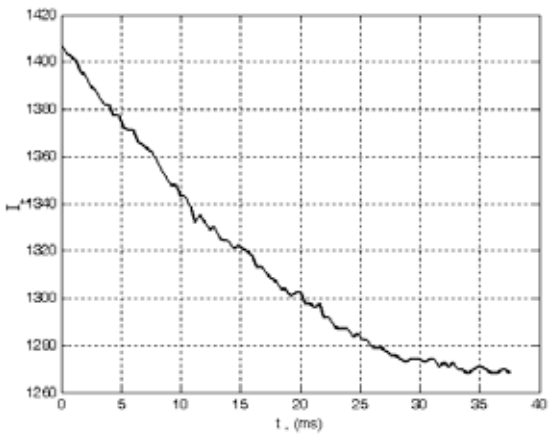

Fig. 2. **Transmitted intensity I_t (mV) as a function of time t [ms] for $[Cu^{2+}] = 5 \times 10^{-3}$ mol dm^{-3}, $[S_2O_3^{2-}] = 5 \times 10^{-3}$ mol dm^{-3} and $[HClO_4] = 2 \times 10^{-2}$ mol dm^{-3}, wavelength $\lambda = 430$ nm and T = 21 °C**

The calculus for the determination of the reaction order was made using Mathlab sheets. E = f(t) (Fig. 2.), lg (E) and 1/E = f(t) were represented graphically as well as dE/dt, which is a measure of the reaction rate.

Using these data, the reaction order with respect to the colored complex was calculated. The plots of logarithm of the rate vs. the logarithm of the extinction gave straight lines with slopes 1, as it is illustrated by Fig. 3., where the reaction order n = 0.98 was calculated with initial concentrations of 5 × 10–3 mol dm–3 for both reactants in aqueous acidic solution (2 × 10–3 mol dm–3 HClO4), wave length λ = 430 nm and T = 21 °C.

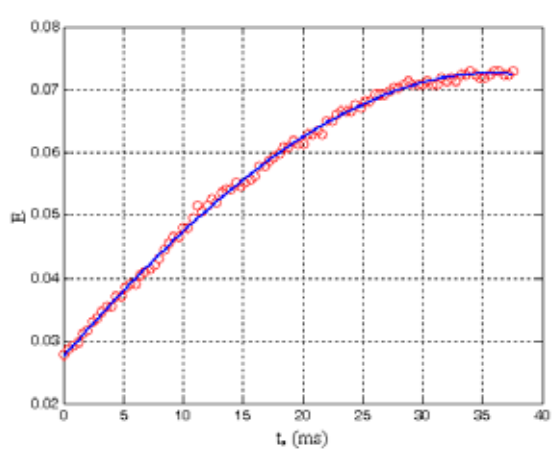

Fig. 3. **Extinction (E) as a function of time t [ms]**

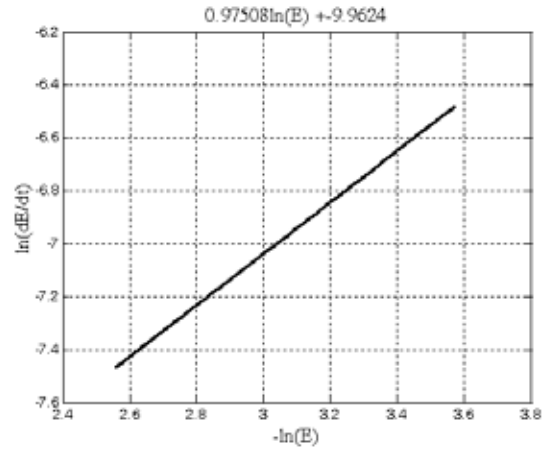

Fig. 4. **The reaction order obtained through experiments**

In conclusion, the reduction of Cu^{2+} with ions of thiosulfate is a reaction with pre-equilibrium, from kinetic point of view 8,9.

Another set of experimental data are presented in Table I.

Conclusions

Table I

The experimental data (at T = 21 °C; λ= 430 nm; $[HClO_4] = 2 \times 10^{-2}$ mol dm^{-3})

The applications of the stopped-flow technique are

Exp. no.	Initial conditions	n
1.	$[Cu(ClO_4)_2] = 10^{-1}$ mol dm^{-3}; $[Na_2S_2O_3] = 10^{-1}$ mol dm^{-3};	1.04
2.	$[Cu(ClO_4)_2] = 5 \times 10^{-2}$ mol dm^{-3}; $[Na_2S_2O_3] = 10^{-1}$ mol dm^{-3};	1.01
3.	$[Cu(ClO_4)_2] = 5 \times 10^{-2}$ mol dm^{-3}; $[Na_2S_2O_3] = 5 \times 10^{-2}$ mol dm^{-3};	0.98
4.	$[Cu(ClO_4)_2] = 10^{-2}$ mol dm^{-3}; $[Na_2S_2O_3] = 5 \times 10^{-2}$ mol dm^{-3};	1.15
5.	$[Cu(ClO_4)_2] = 10^{-2}$ mol dm^{-3}; $[Na_2S_2O_3] = 10^{-2}$ mol dm^{-3};	0.93
6.	$[Cu(ClO_4)_2] = 5 \times 10^{-3}$ mol dm^{-3}; $[Na_2S_2O_3] = 5 \times 10^{-3}$ mol dm^{-3};	0.98
7.	$[Cu(ClO_4)_2] = 5 \times 10^{-3}$ mol dm^{-3}; $[Na_2S_2O_3] = 10^{-3}$ mol dm^{-3};	1.04
8.	$[Cu(ClO_4)_2] = 5 \times 10^{-3}$ mol dm^{-3}; $[Na_2S_2O_3] = 5 \times 10^{-4}$ mol dm^{-3};	1.03
9.	$[Cu(ClO_4)_2] = 5 \times 10^{-4}$ mol dm^{-3}; $[Na_2S_2O_3] = 5 \times 10^{-3}$ mol dm^{-3};	1.01

numerous. Any reaction, which can be initiated by mixing two solutions, can be studied by the stopped-flow technique as far as the reaction is a rapid one.

This studies show that the formation of the copper thiosulfate complex (CuS_2O_3) from the rapid redox reaction between Cu(II) and thiosulfate ions proceed at 21.0 °C is a first order reaction.

REFERENCES

1. Bâldea I., Niac G.: Inorg. Chem. *7*, 1232 (1868).

2. Bâldea I., Niac G.: Inorg. Chem. *9*, 110 (1870).
3. Niac G., Cădariu I.: *Contribuţii la Studiul Reacţiei dintre Ionul Feric şi Ionul Tiosulfuric*, Studia Universitatis Babeş-Bolyai, Series I, Fasciculus 2, p.25. Chemia, 1959.
4. Cădariu I., Niac G., Oniciu L., *Determinarea Spectrului de Absorbţie în Ultraviolet al Complexului* $FeS_2O_3^+$, *Studia Universitatis Babeş-Bolyai,* Series I, Fasciculus 1, p. 27. Chemia, 1962.
5. Niac G., Teza de Doctorat, Universitatea Babeş-Bolyai Cluj-Napoca, 1962.
6. Ungureşan Mihaela Ligia, Niac G.: Rev. Roum. Chim. *52*, 481 (2007).
7. Ungureşan Mihaela Ligia, Niac G., Surducan, E., Surducan, V.: Rev. Chim. *58*, 40 (2007).
8. Niac G., Schonberger E.: Chimie-fizică, *3* Bucureşti, Ed. Tehnică, 1970.
9. Williamson Mark A., Rimstidt Donald J., Geochim. Cosmochim. Acta 57, 3555 (1993).

L11 NEW FINDINGS ON THE CERAMIC PETROGRAPHY OF THE LOŠTICE POTTERY

MIROSLAVA GREGEROVÁ, MARTIN HLOŽEK and DALIBOR VŠIANSKÝ
Institute of Geological Sciences, Faculty of Sciences, Masaryk University, Kotlářská 2, 611 37 Brno, Czech Republic.
mirka@sci.muni.cz

Introduction

The 15th and 16th century ceramic vessels covered with "blebs" called the Loštice pottery (see Fig. 1.) represent unique products of the mediaeval and early modern Central European pottery. These tumblers were exported abroad and become famous in the whole Europe. Workshops producing this pottery were located in the village Loštice in the north Moravia (Czech Republic). Used raw material came from nearby villages' districts.

The presented research is aimed at the raw materials' identification, the examination of the Loštice pottery chemical and mineralogical composition and technological production process.

The paper summarizes the results of micropetrographic, geochemical and experimental examination of the mediaeval pottery from Loštice. The original tumblers' (based on shape and raw material petrographical composition they have been divided into five groups), assumed raw material (clay and loess) and also the experimentally fired vessels were subject to chemical analyses, optical and scanning electron microscopy (SEM) and energy dispersive (EDX) analyses. The firing temperature and the affect of garnets on the formation of "blebs" were experimentally examined.

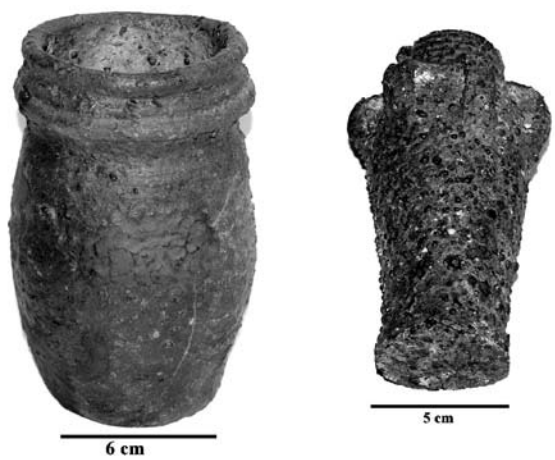

Fig. 1. **The Loštice pottery. Collections of the Moravian Museum in Brno**

Analyses of the Loštice Pottery Artifacts and Raw Materials

Analytical Methods

- SEM and EDX analyses were done on Cameca SX 100 equipment (at 15 kV and 10 nA)
- Chemical silicate analyses were done in the ACME laboratories in Vancouver, Canada. The complete analysis of main oxides was done via ICP-emission spectrometry and trace elements via ICP-MS
- Some of the samples were analysed by so called wet analysis
- Recalculations on normative minerals were done using the MINLITH software
- Optical microscopy; analyses were carried out using covered thin sections on Olympus BX 51 petrological polarising microscope

Chemical Composition of the Assumed Raw Material and Artifacts

Silicate analyses were done to evaluate the complex chemical composition of the original raw materials. Eight original ceramic artifacts, two assumed raw material samples and four samples extracted from the furnace vault were examined. Graphical results – see Figs. 2. and 3.

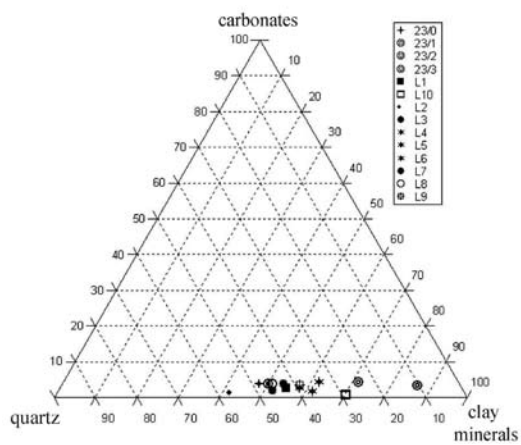

Fig. 2. **Normative composition of examined artifacts and raw materials calculated from the chemical silicate analyses**

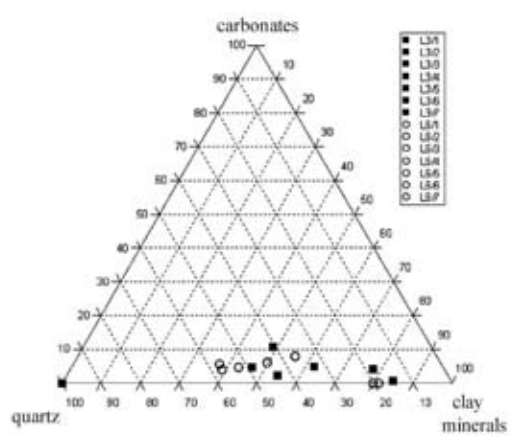

Fig. 3. **Normative composition of examined artifacts calculated from the microchemism of glass and binder. Analyzed by P. Sulovský**

Explanations to Figs. 2. and 3.:
L1 – raw material (grey clay containing graphite)
L2 – raw material (loess soil)
L3 and L7 - ceramic artifacts of the (020) group
L4, L5 and L6 – ceramic artifacts of the (010) group
L8 – ceramic artifacts of the (030) group
L9 – ceramic artifacts of the (040) group
L10 – graphite ceramics of the (050) group
23/0 – 23/3 – samples extracted from the furnace vaults. Chemical analyses of the 23/0, 23/1, 23/2 and 23/3 samples were done on CAMECA SX100 micro analyser. Chemical analyses of the L1–L10 samples were done by wet silicate analysis.

The recalculation results show that the (010), (020), (030) and also (040) pottery groups' chemical composition is very similar. Seven visually different samples (coming from all the five pottery groups) were chosen to verify the application of normative minerals for the identification of the Loštice pottery raw materials.

It is evident that the normative minerals recalculations from silicate and EDX analyses correspond to each other.

The presence of graphite (identified by chemical analyses and also by optical microscopy) represents the evidence of graphitic raw material application. The sorted out graphite clasts of high quality might have been used for graphitic pottery production. The material of lower quality, so called waste (clasts containing less graphite and more micas and iron oxides), might have been a suitable non-plastics supplement in the case of vessels covered with "blebs" (i.e. especially of the (010) pottery group). In the artifacts of the (010) group, graphite was present in the amount of 0.2–1.9 % wt.

Except of cordierite also sekaninaite and osumilite were be identified there – see TableI. Fig. 5. documents that these are new-formed crystals formed from the melt. Along with them, spinelides (magnetite, magnesioferrite and hercynite) occur in the pottery.

In some artifacts of the (040) group, relict garnets were determined – pyrope (94.6 % of pyrope and 4.4 % of almandine component).

The surface red colour of the (010) pottery group is caused by iron enamel with the melting addition. Except of one case, the enamel did not contain Pb. It is very probable that also the other enamels were alkalical and contained the addition of washed brick clay, which is responsible for the red up to red-purple colour of the enamel. The addition of iron clay did not have to be high. In the case of the Loštice pottery, the red colour was also caused by the interlayer under the enamel.

Experimental Firing

Miniature replicas of the Lošice pottery were made of local loess and clay soils found during the archaeological works. The raw material corresponds to tertiary deposits in the surroundings (e.g. in Litovel), which were also mined for the pottery production in later periods. Graphite was added in a form of graphitic clay. The graphitic pigment improves the clinkering properties of ceramic body. The bodies were always white, with grey streaks in the cross section. Apparent darker colour of the clay is explained by re-deposition of the raw material.

The difference between clay and loess is evident even macroscopically. Brownish colour of the fired body is caused by iron oxides.

The raw materials were mixed with water. As non-plastics, a garnet (almandine) concentrate was added to the ceramic paste.

To reach the specific surface colour, the dried replicas were coated with an engobe layer containing minerals of iron and melting addition before the firing. The firing was carried out in oxidation furnace at 1,250 °C.

The high melt content during the firing caused collapse of the vessels made of loess (see Fig. 4.).

Fig. 4. **Experimental firing of the Loštice pottery miniature replicas. The collapsed vessels were made of loess soil**

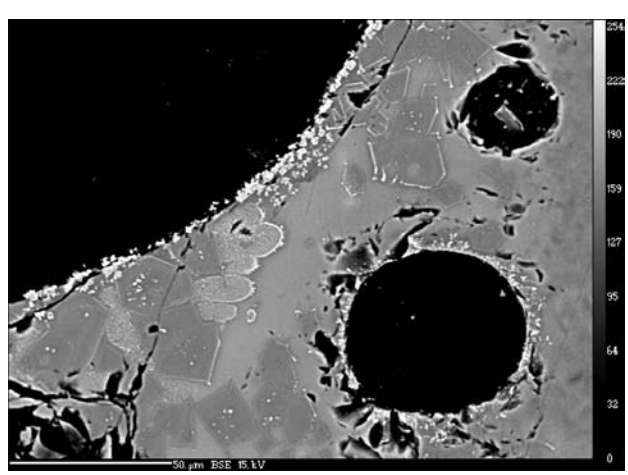

Fig. 5. **"Bleb" in the Loštice pottery of the (020) group (sample no. L 3) lined with a thin layer of spinel and glass matter containing a new-formed cordierite. Photo by R. Škoda**

The experiments bring the evidence of the use of almandine. The Loštice pottery replicas undisputedly display macroscopically the same "blebs", which are found in the original vessels. The correspondence of the mineralogical composition of the replicas and the original artifacts has been proven by optical and electron microscopy and microchemical examination of the new-formed phases (compare Table I and Table II).

Discussion

The basical plastic raw material corresponds to clay with a low content of very fine graphite (5–8 % wt.). The original raw material (pottery clay) from Loštice was used for the experiments. The products made of clay were able to resist high temperatures without a shape deformation. On the other hand, the utilization of local loess has been disproved by the experimental firing. The replicas made of loess collapsed at the temperature about 1,200 °C.

The opinion that the "blebs" on the pottery surface form by the decomposition of sulphides contained in the graphite from Svinov (Měchurová, Čejka, Zalabák 1992) has also been disproved by the experiment. The replica made of soil extracted from a pottery workshop did not contain any surface "blebs" after the experiment. The "blebs" only appeared

Table I
Chemical composition (EDX) of cordierite ($Mg_2Al_3[AlSi_5O_{18}]$), sekaninaite ($(Fe^{2+}_{1.5}Mg_{0.5})\ Al_3[AlSi_5O]_1)_8$) and osumilite ($(K_{0.75}Na_{0.25}Fe^{2+}_{1.5}Mg_{0.5})Al_{2.25}Fe^{3+}_{0.75}[Si_9Al_3O_{30}]$)

Sample	L 3	L 5	L6	L 11	L 15	L 3	L 5	L 9	L-19	L-24
Mineral/oxide		Cordierite			Sekaninaite			Osumilite		
SiO_2	47.6	49.3	47.6	47.1	47.3	58.6	59.8	60	56.5	54.5
TiO_2	0.2	0.1	0.4	0.1	0.1	0.1	0.8	1.1	1.7	1.6
Al_2O_3	36.5	32.6	33.8	32.3	32.4	11.6	18.4	23.2	13.3	14.7
FeO	7.7	7.2	8.5	14	16.7	20.3	15.8	6.6	20.2	15.7
MnO	0.1	0.1	0.1	0	0.1	0.1	0	0.1	0.2	0.4
MgO	7.8	9.1	8.7	4.9	3.2	0.6	0.9	3.1	0.4	1.4
CaO	0.1	0	0	0	0	0.9	1.2	1.2	2.7	3.5
Na_2O	0	0.2	0	0.1	0	0.8	0.2	0.7	0.2	0.7
K_2O	0.3	0.6	0.2	0.4	0.5	4.5	2.7	4.1	3.6	3.2
Cl						0		0.1	0	
F						0	0		0	
BaO						0.2	0	0.1		
P_2O_5	0.1		0	0		0.1		0		
Total	100.5	99.3	99.4	99.1	100.3	97.8	100	100.4	98.8	95.7
NaKCa										
Na	0	0	0	0		0.1	0	0.1	0.1	0.3
K	0.3	0.1	0	0	0.1	0.9	0.6	0.9	0.8	0.7
Ca									0.1	0
sum	0.3	0.1	0	0	0.1	1	0.6	1	1	1
FeMgMn										
Fe*(ii)*	0.6	0.6	0.7	1.2	1.5	1.6	1.5	1	1.4	0.9
Mn	0	0	0	0	0	0	0	0	0	0.1
Mg	1.2	1.4	1.3	0.8	0.5	0.2	0.2	0.8	0.1	0.4
Ca						0.2	0.2	0.2	0.4	0.7
Al	0.1	0	0	0		0	0		0.1	
Subtotal	1.8	2	2	2	2	2	1.9	2	2	2.1
FeAlTi										
Al						1.3	2.4	2.9	1.1	1.2
Ti						0	0.1	0.1	0.2	0.2
Fe						1.5	0.4		1.6	1.6
Subtotal						2.8	2.9	3	3	3
SiAl										
Si	4.8	5	4.8	4.9	5	10.8	10.6	10.2	10.3	10
Al	4.2	4	4.1	4.1	4	1.2	1.4	1.8	1.7	2
Sum	9	9	8.9	9	9	12	12	12	12	12
O	18.1	18	17.9	18	17.9	30.2	30	30.3	30.3	30.1

Table II
Chemical composition (EDX) of cordierite ($Mg_2Al_3[AlSi_5O_{18}]$), sekaninaite ($(Fe^{2+}_{1.5}Mg_{0.5})\ Al_3[AlSi_5O]_1)_8$) and osumilite ($(K_{0.75}Na_{0.25}Fe^{2+}_{1.5}Mg_{0.5})Al_{2.25}Fe^{3+}_{0.75}[Si_9Al_3O_{30}]$) in ceramic miniature replicas of tumblers experimentally fired at the temperature of 1,250 °C

Sample/oxide	1/1	1/2	1/3	1/4	1/5	2/1	2/2	4/1	4/2	4/3	4/4	4/5	4/6
SiO_2	47.6	47.3	47.9	44.6	47.1	56.0	52.5	51.1	51.7	51.7	47.7	50.7	48.9
TiO_2	0.2	0.2	0.2	0.2	0.2	0.4	0.2	0.1	0.0	0.1	0.1	0.2	0.2
Al_2O_3	34.0	34.5	33.5	36.0	34.3	24.4	27.3	32.0	32.5	32.5	29.2	32.3	36.2
FeO	7.7	7.2	7.8	8.5	7.7	14.4	14.0	3.3	2.6	3.6	1.9	4.3	3.2
MnO	0.1	0.0	0.1	0.1	0.1	0.2	0.3	0.1	0.1	0.1	0.1	0.1	0.1
MgO	8.9	9.1	8.6	9.1	8.7	2.0	3.6	11.9	12.3	11.4	4.1	11.2	10.7
CaO	0.1	0.0	0.0	0.0	0.1	0.3	0.2	0.1	0.1	0.1	15.8	0.4	0.0
Na_2O	0.1	0.2	0.1	0.2	0.1	0.0	0.0	0.0	0.0	0.0	0.4	0.0	0.0
K_2O	0.7	0.9	0.7	0.9	0.8	0.9	0.4	0.2	0.3	0.2	0.1	0.5	0.3
P_2O_5	0.0	0.0	0.0	0.0	0.0	0.3	0.1	0.0	0.0	0.1	0.0	0.1	0.0
Total	99.3	99.5	99.1	99.6	99.2	98.9	98.6	98.8	99.6	99.7	99.4	99.7	99.7
NaKCa													
Na	0.0	0.0	0.0	0.0	0.0	0.0	0.0	0.0	0.0	0.0	0.1	0.0	0.0
K	0.0	0.1	0.1	0.1	0.1	0.2	0.1	0.0	0.0	0.0	0.0	0.1	0.0
Ca	0.0	0.0	0.0	0.0	0.0	1.1	0.0	0.0	0.0	0.0	0.0	0.0	0.0
Sum	0.1	0.1	0.1	0.1	0.1	0.3	0.1	0.0	0.1	0.0	0.1	0.1	0.1
FeMgMn													
Mg	1.3	1.4	1.3	1.4	1.3	0.5	0.6	1.8	1.8	1.7	0.6	1.7	1.6
Fe	0.7	0.6	0.7	0.7	0.6	2.3	1.3	0.3	0.2	0.3	0.2	0.4	0.3
Mn	0.0	0.0	0.0	0.0	0.0	0.0	0.0	0.0	0.0	0.0	0.0	0.0	0.0
Ca	0.0	0.0	0.0						0.0	0.0	1.2	0.0	0.2
Subtotal	2.0	2.0	2.0	2.1	1.9	2.8	1.9	2.1	2.0	2.0	2.0	2.0	2.0
FeAlTi													
Al						3.0							
Fe	0.0	0.0	0.0	0.0	0.0	0.0	0.0	0.0	0.0	0.0	0.0	0.0	0.0
Ti	0.0	0.0	0.0	0.0	0.0	0.1	0.0	0.0	0.0	0.0	0.0	0.0	0.0
Subtotal	0.0	0.0	0.0	0.0	0.0	3.1	0.0	0.0	0.0	0.0	0.0	0.0	0.0
SiAl													
Si	4.8	4.8	4.9	4.5	4.8	9.9	5.6	5.1	5.1	5.1	4.9	5.0	4.8
Al	4.2	4.2	4.1	4.5	4.2	2.1	3.4	3.9	3.9	3.9	4.1	4.0	4.2
Subtotal	9.0	9.0	9.0	9.0	9.0	12.0	9.0	9.0	9.0	9.0	9.0	9.0	9.0
O	18.0	18.0	18.0	17.9	17.9	30.5	18.2	18.2	18.1	18.1	18.0	18.1	18.0

on the surface of replicas made of a raw material with the addition of almandine.

The experiments proved that the firing temperature reached 1,200–1,250 °C. The number and appearance of "blebs" depends on the content and chemical composition of almandine (garnet) in the raw material mixture. The reaction of almandine garnet (decomposed on almandine and pyrope components) with kaolinite can be summarized by the following equation:

$$Mg^{2+}_3Al_2Si_3O_{12} + 3Fe^{2+}_3Al_2Si_3O_{12} + 8Al_2Si_2O_5(OH)_4 \rightarrow 2Mg^{2+}_{1.5}Fe^{2+}_{0.5}Al_4Si_5O_{18} + 8Fe^{2+}Al_2O_4 + 6H_2O + 18\ SiO_2 \quad (1)$$

The composition of spinel, formation of cordierite, sekaninaite and possibly osumilite depends not just on the garnet composition but also on the original plastic raw material (Abbott, Clarke 1979, Green 1977).

Conclusion

The results show that the technology of the Loštice pottery production was completely different than described in older papers (e.g. Měchurová, Čejka, Zalabák, 1992).

The firing temperature of the Loštice pottery was nearly 300 °C lower than mentioned by Měchurová, Čejka and Zálabák (1992) based on XRD identification of cristobalite (1,470 °C). Cristobalite already forms at temperature above 1,000 °C.

The mineralogical analyses of the artifacts and the experiments showed that the cause of "blebs" formation was the addition of almandine.

This research has been supported by the MSM 0021622427 research project "Interdisciplinary reserch of prehistory to late mediaeval cultures".

REFERENCES

1. Bláha R., Frolík J., Sigl J.: Archaeologia historica *28*, 525 (2003).
2. Goš, V.: ZVOTAM *2*, 25 (1982).
3. Goš V.: Archaeologia historica *8*, 197 (1983).
4. Goš V.: *Loštice. Město středověkých hrnčířů*, Opava 2007.
5. Goš V., Novák J.: Archeologické rozhledy *XXVIII*, 399 (1976).
6. Měchurová Z., Čejka J., Zalabák P.: Časopis Moravského muzea – vědy společenské *57*, 201 (1992).
7. Měřínský, Z.: Vlastivědný věstník moravský *21*, 1 (1969).
8. Slivka M.: Severní Morava *46*, 65 (1983).

4.2. Posters

P01 OPTIMALIZATION OF LEAD SULPHIDE MECHANOCHEMICAL SYNTHESIS

MARCELA ACHIMOVIČOVÁ, ANNAMÁRIA MOCKOVČIAKOVÁ and ERIKA DUTKOVÁ
Institute of Geotechnics, SAS, Watsonova 45, 043 53 Košice, Slovak Republic,
achimovic@saske.sk

Introduction

Nanocrystalline lead sulphide is an important part of opto-electronic devices such as light emitting diodes and solar cells[1,2]. One of the most problematic issues of particles prepared by mechanochemical synthesis is their tendency for an aggregation, and this problem makes it very difficult to obtain particles with a high degree of dispersity. The dispersity is characterized by the particle size distribution, the particle's shape and morphology as well as their interfacial properties[3]. Stearic acid $C_{17}H_{35}COOH$ is a fatty acid that was used as a process control agent for mechanochemical synthesis of different nanocomposites where the sticking of synthesized particles and mechanical alloying was delayed[4,5]. Also the additional parameters of the mechanochemical synthesis, as the time of mechanochemical synthesis and intensity of milling (mill revolutions) strongly influence the resulting particle size distribution. The reason for this behaviour lies in the different dependencies of nucleation and growth rates on supersaturation[3]. Several authors used statistical factorial design methods for conditions optimalization of the process under study.[6–9] This factorial plan examines the given area thoroughly because it involves all possible combinations of levels of watching factors and provides the determination of an optimum value of search function from minimum number of the experiments. One of the frequently used factorial design method is the 1st order model fitting 2nd (n-number of factors). On the basis of solving of factorial plan designed matrix, it is possible to obtain objective function:

$$Y = b_0 + b_1x_1 + b_2x_2 + b_3x_3 + b_{12}x_1x_2 + b_{13}x_1x_3 + b_{23}x_2x_3 + b_{123}x_1x_2x_3 \quad (1)$$

The aim of this study was a statistical experiment design of PbS mechanochemical synthesis with determined response–mean particle size and three independent factors: time of milling, mill revolutions, the amount of stearic acid and to detect the interaction factors that can affect the output parameters.

Experimental

Mechanochemical Synthesis

Mechanochemical synthesis of PbS particles was performed in a planetary mill Pulverisette 6 (Fritsch, Germany) by high-energy milling of lead acetate and sodium sulphide with stearic acid (SA) as the process control agent in the air according to the reaction[10]:

$$(CH_3COO)_2Pb \cdot 3H_2O + Na_2S \cdot 9H_2O \rightarrow PbS + 2CH_3COONa + 12H_2O \quad (2)$$

The following constant conditions were used: loading of the mill with 50 balls of 10 mm diameter; material of milling chamber and balls: tungsten carbide; weight of $(CH_3COO)_2Pb \cdot 3H_2O$: 4.75 g; weight of $Na_2S \cdot 9H_2O$: 3.01 g; temperature: laboratory. After the completion of reaction (2), the PbS nanoparticles have been washed and dried.

The particle size distribution of mechanochemically synthesized PbS particles was measured by a particle size analyzer HELOS (Sympatec GmbH, Germany) with wet dispergation unit SUCELL 12LA. Mean particle size of PbS particles was determined according to a mathematical model that is based on spherical systems.

Design of Experiment

One 2^3 factorial experiment with the mean particle size D = Y as a response of mechanochemically synthesized PbS and 3 independent variables: time of milling-t_M, mill revolutions-n and weight of stearic acid-m_{SA} used as factors x_1, x_2, x_3 was performed. In Table I are introduced the basic level, variation interval of selected factors and two factor levels which were assigned to each of three factors $x_1 = t_M$, $x_2 = n$ and $x_3 = m_{SA}$ and these levels were varied in all kinds of combination.

Eight experiments of PbS mechanochemical synthesis were performed. Their conditions are specified in the Table II.

Table I
Levels of independent variables (factors)

Factor level	$x_1 = t_M$ [min]	$x_2 = n$ [min^{-1}]	$x_3 = m_{SA}$ [g]
Basic level – x_{0i}	8	400	0.09
Variation interval – Δx_i	2	100	0.05
Low level – x_{Li}	6	300	0.04
High level – x_{Hi}	10	500	0.14

Table II
Specified conditions of PbS mechanochemical synthesis experiments

Trials series n°	$x_1 = t_M$ [min]	$x_2 = n$ [min^{-1}]	$x_3 = m_{SA}$ [g]
1	6	300	0.04
2	10	300	0.04
3	6	500	0.04
4	10	500	0.04
5	6	300	0.14
6	10	300	0.14
7	6	500	0.14
8	10	500	0.14

Results

The 1st order model fitting predicting the values of mean particle size was found, where the coefficients represent the measure of the effects of variables $x_1 = t_M$, $x_2 = n$ and $x_3 = m_{SA}$. The mixed terms x_1x_3 and x_2x_3 indicate the measure of mutual interactions between the variables. The designed matrix, observed responses and predicted values are introduced in Table III and the regression coefficients of model function are in Table IV. Variance of reproducibility S_{Re}^2 of the mean particle size values of synthesized particles is 0.014 calculated from experiments performed in the centre of experiment (trials 9 to 14 from the factorial experiment), the mean value of Y equal to 1.33 μm respectively). On the basis of S_{Re}^2 value, the variance of regression coefficients or parameters of model function, S_{bi}^2 was calculated, that equals to 0.0098. The values of Student's test-t were calculated according to the formula:

$$t_i = \frac{|b_i|}{\sqrt{S_{bi}^2}} \quad (3)$$

The value of this t-test defines the significance of the regression coefficient: regression coefficient is significant if the calculated value of Student's test is greater than the table value, $t_{\alpha,f} = 2.57$(ref.[11]). After separation of insignificant regression coefficients the model function of PbS mechanochemical synthesis has the following form:

$$Y = 1.91 - 0.12x_1 - 0.47x_2 + 0.12x_1x_3 - 0.43x_2x_3 \quad (4)$$

The values of F-Fisher's test were calculated because of verifying of the factors significance according to the formula (5).

Table III
Designed matrix of PbS mechanochemical synthesis system, observed responses – Y_i^{OR} and predicted values – Y_i^{PV} of mean particle size, D

Trials series n°	x_0	x_1	x_2	x_3	x_1x_2	x_1x_3	x_2x_3	$x_1x_2x_3$	Y_i^{OR} [μm]	Y_i^{PV} [μm]
1	1	–1	–1	–1	+1	+1	+1	–1	2.13	2.19
2	1	+1	–1	–1	–1	–1	+1	+1	1.66	1.71
3	1	–1	+1	–1	–1	+1	–1	+1	2.07	2.11
4	1	+1	+1	–1	+1	–1	–1	–1	1.58	1.63
5	1	–1	–1	+1	+1	–1	–1	+1	2.77	2.81
6	1	+1	–1	+1	–1	+1	–1	–1	2.95	2.38
7	1	–1	+1	+1	–1	–1	+1	–1	1.15	1.01
8	1	+1	+1	+1	+1	+1	+1	+1	0.97	1.01
9	0	0	0	0	0	0	0	0	1.25	1.25
10	0	0	0	0	0	0	0	0	1.23	1.01
11	0	0	0	0	0	0	0	0	1.23	1.01
12	0	0	0	0	0	0	0	0	1.53	1.01
13	0	0	0	0	0	0	0	0	1.36	1.01
14	0	0	0	0	0	0	0	0	1.38	1.01

Table IV
1st order model fitting results for PbS mechanochemical synthesis with mean particle size, D as optimization parameter

Variable	Regression coefficients of model function (1) b_0 b_i. b_{ij} b_{ijk}	S_i^2 variance due to factors and factor interactions	t-Student's test	F-Fisher's test
x_0 (constant)	1.91	0.5	60.83	36.34
x_1	–0.12	0.12	3.83	8.72
x_2	–0.47	1.75	14.99	127.80
x_3	0.05	0.02	1.59	1.45
x_1x_2	–0.05	0.02	1.59	1.45
x_1x_3	0.12	0.12	3.83	8.72
x_2x_3	–0.43	1.5	13.72	109.01
$x_1x_2x_3$	–0.04	0.01	1.37	0.73

$$F = \frac{S_i^2}{S_{Re}^2} \quad (5)$$

According to Fisher test the factor is significant if the calculated value of F-test is greater than the table value F = 6.61(ref.[11]).

An adequacy of model function was verified by F-test that consist in a comparison of the variance reproducibility S_{Re}^2 and the variance S_{AD}^2 that is given by the variances of theoretical and experimental values of mean particle size Y = D, according to:

$$F_{AD} = \frac{S_{AD}^2}{S_{Re}^2} \quad (6)$$

The proposed model function sufficiently represents the course of mechanochemical synthesis process in examined region because the calculated F_{AD} value equal to 1.24 is less than the table value of $F_{AD} = 5.41$(ref.[11]).

It can be concluded from Table III, that the observed responses Y_i^{OR} are in close agreement with predicted values Y_i^{PV} of the model. It follows from the model function, that the mean particle size of PbS is mostly influenced by revolutions of mill, less by time of mechanochemical synthesis and the weight of stearic acid did not influence the mean particle size in used range 0.04–0.14 g. The twofactors interaction between the revolution of mill and the amount of stearic acid has larger effect on the PbS mean particle size. The smallest mean particle size from the particle size distribution analysis point of view (Table III) can be obtained at trials 7 and 8 of Table II, it means at high level of the factors – mill revolution and amount of stearic acid.

Conclusions

The role of the process control agent – stearic acid with the aim to decrease the ability of particles to create aggregates during the mechanochemical synthesis of PbS

in a planetary mill was studied. The 1st order model fitting with the mean particle size-Y as a measured response and three independent variables: time of mechanochemical synthesis-x_1, revolutions of mill-x_2 and weight of stearic acid-x_3 was constructed and the model function $Y = 1.91 - 0.12x_1 - 0.47x_2 + 0.12x_1x_3 - 0.43x_2x_3$ was obtained. It resulted from this function that the mean particle size of synthesized PbS nanoparticles was most influenced by revolutions of mill, less influenced by time of mechanochemical synthesis and the weight of stearic acid did not influence the mean particle size of synthesized PbS particles basically.

The research activities were kindly supported by Slovak Grant Agency VEGA (project 2/0035/08), the Slovak Research and Developing Agency (project 0347-06) and Center of Excellence of Slovak Academy of Sciences (project NANOSMART).

REFERENCES

1. Wang W., Liu Y., Zhan Y., Zheng Ch., Wang G.: Mater. Res. Bull. *36*, 1977 (2001).
2. Warner J. H., Watt A. A.R.: Mater. Lett. *60*, 2375 (2006).
3. Peukert W., Schwarzer H. Ch., Stenger F.: Chem. Eng. Process. *44*, 245 (2005).
4. Bhattacharya P., Bellon P., Averback R. S., Hales S. J.: J. Alloy. Compd. *368*, 187 (2004).
5. Byun J. S.: J. Alloy. Compd. *365*, 149 (2004).
6. Agatzini S., Burkin A. R.: Trans. Instn. Min. Metall. (Sect. C: Mineral Process. Extr. Metall.) *94*, 105 (1985).
7. Cunha M. L., Bastos M. H.: *Proceedings of 7th Int. Mineral Processing Symposium*: *Innovations in Mineral and Coal Processing* (Atak S., Önal G., Celik M. S., eds.), p. 899. Istambul, Balkema, Rotterdam 1998.
8. Godočíková E., Baláž P., Leško M.: Uhlí-Rudy-Geologický průzkum *9*, 21 (2002).
9. Box G. E. P., Wilson K. B.: J. Royal Statist. Soc. Series B, *13*, 1 (1951).
10. Baláž P., Boldižárová E., Godočíková E., Briančin J.: Mater. Lett. *57*, 1585 (2003).
11. Eckschlager K., Horsák I., Kodejš Z.: *A Czechoslovak norm: Evaluation of the Analytical Results and Methods*. Publ. House ALFA, Prague 1980.

P02 SYNTHESIS OF DOPED LANTHANUM FERRITE PEROVSKITES

EVA BARTONÍČKOVÁ and JAROSLAV CIHLÁŘ
Brno University of Technology, Purkynova 118, 612 00 Brno, Czech Republic,
bartonickova@fme.vutbr.cz

Introduction

Multicomponent ceramic materials have a variety of industrial applications. Types of application are strongly depended on the properties such as mixed ionic and electronic conductivity, transport properties, ability working at severe reducing conditions and elevated temperatures. The main purpose for study and producing of multicomponent ceramic oxides are applications in syngas production, oxygen membranes or components of SOFCs. These properties are interdependent on the way of preparation. In general the routes of preparation can be divided into two groups. The first one is "wet" chemical routes. There are typical methods as precipitation synthesis, sol-gel processes then the novel ones as self-combustion reactions – glycine nitrate processes (GNP)[1,2], spray pyrolysis or Pechini synthesis[3]. Otherwise the conventional synthesis based on solid state reactions are still frequently applied as well[4,5]. This study is focused on the preparation of multicomponent perovskite system La–Sr–Fe–Ti–O by several methods. System La–Sr–Fe–Ti–O belongs to materials with high oxygen transport and sufficient mixed conductivity at high temperatures.

Doped lanthanum ferrites were studied by Tsipis and all.[6]. They observed the high mixed conductivities in $La_{1-x}Sr_xFeO_{3-\delta}$ when $x = 0.5$. The high strontium content determined the high conductivity values but is associated with poorer thermodynamic and chemical stability under the large oxygen chemical potential gradient. The way to improve the stability in higher temperatures is partial substitution of iron by redox-stable cations such as transition metals e.g. titanium and chromium or cobalt what was published by several authors[7,8]. The work is focused on the preparation and study of composition of La–Sr(Ca)–Fe–Ti–O perovskites.

Experimental

Powder Preparation

Perovskite systems $La_{0.2}Sr_{0.8}Fe_{1-x}Ti_xO_{3-\delta}$ (LSFT) and $La_{0.2}Ca_{0.8}Fe_{1-x}Ti_xO_{3-\delta}$ (LCFT) ($x = 0.2 - 0.4$) were synthesized by two methods. Conventional solid state reaction and glycine-nitrate process (GNP) were used.

The oxides and carbonates of appropriate metals were used as starting material for SSR The suspensions of oxides in isopropanol in stechiometric ratios (Table II) were milled in planetary ball mill for 24 h then dried. These precursors were put to the furnace for SSR for 30 h at the temperature of 1,100 °C.

The nitrates and alkoxides of appropriate metals were used as starting materials in GNP process. The aqueous solutions of each cation were mixed in stechiometric ratios and glycine was added at G/N ratio = 5/9. The concentrations are given in Table 1. Synthesized precursor was calcined (950 °C 4 h^{-1}) for decompositions of carbonates residues and SSR of oxide precursors.

Table I
The data used for preparation of suspensions for compositions ($x = 0.2$, 0.4)

Starting materials	Concentration [mol dm^{-3}] $La_{0.2}Sr_{0.8}Fe_{1-x}Ti_xO_{3-\delta}$		Concentration [mol dm^{-3}] $La_{0.2}Sr_{0.8}Fe_{1-x}Ti_xO_{3-\delta}$	
	$x = 0.2$	$x = 0.4$	$x = 0.2$	$x = 0.4$
La_2O_3	0.0838	0.0940	0.1158	0.1162
$SrCO_3$	0.7507	0.7565	–	–
CaO	–	–	0.9255	0.9345
Fe_2O_3	0.3752	0.2837	0.4627	0.3508
TiO_2	0.1876	0.3783	0.2314	0.4671

Table II
The data used for preparation of solutions

Starting materials	Concentration[mol dm^{-3}]
$La(NO_3) \cdot 9H_2O$	1.2269
$Sr(NO_3)_2$	3.0741
$Fe(NO_3)_3 \cdot 9H_2O$	1.8444
$Ti(C_2H_6O)_4$	0.3074
Glycine	1.0775

Powder Characterization

The phase composition was determined by X-ray diffraction analysis. KCo wavelength (X´pert. Philips. Netherlands). The morphology of powder products was studied by scanning microscopy (SEM XL 30. Philips. Netherlands). The composition was determined by EDS detector of scanning microscopy (SEM XL 30. Philips. Netherlands). The specific surface area (SSABET) was determined by the BET method (Chembet. Quantachrome. USA). Particle size was calculated from BET values.

Table III
Properties of synthetized powders

Sample		XRD	Rietveld analysis	BET [$m^2 g^{-1}$]	Particle size [μm]
SSR	x = 0.2	Cub.	*Pm3m*	1.00	1.08
LSFT	x = 0.4	Cub.	*Pm3m*	3.00	0.36
SSR	x = 0.2	Orth.	*Pbnm*	1.60	0.67
LCFT	x = 0.4	Orth.	*Pbnm*	1.00	1.08
GNP LFST	x = 0.4	Cub.	*Pm3m*	5.20	0.21

Results

All materials obtained by SSR and GNP process were composed of one phase products. The properties of synthesi-

zed powders are given in Table III. Powders prepared by conventional solid state reaction are phase pure and the particle size was in range of 300 nm to 1.2 μm. The perovskite system $La_{0.2}Sr_{0.8}Fe_{1-x}Ti_xO_{3-\delta}$ was single phase with cubic lattice symmetry (space group *Pm3m*). The perovskite system $La_{0.2}Ca_{0.8}Fe_{1-x}Ti_xO_{3-\delta}$ was single phase with orthorhombic lattice symmetry (space group *Pbnm*).

The XRD patterns of ceramic powders of several compositions are given in Fig. 1.

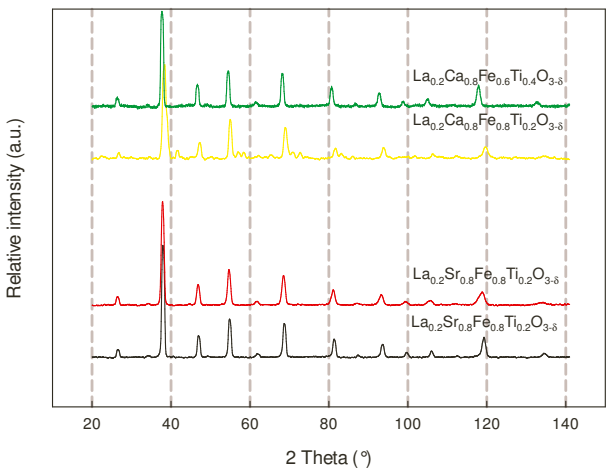

Fig. 1. **XRD patterns of synthetized powders**

The multicomponent system was analysed by EDS SEM and the compositions are given in Table IV.

Table IV
Chemical composition analysed by EDS SEM

Expected compostition	Determined composition (EDS SEM)
$La_{0.2}Sr_{0.8}Fe_{0.8}Ti_{0.2}O_{3-\delta}$	$La_{0.21}Sr_{0.68}Fe_{0.80}Ti_{0.20}O_{3-0.91}$
$La_{0.2}Sr_{0.8}Fe_{0.6}Ti_{0.4}O_{3-\delta}$	$La_{0.21}Sr_{0.73}Fe_{0.61}Ti_{0.39}O_{3-0.41}$
$La_{0.2}Ca_{0.8}Fe_{0.8}Ti_{0.2}O_{3-\delta}$	$La_{0.23}Ca_{0.67}Fe_{0.79}Ti_{0.21}O_{3-0.16}$
$La_{0.2}Ca_{0.8}Fe_{0.6}Ti_{0.4}O_{3-\delta}$	$La_{0.15}Ca_{0.49}Fe_{0.44}Ti_{0.56}O_{3-0.75}$

Systems synthesized via both methods were single phase with cubic lattice symmetry (space group *Pm3m*). The temperature of formation of pure phase was different for each of method. The solid state reactions were performed at 1,100 °C and for 30 hours. The glycine/nitrate combustion synthesis occured several minutes after evaporation of water and was followed by SSR at 950 °C for 4 hours. The particle

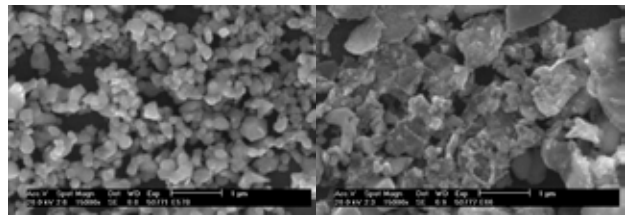

(a) (b)

Fig. 2 **SEM micrographs of syntetized powders: (a) SSR synthesis and (b) GNP combustion reaction**

size of prepared powders is depended on method which was used. In case of SSR the particle size was around 360 nm and 210 nm for GNP process. The SEM micrographs of $La_{0.2}Sr_{0.8}Fe_{0.6}Ti_{0.4}O_{3-\delta}$ are given in Fig. 2.

Conclusions

The single phase multicomponent ceramic systems were successfully prepared via both methods – SSR and GNP. The particle size of synthesized powders was in the range of 0.21 to 1.08 um and specific surface area in the range of 1.0 to 5.2 $m^2\ g^{-1}$.

This work has been supported by the Ministry of Education, Youth and Sports of the Czech Republic (MSM 0021630508).

REFERENCES

1. Liu M., Wang R., Li D. F., Liang D. T.: Mater. Chem. Phys. *102*, 132 (2007).
2. Lee G. Y., Song R. H., Kim J. H., Peck D. H., Lim T. H., Shul Y. G., Shin D. R.: J. Electroceram. *17*, 723 (2006).
3. Lepe F. J., Fernández-Urbán J., Mestres L., Martínez-Sarrión M. L.: J. Power Sources *151*, 74 (2005).
4. Wang S., van der Heidea P. A. W., ChavezaC., Jacobson A. J., Adler S. B.: Solid State Ionics, *156*, 201 (2003).
5. Bayraktar D., Clemens F., et al.: J. Eur. Ceram. Soc. *27*, 2455 (2007).
6. Tsipis E. V., Patrakeev M. V., et al.: Solid State Sci., *7*, 355 (2005).
7. Fagg D. P., Kharton V. V., et al.: Solid State Ionics, *156*, 45 (2003).
8. Fagg D. P., Kharton V. V., et al.: J. Eur. Ceram. Soc. *21*, 1831 (2001).

P03 EFFECT OF HEAT TREATMENT ON THE Al + Si DIFFUSION COATINGS ON Ni-BASED ALLOYS

LADISLAV ČELKO and LENKA KLAKURKOVÁ
Brno University of Technology, Faculty of Mechanical Engineering, Institute of Materials Science and Engineering Technická 2896/2, 616 69 Brno, Czech Republic
ycelko00@stud.fme.vutbr.cz

Introduction

Diffusion barriers are a wide group of protective coatings currently used for high temperature applications. They ensure an improvement of substrate surface stability against degradation processes closely related to the working environment, oxidation and hot corrosion mainly[1]. Generally, the effect of heat treatment is possible to be divided into the protective coating formation and degradation of the coating just formed[2].

In principal, the diffusion coating production is based on thermodiffusion saturation of the substrates by aluminum or aluminum combined with other elements (e.g. Al-Cr, Al-Si). A great variety of techniques for deposition of diffusion coatings were designed. Regarding to the diffusion coating production costs, the powder mixtures with halide activators, circulating gaseous phase and slurry deposition techniques are prefered.

The first and the second technique use similar chemical process for aluminide coating formation (in a shortcut: activator decomposition, saturating gas formation, substrate surface saturation and diffusion coating growth) during annealing in relatively wide temperature range: from 500 °C to 1,200 °C[3]. Nevertheless, to co-deposit aluminum in combination with other elements, suitable pack activators and temperature range to create favourable conditions for coating formation must be found[4,5].

Instead of the techniques mentioned above, the use of slurry deposition has a series of advantages. They are as follows: preparation of arbitrary elements powder mixtures, a shorter thermal cycles necessary to the coating formation, a possibility of local and large-size substrate coating deposition. The slurry is made of saturating elements powder mixtures and of an organic binder. Diffusion annealing (commonly in the temperature range from 650 °C to 1,200 °C) ensures a complete burnout and volatilization of organic components without deteriorating the substrate and coating[2,6,7].

Experimental

Sheets of Ni (nickel of commercial purity, 99.7 % wt. Ni), Ni-Cr (commercial nichrome, Ni-20 % wt. Cr) and Inconel 713LC were used as substrates. The substrate surface was ground with abrasive paper to #600, polished with 3 μm diamond paste and washed with acetone in ultrasonic cleaning bath for 15 min. Slurry was prepared by stirring a mixture of Al, Si powders (up to 90 and 45 μm in diameter, respectively) and amyl acetate based organic binder solution

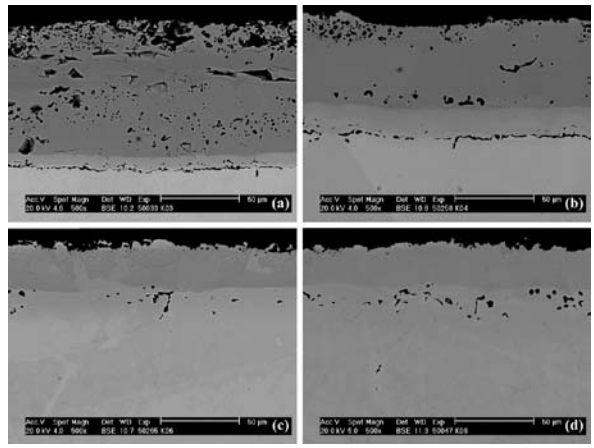

Fig. 1. **The cross-sectional SEM images of coating formed on Ni after annealing at 1,000 °C; (a) – 0 min, (b) – 60 min, (c) – 180 min and (d) – 600 min**

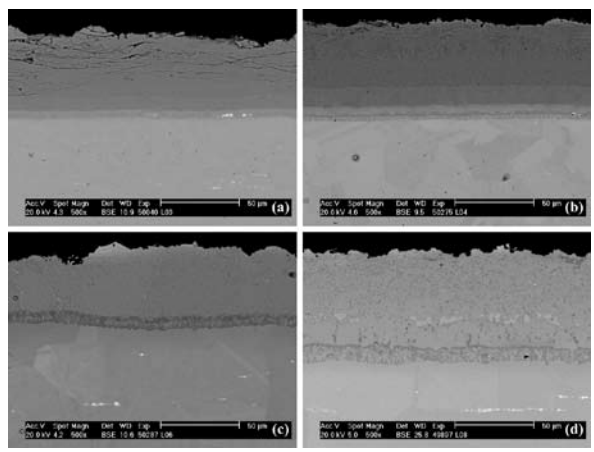

Fig. 2. **The cross-sectional SEM images of coating formed on Ni-Cr after annealing at 1,000 °C; (a) – 0 min, (b) – 60 min, (c) – 180 min and (d) – 600 min**

(100 ml to 38 g of Al and 32 g of Si powder) with propeller stirrer at 150 rpm for 15 min. Viscosity of the slurry measured by Ford Cup (Ø 6 mm, 20 °C) was 13 s. The slurry was sprayed by hand onto the sheets' surface. Specimens prepared this way were heated in a tube furnace with flowing argon-gas atmosphere. Heat treatment conditions were 200 °C 60 min^{-1} (Ar-gas flow 9 dm^3 min^{-1}) to decompose organic binder and 1,000 °C per 0, 60, 120, 180, 360, 600 min (Ar-gas flow 5 dm^3 min^{-1}) to investigate the intermetallic layer formation and development. After heating, the samples were cooled under Ar-gas flow to 550 °C and then in air to room temperature.

For microstructure observation, the scanning electron microscope (Philips XL30) was used. Elements interaction studies, based on energy dispersive microanalysis (EDAX), and layer thickness measurements by means of image analysis (NIS Elements AR 2.3) were performed. Microhardness tester (LM 247AT) was used for layers hardness determination.

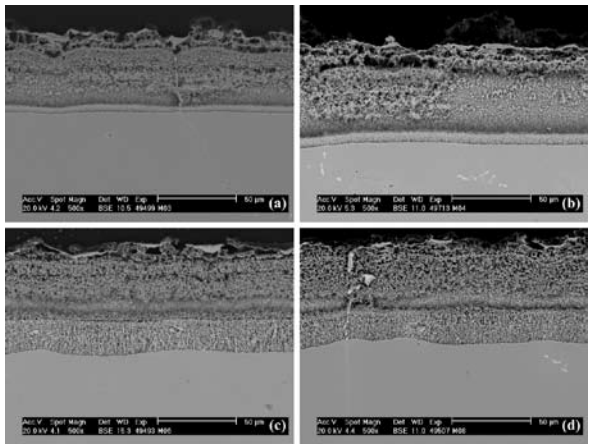

Fig. 3. **The cross-sectional SEM images of coating formed on Inconel 713LC after annealing at 1,000 °C; (a) – 0 min, (b) – 60 min, (c) – 180 min and (d) – 600 min**

Results

Figs. 1., 2. and 3. show SEM images of the course of diffusion coating formation on Ni, Ni-Cr and Inconel 713LC substrates, respectively.

Concentration change of the elements with depth from the surface to nickel-base substrates, measured by EDS, are depicted on Fig. 4. The coating transformation diagrams, based on image analysis measurements were constructed, see Fig. 5. Hardness of the substrates decrease during annealing while the hardness of intermetallic layers is stable within 500 to 950HV.

Conclusions

The first step of annealing is necessary for organic binder decomposition. This leads to partial aluminum powder oxidation. Intermetallic phases start to form when the temperature exceeds the Al-Si eutectic point.

Relatively thin intermetallic layers of NiAl and Ni_3Al were produced at the moment when the temperature 1,000 °C was reached. The part of the coating, termed as "Al reserves", is also intermetallic in this moment but with high degree of open porosity. This layer disappears at the expense of inner layers growth during the annealing dwell.

Silicon addition in the slurry is detrimental in the case of Ni substrate (diffusion coating destroyed after 180min annealing) and beneficial for Ni-Cr and Inconel 713LC (stabilises the lower Cr-rich layer, forms Cr-Si intermetallics and/or carbides, respectively).

The authors are grateful to the Ministry of Education (grants MSM002163058 and 2E08017) and Grant Agency of Czech Republic (grant GAČR 106/05/H008) for financial support.

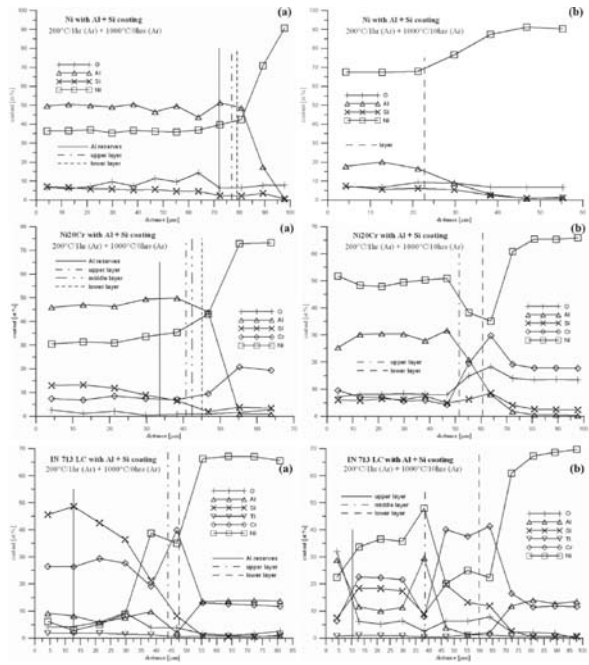

Fig. 4. **Concentration change of the elements with depth from surface to substrate after annealing at 1,000 °C for (a) 0 min, (b) 600 min on Ni, Ni-Cr and Inconel 713LC substrates (from the top)**

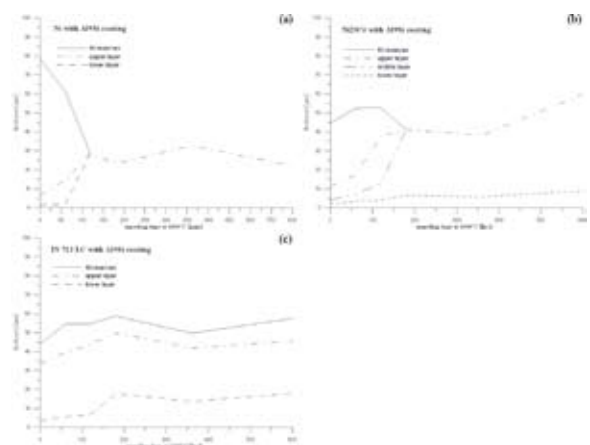

Fig. 5. **Transformation of diffusion coating during annealing at 1,000 °C on (a) Ni, (b) Ni-Cr and (c) Inconel 713LC substrate**

REFERENCES

1. Bose T.: *High Temperature Coatings*. Elsevier, 2007.
2. Tamarin Y.: *Protective Coatings for Turbine Blades*. ASM International, Ohio 2002.
3. Houngninou C., Chevalier S., Larpin J. P.: Appl. Surf. Sci. *236*, 256 (2004).
4. Xiang Z. D., Datta P. K.: Surf Coat Technol *179*, 95 (2004).
5. Xiang Z. D., Datta P. K.: Mater Sci Eng A *356*, 136 (2003).
6. Murakami K., Nishida N., Osamura K., Tomota Y.: Acta mater. *52*, 1271 (2004).
7. Murakami K., Nishida N., Osamura K., Tomota Y., Suzuki T.: Acta Mater *52*, 2173 (2004).

P04 CHEMICAL ANALYSIS OF Al AND Si SURFACE LAYERS ON STEELS

PAVEL DOLEŽAL, LADISLAV ČELKO, ANETA NĚMCOVÁ and LENKA KLAKURKOVÁ
Brno University of Technology
Faculty of Mechanical Engineering
Technická 2896/2, 616 69 Brno, Czech Republic
pavdol@email.cz

Introduction

Great variety of surface modifications was developed in the effort to improve bearing steels' surface properties. In order to achieve an improvement in performance of the bearings working at higher temperatures, the diffusion coatings may be applied. The diffusion coatings are special group of surface modifications commonly used to improve the high temperature alloys' surface protection against degradation processes, closely related to the working environment (oxidation and hot corrosion, mainly)[1].

Several deposition techniques were designed for the diffusion coating application. The most widely used techniques are coating in powder mixtures with halide activators or the in circulating gaseous phase. These techniques use similar chemical processes for diffusion coating formation, i.e. activator decomposition, saturating gas development, substrate surface saturation and diffusion coating growth. Main disadvantages of these techniques lie in the need for favourable multicomponent co-deposition conditions design and in the substrate surface corrosion damage during the coating formation (triggered by incomplete "saturation" halide gas decomposition)[2,3].

Application of the diffusion coatings using slurry is a widely used technique, as well. The slurry is made of saturating elements powder, such as Al, Al-Cr, Al-Si, and of an organic binder. Ready-to-use slurry could be applied by various methods, such as dipping, brushing or spraying onto the substrate surface. When the coating is applied onto the surface and dried, the heat treatment designed for protective layer formation follows[4].

In this article, the influence of temperature on the silicon-alloyed aluminide diffusion coatings formation on the 100Cr6 bearing steel is investigated.

Experimental

The 100Cr6 bearing steel was used as substrate. The substrate was ground, polished and washed with acetone in ultrasonic cleaning bath. Slurry was made of 55 % Al + 45 % Si powders and of amyl-acetate based organic binder solution. The slurry was sprayed by hand onto the substrates' surface.

Samples prepared this way were heated in a tube furnace with flowing argon-gas atmosphere. The two-stage heat treatment for surface layer formation was employed; the first stage, i.e. low temperature dwell, to decompose the organic binder and the second stage, i.e. e. high temperature dwell, at 800, 900 and 1,000 °C 3h^{-1} for intermetallic layers formation.

For microstructure observation, the light microscope (Olympus GX71) and scanning electron microscope (Philips XL30) were used. Elemental interaction studies, based on energy dispersive microanalysis (EDS), glow discharge optical emission spectrometry (GD OES) and layer thickness

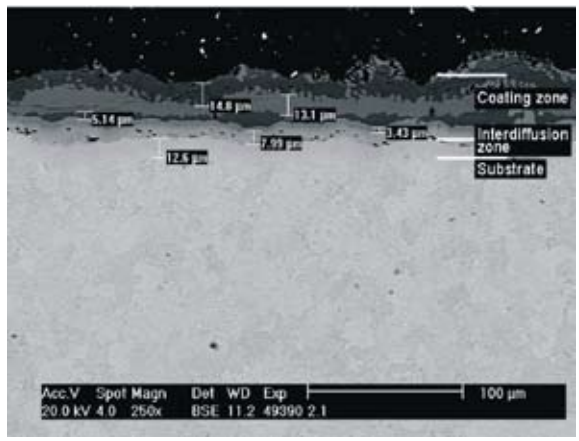

Fig. 1. **The SEM cross-sectional image of Al and Si diffusion layer after annealing at 800 °C 3h^{-1}**

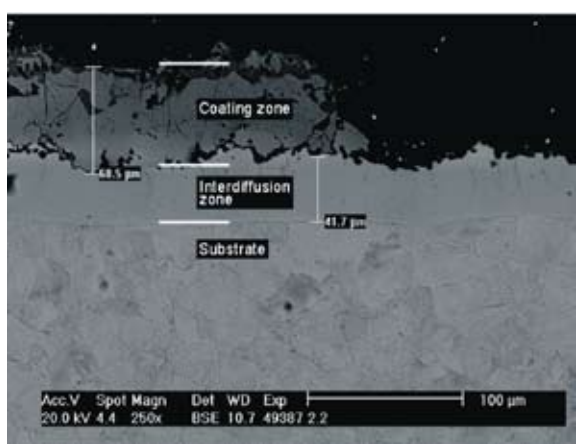

Fig. 2. **The SEM cross-sectional image of Al and Si diffusion layer after annealing at 900 °C 3h^{-1}**

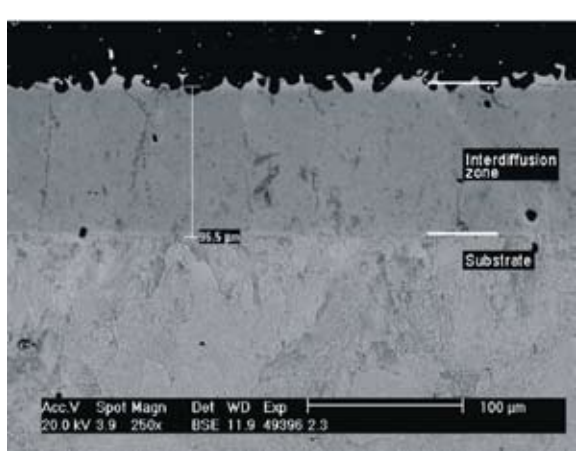

Fig. 3. **The SEM cross-sectional image of Al and Si diffusion layer after annealing at 1,000 °C 3h^{-1}**

measurements by means of image analysis (NIS Elements AR 2.3) were performed. The intermetallics' composition ranges were calculated from Al-Fe binary diagram.

Results

Figs. 1., 2. and 3. show SEM images of Al-Si diffusion coatings on 100Cr6 substrate after annealing at 800, 900 and 1,000 °C, respectively. Changes in concentration of elements with depth, measured by EDS and GD OES, are presented in Figs. 4., 5., 6. and in Figs. 7., 8., 9. for each annealing temperature, respectively. The calculated phase composition results are presented in Figs. 10,. 11. and 12. Fig. 13. shows the thickness of the interdiffusion zone, evaluated by the image analysis from SEM images.

Conclusions

The Si alloyed aluminide layers after annealing at 800, 900 and 1,000 °C were formed on the substrate of 100Cr6 bearing steel.

The coating after annealing at 800°C was divided into three continuous intermetallic layers separated by sharp Al and/or Si concentration gradient. Concentration of Al and Si decreases slowly from the top of the coating towards the substrate. Calculated intermetallics, i.e. $FeAl_3 + Fe_2Al_5$, $FeAl + FeAl_2$ and FeAl were identified. The hardest "Si-rich" layer (1,050 up to 1,100 HV0.025) was identified as $FeAl + FeAl_2$.

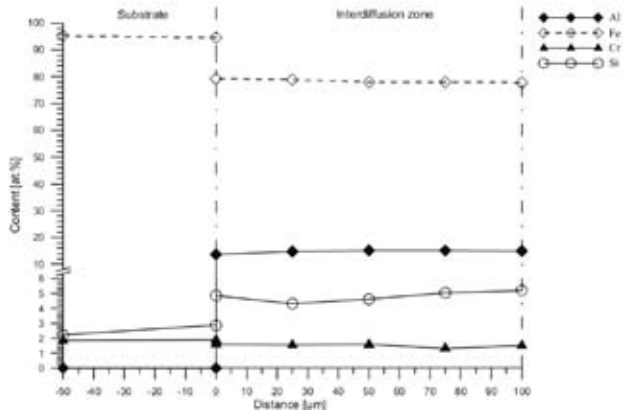

Fig. 6. **Compositional variation with depth from substrate to surface after annealing at 1,000 °C 3h^{-1}, measured with EDS**

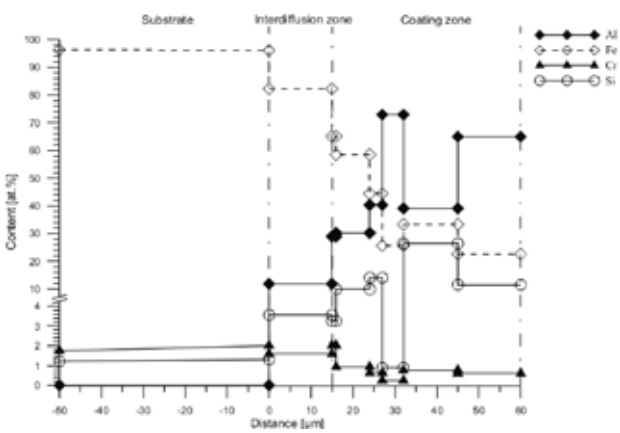

Fig. 4. **Composition change of the elements with depth from substrate to surface after annealing at 800 °C 3h^{-1}, measured by EDS**

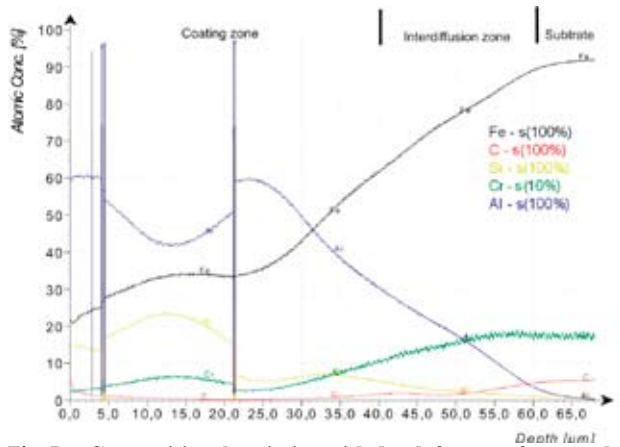

Fig. 7. **Compositional variation with depth from surface to substrate after annealing at 800 °C 3h^{-1}, measured with GD OES**

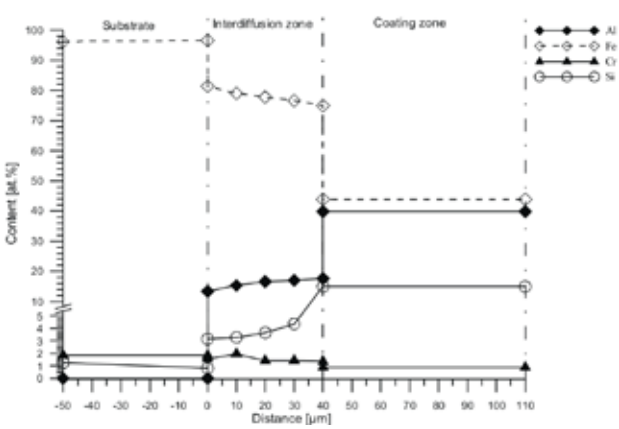

Fig. 5. **Compositional variation with depth from substrate to surface after annealing at 900 °C 3h^{-1}, measured with EDS**

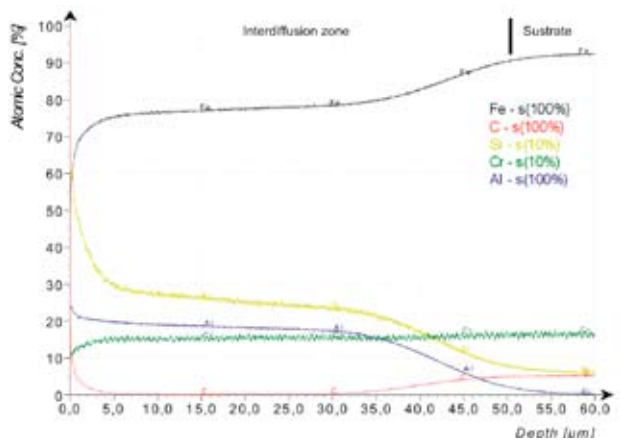

Fig. 8. **Compositional variation with depth from surface to substrate after annealing at 900 °C 3h^{-1}, measured with GD OES**

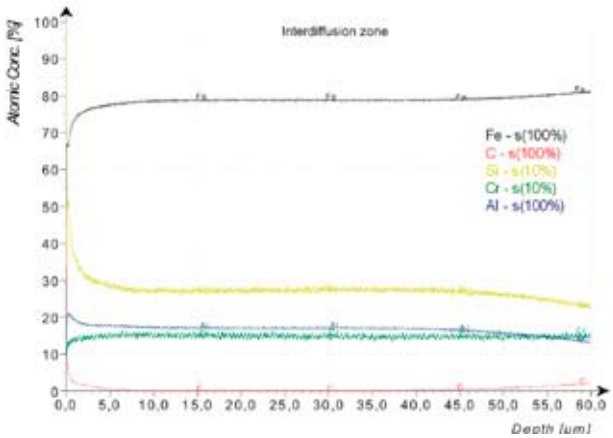

Fig. 9. **Compositional variation with depth from surface to substrate after annealing at 1,000 °C 3h^{-1}, measured with GD OES**

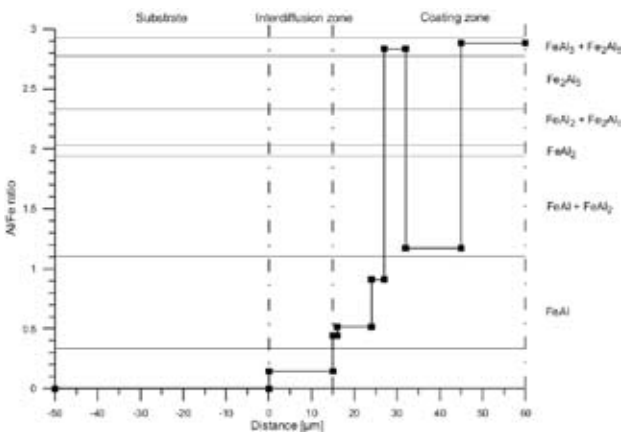

Fig. 10. **Phase composition of Al and Si surface layers calculated on the basis of Al-Fe binary system for 800 °C 3h^{-1}**

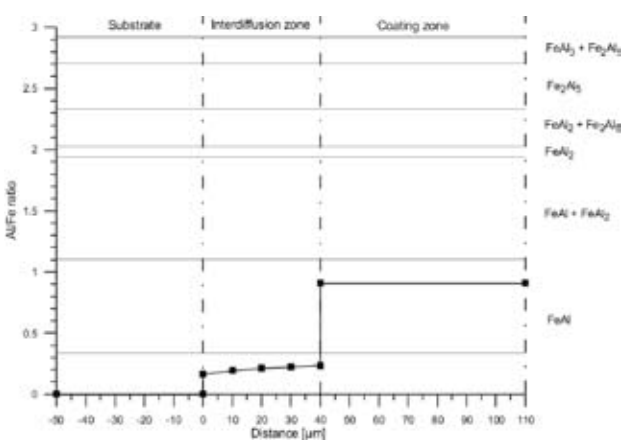

Fig. 11. **Phase composition of Al and Si surface layers calculated on the basis of Al-Fe binary system for 900 °C 3h^{-1}**

The coating after annealing at 900 °C was composed of two layers; the upper one (irregular and incompact), calculated as FeAl aluminide, and the lower one, Fe-Al solid solution, termed as interdiffusion zone.

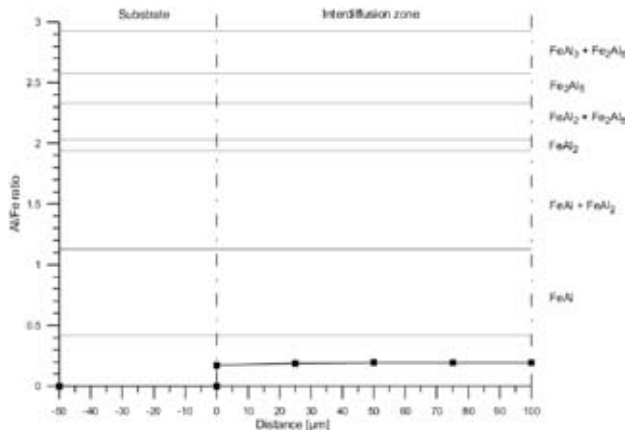

Fig. 12. **Phase composition of Al and Si surface layers calculated on the basis of Al-Fe binary system for 1,000 °C 3h^{-1}**

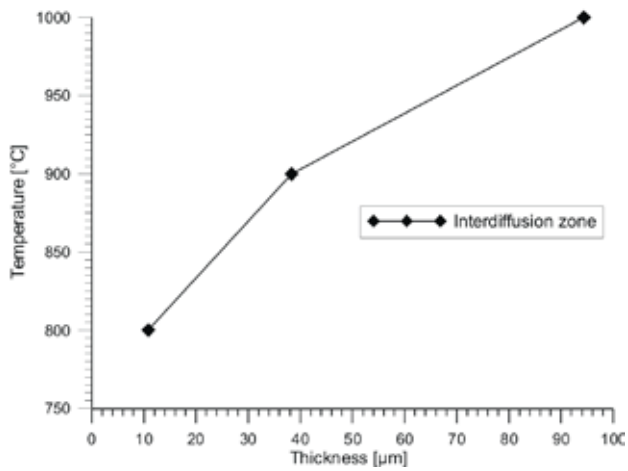

Fig. 13. **Thickness of the interdiffusion zone**

After annealing at 1,000 °C, only the interdiffusion zone was formed.

The higher temperature was used the thicker the interdiffusion zone was observed. Annealing temperature under 900 °C has to be applied to produce stable and continuous surface layer.

This work has been supported by the MSMT (grants MSM002163058 and 2E08017), MPO (project TA3/151).

REFERENCES

1. Cotell C. M., Sprague J. A., Smidt F. A.: *Surface Engineering 5*, ASM, 1994.
2. Hougninou C., Chevalier S., Larpin J. P.: Appl. Surf. Sci. *236*, 256 (2004).
3. Kim M. T., Jung J. S.: Surf. Coat. Tech. *161*, 218 (2002).
4. Bose T.: *High Temperature Coatings*. Elsevier, 2007.

P05 SYNTHESIS OF BELITE CEMENT FROM COAL FLY ASH

IVANA FIĽKOVÁ and NADEŽDA ŠTEVULOVÁ
Technical University of Kosice, Civil Engineering Faculty, Institute of Building and Environmental Engineering, Vysokoskolska 4, 042 00 Kosice, Slovakia,
ivana.filkova@tuke.sk

Introduction

The growing interest is related to synthesis of reactive low-energy belite cements as an alternative to the conventional Portland cement. Cements composed by β-Ca_2SiO_4 (belite) represent great economic and environmental value, mainly because of CO_2 emission reduction and energy saving. Many investigations have been realised in order to synthesize belite cement[1,2]. Also, use of wastes and byproducts from coal combustion processes of fossil fuels in power plants and electric power stations as alternative secondary raw materials for synthesizing belite cements have become the hotspot in cement-concrete materials science at present[3,4].

In our previous works[5,6], mechanochemical synthesis of belite precursors from coal fly ash/portlandite mixture has been reported.

In this paper, hydrothermal method for structure and properties modification of fluidized coal fly ash for belite cement synthesis is presented

Experimental

Materials and Methods

Slovak coal fly ash of chemical composition (Table I) from fluidized bed brown coal combustion in power plant ENO A (Nováky) was used as raw material. In order to reach required finesses of coal fly ash the short termed milling in vibratory mill was carried out (1 min.). Starting mixture consisting of milled coal fly ash and CaO (analytical grade reagent) with CaO/SiO_2 molar ratio of 2 was prepared by homogenization.

Table I
Chemical composition of coal fly ash

LI [%]	SiO_2 [%]	Fe_2O_3 [%]	Al_2O_3 [%]	CaO [%]	MgO [%]	O_3 [%]
5.25	30.36	2.29	16.95	51.21	2.45	33.36

LI – loss of ignition

Initial mixture and demineralised water at a water-to-solid ratio of 5 was hydrotermally activated in rotating autoclave A-08 at 175 °C and 200 °C during 2 and 4 hours, respectively. The products of hydrothermal treatment were filtered and dried at 55 °C during 24 h.

The starting mixture and products of hydrothermal treatment were subsequently calcinated at temperatures of 700 °C, 800 °C and 900 °C. Crystalline phases development after hydrothermal treatment and heating of starting mixture and all products was characterized by XRD analysis (DRON 6.0, Technabsexport, Russia).

Results and Discussion

The main crystalline phases as anhydrite, calcite, quartz, lime and portlandite (Fig. 1.) were identified in starting mixture.

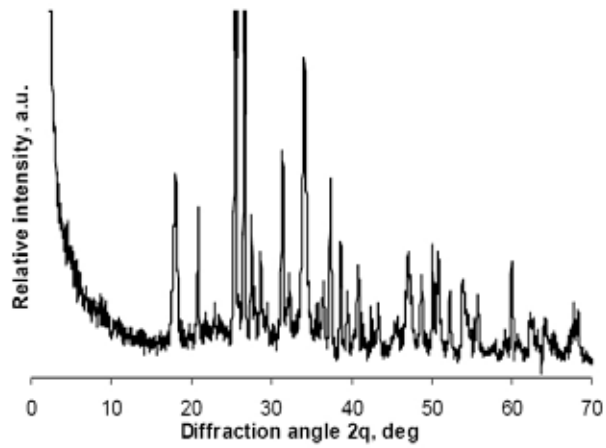

Fig. 1. **XRD diffraction pattern of starting mixture consisting of coal fly ash and CaO (A – anhydrite, C – calcite, Q – quartz, L – lime, P – portlandite)**

Based on XRD diffraction patterns of mixtures after hydrothermal treatment at different conditions, the optimal parameters were defined for formation belite precursors: 200 °C for 4 hours. The changes in integral intensities of XRD reflections of main crystalline phases (without anhydrite) of starting mixture as a consequence of the hydrothermal treatment and subsequent calcinations can be seen in Figs. 2.–5. Formation of new profiles of low intensities corresponding to CSH

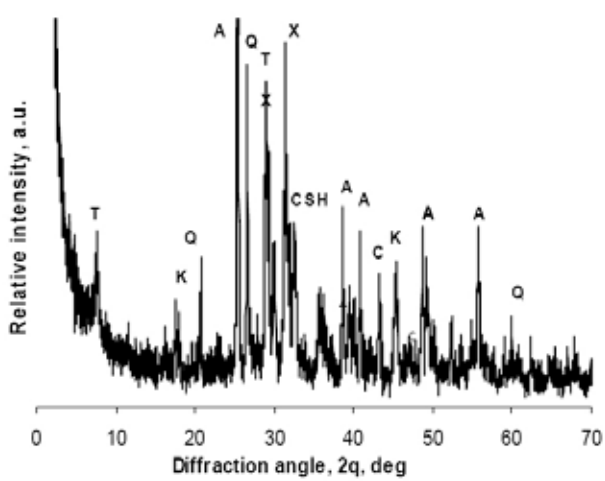

Fig. 2. **XRD diffraction pattern of starting mixture after hydrothermal treatment at 200 °C for 4 hours (A – anhydrite, C – calcite, Q – quartz, t – tobermorite, X – xonotlite, CSH – calcium silicate hydrate, K –katoite)**

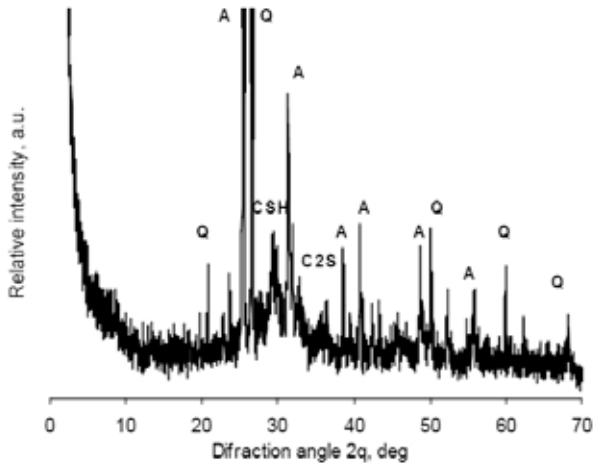

Fig. 3. **XRD diffraction pattern of starting mixture after hydrothermal treatment (200 °C; 4 h) and subsequent calcination at 700 °C (A – anhydrite, Q – quartz, CSH – calcium silicate hydrate, C2S – belite)**

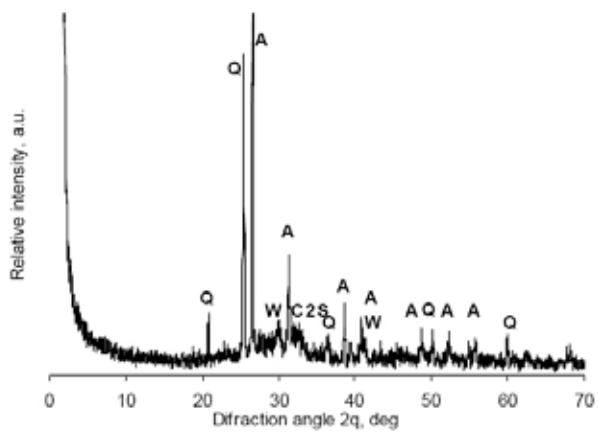

Fig. 4. **XRD diffraction pattern of starting mixture after hydrothermal treatment (200 °C; 4 h) and subsequent calcination at 800 °C (A – anhydrite, Q – quartz, W – wollastonite, C2S – belite)**

phases as belite precursor as well as calcium silicates and aluminosilicates (tobermorite, xonotlite) after hydrothermal treatment of mixture was confirmed (Fig. 2). Calcination of hydrotermally treated products (Figs. 3.–5.) showed that heating at 800 °C led to transformation of CSH phases to wollastonite (CS) and belite phase (C2S). Formation of gehlenite which is known as a retarder of cement hydration was observed at 900 °C. As can be seen in Figs. 2.–5., the high CaO content fixed in anhydrite wasn't changed during the hydrothermal treatment and subsequent calcination and the same quantity of belite phase from CSH phase was reached.

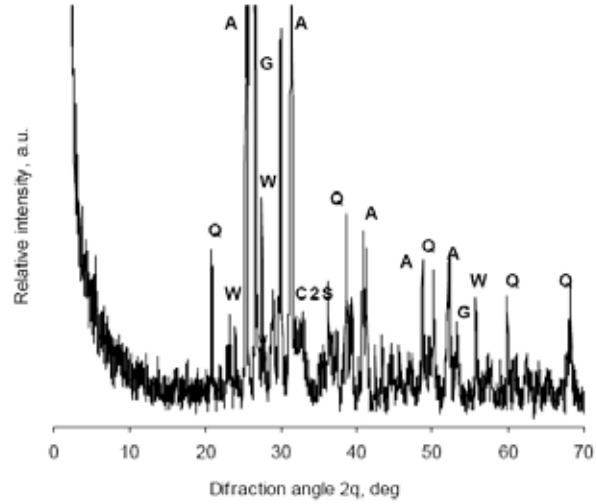

Fig. 5. **XRD diffraction pattern of starting mixture after hydrothermal treatment (200 °C; 4 h) and subsequent calcination at 900 °C (A – anhydrite, Q – quartz, W – wollastonite, C2S – belite, G – gehlenite)**

The reason of low CSH phase content after hydrothermal treatment and low conversion degree of precursors to belite consists in anhydrite that is a very stable compound. Application of pre-treatment focused on decomposition of anhydrite structure in coal fly ash at high temperature for obtaining higher amount of reactive CaO could by successful but we preferred to use coal fly ash as raw material.

Conclusions

The obtained results confirm that the hydrothermal modification in combination with subsequent calcination is not suitable treatment of starting mixture based on coal fly ash with high anhydrite content for preparing belite.

This work has been supported by VEGA č. 1/3343/06.

REFERENCES

1. Jiang W., Roy D. M.: Am.Ceram. Soc. Bull. *71*, 642 (1992).
2. Rodriques F. A.: Cem. Concr. Res. *33*, 1525 (2003).
3. Guerrero A., Goňi S., Macias A., Luxán M. P.: J. Mater. Res. *14*, 2680 (1999).
4. Guerrero, A., Goňi, S., Campillo, I., Moraques, A.: Enviro. Sci. Technol. *38*, 3209 (2004).
5. Števulová, N., Bálintová, M., Briančin, J., Széghyová, Z.: Chem. listy *99*, 420 (2005).
6. Števulová, N., Bálintová, M., Briančin, J., Széghyová, Z.: Chimija v interesach ustojčivogo razvitija *15*, 225 (2007).

P06 MICROBIALLY INFLUENCED CORROSION OF CONCRETE

VLASTA HARBUĽÁKOVÁ, ADRIANA EŠTOKOVÁ, ALENA LUPTÁKOVÁ, NADEŽDA ŠTEVULOVÁ and LUCIA SČIGULINSKÁ
Technical University of Košice, Civil Engineering Faculty, Institute of Building and Environmental Engineering, Vysokoškolská 4, 042 00 Košice, Slovak Republic, vlasta.harbulakova@tuke.sk

Introduction

The adverse effect of microbial activity on the long-term performance of cement materials is often not considered, despite the fact that studies on the effect of microbial activity on concrete have been ongoing for many years[1]. The corrosion process is initiated by the conversion of sulphate to sulphide by sulphate-reducing bacteria[2] (SRB) e.g. *Desulfovibrio desulfuricans* (*Dvs.d*) in anaerobic conditions. *Dvs. d.* are chemoorganotrophic, strictly anaerobic and gramnegative bacteria. Optimal growth conditions are in pH range 6.5–7.3 and temperature range 30–37 °C. Sulphur-oxidising bacteria *Acidithiobacillus thiooxidans (A.t.)* were chosen for microbially influenced corrosion (MIC) of concrete testing; because is most aggressive biological agents promoted[3]. *A.t.* as strictly autotrophic bacteria oxidizes sulphur and thiosulphate to sulphuric acid. Optimal growth temperature was 38–30 °C and pH has been in 2.0–3.5 range.

Experimental

B a c t e r i a a n d G r o w t h C o n d i t i o n

Sulphuretum simulated by *A.t.* and *Dsv.d.* under optimal growth conditions were chosen for experimental plan. Bacteria *Dsv.d.* were isolated from a mixed culture obtained from the potable mineral water (Gajdovka spring, the locality Kosice-north, Slovakia) and for the isolation and cultivation of these bacteria a selective nutrient medium DSM-63[4] was used. During their growth bacteria *Dsv.d.* produce a large amount of hydrogen sulphide that assures the maintenance of anaerobiosis[5].

Sulphur-oxidizing bacteria *A.t* were isolated from the mixed culture obtained from the mine water (the shaft Pech, the locality Smolník, Eastern Slovakia) and the selective nutrient medium 9K[6] was used for the isolation and cultivation of them.

C o n c r e t e S a m p l e s

Concrete cylinder samples of a 25 mm diameter and 20 mm height formed as a drilled core from real concrete cube using drilling mechanism STAM were used for experiment. The cylinder specimens were polished.

U t i l i z e d A p p a r a t u s

MIC proceeded in laboratory reactor, where sulphuretum simulation (simultaneous effect *Dvs.d.* of and A.t.) was under way. Laboratory apparatus of 1 flask with SRB and 1 flask as a trap for H_2S that were mutually joined with reactor consisted. Active bacterial SRB was in first flask and the second flask cadmium acetate contained.

Four samples in the four beakers were into reactor inserted. First beaker was filled with waste water (1), the second with acid mine drainage (2), the third with A.t. cultivating medium (3) and the fourth was with distilled water filled (4). The top of samples was by A.t. inoculated and on the bottom of reactor distilled water was poured.

The samples were every 7 days inoculated by A.t. and in the same period the change of cultivating medium for *Dvs.d.* were realized.

M e t h o d s

The weight changes were determined by gravimetric method. pH changes in leachate were evaluated as differences between initial pH and final pH after the experiment. The values of leachate pH were by pH meter PHH-3X Omega measured. The calcium concentrations in the solution were determined by atomic absorption spectrometry using Varian SpectrAA-30 spectrometer. Structural concrete surface changes were observed by stereomicroscope STM 723 ZOOM.

Results

After 50 days the concrete samples were took out of their solutions, dried and the change of the weight was determined. The results are presented in Table I.

Table I
The change of concrete samples weight

Sample	Weight of sample [g]		Change of weight	
	Before experiment	After experiment	[g]	[%]
(1)	46.1876	46.3041	0.1165	0.25
(2)	43.6003	43.4153	–0.185	–0.42
(3)	21.1463	21.1925	0.0462	0.21
(4)	25.0345	24.1245	–0.0914	–0.09

pH value has been increased into alkali after experiment for all samples. The most increment was in sample (2) and (3) registered as is evident from Table II.

Because of activity of A.t. and bacterial production of H_2SO_4 by SRB, releasing of calcium from concrete matrix was expected. The calcium concentrations in the solution determined are presented in Table III.

Table II
Change in pH value in liquid leachate

Leachate	pH leachate	
	Initial pH	Final pH
(1)	9	10.24
(2)	4	9.95
(3)	4	10.24
(4)	7.80	8.45

Table III
Calcium content in leachate

leachate	Ca [mg dm^{-3}]	
	before experiment	after experiment
(1)	87.14	8.4
(2)	128.38	24.6
(3)	45.7	37.6
(4)	0	45.1

Ca was released from concrete matrix under influence of H_2SO_4 bacterially produced. Consequently precipitations of $CaSO_4$ white crystals were attached on the concrete surface as it was in instances of samples (1)–(3) as Fig. 1 shows.

Fig. 1. **$CaSO_4$ white crystals on the concrete samples surface (20 × 4.5 magnifications)**

The most considerable changes of concrete structure samples were visible on samples (1) and (2). For illustration, surface structure changes of sample (1) after 50 days are pictured in Figs. 2. and 3.

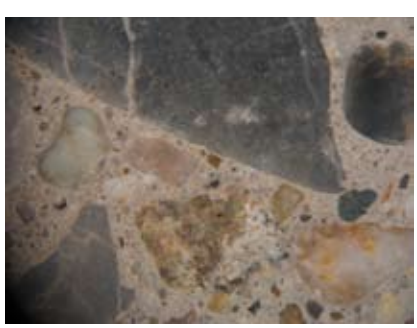

Fig. 2. **Surface of concrete sample (1) before experiment (magnification 20 × 4.5)**

Fig. 3. **Surface of concrete sample (1) after 50 days experiment duration (magnifications 20 × 4.5)**

For every sample except (4) was typical that some gravel components were completely removed and were significantly eroded. It is visible in white crystals probably of gypsum, which are on the surface precipitated. Accept the change of color of sample (4) into grey, there were no changes observed at this sample.

Conclusions

Concrete samples were under sulfuric acid influence corroded. The most considerable activity of microbially influenced corrosion degradation was on sample immerged into wastewater and into acid mine drainage. Experiment simultaneous effect of bacteria A.t. and SRB, which were the source of H_2S has proven.

Acknowledgement: This work has been supported by Grant Agency of Slovak Republic (project No. 2/0075/08).

REFERENCES

1. Sand W., Bock E.: *Seventh International Biodeterioration Symposium*, p.113. England, 1998.
2. Davis J. L., Nica D., et al: Int. Biodeterior. Biodegrad. *42*, 75 (1998).
3. Rogers R. D., Knight J. J., et al: Cem. Concr. Res. *33*, 2069 (2003).
4. Postgate J. R.: *The Sulphate Reducing Bacteria*, 2nd, Cambridge University Press, New York. (1984).
5. Beech I. B.: Microbiol. today *30*, 115 (2003).
6. Karavajko G. I., Rossi G., Agate A. D., Groudev S. N. Avakyan Z. A.: *Biogeotechnology of metals*, Centre of projects GKNT, Moscow, (1988).

P08 PREPARATION OF THAUMASITE

MARKÉTA HERMANOVÁ
Brno University of Technology, Faculty of Chemistry, Purkyňova 118, 612 00 Brno, Czech Republic, hermanova@fch.vutbr.cz

Introduction

Thaumasite $Ca_6Si_2(SO_4)_2(CO_3)_2(OH)_{12}\cdot 24(H_2O)$ is an unusual mineral in that it contains silicon in 6-coordination with hydroxyl. It is sometimes classified as a silicate because it content silicon or as carbonate for presence of carbonate ions. But Thaumasite belongs to sulfate class and to Ettringite Group for his similarity of crystal structure and properities with ettringite.

Thaumasite Formation

Sulphate attack on concrete is considered as a source of damage. Ingressing sulphate ions can react with minerals from the cement paste to form gypsum, ettringite or thaumasite. These phases bind additional water and this effect leads to an increase in volume. If there is no space for such an expansion, micro-cracks are formed, the tension becomes higher than the tensile strength of the hardened cement paste, cracks are formed, which support access of sulphate ions and accelerate the process of destruction.

Conditions of Thaumasite Formation [1]

- a source of C–S–H,
- an external supply of sulfate ions,
- a source of carbonate ions,
- mobile water (condition pro transport iontů),
- cool temperatures(< 15 °C),
- molar ratio C/S (CaO, SiO_2), quantity of CaO, pH, temperature, humidity

Experimental part

Influence of moisture and enviroment temperature on interface of phases and creation rate of thaumasite was observed in these samples T6. Portland cement SiO_2 was used as a source. Proportion of base mixture was designed to agree with materials that are used for production of concrete

Samples were composed from Portland cement, special-milled quartz, $CaSO_4\cdot 2\,H_2O$, calcite $CaCO_3$ and H_2O.

Samples was storaged in four different conditions:

T6vt – moisture, 25 °C; T6vz – moisture, 2 °C; T6st – dry, 25 °C; T6sz – dry, 2 °C

Formula dese[6]:

$$CaSO_4\cdot 2H_2O + H_2O + CaCO_3 + SiO_2 + Ca(OH)_2 \rightarrow CaSiO_3\cdot CaSO_4\cdot CaCO_3.15H_2O \quad (1)$$

Results

It appears from RTG analyses (Table I) that thaumasit began to create in samples T6vz after 4 months. Ideal conditions for thaumasite creation are intense moisture and low temperatures. Thaumasite was created in other 2 samples (T6sz, T6vt) after 10 months. In comparison of these samples we can observe, that low temperature is more essential for creation of thaumasite. It creates faster at these temperatures than at room temperature. C–S–H gel was created in sample T6vt, which can be considered as antecedent of thaumasite. This presumtion was confirmed after 10 months.

$$CSH + H_2O + CO_3^{2-} + SO_4^{2-} + Ca^{2+} \rightarrow \text{Thaumasite} + \text{calcite(ref.}^3\text{)} \quad (2)$$

Morfologies of samples T6sz and T6vz after 10 months are presented on these images. This follows that thaumasit has crystals in columns form of lenght 3 μm.

Volume changes were occured at samples T6vz and T6sz, what is presented in the Fig. 3.. Volume change resulted in a loss of coherence, samples were plastic, which is caused by hydration suppression of Portland cement at low temperatures.

Picture from electron microscope (Fig. 4.) demonstrates baculiform crystals in sample T6st, which was placed at laboratory temperatures and at dry enviroment. These crystals can correspond to crystals of thaumasite. According to RTG analysis existence of thaumasite wasn´t confirmed. These crystals are in insignificant amount in comparison with other phases, which were created during observation, that´s why they weren´t recorded by RTG analysis. Samples didn´t change their volume during the observation.

Table I
Results of RTG analyses

T6sz	After 4 month	gypsum	calcite	SiO_2	–
	After 10 month	gypsum	thaumasite	calcite	SiO_2
T6st	After 4 month	calcite	gypsum	SiO_2	portlandite
	After 10 month	gypsum	calcite	SiO_2	–
T6vt	After 4 month	calcite	SiO2	gypsum	C–S–H
	After 10 month	gypsum	calcite	SiO_2	thaumasite
T6vz	After 4 month	gypsum	calcite	SiO_2	thaumasite
	After 10 month	thaumasite	gypsum	–	–

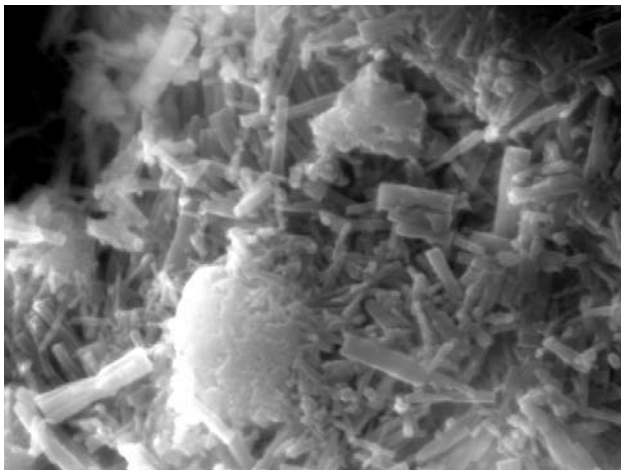

Fig. 1. **Picture of SEM of sample T6sz after 10 months**

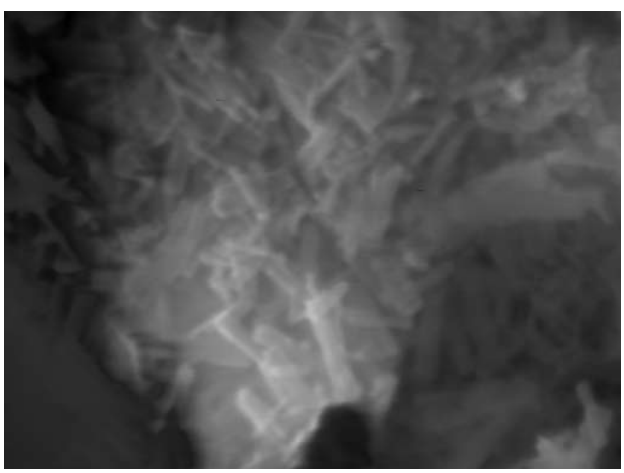

Fig. 2. **Picture of SEM of sample T6vz after 10 months**

Fig. 3. **Comparison of standard sample (left) without volume increase and sample T6vz with volume change**

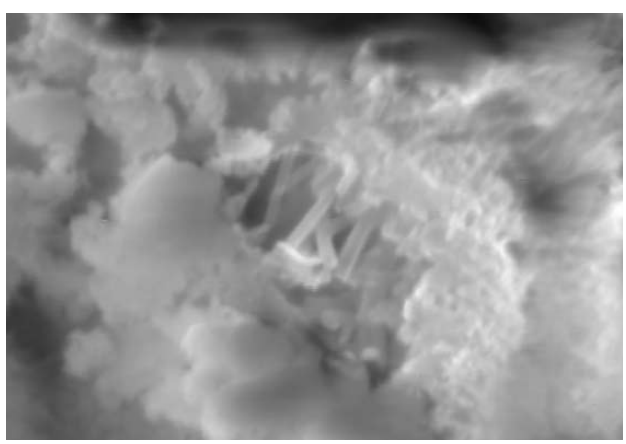

Fig. 4. **Picture of SEM of sample T6st after 10 months**

Discussion

Preparation of thaumasite is long-term process of stabilization of the whole system, when transformation of primary material via transiant phases (portlanit or C–S–H gel) to stable phases (kalcite, gypsum, eventually SiO_2 and thaumasite) is occured.

During observation of thaumasite was discovered, that creation of thaumasite depends on physical conditions – low temperature below 10 °C and intense moisture. Dependence of moisture occured at samples T6, in the concrete at samples T6vz and T6sz, which were kept at low temperatures about 2 °C during the observation, T6vz in moist enviroment, T6sz in dry enviroment. From the RTG and SEM results of these two samples (Table I) follows that presence of water accelerates creation of thaumasite due to easy availability of water, which is necessary for crystallization of thaumasite (15 molecules of water) $CaSiO_3 \cdot CaCO_3 \cdot CaSO_4 \cdot 15H_2O$.

Dependence on temperature is visible at samples T6vz, T6vt. Phase composition of sample T6vt after 10 months was consistent with composition of sample T6vz, which was analysed after 4 months. It means, there is difference of 6 months and in comparison with the sample T1 1a (it has the same phase composition after 2 months, kept at low temperatures and in moist enviroment) there is diference of 8 months. This considerable difference is too perceptible between samples T6st and T6sz (see Table I).

REFERENCES

1. Skalny J., Marchand J., Odler, I.: *Sulfate attack on concrete*. Spon press, MCT 10, 2002.
2. Hlaváč J.: *Základy technologie silikátů*. SNTL.1988.
3. Aguilera J., Blanco Varela M. T., Vázquez T.: Cem. Concr. Res. *31*, 1163 (2001).
4. Romer M., Holzer L., Pfiffner M.: Cem. Concr. Compos. *25*, 1111 (2003).
5. Bellman F.: *Simulation of the formation of thaumasite*

P09 AN APPLICATION OF Al-Si LAYER ON NICKEL-BASED SUPERALLOYS AND THEIR ANALYSIS

SIMONA POSPÍŠILOVÁ, MARTIN JULIŠ and TOMÁŠ PODRBÁBSKÝ
Brno University of Technology, Faculty of Mechanical Engineering, Technická 2, 616 69 Brno, Czech Republic, julis@fme.vutbr.cz

Introduction

Production of new generation of aircraft gas turbine engines is based on designing new constructions and materials, which make it possible to operate under still more severe conditions. The key assembly of the engine is its turbine, whose materials and design determine the tolerable gas temperature. Increased inlet gas temperatures resulted in the shortening of the service life of the blades protected with diffusion coatings. New principles of coating deposition opened up new possibilities for purposive improvement of coating compositions and variation of their properties[1].

A diffusion barrier from Al-Si layer was developed for turbine blades of aircraft engines from nickel-base superalloy ZhS6K as oxidation and corrosion protection. The main subject of the research is application of Al-Si protect layers to alternative materials as are IN713LC and IN738LC.

Experimental

This paper is focused on microstructure and chemical analysis of protective layers created by co-deposition of Al and Si (Al + Si spray application and diffusion annealing at 950 °C for 4 h) on nickel-based superalloys IN713LC and IN738LC (chemical composition is shown in Table I) after thermal and thermal-stress exposition. It also was observed an influence of Al-Si layer on mechanical properties of basic materials with and without Al-Si layer.

An operational degrading process were simulated by high-temperature heat treatment (700 to 1,100 °C – 50 to 1,000 h), by creep tests (750 to 1,000 °C under constant load) and low fatigue tests (at 800 °C).

Table I
Alloy chemical composition [% wt.]

Element	IN713LC	IN738LC
C	0.05	0.11
Cr	12.08	15.86
Ti	0.75	3.27
Al	5.91	3.31
Zr	0.10	0.03
Nb	2.02	0.88
Ta	<0.05	1.65
Mo	4.58	1.74
W	–	2.54
Co	<0.05	8.26
Ni	Bal.	Bal.

Results

Creep Tests Results

For the mutual comparison of the influence of Al-Si layer on creep-resistant properties for IN 713LC and 738LC, we applied the L-M model[2]. A graphical comparison of stress versus Larson-Miller parameter for the coated material by Al-Si layer and the uncoated material are shown in Fig. 1.

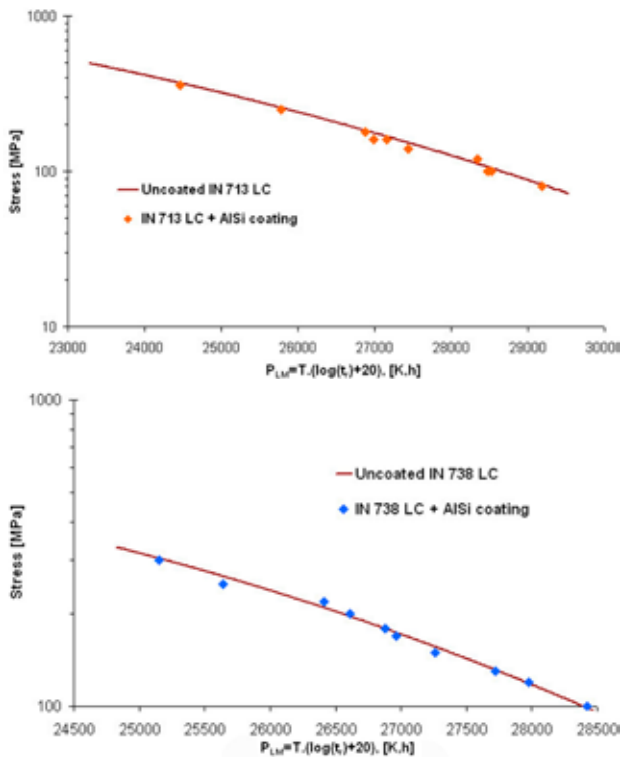

Fig. 1. **The influence of Al-Si layer on creep- resistance**

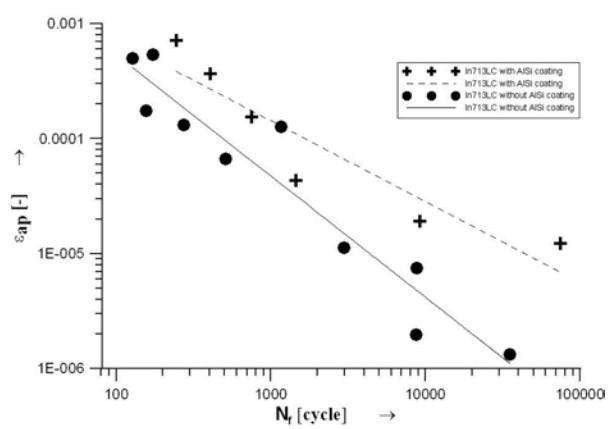

Fig. 2. **Manson-Coffin curves of coated and uncoated IN713LC**

Low-Fatigue Tests Results

Total strain controlled tests have been performed on cylindrical specimens of polycrystalline IN713LC. Results of low cycle fatigue tests made at 800 °C on uncoated samples

are compared with similar tests carried out on specimens with Al-Si coating. Fatigue life curves are documented on Fig. 2. There is dependence plastic strain amplitude ε_{ap} at half life on number of cycles to fracture N_f in the bilogarithmic representation. Experimental data were fitted by the Manson-Coffin law[3]. It can be seen that Al-Si layer increases low cycle fatigue life of the coated specimens.

Metallographic Analysis

According to the pictures and analyses from light and scanning electron microscopy, a split into several areas is evident. The surface of the samples from both materials at the initial state is divided into four sub-layers, see Fig. 3., left. The upper layer, called "oxide layer", is very thin and discontinuous. By the spot and space analysis we detected Al_2O_3 oxides which originated by diffusion from the layer, and under these oxides we can find Cr_2O_3 which are created by diffusion from the base material. Sometimes SiO_2 oxides grow up. The second layer is a "coating zone" with Ni and Al phases. The next layer is called the "inter-diffusion zone" and contains more Si and heavy elements, such as Mo, Nb, Cr, W. Simultaneously the content of Ni and Al decreases. The last sub-layer, a "substrate diffusion zone", is actually a band without γ' phase. Sometimes, this layer can be reached in complex phases and carbides based on Co, Cr, Al with acicular morphology, Fig. 3. right.

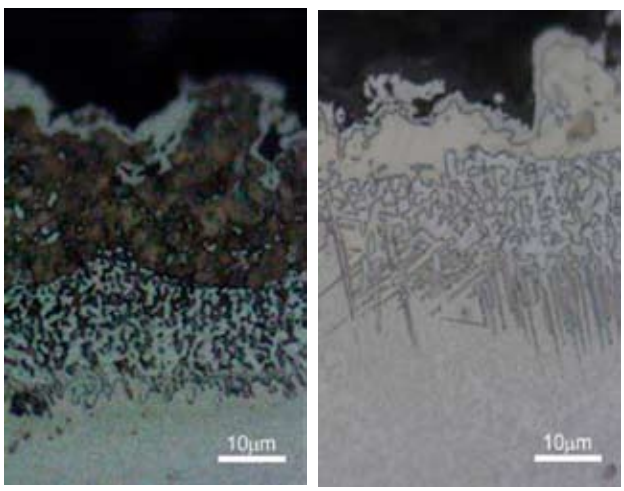

Fig. 3. **Microstructure of AlSi layer on IN738LC, as received (left), after thermal-stress exposition 800 °C – 500 h (right)**

After thermal exposition and thermal-stress exploitation, the thickness of particular layers is changed. Several sub-layers are created while several disappear. The distribution of single elements is also changed (Fig. 4.). After exposition at temperature 1,000 °C (and higher) for longer time one layer remains and gets wider. From EDS microanalysis that followed, the oxygen stays on the surface and its content decreases with the distance from the surface. After temperature and creep exposition, the oxides Al_2O_3 and Cr_2O_3 are more created. After exposition at 1,000 °C and 200 h, this layer is somewhere cracky and sporadically is a surface without layer. However, this temperature highly exceeds the working conditions.

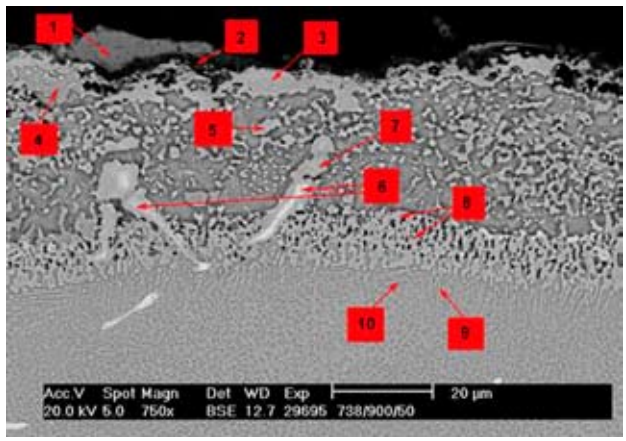

Fig. 4. **Microstructure of Al-Si layer on IN738LC, after thermal-stress exposition 900 °C – 50 h;**
Note: 1 (Cr_2O_3), 2 (Al_2O_3), 3, 4 (solid solution mixture reached in Si, Cr), 5 (solid solution mixture reached in Si, Ti), 6, 7 (Ti, Nb complex carbide), 8 (Cr-Si-Co-Ni complex phase), 9, 10 (Co, Cr, Al complex phase)

The surface of the samples without layer is non-uniform. There is a band without coherent γ', depleted by Cr and Al and with titanium nitrides which have an acicular morphology. This band is extended with time and temperature.

Conclusions

From performed analyses followed that the Al-Si layer improves heat-resistance of materials IN 713LC and 738LC.

It were also estimated that this layer does not nearly have an influence on creep-resistance of observed materials.

The low cycle fatigue life of IN713LC at 800 °C increases with application Al-Si coating.

This work has been supported by the Czech Science Foundation, projects No. 106/07/1507, 106/08/1243.

REFERENCES

1. Tamarin, Y.: Protective *Coatings for Turbine* Blades. ASM Ohio, USA, 2002.
2. Seifert, B., Melzer, B.: Rechnerische *Auswertung von Zeitstandversuchen am Beispiel des Stahles 13CrMo4-4.15*.: Langzeitverhalten warmfester Stähle und Hochtemperaturwerkstoffe, Düsseldorf (1992).
3. Obrtlík, K., Man, J., Polák, J.: *Room and high temperature low cycle fatigue of Inconel 713LC, No.: 894*, In Euromat 2001, Rimini Italy, 2001.

P10 ALKALINE MODIFIED COAL FLY ASH AS AN ADDITION TO CONCRETE

JOZEF JUNÁK and NADEŽDA ŠTEVULOVÁ
Technical University of Košice, Civil Engineering Faculty
Vysokoškolská 4, 042 00 Košice, Slovakia,
Jozef.Junak@tuke.sk

Introduction

Coal fly ash is well-know material utilized in civil engineering, mainly in building materials preparing such as blended cements and concretes. Traditionally, coal fly ashes are used as a pozzolanic material to enhance physical, chemical and mechanical properties of concretes. However, only amounts of 20–30 % of this waste kind are used in these terms and the excess is stored in large extension[1]. The reasons of small quantities coal fly ash exploitation consists in insufficient quality of fly ash required by the standard.

A number of hydrothermal activation methods have been proposed to activation coal fly ash using alkaline solutions (mainly NaOH a KOH solution). The traditional conversion methods differ in the molarity of the alkaline reagents, activation-solution/fly ash ratio, temperature (80–200 °C), reaction time (3–48 h) and pressure, depending on the type of coal fly ash used[2].

In our previous paper has been shown that the zeolite phase formation influences favourably process of physico-chemical consolidation at hardening of coal fly ash/cement pastes and leads to higher compressive strength in comparison to composite prepared without alkaline treatment[3].

The objective of this study was to investigate the hydrothermal alkaline treatment influence of coal fly ash/cement mixture on mechanical properties of hardened composites in dependence on temperature.

Experimental

Portland cement (CEM I 42.5) and coal fly ash originating from Slovakian power plant ENO A in Nováky were used as raw materials. Granulometric composition of original coal fly ash and cement is given in Table I.

Table II summarizes chemical composition of coal fly ash. Total amount of SiO_2 and Al_2O_3 was 82.127 %. Based on the chemical analysis, the used coal fly ash is high silica ash with molar ratio of $SiO_2/Al_2O_3 = 3.2$. The presence of crystalline phases was detected by X-ray diffraction (XRD) analysis on diffractometer DRON 2.0 with goniometer GUR-5 (Technabsexport, Russia). The following minerals as major components present in coal fly ash are quartz, mullite and hematite. Cristobalite, magnetite, illite, anhydrite, some silicates, aluminosilicates and their hydrates (albite, andalusite, kaolinite) were identified too.

Table I
Granulometric composition of coal fly ash and Portland cement

Fraction [μm]	[% wt.] Coal fly ash	Portland cement
180	24.64	–
180–125	10.79	–
125–71	23.67	0.10
71–45	13.09	3.85
<45	27.81	96.05

Table II
Chemical composition of coal fly ash

Component	Content [%]
SiO_2	62.526
MgO	1.900
K_2O	2.879
Na_2O	1.683
Fe_2O_3	8.068
CaO	2.893
Al_2O_3	19.601
LOI*	2.38

LOI* – loss of ignition

Laboratory investigation of alkaline treatment of coal fly ash/cement mixtures with 25 % wt. cement replacement was carried out in 5M NaOH solution at solid/liquid ratio of 0.5. Comparative cement paste was prepared by mixing only cement with water (sample 1). Mixed pastes were given in forms and subsequent 24 hours heated at temperatures of 120, 160 and 200 °C (sample 2, 3, 4) in drying-oven. Hardening samples during 28 and 90 days under laboratory conditions was realized.

The compressive strengths were measured at concrete prisms (40 mm × 40 mm × 160 mm) after hardening and evaluated according to the STN EN 206.

Results

The compressive strength values of composite samples after 28 and 90 days hardening are presented in the Table III. As it can be seen, compressive strengths of hardened experimental coal fly ash/cement composites reach the values ranging from 7 to 14 MPa. Compressive strengths of concretes increase with hardening duration. However, compressive strength values of experimental composites are lower than that of comparative composite (sample 1).

The compressive strength development is closely related

Table III
Compressive strength RC of composites after 28- and 90-days hardening

Sample	RC [MPa] 28 days	90 days
1	32.1	33.6
2	12.4	13.6
3	7.8	9.2
4	7.1	9.8

to the temperature. As it is shown in Table III, compressive strength of composites is in indirect proporcionality with temperature increase. From all investigated composites, the highest value of 28 and 90 days compressive strength accounts the sample 2 that was 24 hours heated at temperature of 120 °C.

Based on the XRD results of hardened products, zeolitic phases such as analcime and hydroxy-sodalite during alkaline treatment of coal fly ash/cement mixtures under selected conditions were formed. It is known that hydroxysodalite can be formed by conversion of the A zeolite in alkaline solution (> 10 % wt. NaOH). According to paper[4], crystalline phase of A zeolite is created in reaction mixture with SiO_2/Al_2O_3 ratio = 2 within temperature range from 25 to 150 °C.

Structures of identified phases are different from those of NaP1 zeolite and phyllipsite designated in the case of hydrothermal alternation of alone coal fly ash in autoclave. These phases favourably influence the concrete structure matrix as well as mechanical properties of hardened composite[3] in difference from composites based on alkaline and subsequent thermally treated coal fly ash/cement mixtures.

Conclusions

According to the standard requirements of STN EN 206, the measured values of 28 and 90 days compressive strengths of composites prepared by alkaline treatment of coal fly ash/cement mixture correspond to concrete class of C 8/10.

Therefore, concretes with hydrothermal alkaline treated coal fly ash at 25 % wt. cement replacement can be used for non-load-bearing constructions.

The authors are grateful to the Slovak Grant Agency for Science (Grant No. 1/3343/06) for financial support of this work.

REFERENCES

1. Puertas, F. et al.: Cem. Concr. Res. *30*, 1625 (2000).
2. Morena, N. et al.: J. Environ. Eng. *11*, 994 (2001).
3. Junák, J., Števulová, N., Kušnierová, M.: Selected Scientific Papers – J. Civ. Eng. *2*, 106 (2007).
4. Vučinič, D. et al. : *Proc. of the conference on Waste Recycling*, pp. 140, Poland, Kraków, Wydawnictwo IGSMiE PAN, 2005.

P11 ELEMENTS INTERACTION ANALYSES DURING PREPARATION OF Al-Al_3NI EUTECTIC COMPOSITES

LENKA KLAKURKOVÁ, LADISLAV ČELKO, PAVEL DOLEŽAL, ONDŘEJ MAN and KAREL NĚMEC
Brno University of Technology, Faculty of Mechanical Engineering, Institute of Materials Science and Engineering Technická 2, 616 69 Brno, Czech Republic, klakurkova@fme.vutbr.cz

Introduction

The Al-Ni binary phase diagram contains five intermetallic compounds (Al_3Ni, Al_3Ni_2, Al_3Ni_5, AlNi and $AlNi_3$). For high temperature coatings and structural materials the AlNi and $AlNi_3$ phases are widely used[1]. The third, considerably lower area of interest, are the aluminum-based matrix composites (AMC) strengthened by Al_3Ni and Al_3Ni_2 phases[2].

The Al-Al_3Ni eutectic composites production consists of the semi-product manufacturing (sharp interface between Al and Ni) and the following mechanical and/or heat treatment (enables the creation of Al_3Ni particles as strenghtening phase).[3–5]

In this paper, the high velocity oxyfuel deposition technique was used for semi-product manufacture. The influence of annealing, at temperatures below the Al-Al_3Ni eutectic point, and dwell time on strenghtening phase formation was studied.

Experimental

Aluminum sheet of commercial purity (99.5 % wt.Al) was used as a substrate. The substrate surface was ground with abrasive paper to #600, blasted by SiO2 particles and washed in acetone bath before plasma coating deposition. For nickel powder (45 ± 5 μm in diameter) deposition, the high velocity oxyfuel technique was employed. The thickness of the layer was approximately 200 ± 10 μm. After the deposition, the specimens were heated in a furnace. Heat treatment conditions were designed closely to the Al-Al3Ni eutectic melting point (639.9 °C). The first set of samples was heated to 600 °C for 50 and 500 h, the second set to 630 °C for 10 and 50 h. The samples were fan-cooled in air after the heat treatment.

For the microstructure observation, the scanning electron microscopes (JEOL 840 and PHILIPS XL30) were used. Eneregy dispersive x-ray microanalysis of selected points and layer thickness measurements by image analysis (NIS Elements AR 2.3) were performed.

Fig. 1. **The cross-sectional SEM image of Al substrate coated by Ni in as-received state**

Results

As-received state

The microstructure of Al substrate coated by Ni without heat treatment is shown on Fig. 1. The chemical concentrations measured by EDS are presented in Table I.

Table I
Chemical composition of selected points, see Fig. 1.

Point	O [% at.]	Al [% at.]	Fe [% at.]	Ni [% at.]
1	8.34	0	0	91.66
2	4.52	95.48	0	0
3	6.60	86.29	7.11	0

Annealing at 600 °C

Binary images used for image analysis based on SEM images were prepared, see Fig. 2. Chemical concentrations measured in selected points are presented in Table II. The values of Al_3Ni particles formed (count, diameter and circularity), are summarized in Table III.

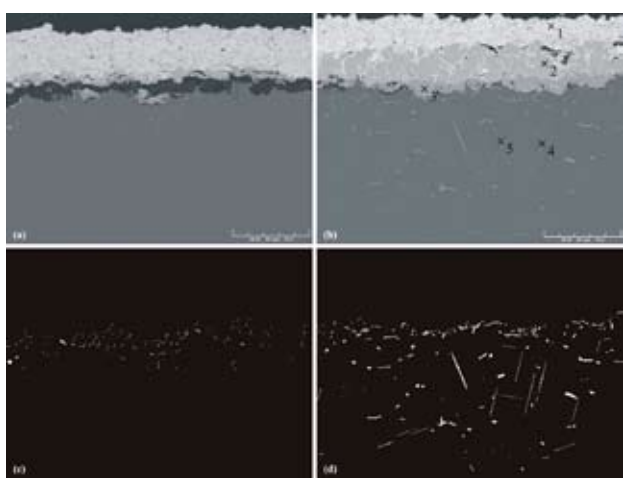

Fig. 2. **The cross-sectional SEM images of HVOF deposited Ni coating on Al substrate and the binary images prepared for image analysis measurements after annealing at 600 °C per (a, c) 50 h, (b, d) 500 h, respectively**

Table II
Chemical composition of selected points, see Fig. 2.b

Point	O [% at.]	Al [% at.]	Fe [% at.]	Ni [% at.]
1	9.03	0	0	90.97
2	5.56	58.17	0	36.27
3	4.27	73.38	0	22.35
4	2.96	86.87	4.06	6.12
5	3.29	79.61	6.99	10.12

Table III
Image analysis data of Al_3Ni particles

Heat Treatment	Count [–]	Diameter [μm]	Circularity [–]
600 °C 50 h^{-1}	202	3.82	0.84
600 °C 500 h^{-1}	253	7.59	0.68

Annealing at 630 °C

Binary images used for image analysis based on SEM images were prepared, see Fig. 3. Chemical concentrations measured in selected points are presented in Table IV. The values of Al_3Ni particles formed (count, diameter and circularity), are summarized in Table V.

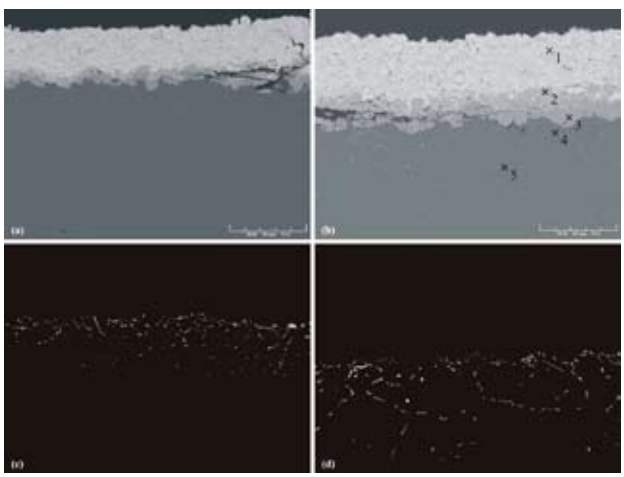

Fig. 3. **The cross-sectional SEM images of HVOF deposited Ni coating on Al substrate and the binary images prepared for image analysis measurements after annealing at 630 °C per (a, c) 10 h, (b, d) 50 h, respectively**

Table IV
Chemical composition of selected points, see Fig. 3.b

Point	O [% at.]	Al [% at.]	Fe [% at.]	Ni [% at.]
1	9.96	0	0	90.04
2	6.41	59.00	0	34.60
3	4.88	72.42	0	22.70
4	3.00	87.90	2.65	6.45
5	4.85	77.89	10.41	20.97

Dependence of annealing time and temperature height on the Al + Al_3Ni band thickness growth and on the Al_3Ni volume fraction is shown on Fig. 4.

Table V
Image analysis data of Al_3Ni particles

Heat Treatment	Count [–]	Diameter [μm]	Circularity [–]
630 °C 10 h^{-1}	341	3.92	0.81
630 °C 50 h^{-1}	239	5.85	0.67

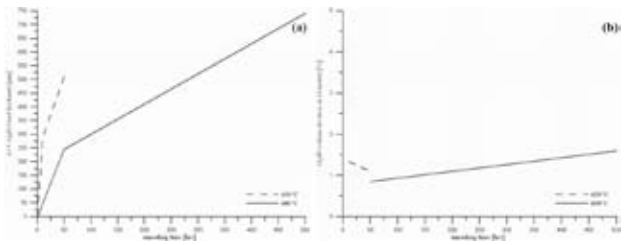

Fig. 4. **The influence of annealing time and temperature on the Al_3Ni + Al band (a) thickness growth, (b) volume fraction**

Conclusions

In this work, the elements interaction on Al and Ni sharp interafce during annealing below the melting point of Al+Al_3Ni eutectic was investigated primarily. The Al_3Ni_2 (light gray) and Al_3Ni phases (dark gray) between the Ni coating and Al substrate were observed and analysed. Platelet-like and needle-like particles of Al_3Ni phase were observed in the Al substrate; the first one formed at the grain boundaries and the second one on the favourable places inside the grains, most probably due to the grain boundary and pipe diffusion mechanisms. These mechanisms are apparently faster then volume diffusion at these "lower" temperatures. Rising temperature accelerates the diffusion of Ni into the Al and increases the thickness of Al+Al_3Ni band. The longer dwell time leads to the formation of coarse and less regular particles, as well.

This work has been supported by the Ministry of Education (grant MSM002163058) and Grant Agency of Czech Republic (grant GAČR 106/05/H008).

REFERENCES

1. Morsi K.: Mat. Sci. Eng. A *299*, 1 (2001).
2. Rajan T. P. D., Pillai R. M., Pai B. C.: J. Alloys Compd. *453*, L4 (2008).
3. Zhu P., Li J. C. M., Liu C. T.: Mater. Sci. Eng A *532*, 239-240 (1997).
4. Zhu P., Li J. C. M., Liu C. T.: Mater Sci Eng A *57*, 329-331 (2002).
5. Min G., Lee J. M., Kang S., Kim H.: Mater Lett *60*, 3255 (2006).

P12 MAGNETIC PROPERTIES OF WASTE VITRIFIED IN MICROWAVE FURNACE

MILOTA KOVÁČOVÁ[a], MICHAL LOVÁS[a], MAREK MATIK[a,b] and VLADIMÍR ŠEPELÁK[a,c]
[a]*Institute of Geotechnics, Slovak Academy of Sciences Watsonova 45, 043 53 Košice, Slovakia,*
[b]*Department of Physical Chemistry, Faculty of Sciences, Palacký University, tř.Svobody 26, 771 46 Olomouc, Czech Republic,*
[c]*Institute of Physical and Theoretical Chemistry, Technical University of Braunschweig, Hans-Sommer Straße 10, D-38106 Braunschweig, Germany,*
kovacova@saske.sk

Introduction

Vitrification is a well established technology that involves the conversion of the waste in a stable and homogenous glass through a thermal treatment of melting, with the additional modification of the starting composition with glass-forming additives[1].

The paper deals with the magnetic properties of an iron-containig waste from the former nickel hydrometallurgy plant in Sereď (Slovakia). The waste, nickel leaching residue (NLR), was used as a model carrier of heavy metals (Co, Cu, Cd, Pb, Ni) from wastewater treatment, which was necessary to stabilize. Recently, microwave enegy has been applied for the waste treatment as an energy efficient alternative to current heating technologies[2]. In the presented work, microwave vitrification was used for the stabilization of heavy metals carriers.

The magnetic properties were studied by magnetic susceptibility measurement and Mössbauer spectroscopy method.

Experimental

Microwave Vitrification

The chemical composition of waste (NLR) and the raw materials used for the glasses is following: NLR 15 % SiO_2, 4.8 % Al_2O_3, 3.54 % CaO, 2.21 % MgO, 38.57 % Fe_2O_3, 22.64 % FeO, 1.06 % Cr_2O_3, 0.17 NiO, glass cullet 72.4 % SiO_2, 1.7 % Al_2O_3, 9.6 % CaO, 1.7 % MgO, 0.05 % Fe_2O_3, 13.8 % Na_2O, 0.6 % K_2O, dolomite 0.59 % SiO_2, 0.34 % Al_2O_3, 29.61 % CaO, 22.47 % MgO, 0.29 % Fe_2O_{3total}, 0.04 % Na_2O, 0.11 % K_2O, 46.35 % loss of ignition, glass sand 99 % SiO_2, soda 58 % Na_2O.

The glasses from S1 series contain 30–60 % of NLR, glass cullet and dolomite. In S2 series, the glasses include 30–50 % of NLR, glass sand and soda, besides glass cullet and dolomite. The theoretical chemical compositions of glasses measured by AAS (Varian, Australia) are described in Table I (S1) and Table II (S2).

Microwave vitrification was carried out in a microwave furnace Panasonic NN-5251B (series S1) and Panasonic NN-Q453 (series S2) with frequency 2.45 GHz and output 900 W (S1) and 1,000 W (S2). The samples were placed in thermal isolated ceramic crucibles and heated during 30 (S1) and 45 (S2) minutes. When the samples achieved the melting temperature, they slowly cooled down in the furnace.

Table I
Chemical analysis of samples from S1 series [% wt.]

Sample	SiO_2	Fe_2O_3	FeO	Al_2O_3	CaO	MgO	Na_2O	K_2O
1-S1	19.28	11.73	6.79	1.95	17.79	12.24	2.78	0.18
2-S1	13.55	15.58	9.06	2.26	17.18	12.29	1.40	0.12
3-S1	42.27	15.48	9.06	2.80	9.18	3.98	6.90	0.31
4-S1	14.99	19.41	11.32	2.71	14.57	10.26	1.40	0.10
5-S1	16.44	23.23	13.58	3.15	11.97	8.24	1.39	0.09
6-S1	30.80	23.19	13.58	3.42	7.97	4.08	4.14	0.19

Table II
Chemical analysis of samples from S2 series [% wt.]

Sample	SiO_2	Fe_2O_3	FeO	Al_2O_3	CaO	MgO	Na_2O	K_2O
1-S2	52.37	11.61	6.79	1.90	6.42	3.34	6.37	0.16
2-S2	46.15	11.64	6.79	2.02	9.86	5.67	4.15	0.20
3-S2	56.92	11.61	6.79	2.22	6.86	2.55	6.21	0.28
4-S2	48.01	11.63	6.79	2.49	9.78	3.93	8.28	0.37
5-S2	53.87	15.46	9.06	2.11	3.86	2.18	10.14	0.07
6-S2	48.92	15.47	9.06	2.38	6.78	3.56	3.45	0.16
7-S2	42.27	15.48	9.06	2.80	9.18	3.98	6.90	0.31
8-S2	46.75	19.30	11.32	2.74	3.69	1.45	5.68	0.12
9-S2	46.38	19.31	11.32	3.08	5.61	1.79	5.62	0.24

Magnetic Susceptibility and Mössbauer Spectroscopy Measurements

Magnetic susceptibility of the melted samples was measured by Kappabridge KLY-2, Geofyzika Brno in magnetic field intensity of 300 Am^{-1} with homogeneity of 0.2 % at frequency 920 Hz.

The room-temperature Mössbauer spectroscopy measurements were realized in transmission geometry using a conventional spectrometer in a constant acceleration mode. A $^{57}Co/Rh$ γ-ray source was used. The velocity scale was calibrated relatively to ^{57}Fe in Rh. A proportional counter was used to detect the transmitted γ-rays. Mössbauer spectral analysis software Recoil[3] was applied to provide a quantitative evaluation of the spectra.

Results

Magnetic Susceptibility Measurements

The magnetic susceptibility of the raw materials and glasses are presented in Table III, IV and V. The measured values are not depending on the iron content. Samples 2-S1 with the highest value of magnetic susceptibility in the series and 4-S2 with the lowest value of magnetic susceptibility have been chosen for Mössbauer spectroscopy measurements.

Table III
Magnetic susceptibility of raw materials

Sample	Magnetic susceptibility × 10^{-6} SI unit
NLR	135,222
Glass cullet	247
Dolomite	36
Glass sand	34

Table IV
Magnetic susceptibility of vitrified samples from S1 series

Sample	Magnetic susceptibility × 10^{-6} SI unit
1-S1	126,943
2-S1	245,918
3-S1	56,441
4-S1	189,272
5-S1	211,601
6-S1	96,101

Table V
Magnetic susceptibility of vitrified samples from S2 series

Sample	Magnetic susceptibility × 10^{-6} SI unit
1-S2	45,792
2-S2	54,739
3-S2	35,318
4-S2	15,066
5-S2	115,310
6-S2	130,587
7-S2	81,010
8-S2	99,680
9-S2	169,626

Mössbauer Spectroscopy Measurements

Fig. 1. shows the Mössbauer spectrum of NLR. The spectrum is characterized by three doublets and two sextets. The doublets correspond to iron in Fe^{2+} state and superparamagnetic Fe^{3+}. The sextets are ordered in tetrahedral and octahedral position. The parameters of NLR Mössbauer spectrum are in Table VI.

The percentage content of iron forms is possible to determine from the intensities. Spectrum 1 and 3 represents Fe^{2+} with iron content of 9.6 % and 10.9 %. The isomer shift of subspectrum 2 presents Fe^{3+} (12.7 %) in polycrystalline state. Subspectrum 4 was found to be Fe in the tetrahedral form of Fe_3O_4 (28.7 %) and subspectrum 5 in the octahedral form of Fe_3O_4 (38.1 %).

Fig. 2 shows the Mössbauer spectrum of glass 2-S1. The spectrum contains a central doublet and a magnetic sextet.

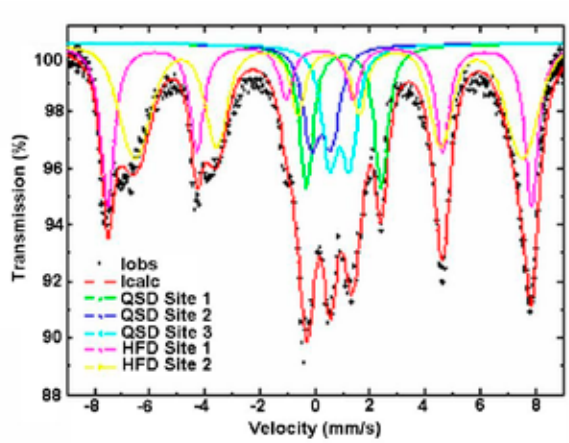

Fig. 1. **Mössbauer spectrum of NLR (lobs–experimental spektrum, lcalc-theoretical spectrum)**

Table VI
Mössbauerspectrum parameters of NLR

Subspectrum	IS [mm s^{-1}]	QS [mm s^{-1}]	I [%]	H	σ_B
1 QSD Site 1	0.36	0.73	9.6	–	0.28
2 QSD Site 2	1.16	2.72	12.7	–	0.04
3 QSD Site 3	1.01	0.72	10.9	–	0.2
4 HFD Site 1	0.30	–	28.7	47.7	0
5 HFD Site 2	0.61	–	38.1	43.6	2.69

The structure of central doublet in the sample confirms the presence of Fe^{2+} and also Fe^{3+} ions. The central doublet corresponds to Fe cations in nanoparticles in superparamagnetic state. Magnetic sextet belongs to magnetite in a polycrystalline (ferrimagnetic) state. The wide spectral lines indicate the presence of iron containing particles with a large distribution of dimensions[4].

Mössbauer spectrum of glass 4-S2 (Fig. 3.) is fitted by three subspectrums – doublets. The presence of doublets confirmed the paramagnetic respectively superparamagnetic

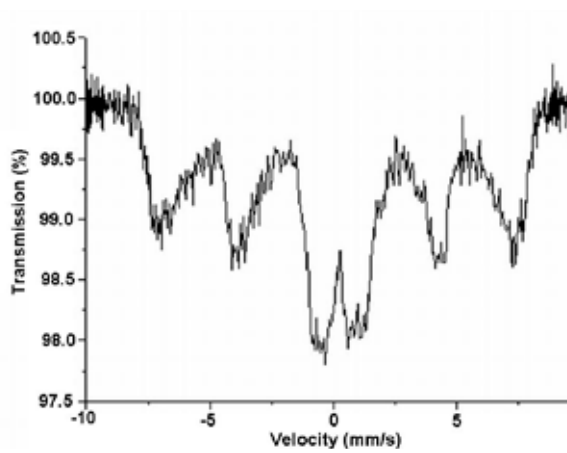

Fig. 2. **Mössbauer spectrum of vitrified sample 2-S1**

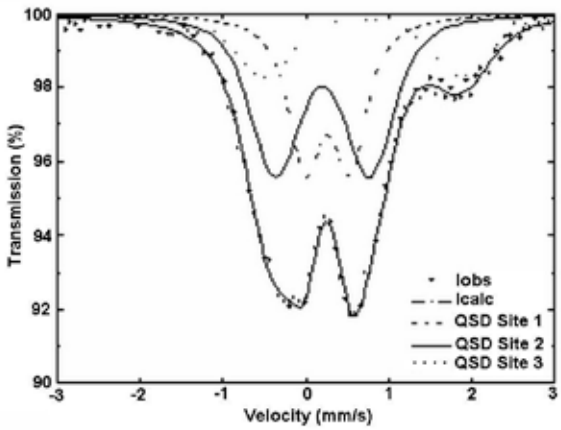

Fig. 3. **Mössbauer spectrum of vitrified sample 4-S2 (lobs-experimental spektrum, lcalc-theoretical spectrum)**

Table VII
Mössbauer spectrum parameters of vitrified sample 4-S2

Subspektrum	IS [mm s^{-1}]	QS [mm s^{-1}]	I [%]
1 QSD Site 1	0.27	0.47	31.3
2 QSD Site 2	0.25	1.03	47.1
3 QSD Site 3	0.68	2.62	21.6

state of iron in the sample. Low magnetic susceptibility is expected for this magnetic state.

The values of isomer shift of subspectrum 1 IS(1) and subspectrum 2 correspond to polycrystalline Fe^{3+}. The content of Fe^{3+} is 31.3 % (subspectrum 1) and 47.1 % (subspectrum 2) respecively. Subspectrum 3 represents Fe^{2+} with the content of 21.6 % (see Table VII).

Conclusions

By the Mössbauer spectroscopy measurements, the magnetic properties of vitrified samples depend on magnetic state that is influenced by grain size[5]. Magnetic susceptibility of glasses is affected by the ratio of iron content in magnetic ordered phase represented by sextet to the iron content in superparamagnetic phase represented by doublet. The grain size of glasses is mainly influeced by a cooling of molten mixture.

This works has been supported by the Slovak Research and Development Agency under the contract No. APVV-51-035505.

REFERENCES

1. Appleton T. J., Colder R. I., Kingman S. W., Lowndes I. S., Read A. G.: Appl. Energ. *81*, 85 (2005).
2. Colombo P., Brusatin G., Bernardo E., Scarinci G.: Curr. Opin. Solid State Mater. Sci. *7*, 225 (2003).
3. Lagarec K., Rancourt D.G.: RECOIL. *Mössbauer Spectral Analysis Software for Windows, version 1.02*. University of Ottawa 1998.
4. Goya G. F., Berquó T. S., Fonesca F. C., Morales M. P.: J. Appl. Phys. *94*, 3520 (2003).
5. Šepelák V., Feldhoff A., Heitjans P., Krumeich F., Menzel D., Litterst F. J., Bergmann I., Becker K. D.: Chem. Mater. *18*, 3057 (2006).

P13 THE USE OF ELECTROKINETIC POTENTIAL MEASUREMENT FOR EXAMINATION OF KAOLINITE DECOMPOSITION

DANA KUBÁTOVÁ, PETR PTÁČEK and JAROMÍR HAVLICA
Výzkumný ústav stavebních hmot, a.s., Hněvkovského 65, 617 00 Brno, Czech Republic,
kubatovad@centrum.cz

Introduction

Metakoalin represents one the important puzzolana materials that are widely used in mortar and concrete technology. It is white amorphous aluminosilicate $Al_2O_3 \cdot 2SiO_2$. It is prepared by calcination of kaolin in temperature range 500–800 °C. This process is possible to describe by the following equation:

$$Al_2O_3 \cdot 2SiO_2 \cdot 2H_2O \xrightarrow{500-800\,^{\circ}C} Al_2O_3 \cdot 2SiO_2 + 2H_2O \quad (1)$$

Adsorbed water is released at 100 °C and the dehydroxylation begins over 400 °C. At the temperature over 900 °C, other reactions occur. Their resultant products are silica and mullite. The dehydroxylation process affects the degree of structure orderliness, disturbances of crystal lattice, particle shape and size, type and amount of mineral admixtures, and also experimental conditions. The electrokinetic potential measurement, FT-IR spectroscopy and differential thermal analysis were used for determination of the kinetics of metakaolin thermal conversion.

Experimental

Sample preparation

Zeta potential

Industrial kaolin was calcinated at the temperatures of 105, 300, 400, 450, 500, 550, 600, 700, and 800 °C in a porcelain cup.

Infrared spectroscopy

Kaolin symples were calcinated by temperatures 440 and 500 °C and were mixed with dried KBr in weight ratio 1 : 100.

Thermal Analyse

Kaolin samples were calcinated at the temperature range 400 to 520 °C for the period of 2 hour. The heating rate was 30 °C min^{-1}.

Results

Zeta Potential

Measured values of zeta potential are displayed in the Fig. 1.

At the temperature range 105–300 °C is capillary and adsorbed water released. Volume change attending capillary water evaporation generate tension that is released by cracks' formation or disintegration of aggregate. The observed growth of zeta potential is possible to explain by the pre-dehydroxylation on the surface of particles. At the temperature range 400–500 °C, dehydroxylation proceeds. Water that is fixed in ions solvation sheets is released in first step. The charge reduction that results in zeta potential decrease is possible to describe by the following reaction:

$$[=Al-O]^-[Na(H_2O)_x]^+ \xrightarrow{T} =Al-O-Na + x\ H_2O(g) \quad (2)$$

Along with the partial water vapour pressure (pH_2O), the water released from the hydration sheath, Si-O bonds of the siloxane bridges ($\equiv Si-O-Si\equiv$) tetrahedic layers and silanol groups $\equiv$Si–OH form. The surface silanoles dissociation is connected with the surface potential increase, which leads to the zeta potential increase of the samples calcinated at 500 °C.

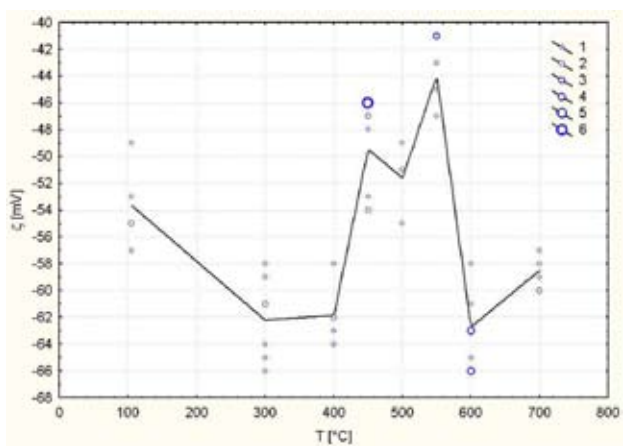

Fig. 1. **Relation of zeta potential on the burning temperature**

Along with the temperature of the thermal treatment, the amount of water released during the condensation between $\equiv Si-OH$ a $HOAl=$ bonds increases. The process may be described by the following reactions:

$$\equiv Si-O-Si\equiv + H_2O \xrightarrow{T,pH_2O} 2 \equiv Si-OH \quad (3)$$

$$\equiv Si-OH + =Al-OH \xrightarrow{T,pH_2O} \equiv Si-O-Al + H_2O(g) \quad (4)$$

$$2 = Al-OH \xleftrightarrow{T,pH_2O} =Al-O-Al= + H_2O(g) \quad (5)$$

The dehydroxylation (decrease of the OH bonds abundance) connected with polykondenzation (500–550 °C) results to the kaolin zeta potential decrease. Above the temperature of 550 °C, a significant zeta potential value increase was observed. The increase can be explained by the formation of a metastable phase – metakaolin. The reconstructive phase transition is connected with the destruction of sheet structure of kaolinite. At lower temperature, the amount of crystal defects forming in the metakaolin structure is significant. The zeta potential increase can be explained by the adsorption of hydroxyl anions on these defects from dispersive environment, which increases the surface potential of a particle.

T h e r m a l A n a l y s e

The dehydroxylation of kaolin proceed at temperature range 400 to 670 °C and there occurs weiht decrease about 13,1%.

Overall activation energy and pre-exponential coefficient were defined from the Arrhenius equation in logarithmic form. The overall activation energy reaches 148.78 kJ mol^{-1} and pre-exponential coefficient reaches 2.71×10^7 s^{-1}, under isothermal conditions.

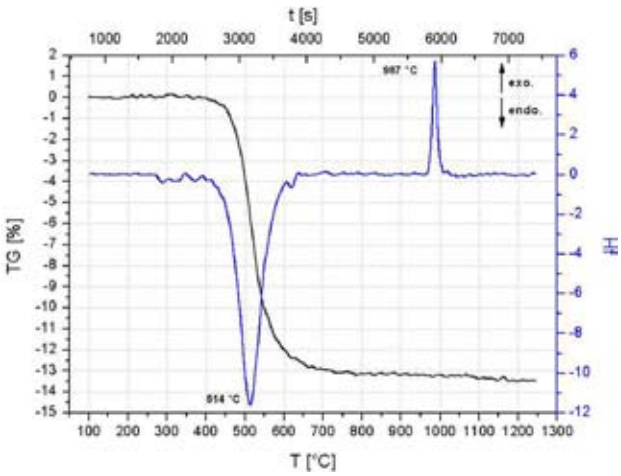

Fig. 2. **TG-DTA curves**

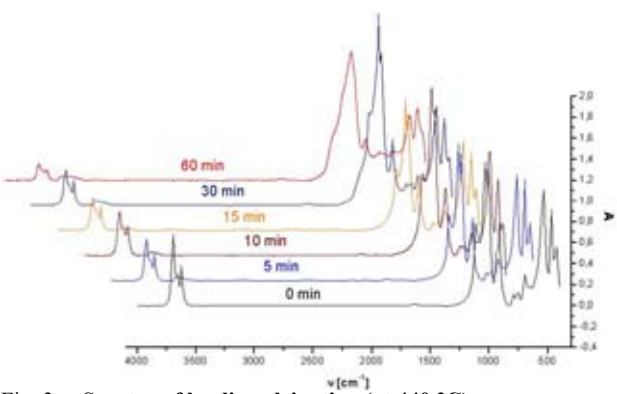

Fig. 3. **Spectra of kaolin calcination (at 440 °C)**

I n f r a r e d S p e c t r o s c o p y

The spectum shape changes show that the dehydroxylation process consists of two steps – see Fig. 3.

The major part of water molecules from layer kaolin structure leaves the structure first.

During this process, reduction of hydroxyl stretching a bendind absorption bands occurs, while SiO and AlO modes do not change. The second step is connected with the loss of selectivity of SiO and AlO modes (30 min.) because of changes in primary coordinate shell during kaolin to metakaolin conversion. The second step, at the temperature 440 °C) begins after 15 minutes. The v1 modes of ouOH groups were used for interpretation of kinetics of kaolin decomposition only. The –ln(1–y) linear dependace on time confirmed F1 model of kaoline dehydoxylation.

Conclusions

The paper demonstrates that zeta potential measurement may be used for characterization of dehydroxylation processes. Zeta potential increases during pre-dehydroxylation process. During dehydroxylation zeta potential reaches its minimum value at 550 °C. Destruction of kaolinite sheet structure during nucleation of metakaolinite leads to the repeated increase of zeta potential values. The good agreement between zeta potential measurement, thermogravimetry and infrared spectroscopy results was achieved. All the methods applied on the examination of isothermal kaolinite dehydroxylation indicate that the dehydroxylation proceeds during a single nucleation process (F1) at the temperature range from 420 to 520 °C. The overall activation energy determined by thermogravimetry reaches 148.78 kJ mol^{-1} (TG). Good agreement with literature sources was achieved. This value lies within the most frequently reported interval: 140–250 kJ mol^{-1}

This work has been supported by research centre MŠMT No. 1M06005.

REFERENCES

1. Heide K., Földvari M.: Thermochim. Acta *446*, 106 (2006).
2. Nahdi K. et al.: Thermochim. Acta *390*, 123(2002).
3. Ptaček P. et. al. Keramický zpravodaj *1*, 5 (2008).
4. Temuujin J. et. al. J. Eur. Ceram. Soc. *19*, 105 (1998).
5. Traore K., Gridi-Bennadji F., Blanchart P.: Thermochim. Acta *451*, 99 (2006).

P14 ALKALI AND VANADIUM OXIDES CORROSION OF HIGHLY ALUMINA RERRACTORIES

TOMÁŠ OPRAVIL, PETR PTÁČEK, JAROMÍR HAVLICA, FRANTIŠEK ŠOUKAL and MICHAL VRŠECKÝ

Institute of Materials Chemistry, Brno University of Technology, Purkyňova 118, 612 00, Czech Republic, opravil@fch.vutbr.cz

Introduction

Refractory materials with height and very height alumina content are commonly used at higher temperatures under reduction conditions. These materials are based on mullite and corundum. Mullite ($3Al_2O_3 \cdot 2SiO_2$) is under ordinary pressures only stable compound in the $SiO_2-Al_2O_3$ system and the other alumosilicates, such as silimamite, andalucite and cyanite, become to mullite at temperatures 1,545, 1,390 and 1,370 °C, respectively. Mullite confers interesting properties to the refractory materials, such as thermal and chemical stability, mechanical resistance, low thermal expansion and thermal impact strength.[1–3]

The aim of this work is study of alumina and vanadium oxides corrosion of shaped high alumina refractory material. The corrosion products were investigated by DTA, FT-IR and XRD.

Experimental

Corrosion process of corundum based refractory materials used in combustion reactor was compared. Phosphate bonded corundum heat-resistant brick Korrath K99 (Al_2O_3 > 99 %) can be employed to the 1900 °C under reducing condition. Material properties were enhanced by addition of Cr_2O_3 and ZrO_2. LS – Kleber 34 (94 % Al_2O_3, 4 % P_2O_5) was used as binding agent.

S i m u l t a n e o u s T G - D T A

The TG-DTA analysis of the Korrath K99 lining fragment in an air oven at ambient atmospheric condition was carried out by TG-DTA Analyzer Setaram 92-18 up to temperature 1,400 °C. Applied heating and cooling rate was 10 °C min^{-1}.

I n f r a r e d S p e c t r o s c o p y

Infrared spectra of samples were recorded in KBr pellets using FT-IR spectrometer Nicolet Impact 400 in the wavelengths range from 4,000 to 400 cm^{-1}. Measurements were done under resolution 8 cm^{-1}.

Grinded samples were mixed with KBr with mass ratio 1:100. Mixtures were homogenized by grinding in dish and its weighted amount was pressed under 40 kPa for 20 s and next 80 kPa for 30 s.

X - r a y D i f f r a c t i o n

Sample phase composition was investigated by X-ray powder diffraction analysis by difractometer X´Pert (Philips).

Results

D i f f e r e n t i a l T h e r m a l A n a l y s i s

The DTA results of unused and corroded heat resistant brick Korrath K99 is shown on Figs. 1. and 2. There is one sharp endothermic peak at temperature 795 °C on Fig. 1. With regard to sample composition is this effect probably caused by unmixing of $Al_2O_3-ZrO_2$ solid solution. Sample mass changes are insignificant.

Material used in refractory line show endothermic doublet at 553 and 583 °C.

This double peak was fitted by first type Voight function (1), due to specify peak's temperature of second endothermic effect – 586 °C.

$$y = y_0 + A\left[m_u \frac{2}{\pi}\frac{w}{4(x-x_c)^2+w^2} + (1-m_u)\frac{\sqrt{4\ln 2}}{\sqrt{\pi}w} e^{\frac{4\ln 2}{w^2}(x-x_c)^2}\right] \quad (1)$$

Where y_0 is offset, x_c peak center, A amplitude, w width and m_u shape factor of peak.

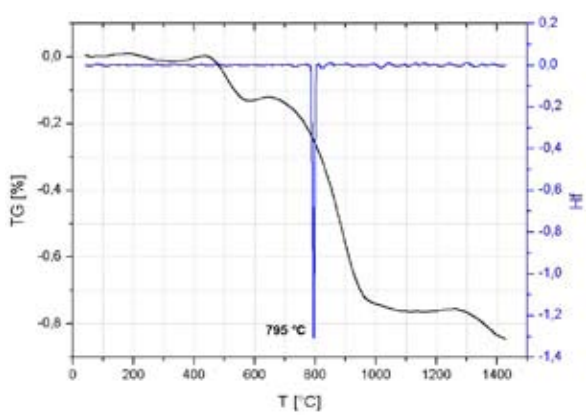

Fig. 1. **DTA of refractory material Korrath K99 unaffected by corrosion**

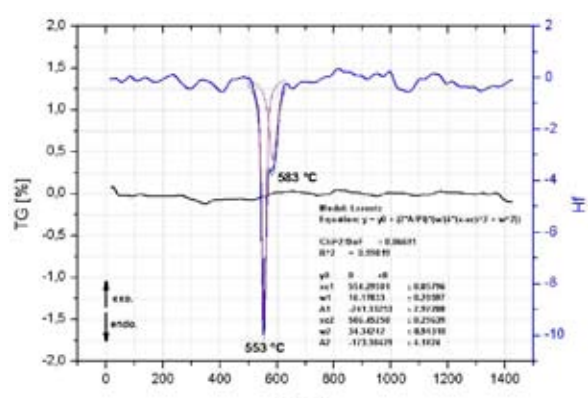

Fig. 2. **DTA of corroded refractory material Korrath K99**

The first peak on Fig. 2. belongs to thermal decomposition of the $CaO \cdot V_2O_5$ (2). Reaction was connected with V_2O_5 reduction to VO_2.

$$2\,CaO \cdot V_2O_5 + C \rightarrow 2\,CaO + 4\,VO_2 + CO_2 \qquad (2)$$

Low temperatures eutectic melts were form between product of reaction (2) and Fe or Ti compounds. Source of Fe, Ti compounds is burning aw material. The second endothermic peak is connected with eutectics melt appearance.

Infrared Spectroscopy

FT-IR spectrum of unused and corroded heat resistant brick Korrath K99 is shown on Figs. 3. and 4. While the first of them is virtually similar like the spectrum of corundum, corroded brick show more complicated XRD pattern.

There was found absorbtion band of silica and mullite. Mullite is part of basic brick material, but SiO_2 spectral bands belong to glassy phase of corrosion product. Silica source is heat resistant binding agent.

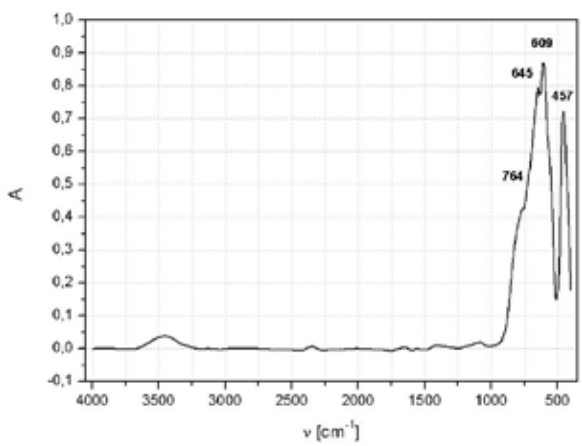

Fig. 3. **FT-IR of unused Korrath K99 material**

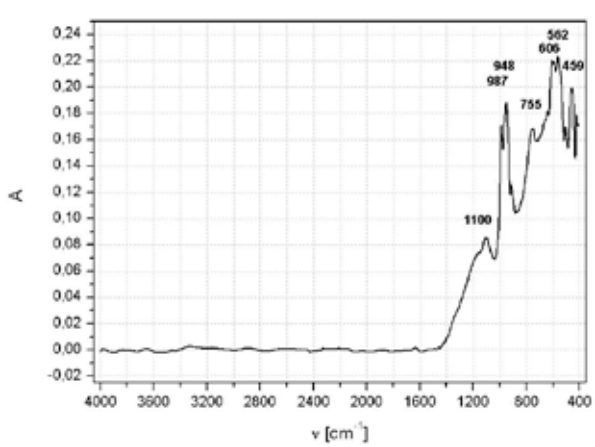

Fig. 4. **FT-IR of corroded Korrath K99 material**

X-ray Diffraction

The XRD patterns of unused and corroded heat resistant brick Korrath K99 is shown on Figs. 5. and 6.

The $Ca_{0.17}V_2O_5$ dual oxide was identified as main crystalline product of Korrath K99 corrosion (Fig.6).

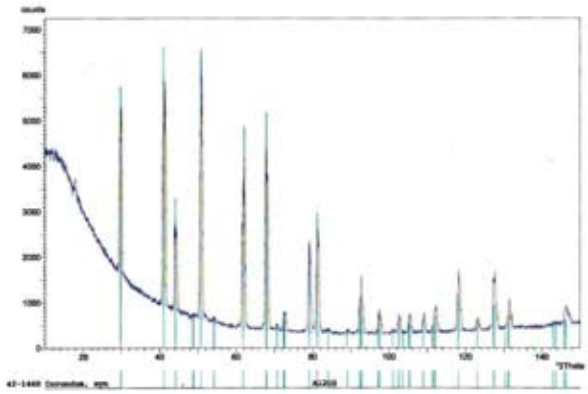

Fig. 5. **XRD of unused Korrath K99 material**

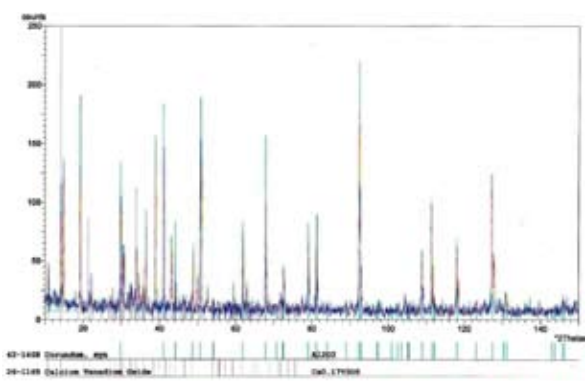

Fig. 6. **XRD of corroded Korrath K99 material**

Conclusions

In XRD pattern of corroded material of Korrath K99 heat resistant brick wasn't found diffractions of mullite. Accord to FT-IR results is this compound more sensitive to corrosion process than corundum. There has been risk of prior corrosion of binding mullite phase.

In addition vanadium oxides corrosion of high alumina refractory line, there was formed glassy phase. Alkali oxides from raw material play significant role on its origin.

This work has been supported by MŠMT poject NPV – NHV – 1 number 2B08024.

REFERENCES

1. Hlaváč J., *Základy technologie silikátů* (trans. name: *The primer of technology of silicates*), chapter II, p. 118, SNTL, Prague 1988.
2. Hanykýř V., Kutzendörfer J., *Technologie keraramiky*, Silis, Vega s.r.o., Hradec Králové, 2000.
3. Ribero D., Restrepo R., Paucar C., García C.: J. Mat. Process. Technol. (2008), aricle in press, aviable on-line *26 March 2008.*

P15 MEASURMENT OF HEAT OF HYDRATATION OF ROMAN CEMENT

TOMÁŠ OPRAVIL, PETR PTÁČEK, FRANTIŠEK ŠOUKAL and JAROMÍR HAVLICA
Institute of Materials Chemistry, Brno University of Technology, Purkyňova 118, 612 00, Czech Republic, opravil@fch.vutbr.cz

Introduction

The old buildings (sights) are very complicated in their composition and function. Some of these buildings survive for hundreds of years, but many of them are not in good condition, so here is a space for restorers, who want a material or materials, which will help them to conserve or repair these sights or presents from our ancestors. Restorers have to respect rules of care of historical monuments (try to use materials similar or the same as the original material of the sight is) which requires searching for materials, that will protect, restore and conservate the object with minimal harm.

This paper describes testing of lime stone from Kurovice, especially chemical, phase composition and hydraulic modulus determination.

Natural cement (Roman cement), which was used as a building material in the last century in the area of Bohemia, isn´t produced nowadays in the Czech Republic and surrounding states. The Roman cement is a historical variation of lime binder, it's important for its hydraulic properies and it is necessary to be interested in this material because of conservators.

Chemical analysis was focused on assesment of loss during annealling and oxides specification (oxides which are useful in characteristic modules calculation – CaO, SiO_2, Al_2O_3, Fe_2O_3, MgO).

For classification prepared roman cements and base materials is good analyses methods TG-DTA method, XRD method and heating microscope showed us the temperature of sintering, melting point and phase composition of tested material from stonepit in Kurovice.

Very important for classification prepared roman cements is hydratation haed. These work is suggests easy method for determination hydratation head. H_2O.

Experimental

The enthalpiometric method for the hydration heat assessment in prepared roman cements was tested. The apparatus consisting of multimeter with thermistor and styrofoam calorimetric cell with magnetic stirrer was made and whole system was connected to PC (Fig. 1.). The measurement itself was performed in styrofoam cup placed in calorimetric cell. Determined amount of distilled water was poured into the cup and after temperature stabilization the exact amount of sample of roman cement was added while slowly stirred. After the temperature stabilization (minimum 15 min of stable temperature) the measurement was finished. From the recorded data the temperature difference was determined and together with roman cement amount, volume of used distilled water, and calorimetric constants it served for the hydration heat calculations according to (1). The number of moles of water was calculated from (2). The calculations resulted in the determination of hydration heat released from the hydration of roman cement.

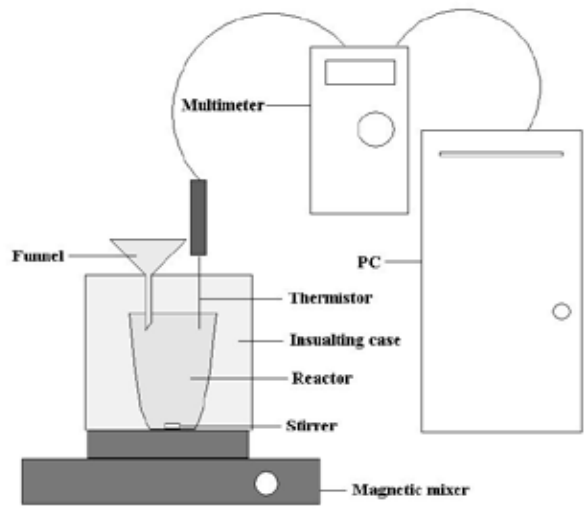

Fig. 1. **The experiments for measuring of hydratation heat**

For calculation hydratation heat was used this formula:

$$Q_{\mathrm{HYD}} = n_{\mathrm{H_2O}} \cdot c_{\mathrm{H_2O}} \cdot \Delta T \quad (1)$$

Q_{HYD} – hydratation head [J mol^{-1}]
n_{H2O} – number of moles (water) [mol]
c_{H2O} – heat capacity (water) [J K^{-1} mol^{-1}]
ΔT – difference of temperatutre [°C]

For calculation number of moles was used this formula:

$$n_{\mathrm{H_2O}} = \frac{m_{\mathrm{H_2O}}}{M_{\mathrm{H_2O}}} \quad (2)$$

Table I
Composition of synthetic roman cement 1

Component	Weight [%]	Grams to 100 g
$CaCO_3$	58.98	80
$CaSO_4 \cdot 2H_2O$	3.09	4.0
$Mg(OH)_2$	1.19	1.6
Kaolinit	8.01	9.0
Fe_3O_4	4.87	6.6
SiO_2	20.65	28.0
K_2CO_3	1.91	2.6
Na_2CO_3	1.03	1.4
$Al(OH)_3$	1.62	2.2

Table II
Composition of synthetic roman cement 2

Component	Weight [%]	Grams to 100 g
$CaCO_3$	60.24	80
$CaSO_4 \cdot 2H_2O$	3.16	4.0
$Mg(OH)_2$	1.81	2.4
Kaolinit	6.78	9.0
Fe_3O_4	2.25	3.0
SiO_2	21.08	28.0
K_2CO_3	1.96	2.6
Na_2CO_3	1.05	1.4
$Al(OH)_3$	1.66	2.2

Table III
Composition of synthetic roman cement 3

Component	Weight [%]	Grams to 100 g
$CaCO_3$	60.24	80
$CaSO_4 \cdot 2H_2O$	3.16	4.0
$Mg(OH)_2$	1.81	2.4
Kaolinit	6.78	9.0
Fe_3O_4	2.25	3.0
SiO_2	21.08	28.0
K_2CO_3	1.96	2.6
Na_2CO_3	1.05	1.4
$Al(OH)_3$	1.66	2.2

Results

In this work the samples of synthetic roman cements were tested. The amount of 50 ml distilled water was poured into the cup. The exact amount of binder sample was added at once while stirring. The temperature inside the vessel was recorded each 5 sec. by thermistor.

Table IV
Results of measurement of hydratation composition of synthetic roman cement 1

Sample	ΔT	Q [J mol^{-1}]	Q [J g^{-1}]
Nature	1.2682	264.522	244.242
RC 1	3.3386	696.368	642.979
RC 2	3.5725	745.155	688.026
RC 3	2.5360	528.96	488.406

Samples of roman cements were prepared by burning out the raw meal at the temperature of 870 °C for the period of 4 hours. Synthetic roman cements were prepared by mixing the pure chemicals at a dry state. (Tables I–III). The refference sample was prepared in the same way from natural raw material from Kurovice quarry.

The results of masurment of hydratation heat are stated in Table IV.

Conclusions

It can be assumed, that the enthalpiometric determination is appropriate method for hydration heat measurement for roman cements as well as for other hydraulic binders. Mainly the easy intrumentation and short measurement times can be pointed out.

Also it was found, that roman cements prepared from natural raw material have the hydration heat values significantly lower than those prepared from pure chemicals. The reason for this is that the silicon oxide in pure state does not likely react with calcite to form dicalcium silicite and the soft lime is formed, which releases large amount of heat when hydrating.

This work has been supported by NPV II program MŠMT ČR project number 2B08024.

P16 DETERMINATION OF PORTLAND CEMENT COMPOSITION BY FT-IR SPECTROSCOPY

TOMÁŠ OPRAVIL, PETR PTÁČEK, JAROMÍR HAVLICA and FRANTIŠEK ŠOUKAL
Institute of Materials Chemistry, Brno University of Technology, Purkyňova 118, 612 00, Czech Republic, opravil@fch.vutbr.cz

Introduction

Cements show variable and sometimes unpredictable hydration behavior which may sometimes leads to operation failures. The rapid and accurate characterization method for identification of clinker and accessory minerals is needed. These requirements are for the Fourier transform infrared (FT-IR) spectroscopy fulfilled. The infrared spectrum provides informative signature of cement, in which is encoded information about its elemental and mineralogical composition. FT-IR methods can be in cement chemistry used for monitoring of hydration reactions and prediction of the performance properties[1,2].

The Portland cement composition was studied by mid-IR spectroscopy. This work is a part of wider FT-IR study about course hydrolysis of clinker minerals and kinetic of hydration processes of in aged Portland cement paste.

Experimental

The Portland cement was used in this study. The sample was characterized in wavelengths range from 4,000 to 400 cm^{-1} by FT-IR analyzer Nicolet Imact 400 with using of KBr pellets technique. Applied resolution for measurements is 8 cm^{-1}.

Dried samples were mixed with KBr with mass ratio 1 : 100. Mixtures were homogenized by grinding in mortar dish. Weighted amount of these mixtures were pressed under 40 kPa for 20 s and next 80 kPa for 30 s.

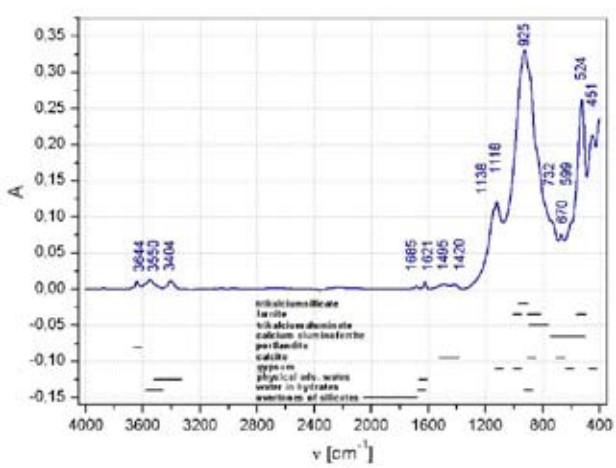

Fig. 1. **Subtracted infrared spectrum of Portland cement and correlation table. The Si–O stretch region was fitted by Lorentz function**

Results

Infrared spectrum of Portland cement is shown on Fig. 1. There were identified absorbtion bands of several clinker minerals relevant to its technical phase: allite – tricalcium-silicate (C_2S), belite – larnite (C_2S) and C_3A – tricalcium-aluminate. Further are present spectral bands of anhydrite ($CaSO_4$), gypsum ($CaSO_4 \cdot 2H_2O$) and hydration product: portlandite, calcite and hexagonal hydrates. Presence of the clinker minerals hydration products indicate that sample was slightly hydrated by air humidity.

From data published in literature[1,3–7] we put together correlation table (Fig. 1.). Portland cement IR bands assignment is summarized in Table I.

Table I
FT-IR spectrum of Portland cement

ν [cm^{-1}]	peak's assignment	compound
3,644	ν(OH)	portlandite
3,550	ν(OH)	water (silanol groups)
3,404	ν_1(OH)	water (adsorbed on the surface)
1,685	ν_2(OH)	water (hydrates)
1,621	ν_2(OH)	water (adsorbed on the surface)
1,495, 1,420	$\nu_3(CO_3^{2-})$	calcite
1,138	$\nu_3(SO_4^{2-})$	anhydrite
1,118	$\nu_3(SO_4^{2-})$	gypsum
925	$\nu_3(SiO_4^{4-})$	tricalciumsilicate (C_3S)
732	$\nu_4(CO_3^{2-})$	calcite
670, 599	$\nu_4(SO_4^{2-})$	gypsum
524	$\nu_4(SiO_4^{4-})$	larnite (C_2S)
451	$\nu_2(SO_4^{2-})$	gypsum

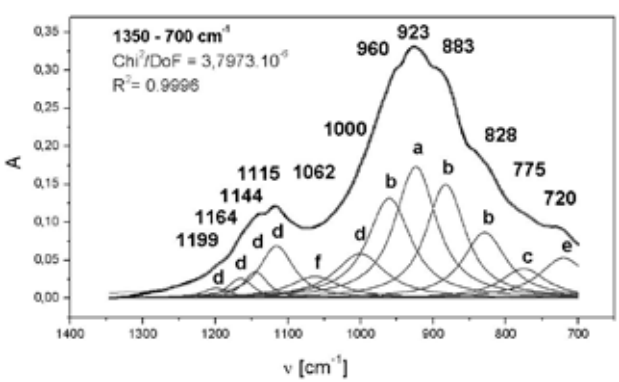

Fig. 2. **IR spectra region from 1,350 to 700 cm^{-1} fitted by Lorentz function. Peaks assignment is noted in Table II**

The peak belongs to stretching of Si–O bond in structure of C_3S, which is centered at wavelength 925 cm^{-1}, implies band complexity. This multiplet was fitted by Lorentz function (1) due to obtain other information about composition of the sample.

$$y = y_0 + \frac{2A}{\pi} \frac{w}{4(x - x_c)^2 + w^2}, \quad (1)$$

where y_0 is offset, x_c is wavelength of peak's center, w is peak's half-width and A is amplitude of peak.

Fitted spectrum of the Portland cement is shown on Fig. 2. There were found absorbtion bands of anhydite, gypsum, larnite, C_2S, C_3S and calcite. Cement IR bands assignment is summarized in Table II.

Table II
Fitted FT-IR spectrum of Portland cement

ν[cm^{-1}]	peak's assignment	compound
1,199	ν_3, $b_1(SO_4^{2-})$	
1,164	ν_3, $a_1(SO_4^{2-})$	anhydrite
1,144	ν_3, $a_2(SO_4^{2-})$	
1,115	$\nu_3(SO_4^{2-})$	gypsum
1,062	ν(Al–O)	hexagonal hydrates
1,000	$\nu_1(SO_4^{2-})$	anhydrite
960, 883	$\nu_3(SiO_4^{4-})$	larnite (C_2S)
923	$\nu_3(SiO_4^{4-})$	tricalciumsilicate (C_3S)
828	$\nu_1(SiO_4^{4-})$	larnite (C_2S)
775	ν(Al–O)	tricalciumaluminate
720	$\nu_4(CO_3^{2-})$	calcite

Conclusions

The Fourier transform infrared spectroscopy is a suitable tool for determination of cement phase composition, because enable monitored course of hydration processes by changes of spectroscopic variables (ν, w and A) in the time. These parameters may provide secondary information about changes in the sample.

Main absorbtion area of clinker minerals is spread over spectral region from 1,000 to 400 cm^{-1}. Peaks coincidence make interpretation of spectrum more difficult, but is possible distinguished of individual peaks.

Amount of spectral bands in hydrated or partially hydrated cement has increasing due to intermolecular interaction of cations with SO_4^{2-} and CO_3^{2-} anions leading to reduction of their symmetry.

This work has been supported by MŠMT poject NPV – NHV – 1 number 2B08024.

REFERENCES

1. Hughes L. T., Methven M. C., Jones J. G. T., Pelham E. S., Fletcher P., Hall Ch.: Adv. Cem. Based Mater. *2*, 91 (1995).
2. Mueller J. H., Freeman D.: Mater. Charact. *35*, 113 (1995).
3. Papoušek D., Horák M., *Infračervená spektra a struktura molekul*, Academica, Praha 1976.
5. Mollah A. Y. M., Kesmez M., Cocke D.: Sci. Total Environ. *325*, 255 (2004).
6. Smith H. D., Seshadri S. K.: Spectrochim. Acta Part A 55, 795 (1999).
7. Trezza A. M., Lavat E. A.: Cem. Concr. Res. *31*, 869 (2001).

P17 THERMAL BEHAVIOR OF POWDER PRECURSOR FOR LAS CERAMIC DOPED BY HYDROXYAPATITE

PETR PTÁČEK, HELENA KREJČOVÁ, JAROMÍR HAVLICA, FRANTIŠEK ŠOUKAL and TOMÁŠ OPRAVIL

Institute of Materials Chemistry, Brno University of Technology, Purkyňova 118, 612 00, Czech Republic, ptacek@fch.vutbr.cz

Introduction

The performance of precision devices and instruments has been limited by the problem of thermal stress induced by the thermal expansion between different materials. To avoid this problem, one of the choices is to develop negative thermal expansion materials[1]. It has been known that thermal shock resistance of ceramics is influenced by the thermal expansion coefficient[2]. LAS ($Li_2O \cdot Al_2O_3 \cdot SiO_2$) system has been investigated extensively, because its show low, zero or even negative thermal expansion coefficient as well as high thermal shock resistance[3].

The most important crystaline phases present in the LAS system are β-eucryptite ($Li_2O \cdot Al_2O_3 \cdot SiO_2$), β-spodumene ($Li_2O \cdot Al_2O_3 \cdot 4SiO_2$), virgilite ($Li_2O \cdot Al_2O_3 \cdot 6SiO_2$), petalite ($Li_2O \cdot Al_2O_3 \cdot 8SiO_2$) as well as metastable solid solutions that are derived from the hexagonal high quartz structures by the substitution of Al^{3+} and Li^+ for Si^{4+}. These solid solutions are denoted as β-quartz (ss) and have general composition $Li_2O \cdot Al_2O_3 \cdot nSiO_2$, where n varies from 2 to 10(ref.[2]).

There are many methods to prepare ultra-fine powders for synthesis of LAS ceramic or glass-ceramic. The conventional method is melt processing, which has many problems, such as too high melting temperature and high viscosity of melt. Lately, sol-gel processing has been widely used in the manufacture of LAS. This method reduces the sintering temperature and can obtain high purity and homogenous products.[4–6]

The present study on the LAS ceramic based on spodumene is mainly concentrated to investigation of influence of $Ca_2(PO_4)_3OH$ on thermal behavior of sol-gel derived precursor. Processes whose take place during thermal treatment were analyzed by DTA and heating microscopy.

Experimental

The β-spodumene powder precursor was prepared from Li_2OH, $Al(NO_3)_3 \cdot 9H_2O$, both in analytical purity grade. Silica sol containing 30 % wt. of SiO_2 (Tosil) was applied as source of SiO_2. A weighed quantities of lithium carbonate and $Al(NO_3)_3 \cdot 9H_2O$ were first dissolved in hydrochloric acid and Tosil, respectively.

Both prepared solutions were next slowly mixed together. Resulting sol contain LiCl, $Al(NO_3)_3 \cdot 9H_2O$ and SiO_2 in weight ratio 1 : 1.77 : 1.89 that is equal to spodumene composition. The gelation of mixed sol at 80 °C took place after 20 min. The resulted gel was dried at 105 °C for 24 h. Powder LAS ceramic precursor was prepared by calcination and subsequent milling of grinded xerogel at 750 °C for 2 h.

The powder precursor was next doped with 0.25, 0.50, 0.75 and 1.00 % wt. hydroxyapatite ($Ca_5(PO_4)_3OH$) working as sintering additive (agent of mineralization).

D i f f e r e n t i a l T h e r m a l A n a l y s i s

The DTA analysis of the $Ca_5(PO_4)_3OH$ doped powder precursor in an air oven at ambient atmospheric condition was carried out by TG-DTA Analyzer Setaram 92-18 up to temperature 1,400 °C. Applied heating and cooling rate was 10 °C min^{-1}.

H e a t i n g M i c r o s c o p y

Test piece (cube, a = 3 mm) was prepared by pressing of precursor and hydroxyapatite mixture under pressure 1 MPa. Sample was heated in an air oven at ambient atmospheric condition up to sample melting temperature at heating rate 10 °C min^{-1}.

Results

D i f e r e n t i a l T h e r m a l A n a l y s i s

Fig. 1. shows the DTA curves of powder precursor with hydroxyapatite content from zero to 1 % wt.. The endothermic peak at temperature about 1,360–70 °C belong to melting of sample. Peak shape and temperature (T_m) depend on concentration of $Ca_5(PO_4)_3OH$.

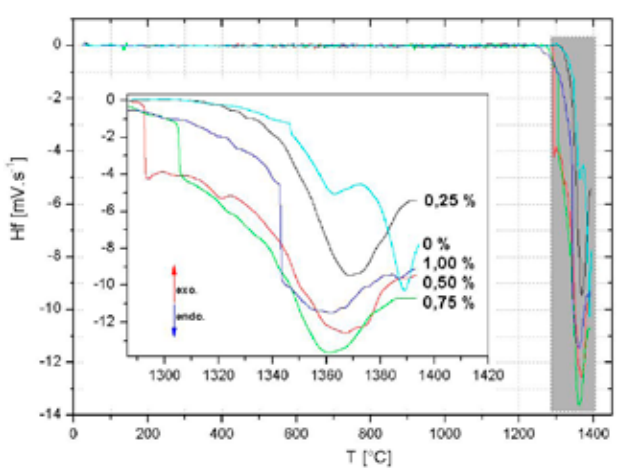

Fig. 1. **Heating step of DTA of the LAS powder precursor with 0, 0.25, 0.50, 0.75 and 1.00 % wt. $Ca_5(PO_4)_3OH$**

The values of melting temperature, that are found for individual samples is shown in Table I. This table further contains the peaks temperature shift against system without additive (ΔT).

Table I

The DTA curves of cooled powder precursor with hydroxyapatite are shown on Fig. 2. Only one exotherm was observed in each curve. This peak is associated to crystallization of glass (T_k).

Table I
Temperature of melting of LAS ceramic (T_m) and peak shift (ΔT) for different $Ca_5(PO_4)_3OH$ content. Significat correlation coeficien (R) level is typed bold

$Ca_5(PO_4)_3OH$ [%]	T_m [°C]	ΔT [°C]
0	1,388.9	–
0.25	1,368.6	–20.3
0.50	1,367.0	–21.9
0.75	1,361.1	–27.8
1.00	1,359.8	–29.1
R	–0.888	

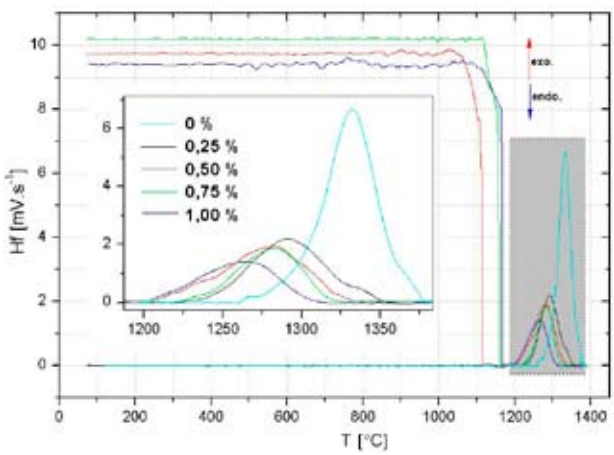

Fig. 2. **Cooling step of DTA of the LAS powder precursor with 0, 0.25, 0.50, 0.75 and 1.00 % wt. $Ca_5(PO_4)_3OH$**

The values of crystallization temperature, that are found for individual samples is shown in Table II. This table further contains shift of peaks temperature against crystallization in pure LAS system (ΔT).

Table II
Crystallization peaks temperature and peak shift (ΔT) for different $Ca_5(PO_4)_3OH$ content. Significant correlation coefficient (R) level is typed bold

$Ca_5(PO_4)_3OH$ [%]	T_k [°C]	ΔT [°C]
0	1,333.1	–
0.25	1,290.8	–42.3
0.50	1,279.8	–53.3
0.75	1,281.2	–51.9
1.00	1,267.0	–66.1
R	–0.885	

The shift of baseline, which takes place in samples with hydroxyapatite content equal and higher than 0.25 % wt. was recognized as high quartz solid solution phase separation. The found values are listed in Table III.

Table III
The phase separation temperature for different $Ca_5(PO_4)_3OH$ content in heating ($T_{g,1}$) and cooling ($T_{g,2}$) step

$Ca_5(PO_4)_3OH$ [%]	$T_{g,1}$ [°C]	$T_{g,2}$ [°C]
0	–	–
0.25	–	–
0.50	1,292.9	1,113.7
0.75	1,305.4	1,158.0
1.00	1,343.3	1,166.6

Heating Microscopy

The dependences of test piece on temperature were shown on Fig. 3. Height of sample without agent of mineralization has been decreased about 9.5 % on temperature interval 600–810 °C due to formation of β-spodumene. This process begin at higher temperature if samples containing the $Ca_5(PO_4)_3OH$.

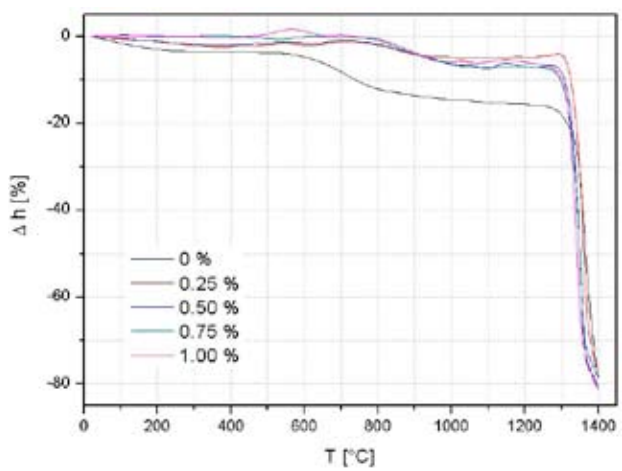

Fig. 3. **Heat microscopy of the LAS powder precursor with 0, 0.25, 0.50, 0.75 and 1.00 % wt. $Ca_5(PO_4)_3OH$**

The influence of hydroxyapatite concentration in sample on spodumene formation interval and sample melting temperature is shown in Table IV.

Photos for significant temperatures, whose were taken during thermal treatment of sample placed in heat microscope furnace are shown on Fig. 4.

Influence of $Ca_5(PO_4)_3OH$ content on temperature
Table IV
Temperature synthesis of spodumene (T_s) and melting of sample (T_m). Significant correlation coefficient (R) level is typed bold

$Ca_5(PO_4)_3OH$ [%]	T_s [°C]	T_m [°C]
0	600–805	1,335.5
0.25	792–918	1,337.0
0.50	767–1,016	1,325.2
0.75	789–997	1,325.2
1.00	789–957	1,316.1
R		–0.933

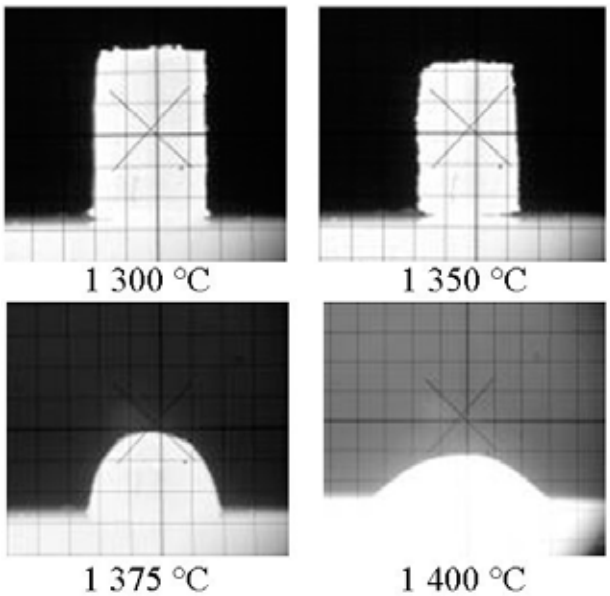

Fig. 4. **Picture of powder precursor test peace at temperature of sintering, deformation, hemisphere and pouring**

of sintering, deformation, hemisphere a pouring of melt is shown in Table V.

Conclusions

Table V
The significant thermal points of fired LAS powder precursor with different $Ca_5(PO_4)_3OH$ content

$Ca_5(PO_4)_3OH$ [%]	Sintering [°C]	Deformation [°C]
0	1,300	1,350
0.25	1,325	1,350
0.50	1,300	1,325
0.75	1,300	1,325
1.00	1,250	1,300
$Ca_5(PO_4)_3OH$ [%]	Hemisphere [°C]	Pouring [°C]
0	1,375	1,400
0.25	1,360	1,380
0.50	1,350	1,370
0.75	1,350	1,370
1.00	1,350	1,360

In presence of hydroxyapatite is spodumene stabilized in solid solution with β-SiO_2 (ss) and melting was changed from incongruent to congruent. In range from 0 to 1.0 % wt. of $Ca_5(PO_4)_3OH$ content has been melting temperature fall about 29.1 °C.

Solid solution immiscibility process was proceed in samples with $Ca_5(PO_4)_3OH$ concentration 0.50 % wt. and higher. Temperature of process has been increased with content of hydroxyapatite.

Temperature of sample melting and β-SiO_2 (ss) precipitation has been decreased with increasing content of hydroxyapatite.

In presence of hydroxyapatite in the sample, the temperature of the β-spodumene formation was shifted to higher temperature. Temperature of β-spodumene was average increased about 184 ± 6 °C.

Significant negative correlation of melting temperature on hydroxyapatite content in the sample was found by heating microscopy. In range from 0 to 1.0 % wt. can by this relationship expressed as:

$$T_m = 1337.9 - 20.24\, w_{(Ca_5(PO_4)_3OH)} . \quad (1)$$

Significant thermal points, i.e. temperature of sintering, deformation, hemisphere and melting, has generally decreased in presence of $Ca_5(PO_4)_3OH$.

This work has been supported by MŠMT poject NPV – NHV – 1 number 2B08024.

REFERENCES

1. Sheu G. J., Chen J. C., Shiu J. Y., Hu C.: Scr. Mater. *53*, 577 (2005).
2. Mandal S., Chakrabarti S., Das S. K., Ghatak S.: Ceram. Int. *33*, 123 (2007).
3. Guo X., Yang H., Han Ch., Song F.: Thermochim. Acta *444*, 201 (2004).
4. Wu S., Liu Y., He L., Wang F.: Mat. Lett. *58*, 2772 (2004).
5. Chatterjee M., Naskar N. K., Ceram. Int. *32*, 623 (2006).
6. Amini M. M., Mehraban Z., Sabounchei S. J. S., Mater. Chem. Phys. *78*, 81 (2002).

P18 SYNTHESIS AND CATALYTIC ACTIVITY OF TITANIA – KAOLINE SYSTEM

PETR PTÁČEK, MICHAL FIALA, JAROMÍR HAVLICA, FRANTIŠEK ŠOUKAL and TOMÁŠ OPRAVIL
Institute of Materials Chemistry, Brno University of Technology, Purkyňova 118, 612 00, Czech Republic, ptacek@fch.vutbr.cz

Introduction

Heterogeneous catalysis is the most promising technology for the reduction of environmental pollution in soil, air and water. The pillared clays (PILCs) are an interesting group of microporous materials, because they combined catalytic activity, porous structure and surface acidity. The PILCs have great potential either as support or directly as catalyst. Pillared clays were prepared by calcination of intercalate of clay minerals (smectite and mica group) with polynuclear metal cation. Specific surface are higher than 300 $m^2 g^{-1}$.[1–5]

Generally is the synthesis of TILCs with well defined bidimensional zeolite structure and good thermal stability difficult, because obtaining of adequate polymeric cationic species depends on several related parameters. The bes results were reached by acidic (HCl, H_2SO_4...) hydrolysis of $TiCl_4$ or $Ti(OC_3H_7)_4$ (TTIP)[2].

Interlayer surface of TiO_2 pillared montmorillonite is hydrophobic and that hydrophobic interaction between adsorbate and interlayer surface of the pillared clay is one of the most predominant factors in adsorption of various organic compounds. Surface hydrophobicity of TiO_2 pillared clay has been increasing in the order saponite < fluorine hectorite < montmorillonite < fluorine mica[3].

The aim of this work is preparation, characterization and study of the efficiency of the Na-kaolin/TiO_2 and metakaolin/TiO_2 catalysts. The catalytic performance was compared with pure Na-kaolin. Simultaneous TG-DTA (TG-DTA Analyzer Setaram 92-18), infrared spectroscopy (FT-IR Analyzer Nicolet Impact 400), X-ray diffraction (Difractometer X´Pert Philips) were used for investigation of prepared samples.

Experimental

Washed kaolin Sedlec Ia produced by Sedlecký kaolin a.s. was used for sample preparation. Content of kaolin is higher than 90 % wt. with equivalent diameter grain median in range 1.2–1.4 μm. The main impurities are mica group minerals and quartz. The content of colorant oxides – hematite (α-Fe_2O_3) and tetragonal TiO_2 (rutile), is lower than 0.85 and 0.2 % wt., respectively.

Two kinds of catalyst were prepared by hydrolysis of $TiCl_4$ in 30 % wt. aqueous suspension of washed Na-kaolin:

- kaolin/TiO_2,
- metakaolin/TiO_2

Titanium tetrachloride was introduced in to stirred suspension in the flow of carrier gas (argon) at laboratory temperature for 30 min. The suspension was deposit on the surface of substrate – glass balls with diameter about 5 mm. Film on the glass support was solidified by drying at laboratory temperature for 24 h. Metakaolin/TiO_2 type sample was still calcined at 600 °C for 2 h. Purely kaolin deposited on the glass support surface was used as standard.

Catalytic performance of prepared catalysts was examined on flow reactor in temperature range from 100 to 400 °C. The ordering of experiment is shown on Fig. 1. Ethanol vapor was flow (1.48 mol min^{-1}) through heated catalyst in the flow of carrier gas (12.85 cm^3 min^{-1}). In periodic interval was into reactor introduced oxygen from 356.4 cm^3 stack pressurized to 700 mbar. Concentration of oxygen in reactor leaving gas was measured by oxymeter.

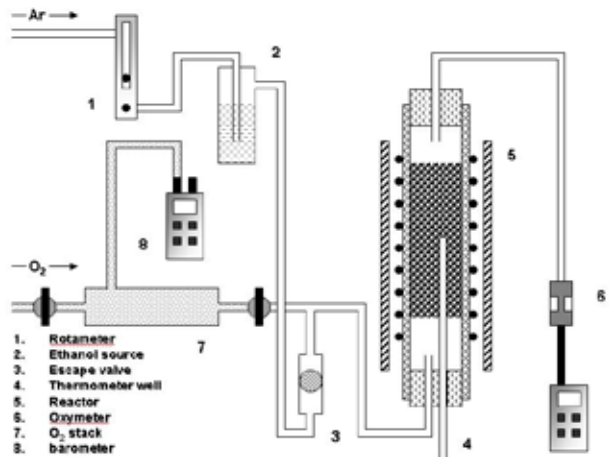

Fig. 1. **Schematic representation of the apparatus for investigation of catalytic performance**

Relative degree of conversion (α_r) and extend of reaction (ξ_r) were evaluated as follow:

$$\alpha_r = \frac{A_K - A_{KT}}{A_K}, \quad (1)$$

$$\xi_r = -\frac{A_{KT} - A_K}{3}, \quad (2)$$

There A_K and A_{KT} are peaks area obtained for pure kaolin and kaolin (metakaolin)/TiO_2 catalyst, respectively. The denominator value in (2) is equal to stoicheiometric coefficient of ethanol ($\nu_{O2} = -3$) in reaction:

$$C_2H_5OH + 3O_2 \rightarrow 2CO_2 + 3H_2O \quad (3)$$

Values of α_r and ξ_r can be converting according to (4).

$$A_K \alpha_r = 3\xi_r \quad (4)$$

Results

Thermal Analysis

TG-DTA experiments results is shown on Fig. 2. There are endothermic peak at 525 °C accompanied with sample mass decrease about 8 % wt. and exothermic peak at 984 °C. Any changes takes place at this temperature.

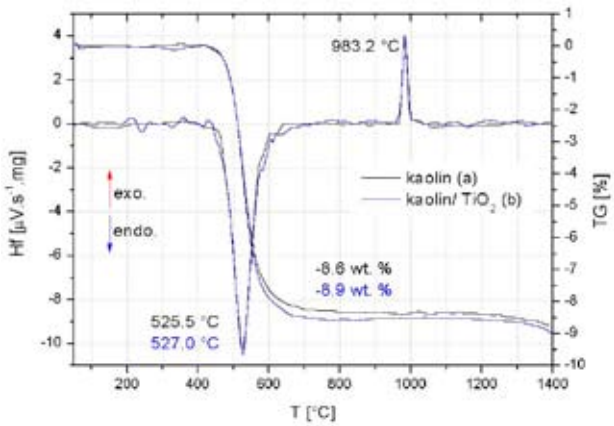

Fig. 2. **TG-DTA of kaolin (a) and kaolin/TiO_2 catalyst (b)**

Endoterm belong to course of dehydroxylation process of kaolin to metakaolin. Cubic phase formation – spinel phase ($2Al_2O_3 \cdot 3SiO_2$) or γ-Al_2O_3, is on the contrary exothermic process.

Infrared Spectroscopy

Fig. 3. show FT-IR spectrum of kaolin/TiO_2 and metakaolin/TiO_2 catalyst. The bands located at wavelengths 3,696, 3,673, 3,652 and 3,619 cm^{-1} are ν_1, ν_2, ν_3 and ν_4 stretching of O–H bonds in outer (ν_{1-3}) and inner hydroxyl groups (ν_4) of kaolinite. Bending and translation modes of these groups are appeared at 939, 912 and 791, 754 cm^{-1}, respectively.

The broad band centered at 3,440 cm^{-1} and band located at 1,634 cm^{-1} belongs to O–H bond stretching and bending of surface adsorbed water molecules, respectively. Bands at 1,115, 1,032 and 1,007 cm^{-1} are stretching, symmetric and asymmetric stretching of Si–(apical)O and Si–O–Si, respectively. Bending vibration is appearing at 421 cm^{-1}. The Si–O–Al and Al–O out of plane deformation shows the band at wavelengths 536 and 496 cm^{-1}, respectively.

The calcination leads to dehydroxylation of kaolinite and product of $TiCl_4$ hydrolysis – $TiO(OH)_2$. Sample may also contain a small amount of $TiOCl_2$. The O-H bands were almost disappeared during this process, but small amount of "residual hydroxyl groups" is still present. The Si–O bond stretching and bending modes show lose of his selectivity.

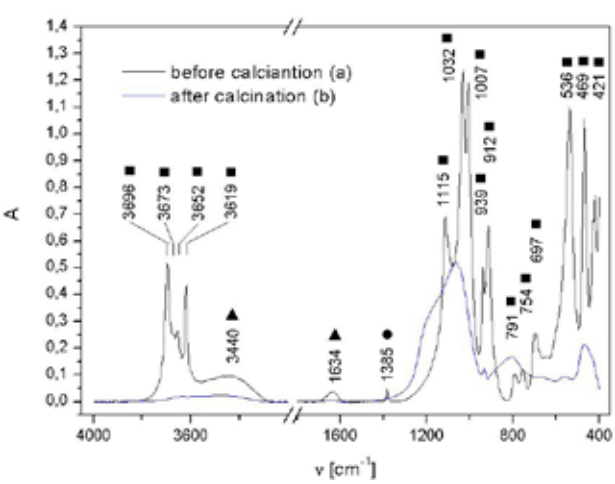

Fig. 3. **Baseline corrected infrared spectrum of kaolin/TiO_2 (a) and metakaolin/TiO_2 catalyst (b): ■ kaolinite bands, ● product of hydrolysis of $TiCl_4$, ▲ molecules of surface adsorbed water**

X-ray Diffraction

The XRD patterns on Fig. 3.(a) show intensities of kaolinite and other component of applied kaolin Sedlec Ia – montmorillonite, hematite and quartz. Anatase was formed via titanium tetrachloride hydrolysis. Metakaolin is amorphous and diffractions related to kaolinite were disappeared after sample calcination (b).

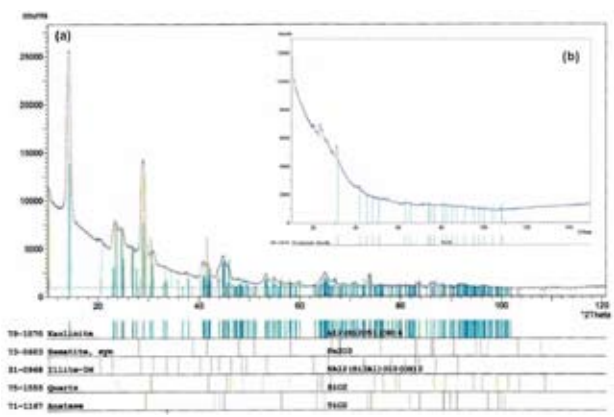

Fig. 4. **Powder XRD patterns of the kaolin/TiO_2 catalyst before (a) and after calcination (b)**

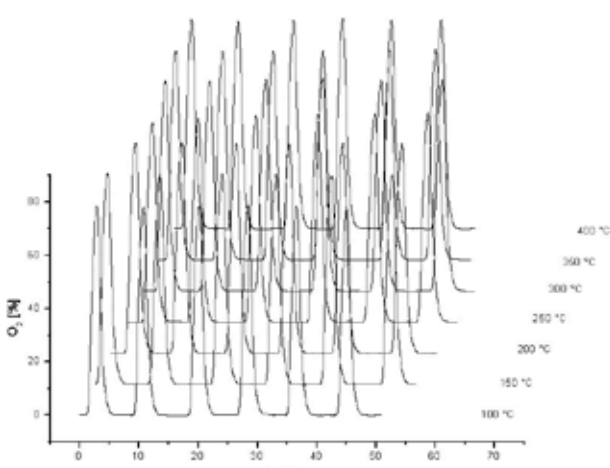

Fig. 5: **Results obtained for kaolin Sedlec Ia**

C a t a l y t i c P e r f o r m a n c e

Recorded data about answer of catalyst on oxygen "pulse" is for kaolin shown on Fig. 5. Individual peaks were next integrated due to determination of their area, height and width. Results obtained for kaolin is of Fig. 6. Analogical procedures were applied on kaolin or metakaolin/TiO_2 catalyst.

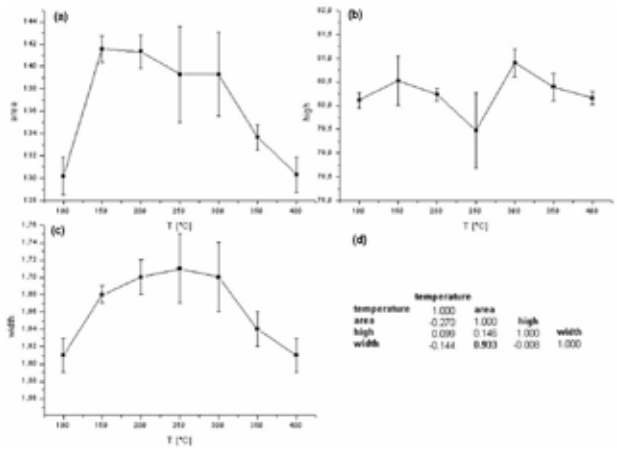

Fig. 6. **Changes of oxygen peaks parameters with temperature for kaolin Sedlec Ia: area (a), height (b) and width (c). Correlation matrix is shown on (d). Significant correlation level is typed by bold**

Catalytic performance results obtained for kaolin/TiO_2 system is shown on Fig. 7. The process is strongly influenced by thermal behavior of product of $TiCl_4$ hydrolysis. Water evolving during dehydroxylation process was influenced of specific surface of catalyst and partial water vapor pressure (p_{H2O}) over sample. Exchange adsorption of ethanol on the internal catalyst surface is influenced by p_{H2O} value.

Temperature dependence of relative degree of conversion (α_r) and extend of reaction (ξ_r) are plotted on Fig. 9.(a) and (b). The best results were found for 300 °C.

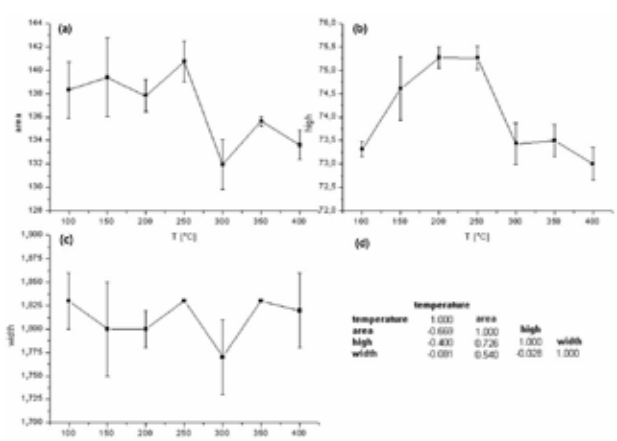

Fig. 7. **Changes of oxygen peaks parameters with temperature for kaolin/TiO_2 system: area (a), height (b) and width (c). Correlation matrix is shown on (d)**

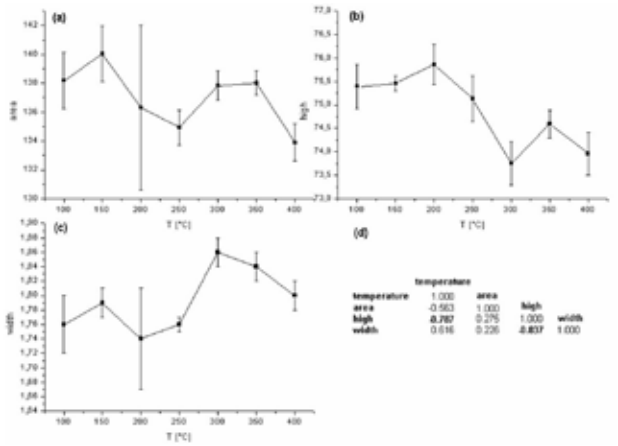

Fig. 8. **Changes of oxygen peaks parameters with temperature for metakaolin/TiO_2 system: area (a), height (b) and width (c). Correlation matrix is shown on (d). Significant correlation level is typed by bold.**

Result obtained for metakaolin/TiO_2 system is shown on Fig.8 and temperature dependence of α_r and ξ_r are plotted on Fig. 9(c) and (d).

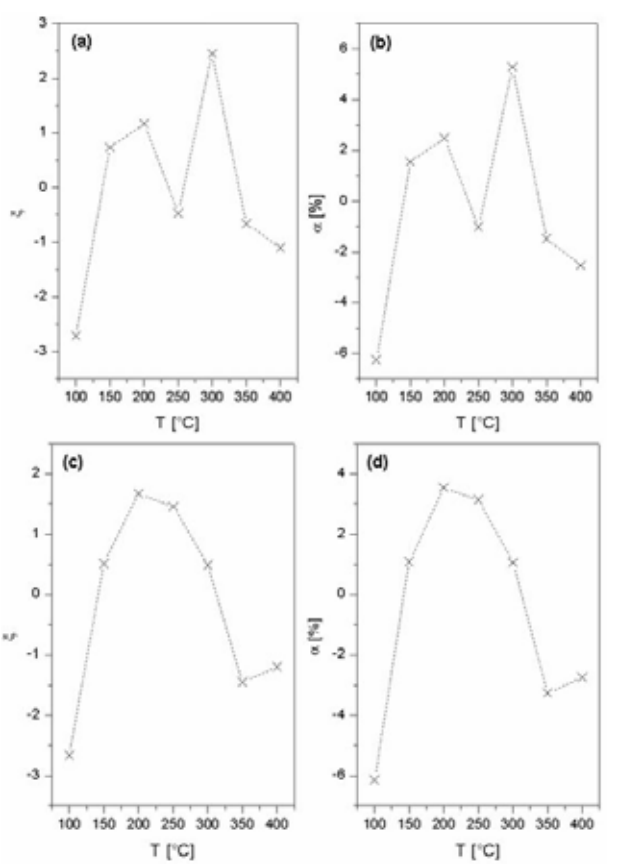

Fig. 9. **Temperature dependences of relative degree of conversion (α_r) and extend of reaction (ξ_r)**

Conclusions

The $TiCl_4$ hydrolysis product shows any significant influence on the results of TG-DTA experiment. Dehydroxylation peak was slightly increased about 2.5 °C. Temperature formation of cubic phase isn't influenced.

Peaks height and width must depend of specific surface of catalytic system. While value of the first parameter has decreased with growth of specific surface, the second has increased.

Area of peak is directly proportional to amount of moles of oxygen. The minimum values of α_r was found for kaolin/TiO_2 catalyst at 250 °C, due to course of $TiO(OH)_2$ dehydroxylation.

High p_{H2O} value makes adsorption of ethanol on the catalyst surface more difficult. Temperature 300 °C show the best catalytic performance, because dehydroxylation of $TiO(OH)_2$ be on the wane and kaolinite dehydroxylation doesn't proceed till this time.

The metakaolin/TiO_2 catalyst show higher catalytic performance than kaolin on temperature interval from 350 to 350 °C. Dehydroxylation has in general negative influence on catalytic performance, because this process leads to specific surface reduction.

This work has been supported by MŠMT poject NPV – NHV – 1 number 2B08024.

REFERENCES

1. Ding Z., Zhu Y., Greenfield P. F., Lu Q. G.: J. Colloid Interface Sci. *238*, 267 (2001).
2. Boudali K. L., Ghorbel A., Tichit D., Chiche B., Dutartre R., Figueas F.: Microporous Mater. *2*, 525 (1994).
3. Ooka Ch., Yoshida H., Suzuki K., Hattori T.: Microporous Mesoporous Mater. *67*, 143 (2004).
4. Pernyeszi T., Dékány I.: Colloids Surf., A *230*, 191 (2004).
5. Belessi V., Lambropoulou D., Konstantinou I., Katsoulidis A., Pomonis P., Petridis D., Albanis T.: Appl. Catal., B *73*, 292 (2007).

P19 DEPOSITION OF THE TiO_2 ON A GLASS AND CERAMICS SURFACE

ALENA RUTTEOVÁ, PETR PTÁČEK and JAROMÍR HAVLICA
Institute of Material Chemistry, Brno University of Technology, Purkynova 118, 62100 Brno, Czech Republic, xcrutteova@fch.vutbr.cz

Introduction

Photocatalysis has recently become a common word and various products using photocatalytic functions have been commercialized. Photocatalytical self cleaning surfaces offer many advantages in household, construction, industrial and medical sectors. Among many candidates for photocatalysts, TiO_2 is almost the only material suitable for industrial use at present and also probably in the future. This is because TiO_2 has the most efficient photoactivity, the highest stability and the lowest cost[1,2].

Experimental

Deposition of the TiO_2 on a glass and ceramics surface was provided by precipitation of gas phase at temperature of 22, 100, 200, 300, 400 and 500 °C for 3 hours (1). $TiCl_4$ (Lachema, p.a., in gaseous state) and water vapour in current of argon were leaded into tempered tube reactor within three supports (glass or ceramics). Flow rate of argon was regulated at 30 cm^3 min^{-1}. The ordering of experiment is schematically drawing in Fig. 1.

$$TiCl_{4\,(g)} + 2H_2O_{(g)} \rightarrow TiO_{2\,(s)} + 4HCl_{(g)} \qquad (1)$$

Surface of support was studied by the optical microscopy. The photos of TiO_2 layer were taken by Olympus BX 50F4.

Unprecipitated $TiCl_4$ went out from reactor at the temperature of 500 °C and hydrolyzed in water bath or Tosil (Koma, s.r.o., colloidal solution of SiO_2, 30 % wt. of SiO_2). Temperature of Tosil was 20, 40, 50 and 60 °C.

TiO_2 dispersion in water and SiO_2–TiO_2 hydrosol were analyzed by infrared spectroscopy (FT-IR spectroscope Nicolet Imapct 400), particulates size distribution (Zetasizer 3000HS), differential thermic analysis (TG-DTA Analyzer SETARAM 92–18) and X-rays diffraction.

Results

The morphological properties depend on temperature. Polycrystalline agglomerates arise from decreased temperatures whereas continuous layer come up from increased temperature. Further quality of substrate's surface proves on appearance deposit layer. Sintered corundum ceramics have much more active adsorptive centres (e.g. edges and tops of crystal).

Table I
Layers of TiO_2 on glass and ceramics support (place in the middle of tube reactor)

T [°C]	Glass support	Ceramics support
22	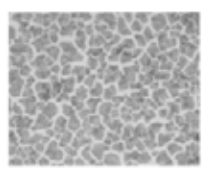	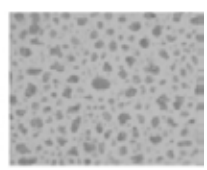
200	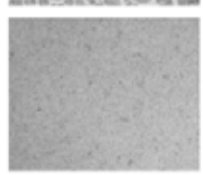	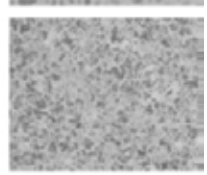
500	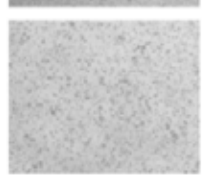	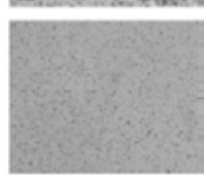

System which is created by hydrolysis $TiCl_4$ approaches monodispersive. It results from shape distribution curve (Fig. 2.). The fraction has major representation about 233.3 nm particles size and minor about 293.7 nm.

Distribution curves SiO_2–TiO_2 hydrosol indicate three peaks (Fig 3.). The first part shows SiO_2 particles size

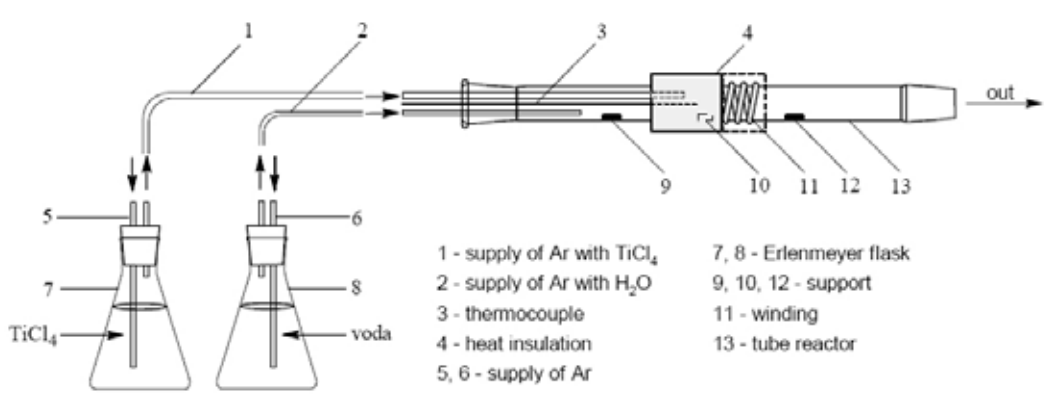

Fig. 1. **Ordering of the experiment**

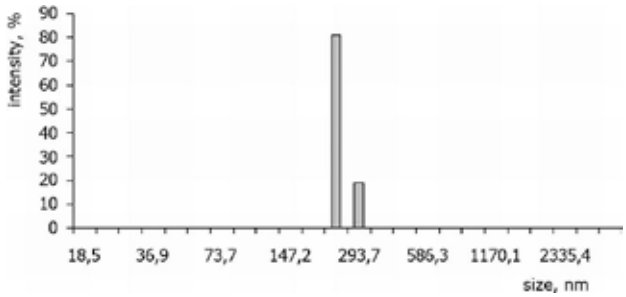

Fig. 2. **TiO_2 dispersion in water**

(Fig. 3. (a) peak 7.6 nm, (b) peak 7.1 nm), the most of TiO_2 particles are included in the second part (Fig. 3. (a) peak 121.1 nm, (b) peak 90 nm) and the third peak proves the particles coagulation.

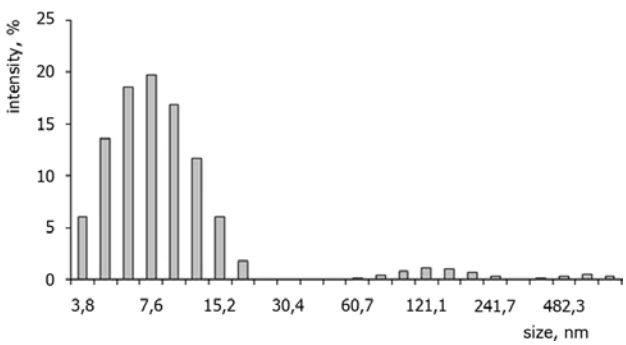

Fig. 3. **SiO_2–TiO_2 hydrosol prepared at 20 °C under ultrasound treatment**

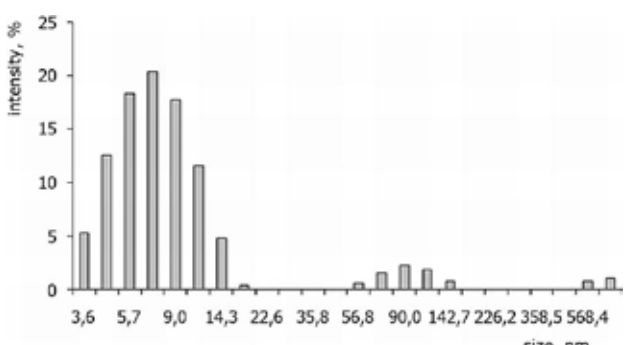

Fig. 4. **SiO_2–TiO_2 hydrosol prepared at 50 °C under ultrasound treatment**

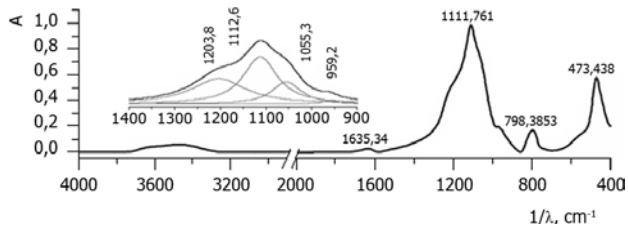

Fig. 5: **FT-IR SiO_2–TiO_2 hydrosol prepared at 20 °C**

Table II
Peaks assignment

T [°C]	20	Assignment
	1,203.8	δ(Ti–OH)
	1,112.6	ν(Si–O)
1/λ	1,055.3	ν(Si–OH)
[cm^{-1}]	959.2	ν_s(Si–O–Si)
	798.4	γ(Si–O–Si)
	473.4	δ(Si–O–Si)

The FT-IR spectrogram contains only absorption bands of silica (Fig 4.). Assign of recognized peaks are summarized in Table II.

Conclusions

The presented work compares TiO_2 layers on glass surface with layers on ceramics surface. Morphological characteristic TiO_2 layer is significantly influenced by temperature of deposition and substrates type. Smaller TiO_2 particles arise by hydrolysis $TiCl_4$ in Tosil than hydrolysis in water.

REFERENCES

1. Hashimoto K., Irie H., Fujishima A.: JSAP International *14*, 4 (2006). http://www.jsapi.jsap.or.jp/Pdf/Number 14/04_JJAP-IRP.pdf, download: 11.03.2007.
2. http://www.dyo.com.tr/uploads/yayinlar_ 082206163146_ yayinlar_08150683358_NEW.pdf, download: 11.03.2007.

P20 THE INFLUENCE OF P_2O_5 ON THE FORMATION OF PORTLAND CEMENT CLINKER

THEODOR STANĚK[a] and PETR SULOVSKÝ[b]
[a]*Research Institute of Building Materials, Hněvkovského 65, 617 00 Brno, Czech Republic,*
[b]*Department of Geological Sciences, Faculty of Science, Masaryk University, Kotlářská 2, 611 37 Brno, Czech Republic,*
stanek@vustah.cz

Introduction

The nature of the cement production process allows utilizing various secondary raw materials and wastes. One of such wastes is the meat and bone meal (MBM). This material, especially if coming from herds in which BSE-positive cows were identified, has to be liquidated by a high-temperature process. This can be done in incineration plants, but also in rotary cement kilns. The advantage of the latter is that MBM is utilized as a low-grade[1] fuel and at the same time it is degraded and the hazardous substances are liquidated, while its incombustible components are built in the clinker. The main problem is the relatively high P_2O_5 content, contained in the ash as calcium phosphate. P_2O_5 influences the properties of the clinker melt[2], enters the structure of clinker minerals, and influences the phase composition of clinker[3–5] and thus also the quality of cement[4,5]. So far, the common cement production practice is that only such amounts of MBM are combusted that do not adversely affect the clinker properties. Maximum safe amount is around 0.5 % wt.P_2O_5 in the clinker (only exceptionally more[6]). We assume that the study of reaction kinetics and of the phase changes in clinkers containing P_2O_5 will enable to produce clinker with much higher levels of this oxide without negative impact on clinker properties, along with discovering new findings on its influence on clinker minerals.

Methods and Results

The raw meal for laboratory experiments, prepared from common raw materials, was mixed to have the following basic chemical parameters: SLP = 98, Ms = 2.3 a Ma = 1.8. P_2O_5 was added to this basic raw meal in graded amounts of finely ground $Ca_3(PO_4)_2$ or ashed MBM.

The burning of these P_2O_5-enriched raw meals was performed in a superkantal oven in equilibrium- as well as non-equilibrium burning regime at 1,450 °C. Quantitative phase composition was determined by microscopic point counting[7] and the chemical composition of clinker minerals by spot microanalyses performed with electron microprobe CAMECA SX100 (accelerating voltage 15 kV, beam current 20 nA).

The results obtained with MBM ash were in equilibrium-burned clinkers very similar to those acquired with raw meals enriched with pure $Ca_3(PO_4)_2$. Incompletion of reactions in non-equilibrium burnings of raw meals blended with MBM ash leads to the increased volumes of the clinker melt, to incomplete consumption of free lime at low P_2O_5 contents in clinker, and to the increase of alite proportion in clinkers high in P_2O_5. The trend of the influence of P_2O_5 on the phase composition of clinker is nevertheless the same, with critical limit around 0.7 % wt. P_2O_5 in clinker, when the C_2S and free lime proportions start to enhance on the expense of C_3S (Fig. 1.).

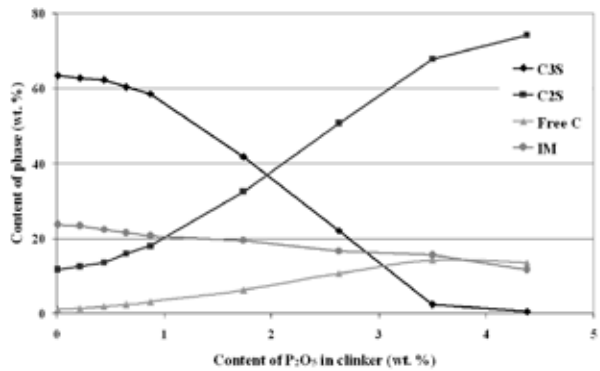

Fig. 1. **The influence of P_2O_5 content (added in the form of MBM ash) on the phase composition of non-equilibrium burned clinkers (IM – interstitial mass)**

The results of electron microanalysis indicate that both in alite and in belite the increase in P_2O_5 in clinker leads to the decrease of SiO_2, TiO_2 and MnO, and to an increase of P_2O_5, Al_2O_3, MgO, Na_2O, and K_2O. All minor oxides (besides MgO) are in belite present in higher levels than in alite.

An interesting finding ensued from the comparison of concentrations of P_2O_5 and Al_2O_3 (Fig. 2.). It occurs that P enters the structure of both clinker minerals at least partially through the so called berlinite substitution: $Al^{3+} + P^{5+} \leftrightarrow 2Si^{4+}$, where $AlPO_4$ (the berlinite component), isostructural with quartz, substitutes SiO_4 tetrahedrons. The berlinite substitution is the more important, the higher is the P_2O_5 content in clinker.

Based on the obtained results, experiments aimed on more detailed elucidation of the entry of P_2O_5 into clinker phases in the presence of Al_2O_3 were run. For the burning of clinkers without either Al_2O_3 or Fe_2O_3, raw meals were blended from pure components; the theoretical content of P_2O_5 in clinker was chosen to be 0, 1, 3 and 5 % wt. (added as $Ca_3(PO_4)_2$).

The phase composition of such equilibrium-burned clinkers without Al_2O_3 develops in relation to the P_2O_5 levels in a way similar to the common clinker with all four main oxides. The degree of alite conversion is anyway higher with increasing P_2O_5 content and as the Al_2O_3 is missing, the interstitial mass is formed above all by C_2F. In clinkers without Fe_2O_3 the evolution of phase composition is distinctly different. The alite proportion in these clinkers is at the same lime saturation lower, but the negative impact of P_2O_5 on alite formation manifests itself only at the theoretical content of 3 % wt. P_2O_5 in clinker; and at the content of 5 % wt., certain

small amount of alite still forms. Mutual comparison of alite contents in individual clinkers from all three series of experiments is shown on Fig. 3.

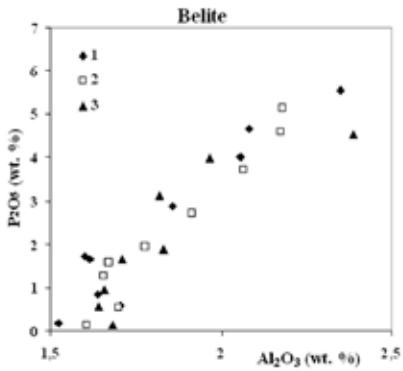

Fig. 2. **Relationship between average P_2O_5 and Al_2O_3 contents in belite. Each point represents an average of 15–20 spot analyses. (1 – non-equilibrium burning, MBM addition, 2 – equilibrium burning, MBM addition, 3 – equilibrium burning, MBM addition, C3P addition)**

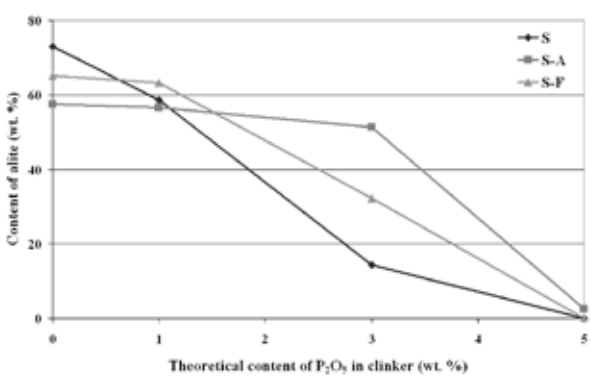

Fig. 3. **The dependence of alite content on the theoretical concentration of P_2O_5 in clinker (S – clinkers with 4 main oxides, S-A – clinkers without Fe_2O_3, S-F – clinkers without Al_2O_3)**

Discussion and Conclusions

The experiments have confirmed that P_2O_5 has distinctly negative impact on the nucleation of alite and that it stabilizes belite by entering the structure of C_2S, forming a solid solution with C_3P.

Starting from 0.7 % wt. P_2O_5 in the clinker, negative impact of P_2O_5 on the phase composition of clinker was observed, involving the increase of belite and free lime contents on the expense of alite. Even after four hours burning at 1,450 °C, which can be considered due to their length as equilibrium, with increasing P_2O_5 full reacting of free lime with belite to alite does not happen. 4.5 % wt. of P_2O_5 in clinker completely block the formation of alite. The result of P_2O_5 addition is similar to that of SO_3(ref.[8]), but the mechanism of their operation is most probably different.

Electron microanalysis documented distinctly increasing content of P_2O_5 in the structure of clinker silicates, above all of belite, with increasing bulk P_2O_5 content in clinker. It was found that P enters the structure of both clinker silicates partially by means of the berlinite substitution: $Al^{3+} + P^{5+} \leftrightarrow 2Si^{4+}$.

These findings led to experiments with clinker composed of only three main oxides, i.e. without either Al_2O_3 or without Fe_2O_3. It was found that the raw meal mix without Fe_2O_3, characteristic for clinkers used for production of white cement, to a certain extent eliminates the negative effect of P_2O_5 on the alite formation.

This article was worked out within the frame of Ministry of Industry and Trade of the Czech Republic project No. FT-TA3/026.

REFERENCES

1. Scheuer A.: Cem. Inter. *1*, 48 (2003).
2. Timashev V. V., Osokin A. P.: Cement *9*, 4 (1982).
3. Goetz-Neunhoeffer F., Neubauer J.: *Proceedings of 20th International Conference on Cement Microscopy*, (ICMA, ed.), p. 130. Guadalajara 1998.
4. Puntke S.: *Dissertation*. Technical University at Clausthal, Clausthal, Germany, 2004.
5. Gutt W., Smith M. A.: *Proceedings of 6th International Congress on the Chemistry of Cement*, (Boldyrev A.C., ed.), p. 115. Stroyizdat, Moscow 1974.
6. Martauz P., Strigáč J., Orság Z., Tiso I., Gach F., Ježo L., Ivanka V. (PCLA Corp): CZ 291729 B6.
7. Chromý S.: Silikáty *22*, 215 (1978).
8. Staněk T.: *Proceedings of conference CEMENT 2002*, (Kostka J., ed.), p. M1. Cemdesign, High Tatras 2002.

P22 THE STUDY OF COMPRESSIVE FLEXURAL STRENGTH OF HIGH PERFORMANCE CONCRETE (HPC) AS THE FUNCTION OF ITS COMPOSITION

PAVEL ŠILER, JOSEF KRÁTKÝ and PAVEL JEDLIČKA
Institute of Materials Science, Faculty of Chemismy, Brno University of Technology, Purkyňova 118, 612 00, Czech Republic,
siler@fch.vutbr.cz

Introduction

Lots of important material parameters of high performance concrete (HPC) can be improved by application of chemical modifying admixtures called superplasticizers (SP). Also the desired properties can be achieved by proper mixture design. This work is aimed at the study of the compressive and flexural strength of high performance concrete (HPC) as the function of its composition. The influence of the HPC composition on hydration process was observed by means of isoperbolic calorimetry.

Experimental

The mixtures composition was selected as the constitution of ordinary used HPC (Table I). Constituents used for HPC preparation were: white cement (A), silica fume (S), finely ground granulated blast furnace slag (VPS), finely ground silica (SUK), calcinated bauxite (B), polycarboxylate superplasticizer (SP) and water. The compressive and flexural strength of HPC prepared was measured after 28 day moist curing.

Table I
The constitution of mixtures

Number of mixture	A [g]	S [g]	B [g]	SUK [g]	VPS [g]	SP [g]	H_2O [g]
1	750	300	1,050	0	0	25	148
2	750	225	500	0	0	25	130
3	750	300	1,050	150	0	25	171.5
4	750	300	1,050	0	150	25	176
5	750	300	1,050	150	150	25	189
6	750	300	500	0	0	25	148
7	750	300	0	300	300	25	205
8	750	300	500	300	300	25	215
9	750	300	500	150	150	25	180
10	750	300	500	300	300	25	220
11	750	150	0	150	150	25	169.5
12	750	150	500	0	0	25	110
13	750	0	500	0	0	25	176.5
14	750	300	0	0	0	25	130
15	750	0	0	300	0	25	173
16	750	0	0	0	300	25	207
17	750	0	500	150	0	25	172
18	750	0	500	0	150	25	175

The influence of HPC composition on hydration process was observed by means of isoperbolic calorimetry. From obtained calorimetric curves, the maximal achieved temperature and time from mixing to reaching this temperature was evaluated.

Results

The controlling samples of cement and one constituent studied was prepared. Flexural strength of these mixtures decreased in the following sequence: silica fume > SUK > VPS > bauxite and compressive strength in this sequence: silica fume > VPS > SUK > bauxite.

From mixtures prepared by combination of selected components, the highest strength was measured in mixtures

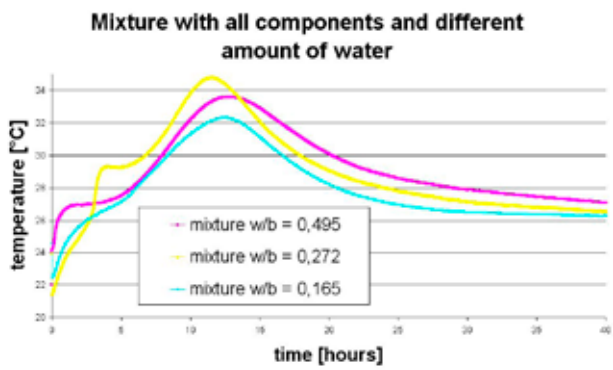

Fig. 1. **Influence of water to binder ratio on temperature changes**

Table II
The constitution of mixtures

Number of mixture	Max. temperature [°C]	Time of max temperature [hours]	Flexural strength [MPa]	Compressive strength [MPa]
1	32.35	12.54	18.87	154.40
2	36.11	10.65	19.66	146.80
3	33.64	11.58	22.76	160.30
4	31.81	10.59	20.55	161.20
5	31.15	11.24	21.26	145.10
6	36.05	11.44	16.03	123.05
7	34.85	8.95	19.5	147.90
8	32.44	9.03	20.6	139.80
9	34.31	8.19	17.77	133.70
10	34.09	6.21	20.23	138.48
11	41.33	6.80	17.92	147.48
12	36.00	7.36	20.27	164.10
13	39.88	7.21	10.31	98.50
14	42.41	10.51	14.48	140.55
15	43.49	8.75	13.34	102.40
16	44.80	9.22	9.53	123.40
17	37.45	8.91	13.28	125.20
18	37.82	10.44	14.34	123.20

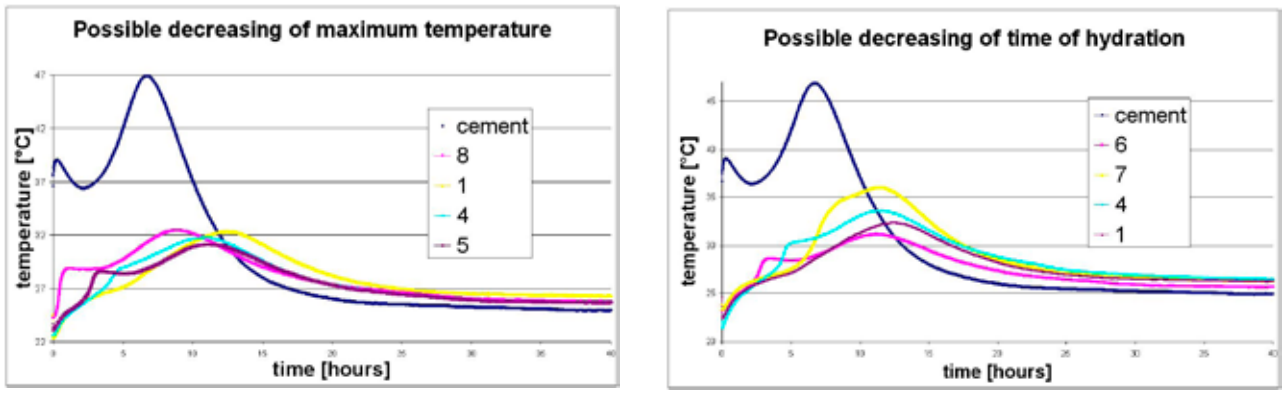

(a) (b)

Fig. 2. **Decreasing of the maximum temperature and delaying of the second peak on the hydration curve**

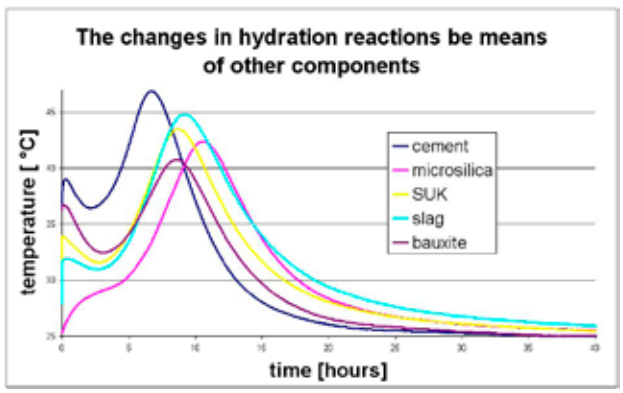

Fig. 3. **The changes in hydration process by using of other components**

with cement, silica fume, bauxite and only minimal amount of other components.

The influence of water to binder ratio on temperature changes was observed by measuring of mixture with all components and different amounts of added water.

When the w/b ratio is increased, total amount of heat is increased too. The temperature is increasing only to fixed amount of added water. Increasing the quantity of added water results in better contact of elements with water and hence supports the heat releasing hydration reaction. When the amount of added water is higher than quantum necessary for the hydration processes, this water becomes the "inert water", which does not contribute to the hydration, hence the maximum temperature reached during the hydration process is lowered.

From evaluated data (Table II) we can see, that as expected the highest temperature was reached by the mixtures with the highest amount of cement.

When some cement is replaced by other component, the maximum temperature and heat release is decreased. This decreasing is probably possible thanks to reaction of components with free lime, which going to decreasing of pH value. When the pH is changed, total heat of reactions is changed too. The bauxite is probably use as "inert element", which is effecting similarly as "inert water". For decreasing of maximum temperature are components more effectively in this sequence: bauxite > silica fume > SUK > VPS.

Some constituents studied also caused the retardation of the hydration process, which can be observed on the calorimetric curves as the shift of the second peak maximum. The constituents used are increasing time of hydration process in following sequence: silica fume > VPS > SUK > bauxite.

When we change some dosage of cement by other components, may be maximum temperature decreased by 20 °C and time of hydration increased two times. In compare with measuring of strength we can look that the highest strength is in mixtures with lower maximum temperature.

Conclusions

The compressive and flexural strength of HPC prepared was measured after 28 day moist curing. The influence of HPC composition on hydration process was observed by means of isoperbolic calorimetry. From obtained calorimetric curves, the maximal achieved temperature and time from mixing to reaching this temperature was evaluated. Flexural strength of prepared mixtures decreased in the following sequence: silica fume > SUK > VPS > bauxite and compressive strength in this sequence: silica fume > VPS > SUK > bauxite. For decreasing of maximum temperature are components more effectively in this sequence: bauxite > silica fume > SUK > VPS, for increasing time of hydration process in following sequence: silica fume > VPS > SUK > bauxite.

P23 TEMPERATURE AND MOISTURE EFFECTS ON MACRODEFCT-FREE COMPOSITE STRUCTURE AND PROPERTIES

FRANTIŠEK ŠOUKAL, JIŘÍ MÁSILKO, JAROMÍR HAVLICA, PETR PTÁČEK and TOMÁŠ OPRAVIL
Brno University of Technology, Faculty of Chemistry, Institute of Materials Science, Purkyňova 118, 612 00 Brno, Czech Republic,
soukal@fch.vutbr.cz

Introduction

Nowadays a part of hydrated cementitious materials research branch is focused on the polymer-cement composites with unusual manufacture qualities. The high-strength polymer-cement composites based on a water-soluble polymer are also known as macrodefect-free (MDF) composites. The name originates from its typical structure free of macrodefects such as large pores and flaws. MDFs have a privileged position due to its superior mechanical properties in the field of cementitious materials. Its flexural strength is reaching up to 300 MPa compared with values of about 5 MPa typical ones for ordinary Portland cement paste. The strength improvement is reached only by addition of up to 10 % of polymer and subsequent high-shear processing[1].

Macrodefect-free composites exhibit high sensitivity to moisture[2] due to its water-soluble polymer that interpenetrates throughout the whole bulk of composite forming an organo-inorganic matrix. The used polyvinylalcohol-acetate polymer forms the matrix with hydration product of aluminate cement during the high-shear processing and especially during the subsequent curing. The curing condition such as temperature and moisture plays important role in the matrix formation and further chemical composition and physical properties.

Experimental

The tested MDF composites were prepared using aluminate cement Secar 51 (Lafarge Aluminates) whose major phase is $CaO \cdot Al_2O_3$ supplemented with $12CaO \cdot 7Al_2O_3$, $2CaO \cdot Al_2O_3$ and $CaO \cdot TiO_2$ with total Al_2O_3 content above 50 % and with polyvinylalcoholacetate Sloviol P-8810 (NCHZ) of hydrolysis degree 88 % and viscosity of 4% water solution 11.6 mPa s.

Cement with polymer was mixed in amount from 2 up to 7.5 % wt. The water was added certainly to obtain an optimal consistency for subsequent high-shear processing. The water – solidus ratio varied around the value of 0.16. 1 % wt. of superplasticizer Glenium C151 (Degussa) was also added. The mixture of cement, polymer, water and superplasticizer was compacted and high-shear processed with twin-roll mixer. 100 × 20 × 2 mm sized thin specimens were pressed at 5 MPa to constant pressure. These specimens were heated at 20, 40, 60, 80 and 100 °C in open atmosphere and afterwards for 1 and 7 days put into three types of surroundings – dry (polyethylene bags), moist (at almost 100% RH.) and immersed in water.

After 1 or 7 days of curing the specimen's flexural strength was tested in three-point bend instrumentation with 40 mm distance of supports.

Results

The flexural strength results of tested composites with different polymer content, cured at various temperatures and moisture conditions are shown at Figs. 1.–5. The results are divided according to moisture conditions to five histograms. The first graph at Fig. 1. represents samples cured in dry condition in closed PE bags. The effect of moisture was studied in two intensities – at almost 100% relative humidity and immersed in water, and after two periods – 1 day and 7 days, that is shown at following four histograms at Figs. 2.–5. Flexural strength is served in dependence on polymer content together with curing temperature.

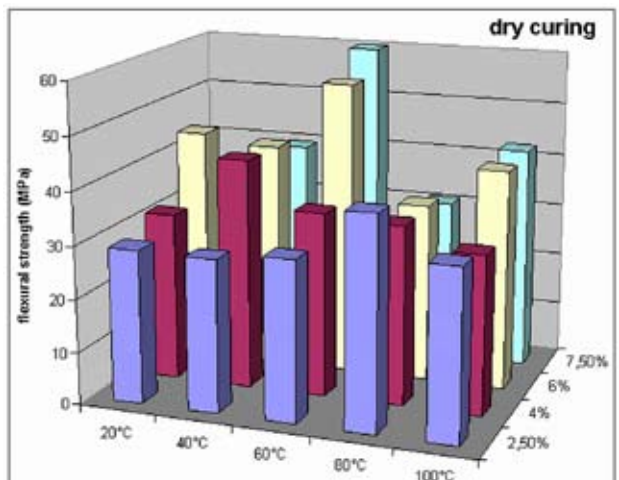

	20°C	40°C	60°C	80°C	100°C
2,50%	29,07	28,78	30,3	39,94	32,23
4%	31,81	43,44	34,83	33,94	30,02
6%	44,38	42,84	55,86	33,89	41,69
7,50%	31,13	39,69	61,3	30,87	42,26

Fig. 1. **Flexural strength of MDF composites with different polymer content and curing temperature, cured in dry atmosphere**

Fig. 1. shows that composites with given polymer content have different flexural strength dependence on curing temperature stored in dry conditions. The highest flexural strengths at given polymer dosage are following: 2.5 % – 40 MPa at 80 °C, 4 % – 43 MPa at 40 °C, 6 % – 56 MPa at 60 °C and 7.5% – 61 MPa at 60 °C.

Samples cured at almost 100% relative humidity (Fig. 2. and Fig. 3.) generally exhibits lower flexural strength compared with that ones cured in dry atmosphere. The strength decrease at higher polymer content is over 50 % and at lower polymer content (2.5 %) about 30 %. It can be explained by lower initial strengths due to insufficient polymer content. At curing temperature of 60 and 80 °C the decrease is more outstanding (up to 75 %).On the other hand the most expressive

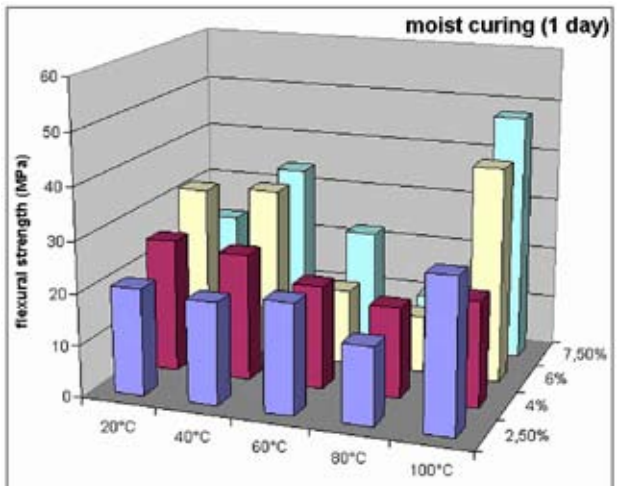

	20°C	40°C	60°C	80°C	100°C
2,50%	20,74	19,76	21,33	15,04	29,41
4%	25,72	24,49	19,98	17,47	20,52
6%	32,15	33,19	14,62	11,14	41,41
7,50%	22,79	33,99	22,24	10,59	47,9

Fig. 2. **Flexural strength of MDF composites with different polymer content, curing temperature, cured in moist atmosphere for 1 day**

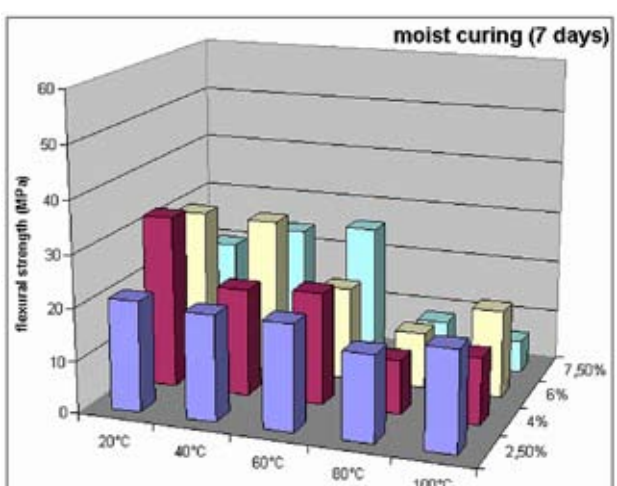

	20°C	40°C	60°C	80°C	100°C
2,50%	21,14	20,19	20,28	16,4	19,09
4%	32,94	20,53	21,33	10,35	12,64
6%	30,22	29,76	17,91	10,74	16,8
7,50%	19,99	24,14	25,86	8,43	6,23

Fig. 3. **Flexural strength of MDF composites with different polymer content, curing temperature, cured in moist atmosphere for 7 days**

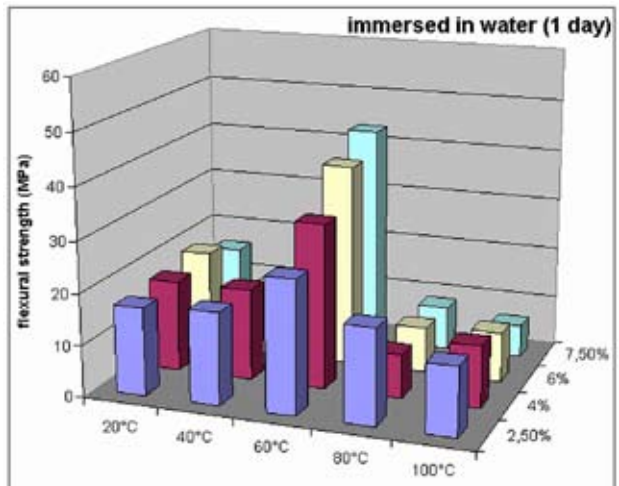

	20°C	40°C	60°C	80°C	100°C
2,50%	17,08	17,83	25,79	18,51	13,27
4%	17,68	17,63	31,86	8,57	12,02
6%	19,26	13,61	39,28	8,9	9,65
7,50%	16,03	8,81	42,99	8,4	6,3

Fig. 4. **Flexural strength of MDF composites with different polymer content, curing temperature, immersed in water for 1 day**

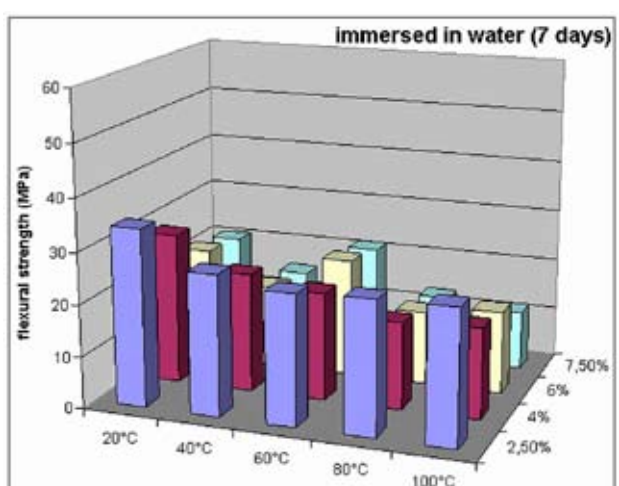

	20°C	40°C	60°C	80°C	100°C
2,50%	34,14	27,14	25,13	25,7	25,9
4%	29,17	22,9	20,86	16,86	17,52
6%	22,11	16,07	22,94	14,29	16,02
7,50%	20,65	14,89	21,28	12,72	11,36

Fig. 5. **Flexural strength of MDF composites with different polymer content, curing temperature, immersed in water for 7 days**

difference is at 100 °C. After 1 day of moist curing the flexural strengths keep almost the same values compared with dry curing, whereas flexural strengths after 7 days of moist curing are very low especially at polymer content of 7.5 %, where the flexural strength exhibits only almost 10 % of the initial value. Composites cured at other temperatures generally are not influenced by time of moist curing.

MDF composites immersed in water for 1 day (see Fig. 4.) exhibit overall more lower flexural strengths than composites cured in moist atmosphere. One significant irre-

gularity is in the case of composites cured at 60 °C. These samples have almost the same flexural strength like that ones cured in dry atmosphere. On the other hand composites immersed for 7 days exhibits markedly lower decrease of flexural strength. The lower polymer content and temperature is, the lower decrease is monitored. Polymer in MDF composites immersed in water is washed out during the first day that leads to very porous structure and lower strength. In the following period up to 7 days of immersion water come into the open pores and the non-hydrated cement grains undergoes further hydration. Large pores after polymer agglomerates are filled with $Al(OH)_3$ precipitated from solution and CAH gel forms the binder matrix. Therefore the flexural strength of MDF composites after longer immersion increases again.

Fig. 6. **Image in polarized light of thin section of MDF composite containing 6 % of polymer after 7 days in moist atmosphere**

Conclusions

Prepared MDF composites exhibits extreme mechanical properties in terms of cementitious materials. The best reached flexural strength was 61.3 MPa in the case of 7.5 % of PVAl cured at 60 °C. Overall the best performing composite consist of 6 % of PVAl at all curing temperatures. Its best flexural strength was reached after curing at 60 °C in the value of 55.7 MPa.

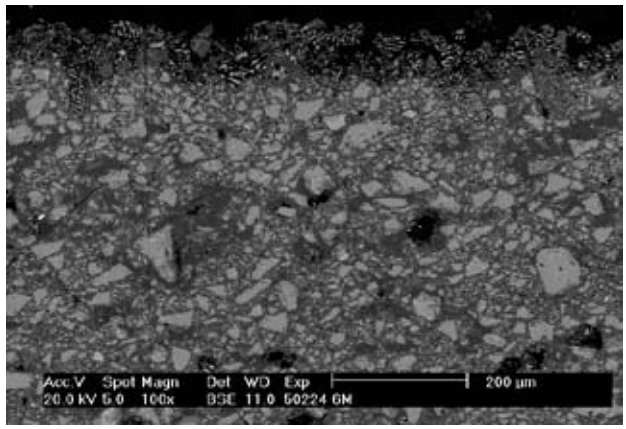

Fig. 7. **SEM image of thin section of MDF composite containing 6 % of polymer after 7 days of immersion in water**

Generally, the mechanical properties of tested composites were significantly influenced by contact with water. Samples stored in moist atmosphere for 7 days exhibited higher strength decrease then that ones stored for only 1 day. Immersion in waterfor 1 day leads to even higher strength fault compared with moist atmosphere. On the other hand the longer storage under water evoked follow-up increase of flexural strength. In the first stage polymer was washed up from pores of composite and subsequently water hydrated exposed clinker grains throughout the open pores.

This work has been supported by project MPO ČR FT-TA3/026

REFERENCES

1. Šoukal F.: Disertační práce, Brno: Vysoké učení technické v Brně, 2007.
2. Drabik, M., et al.: J. Therm. Anal. Calorim. *76*, 91 (2004).

P24 LATEX MODIFIED CEMENT COMPOSITES: EFFECT OF POLYMER TYPE

FRANTIŠEK ŠOUKAL, VÁCLAV VINTER, JAROMÍR HAVLICA, PETR PTÁČEK and TOMÁŠ OPRAVIL
Brno University of Technology, Faculty of Chemistry, Institute of Materials Science, Purkyňova 118, 612 00 Brno, Czech Republic,
soukal@fch.vutbr.cz

Introduction

Nowadays an extensive research is aimed to polymer-cement materials. Generally, two ways can be mentioned how to combine organic polymer with the inorganic cement. The first one is concrete impregnation with polymer, where polymer in form of solution, emulsion or dispersion is transported into the open pore structure of concrete. The second type of these materials is the polymer modified concrete (PMC), where the polymer is mixed within fresh cement paste building up two component composite binder. The nature of mineral phases – polymer chemical interactions decides on the consequent properties of composite[2].

Polymer latex modified cement composites forms within its structure two different binder – cement paste and polymer films. Properties of these binders can supplement each other due to intramolecular forces interactions. Water from latex is consumed during the hydration of cement that leads to formation of polymer films. Interactions of polymer with the surrounding mineral phases are primarily of van der Walls type. Almost no chemical bonds are supposed in this system. Latex modified mortars exhibit increased flexural strength. Elastic polymer films fulfill pores and flaws which avoids premature failure of the material. On the other hand pressure strength is not so influenced by polymer films formation. Its value is preferably determined with concretion of gel and crystalline phases of hydrated cement[1,2].

The paper deals with effect of polymer in latex on mechanical properties of latex modified cement materials.

Experimental

Preparation and Curing of PMC

There were selected 5 types of latexes according to polymer nature. Some of their basic properties are presented at Table I. Lipaton XA 491 represents styrene-vinylacrylic esters (SAE), Lipaton SB 5813 is representative of styrene-butadiene rubbers (SBR), Plextol × 4002 of polyacrylic esters (PAE), Plextol D 509 is latex of copolymer of methylmethacrylate and n-butylacrylate (MBR) and Duvilax BD-20 is latex of polyvinylacetate (PVAc). Latexes of series Lipaton and Plextol are produced by PolymerLatex company in Germany and Duvilax is produced by Duslo Šala in Slovakia. Polymer latexes were combined with Portland cement CEM I 42.5 R (Turňa nad Bodvou, Slovakia).

Polymer latexes were mixed with cement from 1 to 15 % of weight to cement. Various amount of water was added to obtain always the same consistency. Fresh pastes were formed to testing beams of dimensions of 20 × 20 × 100 mm. Thereafter smples were cured in atmosphere of almost 100% relative humidity.

Table I
Basic properties of tested polymer latexes

Properties	Polymer latex				
	Lipaton XA 491	Lipaton SB5813	Plextol X 4002	Plextol D 509	Duvilax BD–20
Polymer	SAE	SBR	PAE	MBR	PVAc
Solids content [%]	57	48.5	60	50	53.5
pH [20°C]	8.0	8.0	2.0–2.5	7.5	3.0–5.0
Density [g cm^{-3}]	1.04	1.01	1	1.05	–
Viscosity [mPa s]	500–4,000	30	100–2,000	100–2,000	4,000–19,000

Results

Mechanical Properties

The whole range of tested latexes was primarily tested in PMC pastes of polymer content of 5, 10 and 15 % of weight to cement. Compressive and flexural strength after 28 days of curing was tested as the basic mechanical parameters. For comparation a pure cement paste without latex was prepared and its compressive strength was 64.06 MPa and flexural strength was 9.14 MPa and this values are marked in graphs with red line. The experimental results are shown at Fig. 1. and Fig. 2. Polymer latexes Plextol × 4002 (PAE) and Duvilax BD-20 (PVAc) in dosage 10 and 15 % markedly fall behind the other types in strength parameters. We can see that PMC pastes with PAE and PVAc latex in dosage of 5 % exhibit almost the same flexural strength compared with pure cement paste. Higher polymer dosage leads to decrease of flexural strength up to 50 % of initial value. Polymer addition decreased the compresive strength in all cases beyond SBR latex. SBR latex decreased compressive strength under the value of pure cement paste after dosage of 15 %. PAE and PVAc

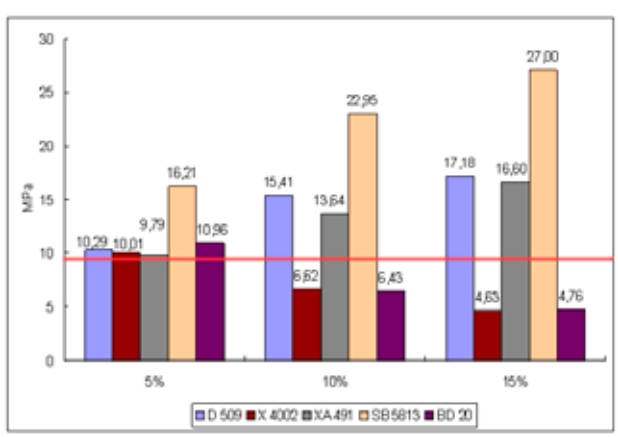

Fig. 1. **Compressive strength of PMC after 28 days of curing**

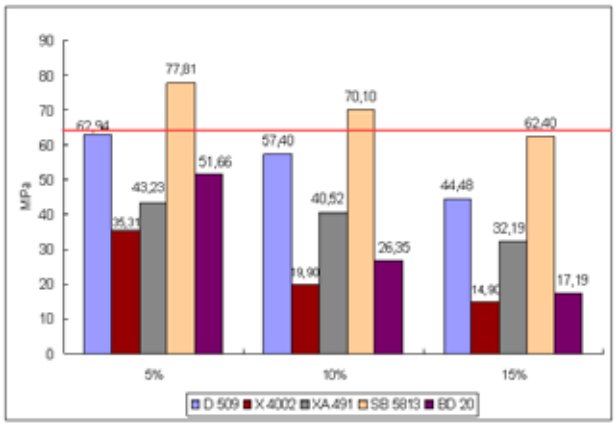

Fig. 2. **Flexural strength of PMC after 28 days of curing**

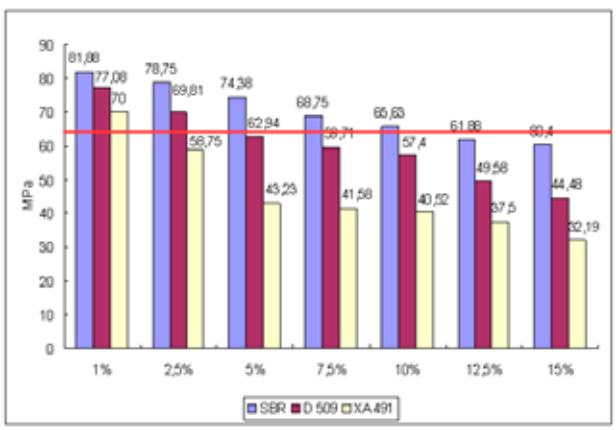

Fig. 3. **Compressive strength of selected PMC after 28 days of curing**

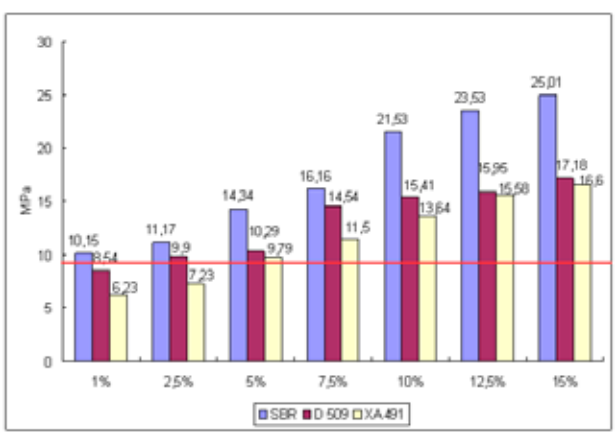

Fig. 4. **Flexural strength of selected PMC after 28 days of curing**

latexes leads to compressive strength decrease up to 20 % of pure cement paste. Therefore the following experiments targeted the only three perspective latexes – Lipaton SB 5813 (SBR), Lipaton XA 491 (SAE) and Plextol D 509 (MBR).

Subsequently the selected polymer latexes were used to prepare PMC pastes of polymer dosage 1, 2.5, 5, 7.5, 10, 12.5

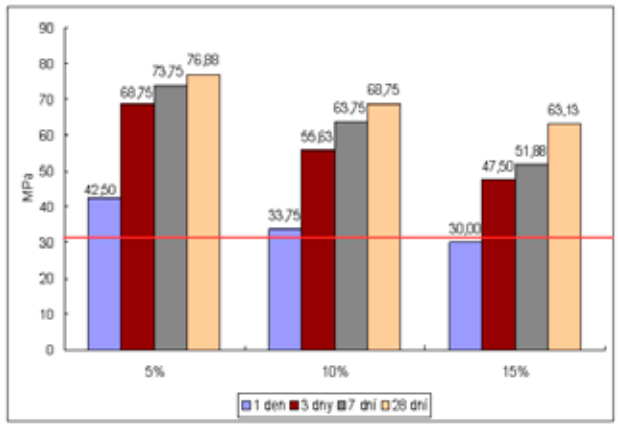

Fig. 5. **Compressive strength development of PMC with latex SB 5813**

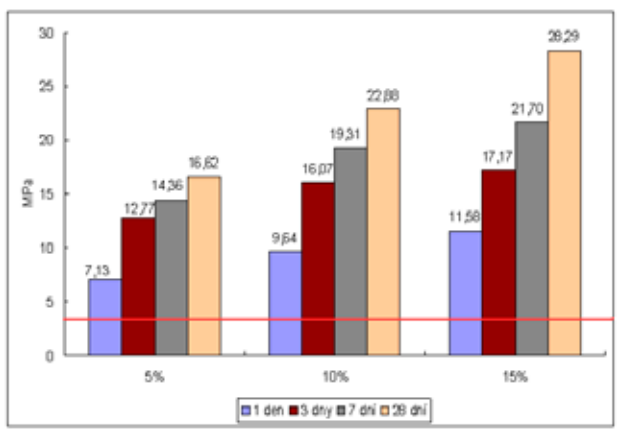

Fig. 6. **Flexural strength development of PMC with latex SB 5813**

and 15 % of weight to cement. Again flexural and compressive strength was tested and its results are shown at Fig. 3 and Fig. 4. At Figs. 3. and 4. we can see that increasing content of polymer in all cases increases flexural strength and on the other hand it decrases compressive strength. The highest increase is notable in the case of SBR latex from 10.15 MPa up to 25.01 MPa. PMC pastes with 15 % of polymer reach almost double flexural strength in case of SAE and MBR latexes and paste with SBR latex reached even triple flexural strength compared to pure cement paste. SAE latex leads to flexural strength increase after 5% addition to paste and under this value flexural strength is decreased. Compressive strength decrease was lowest in pastes with SBR latex again. The pastes with polymer dosage up to 10 % exhibited higher compressive strength even than pure cement paste. PMC paste with MBR latex holds its compressive strength over the pure cement one up to 2.5% of polymer content and paste with SAE latex only at 1% dosage.

PMC paste with the most perspective SBR latex was tested also for strength development in time. The experiment were hold with 5, 10 and 15 % polymer dosage and compressive and flexural strength was test after 1, 3, 7 and 28 days of

hydration. Experimental results are introduced at Figs. 5. and 6. We can see that increasing polymer content increases also flexural strength development and decreases development of compressive strength. Producent declared 2–day flexural strength of pure cement paste is 3.3 MPa and compressive strength 31.1 MPa (red lines in Figs. 5. and 6.). Flexural strength development of tested PMC paste with SBR latex is several times faster. Strength development of PMC paste with low polymer dosage significantly slows down after 3 days of hydration in contrast to high polymer dosage PMC paste whose strength development rate is quite extensive up to 28 days of hydration. Development of compressive strength is markedly fast up to 3 days in all polymer dosage.

Conclusions

The measured strength characteristics show that the most promissing type of polymer latex for preparation of polymer modified concrete is styrene-butadiene ruber latex (SBR). Its 15% addition to cement paste leads to triple flexural strength after 28 days of hydration, while compressive strength is not reduced up to 10% dosage. Its flexural strength development in time is very fast. It reaches more than 30 % of final strength after 1 day of hydration. Very good results were achieved also with styrene-vinylacrylic ester latex and methylmethacrylate n-butylacrylate copolymer latex. They higher addition leads to higher compressive strength decrease, therefore they should be preferably used in low dosage. Polyacrylic ester latex and polyvinylacetate latex exhibited decrease of the compressive even the flexural strength so that they are not suitable for PMC preparation.

This work has been supported by project MPO ČR: FT-TA3/026 and project MŠMT NPVII: 2B08024.

REFERENCES

1. Eve S., Gomina M.,: J. Eur. Ceram. Soc. *27*, 1395 (2007).
2. V. S. Ramachandran: *Concrete admixtures handbook – properties*, science and technology, 2nd edition. ISBN O-8155–1373-93.

P25 INFLUENCE OF CONDITIONS ON HYDRAULIC CALCIUM ALUMINATE PHASES HYDRATION MECHANISMS

FRANTIŠEK ŠOUKAL, JAN KOPLÍK, JAROMÍR HAVLICA, TOMÁŠ OPRAVIL and VITĚZSLAV FRANK
Brno University of Technology, Faculty of Chemistry, Institute of Materials Science, Purkyňova 118, 612 00 Brno, Czech Republic,
soukal@fch.vutbr.cz

Introduction

Aluminate cement is known since beginning of 20th century. After a few collapses of constructions made from aluminate cement its utilization such as construction material was prohibited in many countries. Nowadays aluminate cement finds utilization especially in refractories and some non-traditional material e.g. macrodefect-free composites.

CA ($CaO \cdot Al_2O_3$), the major component of common aluminate cements, is responsible for the characteristic properties of aluminate cements, namely strength and hydration rate. CA_2 ($CaO \cdot 2Al_2O_3$) mineral grossite and $C_{12}A_7$ ($12CaO \cdot 7Al_2O_3$) mineral mayenite are usually minor hydraulic phases of aluminate cements, but CA_2 can major component of high-aluminate cement. Their presence influences the properties of cement, chiefly hydration rate and early and late strength. C_3A ($3CaO \cdot Al_2O_3$) is an important component of Portland cement. Although it is not major component, it plays significant role in hydration process of Portland cement especially in reactions with gypsum.

Despite of cement hydration has been studied for a long period and there were established a number of reaction mechanisms (Le Chatelier, Michaelis) and there were identified some of hydration products, the process of hydration of the individual phases has not been clearly explained. In contrast to calcium silicates primarily not all the hydration products of calcium aluminates have been identified to date as well as their hydration kinetics at various pH environments.

Experimental

Preparation of Hydraulic Calcium Aluminate Phases

Calcium aluminate phases can be prepared in several ways. The most common preparation method is based on solid phase clinkering that was used. $CaCO_3$ and Al_2O_3 in p.a. clearness were well mixed in stoicheiometric rate appropriate for the individual phases.

According to results the sintering has to be done at least twice to establish thermodynamic equilibrium and to obtain the pure phase. Throughout the first sintering the mixture was heated to 900 °C at rate of 10 °C min^{-1} for 1 hour. Then the heating continued at the same rate to the final temperature and there kept out for 5 hours. The final temperature depends on the prepared phase: CA and C_3A – 1,450 °C, CA_2 – 1,600 °C, $C_{12}A_7$ – 1,360 °C. The second heating was accomplished without the holding at 900 °C right to final temperature for 5 hours as well. The products were grounded after each sintering in vibration mill. The clearness of prepared calcium aluminate phases was verified with XRD analysis. Only the powder fraction with particles passed sieve mesh of 90 μm was used for the following hydration.

Hydration and Semiadiabatic Calorimetry

For the evaluation of hydration kinetics the semiadiabatic calorimeter has been utilized. The calorimeter consists of thermo-isolation cell from polystyrene foam, 250 ml reaction vessel, magnetic stirrer, thermistor, digital multimeter and data logging software in PC.

Hydration of the individual phases was monitored at four different pH values varying from neutral to high alkali: 6, 9, 11, 12.65. 30 g of the phase was poured into 50 ml of water with appropriate puffer. The pH 6 was measured in the pure distilled water. The temperature logging was started immediately after the pouring of oxide into water with logging interval of 2 seconds for following 48 hours. Afterwards the hydrated mixture was filtrated and several times rinsed with distilled water. The solid hydration products were dried at 40 °C at decreased pressure for 4 hours.

Results

Semiadibatic Calorimetry

Hydration of C_3A is the most intensive between 20 and 50 minutes after mixing with water depending on pH value (see Fig. 1.). This hydration process is very fast and linked with high evolution of heat and its kinetics is enough fast until 5 hours after mixing. At pH of 6, 9 and 11 can observed very weak exotermic process at 32–36 hours after mixing. Compared with other oxides the hydration of C_3A is the fastest. Hydration at pH value of 6 is connected with the highest temperature increase of all oxides.

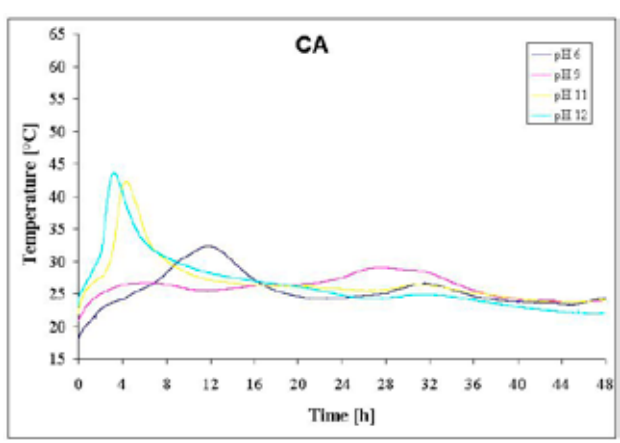

Fig. 1. **Semiadiabatic calorimetric curves of CA hydrated at pH 6–12**

Hydration of CA at all environments is characteristic by two separated processes evolving heat. The first one has maximum of rate at 3–12 hours after mixing and its rate strongly

depends on pH value (see Fig. 1.). The hydration rate is increasing with increasing pH, only hydration at pH 9 is totally inhibited in this first step. On the other hand the intensity of the second weak process occurring after 27–32 hours is higher then intensity at the other pH values. Overall hydration rate of CA is the second slowest of the examined oxides.

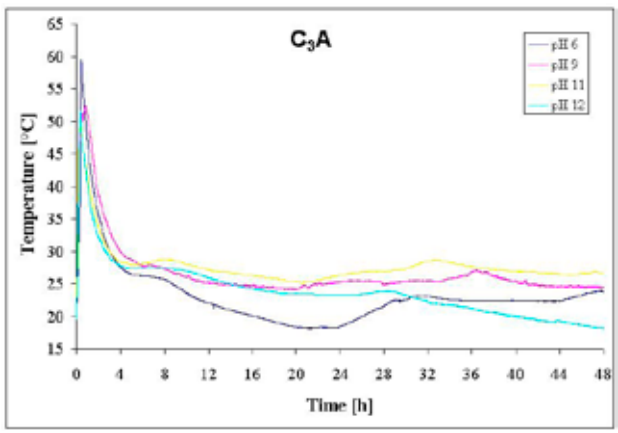

Fig. 2. **Semiadiabatic calorimetric curves of C_3A hydrated at pH 6–12**

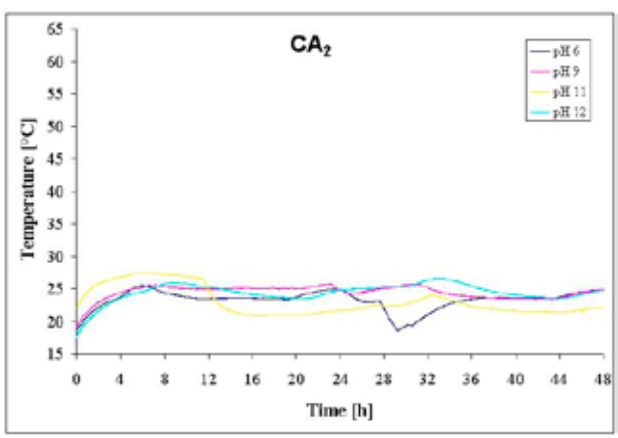

Fig. 3. **Semiadiabatic calorimetric curves of CA_2 hydrated at pH 6–12**

CA_2 exhibits the lowest hydration activity (see Fig. 1.). The hydration process starts during the first 5 hours and the evolution of heat is poorly identifiable. The hydration continues whole monitored 48 hours at very low intensity. Two weak separated processes could be found at 6–9 hours, that is most clear at pH 6, and about 23 hours of hydration detectable at pH 11 and 12.

The kinetics of hydration process of mayenite is very similar to that of C_3A (see Fig. 1.). The highest evolution of heat comes on after 40–60 minutes of hydration. This process is also very fast. A weak process can be observed at 30–36 minutes after mixing as well. $C_{12}A_7$ is the second most reactive oxide.

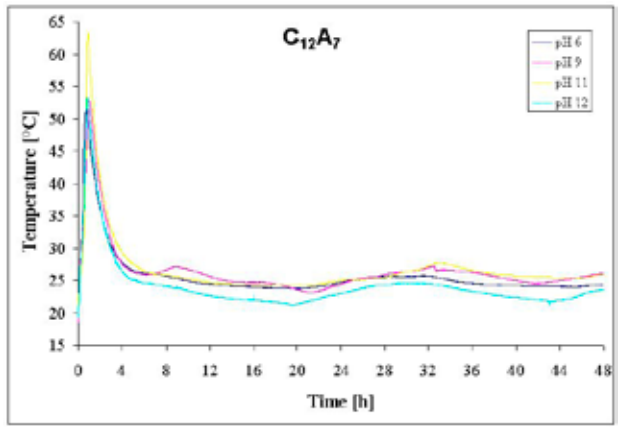

Fig. 4. **Semiadiabatic calorimetric curves of $C_{12}A_7$ hydrated at pH 6–12**

DTA and X-ray Diffraction Analysis

Samples cured at almost 100% relative humidity (Figs. 2. and 3). The DTA curves of hydrated C_3A exhibit three endothermal effects at all pH (see Fig. 2.). XRD analysis identified only one crystalline hydration product – hydrogrossular C_3AH_6 (see Fig. 3.). The first endotherm without weight loss at 150 °C can be connected with decomposition of C_3AH_6 to C_2AH_5 and portlandite CH. The second strong endothermal effect at 310 °C is invoked by dehydration of C_2AH_5 followed by dehydration of portlandite at 460 °C. This process is confirmed by the proportion of weight loss during these dehydrations that is always strictly 5 : 1. TGA curves shows that the most amount of hydrogrossular was created at pH 9 and the least at pH 11.

The hydrated CA exhibits more hydration product than C_3A and their amount only slightly depends on pH (see Fig. 2.). As well as in the case of C_3A there can be found hydrogrossular, but only as the minor hydration product, especially at pH 12 (well observable is only endotherm at 310 °C). Endotherms at 150 and 275 °C at all pH are joined with dehydration of C_2AH_8. This hydrate was not identified by XRD (see Fig. 3.), so that it has to be of amorphous or microcrystalline nature. The amount of C_2AH_8 is comparable at all pH values. A distinct endothermal effect is connected with a crystalline hydrate that was identified also by XRD. The nature of this hydrate was not clarified. Its diffractions are not published in available XRD databases. The highest amount of this hydrate is at pH 6 and 12, the least at pH 11. Another weak endothermal maximum can be observed at 225 °C mainly at pH 11 (see Fig. 2.) and one at 320 °C noticeable at pH 6. These effects have not been assigned.

DTA curves of hydrated CA_2 are shown also at Fig. 2. DTA and TGA curves correspond with measured calorimetry results (see Fig. 1.). The extent of hydration is very low. No hydration products at pH 9 were identified. Hydration at pH 6 and partially at pH 11 and 12 leads to lower amount of hydration products. As well as in the case of CA there can

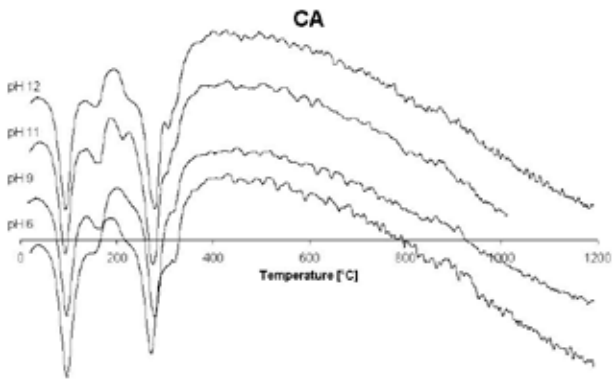

Fig. 5. **DTA curves of hydrated CA at pH 6–12**

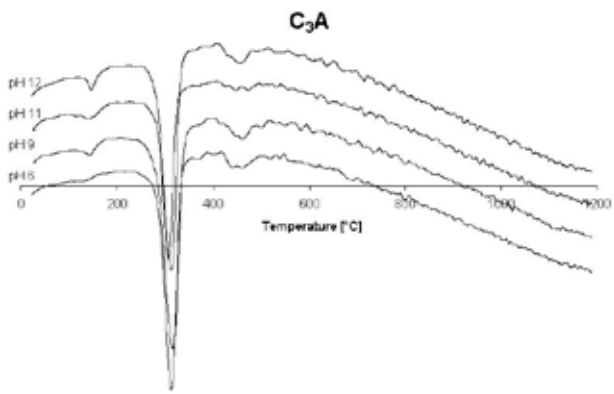

Fig. 6. **DTA curves of hydrated C_3A at pH 6–12**

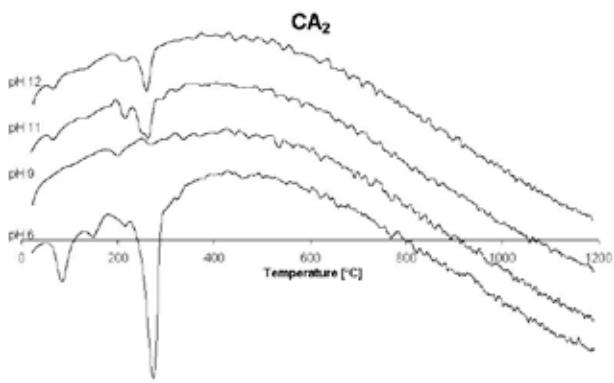

Fig. 7. **DTA curves of hydrated CA_2 at pH 6–12**

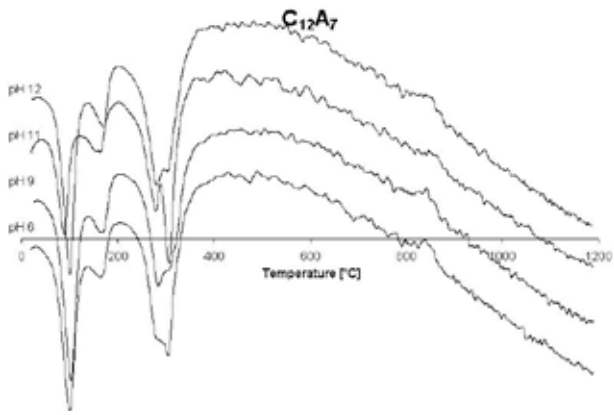

Fig. 8. **DTA curves of hydrated $C_{12}A_7$ at pH 6–12**

be identified hydrate C_2AH_8 and not clarified hydration products (at 70 and 215 °C).

Hydration of mayenite leads to similar hydration products as in the case of CA. There can be identified hydrogrossular C_3AH_6 at pH 11 and 6 such as main hydration, whereas at pH 9 and 12 its amount is lower. C_2AH_8 was found mainly at pH 6, 9 and 12 as well as the not clarified crystalline hydration product at 100 °C that is the main hydration at pH 6, 9 and 12. Analogous to C_3A the lowest conversion of oxide to hydration products is at pH 11.

Conclusions

According to obtained results oxides C_3A and $C_{12}A_7$ exhibit highest hydration activity. Hydration products and their formation kinetics are very similar at all tested pH values. The least reactive calcium aluminate phase is CA_2. Hydration of C_3A at all pH values evokes only one product – cubic hydrogrossular C_3AH_6. Hydration of CA at all pH and $C_{12}A_7$ at pH 9 and 12 leads also to formation of hydrate C_2AH_8. Less amount of C_2AH_8 was also found in hydration products of mayenite at pH 6 and 11 and CA_2 at pH 6, 11 and 12. During the hydration of CA and $C_{12}A_7$ an unidentified crystalic hydration product is generated. Its X-ray diffractions were not found in the newest databases. Generally, hydration of CA and $C_{12}A_7$ leads to formation of the same products, only changes are in the amount of hydrates.

This work has been supported by project MPO ČR: FT-TA3/026 and project MŠMT NPVII: 2B08024.

P26 THE STUDY OF BUILDING BIOCORROSION

EVA TERPÁKOVÁ
Technical University of Košice, Civil Engineering Faculty, Institute of Building and Environmental Engineering, Vysokoškolská 4, 042 00 Košice, Slovak Republic, eva.terpakova@tuke.sk

Introduction

Biodeterioration or biocorrosion of building materials – stone, concrete, mortar, etc., can be caused by such microorganisms as bacteria, fungi, lichens, algae, and plants (Wasserbauer, 2000). Multidiscipline methods are available for the study of biodeterioration each other materials. Almost of them is bearing to biological part of problem e.g. identification of biodeteriorates, evaluating of birth biofilm or studies of metabolites. Biofilms are complex communities of microorganisms attached to surfaces of materials generally, or associated with interfaces. Bacterial biofilm formation on inert surfaces is a significant technical and economic problem in a wide range of environmental, industrial, and medical areas. Bacterial adhesion is generally a prerequisite for this colonization process and, thus, represents an attractive target.

Experimental

To the purpose of concrete corrosion study (chemical, physical and structural changes) is important to obtain the representative sample from damaged part. Drilling corps are the most suitable for these purposes. On the other hand, there is some risk to damage of biodeteriogen or biofilm in consequence of high temperature beside drilling procedure. The cores of 75 mm diameter and about 100 mm length were obtained by coring equipment Hilti. The experimental samples are from concrete material of sewerage system of 30 years old building with very aggressive environment, because mineral water sources with H_2S are in this locality. Consequently potential risk of biodeterioration follows to SRB (sulphate reducing bacteria) which living in this type of water.

Chemical impact on to concrete samples was tested by classical methods; results are in Tables II and III. From surface were taken small amounts of sample under sterile conditions for microbiological tests and examination of MID of concrete.

Analytical Evaluation

The dependence of pH values changes and aggressive ions on depth e.g. their profile was determined. The samples were separated mechanically by gradual depth up to 3.0 mm. Concrete powder after grinding procedure was collected; the each other portion of samples was dried up to constant weight at 105–110 °C. For potenciometric determination of alkality we used 1 ± 0.0005 g of samples after their separation, and dissolute in 100 ml distilate water. Solutions were shaken for 2 hours. Filtrate was used to determine Cl^- ions by potentiometric method. The result expressed as % wt. in cement stone are in Tables II and III. The pH values were determined by potentiomeric method, too. Concentration of inorganic sulphates was determined by gravimetric method follow to Slovak standard rules (Priganc, Terpáková, 2003).

Biocorrosion Evaluation

The media used for isolation and continued cultivation of samples obtained from concrete surface were neutrophilic media (N) and acidophilic media (A) prepared follow to (Sand, 1987). Experiment continues in this time and details of biodegradation inner parts of concrete will be tested by AFM (atomic force microscope) in a future.

Results

Table I
Colonial types of bacteria cultivated from concrete

	(N)	(A)
Sample 1	Opaque, white spreader with irregular edges Small, round, creamy collared	Large, white with very good growth
Sample 2	Small, round, creamy collared Opaque, white spreader with irregular edges	Small, round, white translucent colonies Small, round, shiny yellow colonies

(N) – neutrophilic medium
(A) – acidophilic medium

Table II
Chemical results of concrete core 1

Depth of sample [mm]	Concentration [%]			
	pH ± 0.01	Cl^-	SO_4^{2-}	l.o.i 1,000 °C
0–3	9.25	0.025	0.13	12.23 ± 0.01
3–6	9.36	0.021	0.12	10.95 ± 0.02
6–9	9.40	0.020	0.11	9.86 ± 0.02
9–12	9.55	0.020	0.09	9.78 ± 0.01
12–15	9.73	0.017	0.09	9.53 ± 0.01
Comprehensive strength values [MPa]				20.3

Table III
Chemical results of concrete core 2

Depth of sample [mm]	Concentration [%]			
	pH ± 0.01	Cl^-	SO_4^{2-}	l.o.i 1,000 °C
0–3	9.12	0.028	0.16	13.40 ± 0.01
3–6	9.20	0.022	0.13	11.24 ± 0.01
6–9	9.23	0.019	0.11	10.18 ± 0.01
9–12	9.35	0.018	0.08	10.25 ± 0.01
12–15	9.62	0.015	0.07	10.13 ± 0.01
Comprehensive strength values [MPa]				19.5

Fig. 1. **Detail view of surface sample number 1**

Fig. 2. **Detail view of surface sample number 2**

Major colonial types of bacteria obtained from corroded concrete product are described in Table I.

Determination the typical corrosive agents confirmed their presence in the structure of concrete and consequently manifestation of sulphate corrosion and carbonisation above all.

Conclusions

Aggressive MID microorganisms can form a biofilm on the surface of samples so that when nutrients are provided the microbes remain active. The changes of physical – chemical characteristics expressed as the differences in alkaline reaction confirme the neutralisation process of cement stone due to MID up to 3–6 mm depth. Follow to alkali reaction values is possible to confirm that 2–3 degree of carbonisation concrete is present in both samples, (Matoušek, Drochytka, 1998). The statistically significant changes were obtained in case determination of loss weight by ignition too. Results of long time experiment after incubation by neutrophilic and acidophilic medium were present in future.

Acknowledgement: This work has been supported by Grant Agency of Slovak Republic (project No. 2/0075/08).

REFERENCES

1. Wasserbauer R.: *Biologické znehodnocení staveb*. ABF,a.s. Nakladatelství ARCH, Praha, 2000.
2. Priganc S., Terpáková E.: *Diagnostic of concrete construction parts*. TU-SvF, TULIP, Košice, 2003.
3. Matošek M. Drochytka R.: *Atmosferická koroze betónu*. IIKAS, Praha, 1998.

P27 MILLING OF OLIVINE $(Mg, Fe)_2SiO_4$ IN HIGH-ENERGY MILLS BY WET AND DRY WAY

ERIKA TURIANICOVÁ and PETER BALÁŽ
Institute of Geotechnics, Slovak Academy of Science, Watsonova 45, 043 53 Košice, Slovak Republic, turianicova@saske.sk

Introduction

High-energy milling is now one of the materials processing methods that is widely used in powder technology. The advantage of high-energy milling is its simplicity and effectiveness. The disintegration of mineral particles by mechanical activation is accompanied by an increase in the number of particles and by generation of fresh, previously unexposed, surface[1,2].

Particle size reduction in olivine is produced by milling (either wet or dry), the nature of which plays an important role in the physicochemical properties of the resulting powders and in the further processing steps.[3–5] The effects of milling have been studied extensively, mainly for silicates minerals such as olivine because it is a mineral possible to use as a suitable feedstock for carbon dioxide sequestration[3,4].

The basic concept behind CO_2 disposal by means of silicates well known as mineral sequestration was originally proposed by Seifritz in 1990 and first studied in more details by Lackner. This idea mimics very slow (of thousands to millions of years) natural weathering process of silicate minerals conversion.

Mechanical activation by high-energy milling can results in major improvement of the reaction rate[1].

Experimental

M a t e r i a l

The olivine sample used in this study was kindly supplied by the Norwegian mining company North Cape Minerals (NCM) and originates from the production plant at Åheim (Norway).

The sample contains approximately 93 % forsterite (Mg_2SiO_4) and 7 % fayalite (Fe_2SiO_4). This olivine composition is referred to as Fo_{93}. Small amounts of accessory minerals like chlorite, chromite, enstatite, serpentinite and talc can also be found in the sample. The olivine product used in this study is a foundry sand (AFS50) and contains approximately 95 % pure olivine.

The bulk chemical composition (as analysed by NCM using X-ray fluorescence (XRF) analysis) of the sample is following: 50.2 % MgO, 41.5 % SiO_2, 7.41 % Fe_2O_3, 0.36 % Al_2O_3, 0.33 % NiO, 0.30 % Cr_2O_3, 0.08 % MnO, 0.08 % CaO, 0.01 % Na_2O, 0.01 % K_2O, LOI 0.27 %.

M e c h a n i c a l A c t i v a t i o n

Two milling models including dry and wet modes are applied in the milling processes such as mechanical activation of material and/or minerals. The comparison of the wet and dry milling effects on the structural changes usually was made at the same grinding mill.

The olivine sample was mechanically activated in two high-energy mills by various conditions:

Laboratory planetary ball mill (Pulverisette 6, Fritsch, Germany) (PM) (Fig. 1.a):

- Weight/diameter of balls: 360 g 10 min^{-1}
- Volume of milling chamber: 250 ml
- Material of milling chamber and balls: WC
- Rotation speed: 450 min^{-1}
- Weight of sample: 18 g
- Volume of added water: 0–100 %
- Milling times: 2–30 min
- Conditions of milling: ambient temperature, free access of air

Industrial nutating mill (Hicom 15, Hicom International Pty, Ltd., Australia)(NM)(Fig. 1.b):

- Weight/diameter of balls: 10 kg 5 mm^{-1}
- Volume of milling chamber: 5,000 ml
- Material of milling chamber and balls: stainless steel
- Rotation speed: 900 min^{-1}
- Weight of sample: 1,000 g
- Volume of added water: 0–50 %
- Milling times: 1–10 min
- Conditions of milling: ambient temperature, free access of air

S p e c i f i c S u r f a c e A r e a

The specific surface area was determined by the low temperature nitrogen adsorption method in a Gemini 2360 sorption apparatus (Micromeritics, USA).

Results and Discussion

The olivine sample was mechanically activated in one laboratory and one industriall mill. Conditions of milling are described in previous part. The aim of the present investigation was to study the effects of dry and wet milling on the

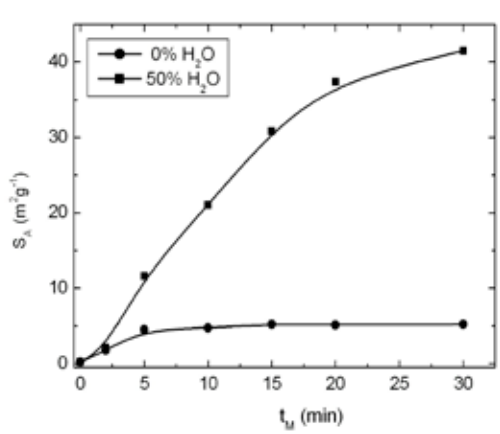

Fig. 1. **Specific surface area S_A as a function of milling time in a planetary mill**

Table I
Milling parameters and specific surface area

Type of mill	Milling time [min]	H_2O addition [%]	Specific surface area [$m^2 g^{-1}$] Dry milling	Wet milling
–	–	–	0.25	
PM	2	50	1.82	2.19
PM	5	50	4.51	11.61
PM	10	50	4.76	21.06
PM	15	50	5.25	30.86
PM	20	50	5.11	37.34
PM	30	5		13.19
PM	30	20	5.21	38.29
PM	30	50		41.49
PM	30	100		40.49
NM	1	–	0.88	–
NM	3	–	1.76	–
NM	5	–	2.46	–
NM	10	5		21.64
NM	10	10	3.03	17.57
NM	10	20		12.31
NM	10	50		9.43

changes in surface area of olivine sample. Summary of the milling results is given in Table I.

As can be seen from results in Table I, milling of olivine in laboratory planetary mill produces an increase of starting surface area from 0.25 $m^2 g^{-1}$ to 5.21 $m^2 g^{-1}$ at 30 min without water addition and to 41.49 $m^2 g^{-1}$ at the same time with addition of 50 % of water (Fig. 1.). It was observed increase of specific surface area (S_A) by milling with various addition of water (0, 5, 20, 50, 100 %) at the same time (30 min). Progressive increasing up was observed in the presence of 50 % of water, in the presence of 100 % of water the S_A decrease (Fig. 2.).

The increase of specific surface area was observed by milling in industriall nutating mill from value 0.25 $m^2 g^{-1}$ to 3.03 $m^2 g^{-1}$ at 10 min without water (Fig. 3.). Special effect

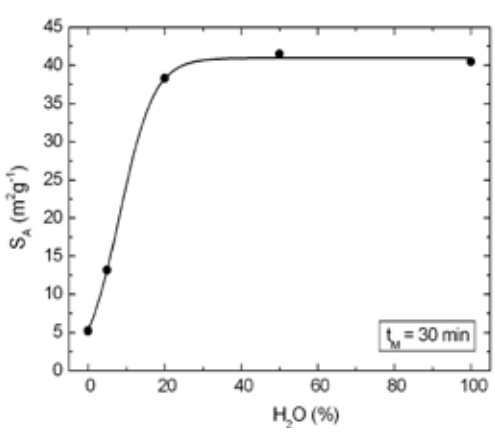

Fig. 2. Specific surface area S_A as a function of H_2O addition by milling in a planetary mill

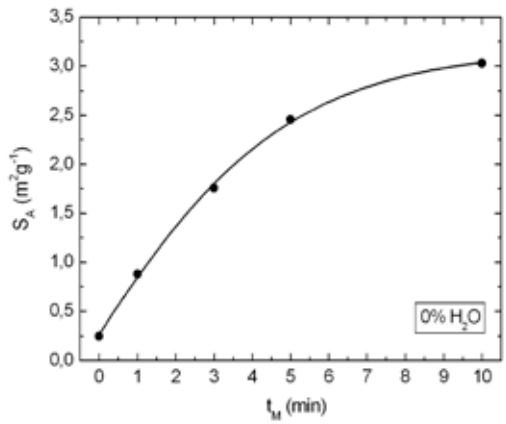

Fig. 3. **Specific surface area S_A as a function of milling time in a nutating mill**

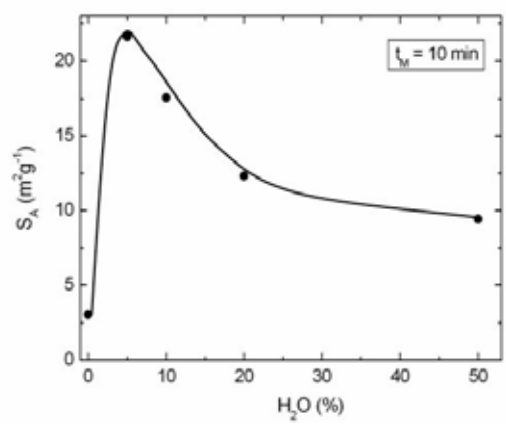

Fig. 4. **Specific surface area S_A as a function of H_2O addition by nutating milling**

has been observed by milling of olivine for 10 min in nutating mill in the presence of small amounts of water (Fig. 4.).

The less water is applied, the higher values for specific surface area have been obtained: for 5 % wt. H_2O the value of S_A was 21.6 $m^2 g^{-1}$. The effect of the addition of small amounts of a liquid to accelerate the solid-state reactions carried out by milling is called kneading in the chemical engineering. Kneading has been described as a sort of catalysis, where the small amount of solvent provides a lubricant for solid-state diffusion[6,7].

The corresponding micrographs for as-received olivine as well as for the same samples activated by dry milling for 30 min in a laboratory planetary mill and in an industriall nutating mill for 10 min are given in Fig. 5. The as-received sample shows particles irregular in shape with characteristic sharp edges. During milling the particles are rounded, fractured and diminished. Some large particles still exist but an overall reduction in size appears to have occurred as a result of high-energy milling. The evidence of well-bonded aggregates can be seen.

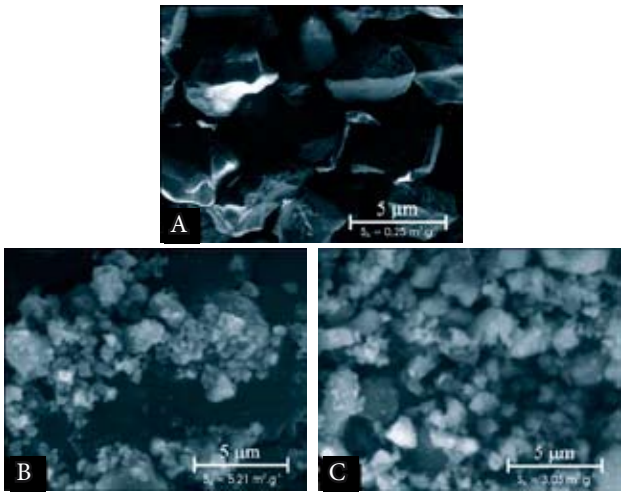

Fig. 5. SEM photos of olivine: A – as received sample, samples after dry milling in (B) planetary mill, (C) nutating mill

Conclusions

Changes in specific surface area of mechanically activated olivine in high-energy mills were detected. Milling in wet mode results in the highest values of specific surface area.

This work has been supported by the Slovak Research and Development Agency APVV (project LPP 0196-06), the Slovak Grant Agency VEGA (project 2/0035/08) and Center of Excellence of the Slovak Academy of Sciences (project NANOSMART). Gratefully acknowledge is to the Norwegian University of Science and Technology for supplying the olivíne sample.

REFERENCES

1. Baláž P.: *Extractive Metallurgy of Activated Minerals*. Elsevier, Amsterdam, 2000.
2. Baláž P.: *Mechanochemistry in Nanoscience and Extractive Metalurgy*. Springer, Heidelberg, 2008.
3. Tkáčová K.: *Mechanical Activation of Minerals*. Elsevier, Amsterdam, 1989.
4. Kleiv R. A., Thornhill M.: Miner. Eng. *19*, 340 (2006).
5. Huijgen W. J. J., Witkamp G .J., Comans R. N. J.: Chem. Eng. Sci. *61*, 4242 (2006).
6. Braga D., Grepioni F.: Angew. Chem. Int. Ed. *43*, 4002 (2004).
7. Braga D., Grepioni F.: Chem. Commun. 3635 (2005).

P28 NUMERICAL MODELLING AND SIMULATION FOR INTERACTION BETWEEN Cu^{2+} AND $S_2O_3^{2-}$

MIHAELA-LIGIA UNGUREŞAN[a], MIHAIL ABRUDEAN[b], PAULA RAICA[b], EVA H. DULF[b] and TIBERIU COLOŞI[b]

[a]*Technical University of Cluj-Napoca, Chemistry Department, Romania,*

[b]*Technical University of Cluj-Napoca, Automation Department, Romania,*

Mihaela.Unguresan@chem.utcluj.ro

Introduction

Reactions between thiosulfate and ions of metallic elements in solution have been studied[1,2].

Cu^{2+} – thiosulfate reaction kinetics explanation is of interest since Cu^{2+} is used as catalyst within the reaction between Fe^{3+} and thiosulfate, allowing determining the presence of copper traces, but also because copper ions play important roles in biological processes, as enzymes components and as antioxidants[3].

The kinetics of Cu^{2+} reduction with $S_2O_3^{2-}$ in aqueous acidic solutions is not yet known, there is just one paper dealing with the reaction of $Cu[NH_3]_4^{2+}$ with $S_2O_3^{2}$, the observed half time of this reaction being about 0.15 s(ref.[4]).

Reaction between Cu(II) and thiosulfate ions results in the formation of a colored intermediate, supposed to be CuS_2O_3, similar to the intermediate $FeS_2O_3^{+}$, but unloaded.

The evolution of this complex can be followed spectrophotometrically, but the reaction's half time is three or four orders of magnitude smaller than the one of the $FeS_2O_3^{+}$-complex, therefore the disappearance of CuS_2O_3 study requires a stopped-flow apparatus.

The Analytical Modelling of the Process

For the input signal u(t) with the amplitude (u_0) and period (τ), the output light intensity y(t, p) experimentally measured can be approximated by:

$$y(t, p_1) = J(p_1)\cdot t\cdot \varepsilon^{-\frac{t}{T}}, \qquad (1)$$

as shown in Fig. 1, for $p = p_1 > 0$.

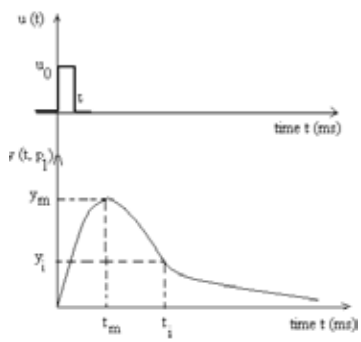

Fig. 1. **Light intensity y [mV] = f(time t [ms])**

The J(p) function it is approximated to be polynomial decreasing of the form[5,6]:

$$J(p) = J_0 + J_1 p + J_2 p_2 + J_3 p_3 . \qquad (2)$$

The maximum value for (1) results from:

$$\left(\frac{\partial y}{\partial t}\right)_{p_1} = J(p_1)\cdot\left(1-\frac{t}{T}\right) = 0 , \qquad (3)$$

so that

$$t_m = T , \qquad (4)$$

$$y_{m1} = y(t_m, p_1) = \frac{t}{\varepsilon}\cdot J(p_1), \qquad (5)$$

$$\left(\frac{\partial^2 y}{\partial t^2}\right)_{p_1} = \frac{J(p_1)}{T}\varepsilon^{-\frac{t}{T}}\cdot\left(-2+\frac{t}{T}\right) = 0 , \qquad (6)$$

for which

$$t_i = 2T , \qquad (7)$$

$$y_{i} = \frac{2T}{\varepsilon^2}\cdot J(p_1). \qquad (8)$$

As a result, the analytical modelling for y(t, p) can be qualitatively illustrated in Fig. 2, where the maximum values ym(t, p) become proportional to curve 2, as it results from (5).

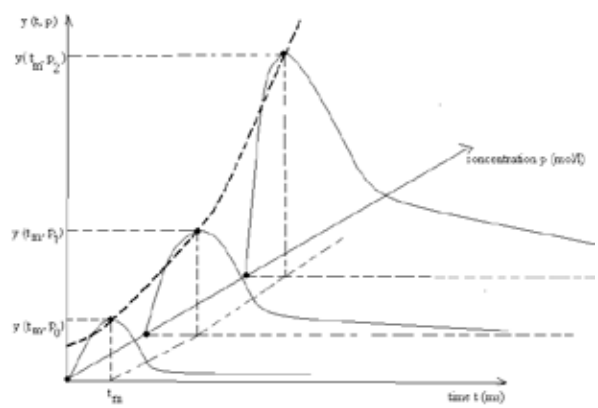

Fig. 2. **Light intensity *vs*. concentration and time**

The decreasing polynomial curve (2) results from experimental measurements and it has been approximated in the following two variants, associated to Fig. 3.

We define: $J(p_0)$, $\left(\frac{\partial J}{\partial p}\right)_{p_0}$, $J(p_f)$ and $\left(\frac{\partial J}{\partial p}\right)_{p_f}$ from which we can obtain the coefficients in (2): $J_0 = J(p_0)$;

$$J_1 = \left(\frac{\partial J}{\partial p}\right)_{P_0}\ ;\ J_2 = \frac{3}{p_f^2}\cdot\left[J(p_f) - J_0 - \frac{p_f}{3}\cdot\left(\frac{\partial J}{\partial p}\right)_{P_f} - \frac{2}{3}p_f\cdot J_1\right];$$

$$J_3 = \frac{1}{p_f}\left[J(p_f) - J_0 - J_1\cdot p_f - J_2\cdot p_f^2\right].$$

The variant has the advantage of following a rigorous polynomial trajectory and the disadvantage of a more difficult choice of the slopes from the ends of this curve.

We define the four points where that the polynomial curve (2) needs to pass, respectively $J(p_0)$, $J(p_1)$, $J(p_2)$ and $J(p_f)$, finally having: $J_0 = J(p_0)$; $J_1 = \frac{DET1}{DET\Phi}$; $J_2 = \frac{DET2}{DET\Phi}$ and $J_3 = \frac{DET3}{DET\Phi}$. The four determinants correspond to a system of four linear algebraic equations, written in the points (p_0, p_1, p_2 and p_f) from the polynomial curve (2).

This variant has the advantage of this curve passing through those four predetermined points (usually experimental) and the disadvantage of eventually deformations of the curve between the four predetermined points.

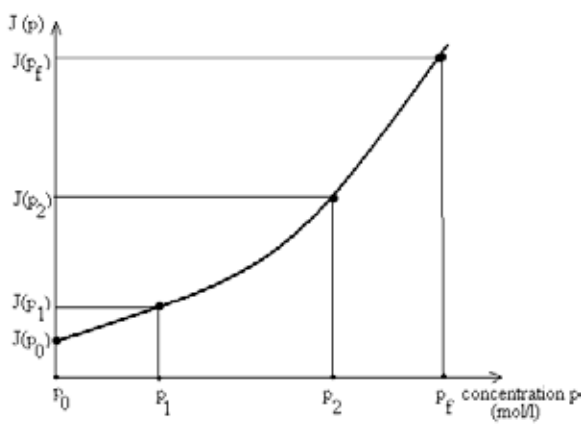

Fig. 3. **J [mV ms^{-1}] = f (concentration p [mol dm^{-3}])**

Results

The experimental measurements have been done for stoechiometric mixtures of reactants with concentrations between 5×10^{-4}–1×10^{-1} mol dm^{-3}.

The polynomial approximation (2) has been achieved by using the experimental data obtained for the domain of the above concentrations.

The results obtained by simulation for the second variant of calculus are:

(i) $[Cu^{2+}] = 5\times10^{-3}$ mol dm^{-3}; $[S_2O_3^{2-}] = 5\times10^{-3}$ mol dm^{-3}, J = 9.54 mV ms^{-1}; $t_m = T = 59.6$ ms; $y_m = 209.3$ mV

The curve obtained by simulation overlapped on the curve obtained experimentally, for $[Cu^{2+}] = 5\times10^{-3}$ mol dm^{-3}; $[S_2O_3^{2-}] = 5\times10^{-3}$ mol dm^{-3}, is presented in Fig. 5.

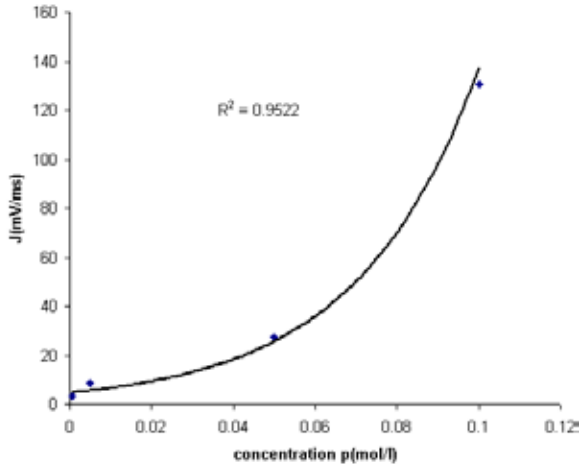

Fig. 4. **J [mV ms^{-1}] = f (concentration p [mol dm^{-3}])**

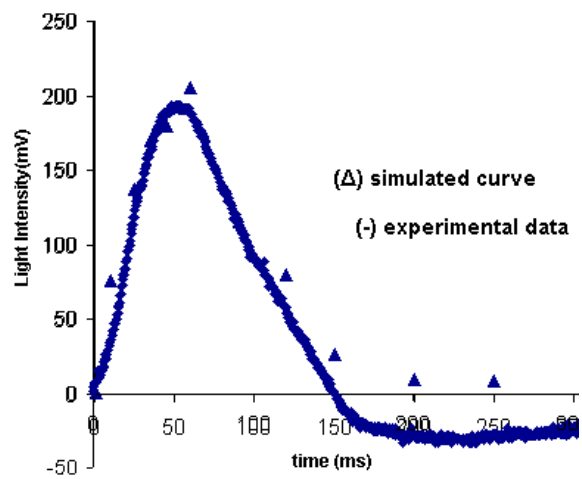

Fig. 5. **Superposition experimental curve; (-) to the simulated curve, (▲) for $[Cu^{2+}] = 5\times10^{-3}$ mol dm^{-3}; $[S_2O_3^{2-}] = 5\times10^{-3}$ mol dm^{-3}**

(ii) $[Cu^{2+}] = 10^{-1}$ mol dm^{-3}; $[S_2O_3^{2-}] = 10^{-1}$ mol dm^{-3}, J = 130.6 mV ms^{-1}; $t_m = T = 15.6$ ms; $y_m = 650$ mV.

The curve obtained by numerical simulation overlapped on the curve obtained experimentally, for $[Cu^{2+}] = 10^{-1}$ mol dm^{-3}; $[S_2O_3^{2-}] = 10^{-1}$ mol dm^{-3}, is presented in Fig. 6.

The parameters k_1, k_{-1} and k_2 and molar absorption coefficient for the initial conditions ($[Cu^{2+}] = [S_2O_3^{2-}] = 5\times10^{-3}$ mol dm^{-3}, l = 0.4 cm, I_0 = 2,950 mV, $E = \lg I_0/I$) is obtained by optimization, realized by multiple iterations, so as the square middle error tend to small values for a better superposition of the simulated response and the experimental response. It has to be mentioned that the flat section of the maxim was moved. This section seems to appear due to hydrodynamic conditions and due to diffusion phenomena existing in thoroidal mixing chamber, although at much reduced scale, and also due to fact that in flow time the reaction may start beyond the measuring cell.

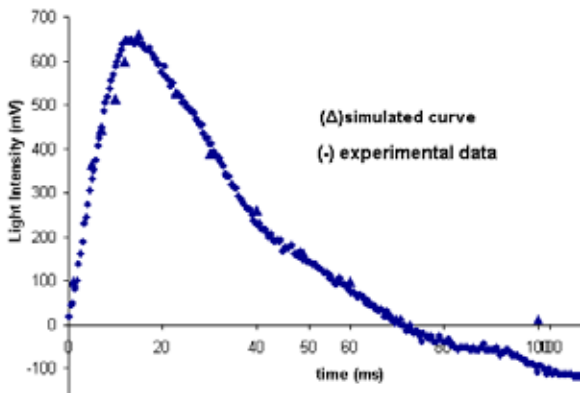

Fig. 6. Superposition experimental curve (-) to the simulated curve (▲)

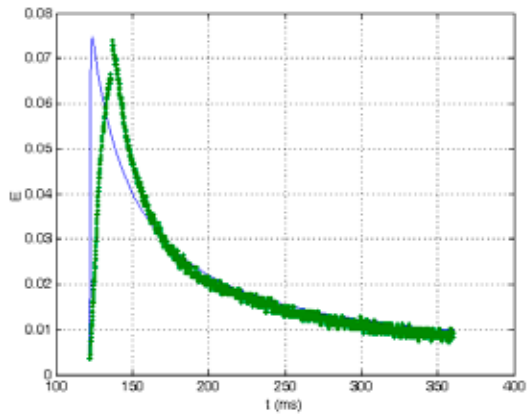

Fig. 7. **The absorbance E = f(t); experimental curve (bold); simulated curve (line)**

Due to imperfect mix, it was necessary the translation of the experimental values – corresponding to decomposition of the intermediary compound – toward the values corresponding to forming operation of the intermediary compound.

The obtained results from the optimization of the simulated curve (Fig. 7.): $k_1 = 9.7$; $k_{-1} = 0.7$; $k_2 = 8{,}222.5$; $\varepsilon = 1489.7\ M^{-1}\,cm^{-1}$, the reaction order for decomposition of the intermediate compound is n = 2.

The value of the formation constant of CuS_2O_3 at 19.5 °C is $K = k_1/k_{-1} = 13.86$.

Conclusions

It was simulated and modeled the kinetic of rapid redox reaction between Cu^{2+} and $S_2O_3^{2-}$ (Figs. 5., 6.). The proposed mathematical model, which is based on the reaction mechanism determined in conformity with the obtained experimental values, allow – by numerical simulation – the approximate calculus of the kinetic parameters: $k_1 = 9.7$; $k_{-1} = 0.7$ and $k_2 = 8{,}222.5$; $\varepsilon = 1{,}489.7\ M^{-1}\,cm^{-1}$ and n = 2. The results obtained by analogical modeling and numerical simulation are in accordance with the experimental values.

REFERENCES

1. Baldea I., Niac G.: Inorg. Chem. *9*, 110 (1970).
2. Cadariu I., Niac G., Oniciu L., Studia Universitatis Babeş Bolyai, Chemia *1*, 27 (1962).
3. Biesalski H. K., Grimm P.: *Taschenatlas der Ernährung*, Thieme Verlag, Stuttgart 1999,.
4. Byerley J. J., Safaa A., Rempel F., Garry L.: J.C.S.Dalton *1973,* 889.
5. Ungureşan M. L.; Abrudean M., Coloşi T.: *Nonlinear-Exponential Numerical Modelling and Simulation of the Kinetic Rapid Redox Reaction Cu^{2+} with $S_2O_3^{2-}$*, SINTES 12,p. 215, Craiova, 2005.
6. Dulf E., Coloşi T., Abrudean M.; Ungureşan M. L.: *Modeling and Numerical Simulation of First and Second Order Distributed Parameters Processes, using M_{dpx} Operating Matrix*, SINTES 12, p. 66, Craiova, 2005.

P29 BIOACTIVITY AND CYTOTOXICITY OF FLUORHYDROXYAPATITE CERAMIC

MARTIN VITKOVIČ, MAHA SALIH MAHAMMED NOAMAN and MARTIN PALOU
Slovak University of Technology, Faculty of Chemical and Food Technology, Radlinského 9, 812 37 Bratislava, Slovak Republic,
martin.vitkovic@stuba.sk

Introduction

There is an increasing need for medical implants, due to an increasing aged population. Bone defects resulting from trauma, disease or developmental anomalies can substantially be improved by reconstructive surgery.

Bone is essentially constituted of nanoscale inorganic materials and proteins. The inorganic materials are minerals which are structurally apatite-like, such as hydroxyapatite [HA, $Ca_5(PO_4)_3OH$], fluorapatite [FA, $Ca_5(PO_4)_3F$] and carbonate-apatite.

Therefore, composite fluorhydroxyapatite (FHA) materials have been developed by different synthesis routes and techniques in order to improve both bioactivity and mechanical properties of various orthopaedic prosthesis and dental implants. Besides bioactivity and mechanical properties, the non-cytotoxicity is one of the most important requirements for applications of these materials.

The present work deals with the bioactivity and the cytotoxicity investigation of ceramic materials on the base of apatites with general formula $Ca_5(PO_4)_3(OH)_{1-x}F_x$ (x = 0, 0.5 and 1).

Experimental

S a m p l e s P r e p a r a t i o n

The samples of hydroxyapatite (HA), fluorapatite (FA) and fluorhydroxyapatite (FHA) were prepared by homogeneous precipitation method using $Ca(NO_3)_2 \cdot 4H_2O$ and $(NH_4)_2HPO_4$ as starting materials and ammonia solution as agents for pH adjustment. Equations (1)–(3) illustrate chemical reactions leading to the precipitation of HA, FA and FHA, respectively. A suspension of $Ca(NO_3)_2 \cdot 4H_2O$ powder was diluted in deionised water. Then, a solution of $(NH_4)_2HPO_4$ was slowly added by drop-wise to the $Ca(NO_3)_2 \cdot 4H_2O$ solution. In all experiments the pH of $Ca(NO_3)_2 \cdot 4H_2O$ solution was kept by ammonia solution at 10. The final solution was stirred at room temperature for 3 h. Then, the precipitate formed was filtered off, washed with deionised distilled water several times to the neutral pH, and finally dried in owen at 70 °C for 24 h. After drying, the samples were powdered and treated at 1,000 °C for 1 h. After heat treatment at 1,000 °C, the pellets were compressed from powdered samples and heated at the same temperature.

The chemical process leading to HA can be explained by the following reaction (1):

$$5Ca(NO_3)_2 \cdot 4H_2O + 3(NH_4)_2HPO_4 + 4NH_4OH \rightarrow Ca_5(PO_4)_3OH + 10NH_4NO_3 + 23H_2O \quad (1)$$

Likewise the FA was obtained according to the reaction (2):

$$5Ca(NO_3)_2 \cdot 4H_2O + 3(NH_4)_2HPO_4 + 4NH_4F \rightarrow Ca_5(PO_4)_3F + 10NH_4NO_3 + 3HF + 20H_2O \quad (2)$$

The solid solution of FHA (FA : HA = 1 : 1) was prepared according to the reaction (3):

$$5Ca(NO_3)_2 \cdot 4H_2O + 3(NH_4)_2HPO_4 + 3.5NH_4F + 0.5NH_4OH \rightarrow Ca_5(PO_4)_3OH_{0.5}F_{0.5} + 10NH_4NO_3 + 3HF + 20H_2O \quad (3)$$

U s e d M e t h o d s

Obtained HA, FA and FHA powders were controlled by powder X-ray diffraction.

The bioactivity of the samples was evaluated by in vitro testing in simulated body fluid (SBF). SBF, which ion concentrations are almost identical with inorganic ion concentrations of human blood plasma, was prepared according to literature[1]. The calculated volumes of SBF (4) were poured in the plastic containers and heated up to the temperature of 36.5 °C.

$$VS = \frac{S_a}{10}, \quad (4)$$

V_S – volume of SBF [ml],
S_a – apparent surface area of specimen [mm^2].

The pellets of FA, HA and FHA were immersed in SBF for 4 weeks at 36.5 °C. Changes of the surface microstructure of the samples were observed by scanning electron microscopy (SEM).

HA, FA and FHA have also been used to investigate the cytotoxic effect on murine fibroblast. The cytotoxicity was determined using the method of direct cell counting[2]. NIH–3T3 cells were cultured with biomaterial discs for 24 h, 48 h and 72 h. The cell proliferation and the morphology were examined.

Results

The results of SEM analysis after SBF acting are showed in Figs. 1., 2. and 3., respectively. The high *in vitro* bioactivity of all samples is demonstrated by the growth of new apatite-like phase on the surface of them.

Fig. 4. shows the direct effect of HA, FA and FHA on cell proliferation evaluated at 24, 48 and 72 h of culture. HA, FA and FHA induced slight inhibition of NIH–3T3 cell proliferation. In the first time interval cells affected by biomaterials proliferated was 92.68 % for HA, 97.56 % for FA and 96.34 % for FHA. After 72 h incubation the inhibition of cell division was the same for all the biomaterials (25 %). According to this, the cytotoxicity was in the range of 5 49–27.19 %.

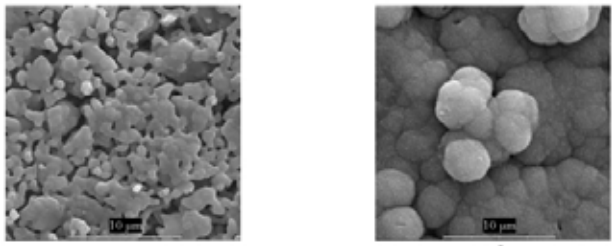

(a) (b)

Fig. 1. **Surface microstructure of HA: (a) before immersion in SBF, (b) after 4 weeks in SBF**

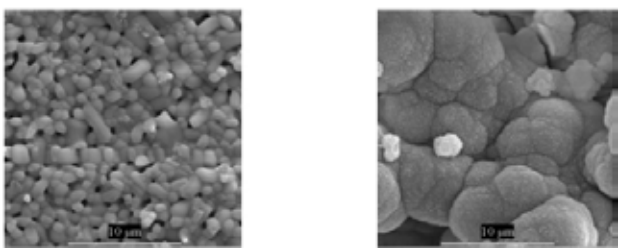

(a) (b)

Fig. 2. **Surface microstructure of FA: (a) before immersion in SBF, (b) after 4 weeks in SBF**

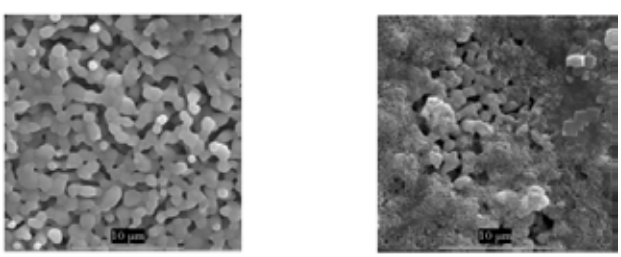

(a) (b)

Fig. 3. **Surface microstructure of FHA: (a) before immersion in SBF, (b) after 4 weeks in SBF**

The morphology of NIH–3T3 cells grown in direct contact with apatites was completely similar to that of control cells and did not show any morphological damages.

Conclusions

The new layer of apatite-like phase covered the surface of all samples. The creation of the new biologic active layer confirmed the bioactivity of apatites.

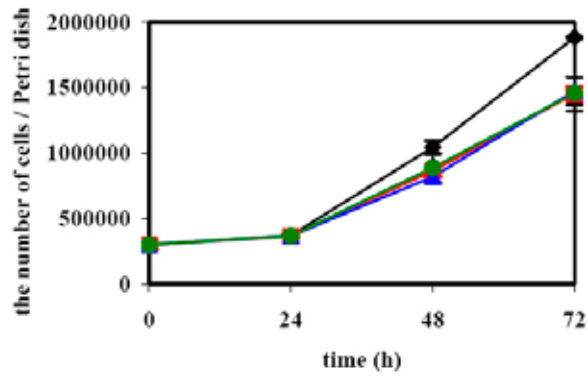

Fig. 4. Growth curve of NIH–3T3 cells cultured with biomaterials : ♦ – C; ● – FHA; ▲- FA; ■ – HA

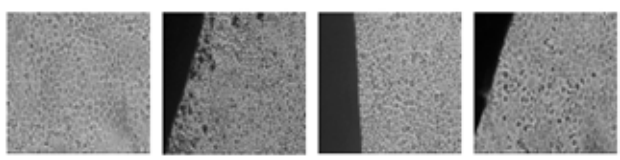

Fig. 5. **Morphological analysis of NIH–3T3 cells cultured for 72 h in presence of FHA, FA and HA. Magnification: 80×**

HA, FA and FHA induced slight inhibition of cell proliferation, which was the same for all apatites after 72 h incubation. The cell number monitoring showed their slight cytotoxicity.

The morphology of cells grown in direct contact with apatites did not show any morphological damages.

This work has received financial support from Slovak Grant for Science and Technology APVT No. 20-015904.

REFERENCES

1. Kokubo T., Takadama H.: Biomaterials *27*, 2907 (2006).
2. Lang H., Mertens T .H.: J. Oral. Maxillofac. Surg. *48*, 606 (1990).

P30 MICROWAVE-HYDROTHERMAL SYNTHESISOF HYDROXYAPATITE FROM $CaSO_4 \cdot 1/2H_2O$ FOR DENTAL REPARATION

P. ZAMAZALOVÁ[a,b], C. DAMIA[a], E. CHAMPION[a] and O. GEDEON[b]

[a]*SPCTS UMR 6638 CNRS, Faculté des Sciences et Techniques, 123 avenue Albert Thomas, 87060 Limoges Cedex, France,*

[b]*Department of Glass and Ceramics, ICT Prague, Technická 5, 166 28 Prague 6, Czech Republic,*

Petra.Zamazalova@vscht.cz

Introduction

The aim of present work is to obtain particles of hydroxyapatite (HA – $Ca_{10}(PO_4)_6(OH)_2$) suitable for the reparation of defects occurring on the surface of dental enamel as a result of demineralization process. HA was chosen as the filling material due to its composition similar to enamel which can be chemically defined as non-stoichiometric apatite ($Ca_{10-x}(HPO_4)_x(PO_4)_{6-x}(OH)_{2-x} \cdot xH_2O$, $0<x<2$)[1]. However, particle size of HA is limited to be sub-micron by the micrometric size of surface defects.

Numerous techniques of HA synthesis have been developed during past years, particularly wet chemical methods based on the low temperature precipitation from aqueous solutions. Usually $Ca(NO_3)_2 \cdot 4H_2O$ is used as a source of calcium[2], however, several authors have already reported the use of gypsum ($CaSO_4 \cdot 2H_2O$)[3,4] as a starting material. Recently, microwave irradiation has been used in order to obtain nanoparticles of a variety of inorganic materials in a short time including HA.[5–7] Despite our effort we did not find any mention of the utilization of plaster ($CaSO_4 \cdot 1/2H_2O$) even though its higher reactivity in aqueous solutions is well known.

Therefore, in this report the preparation of HA by microwave-hydrothermal synthesis from plaster and the application of obtained powder on tooth enamel are presented.

Experimental

$CaSO_4 \cdot 1/2H_2O$ (Aldrich) and $(NH_4)_2HPO_4$ (Aldrich) were used as starting materials for the synthesis of HA according to the following equation which is the modification of the formulation reported by Katsuki *et al.*[7]:

$$10CaSO_4 \cdot 1/2H_2O + 6(NH_4)_2HPO_4 \rightarrow Ca_{10}(PO_4)_6(OH)_2 + 6(NH_4)_2SO_4 + 4H_2SO_4 + 3H_2O \quad (1)$$

Plaster was mixed with a 1M solution of $(NH_4)_2HPO_4$ in a Teflon beaker with molar ratio of Ca/P equal to 10/6 corresponding to stoichiometric HA. The pH of the mixture was adjusted to a value between 9–10 using NH_4OH solution. Reaction mixture was then irradiated for 40 min. with a microwave power of 750 W in home microwave oven (Whirlpool JT357, 2.45 GHz). After the reaction, sample was filtered, washed by distilled water and dried at 100 °C in air.

Calcination of sample at 1,000 °C for 15 h permitted to determine the stoichiometry of powder[8]. Powder was characterized by XRD (Siemens D5000 diffractometer), FT-IR (Bomen MB2), BET (analyzer Micromeritics ASAP 2010) and SEM (Hitachi S2500 and Hitachi S4700).

For the study of defect reparation a gel of methyl cellulose containing 5 % wt. of HA powder was prepared and applied on the tooth surface using classical toothbrush. Artificial defect was created on the tooth enamel in order to facilitate microscopic observations.

Results and Disscussion

Phase composition of HA powder was studied by XRD (Fig. 1.). In non-calcinated powder, large peaks of low crystalline HA occurred without any other phase (Fig. 1.a). The XRD of calcinated powder confirmed full conversion of starting materials and revealed the presence of sharp peaks of HA and β-TCP (β-Tricalcium phosphate; β-$Ca_3(PO_4)_2$) (Fig. 1.b). It was reported that peaks of HA accompanied by β-TCP occur in samples with Ca/P ratios between 3/2 (stoichiometric β-TCP) and 10/6 due to the decomposition of a Ca-deficient hydroxyapatite (CDHA, $Ca_{10-x}(HPO_4)_x(PO_4)_{6-x}(OH)_{2-x}$, $0<x<1$)(ref.[2]). Therefore, it can be supposed that non-calcinated powder contain CDHA.

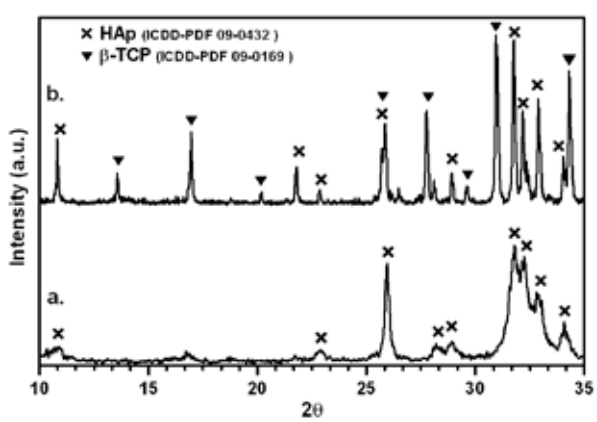

Fig. 1. **XRD patterns of HA sample (a) non-calcinated and (b) calcinated**

This supposition was confirmed by FT-IR analysis (Fig. 2.) showing the presence of an absorption band of HPO_4^{2-} (874 cm^{-1}) characteristic for CDHA. Apatitic structure was supported by the observation of the splitting of PO_4^{3-} bands (602–562 cm^{-1}, 1,095–1,029 cm^{-1}) and the presence of OH^- bands (630 cm^{-1}, 3,570 cm^{-1}). As expected, since the sample was not calcinated, bands of adsorbed water (3,433 cm^{-1}, 1,638 cm^{-1}) and carbonate (CO_3^{2-}) groups (1,420–1,500 cm^{-1}) were also visible.

The specific surface area (SSA) of HA powder obtained by BET measurement is 73.1 ± 0.7 $m^2 g^{-1}$. The microstructure of the sample can be observed in Fig.3. SEM micrographs reveal fine needle-like particles 200 nm long and 30 nm wide which corroborates BET measurement.

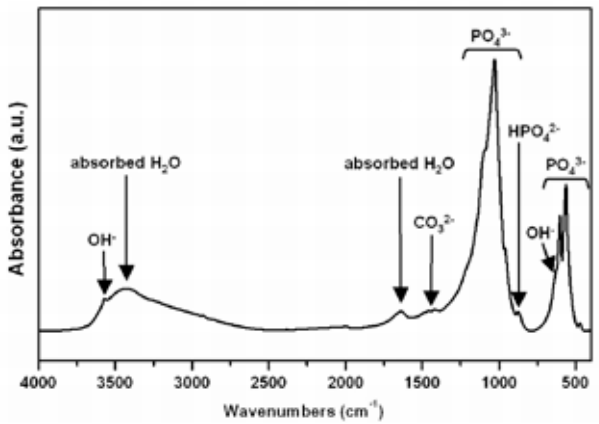

Fig. 2. **FT-IR spectrum of non-calcinated HA powder**

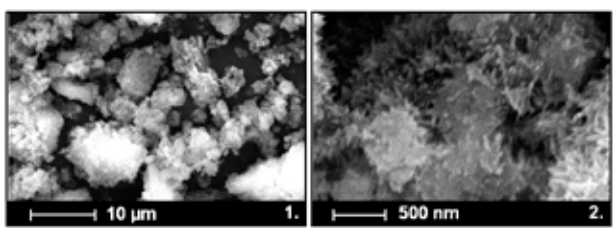

Fig. 3. **SEM micrographs of sample HA at (1.) low magnification and (2.) high magnification**

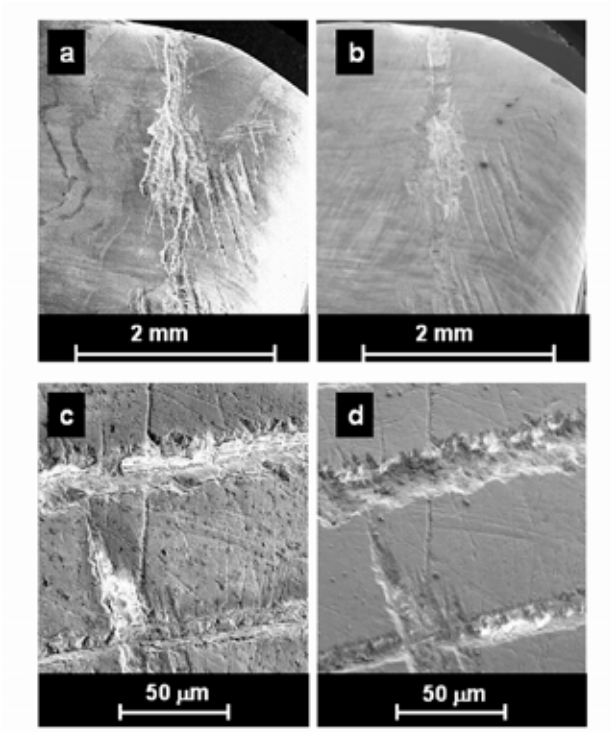

Fig. 4. **SEM micrographs of tooth surface (a), (c) before and (b), (d) 3 days after the application of gel with HA**

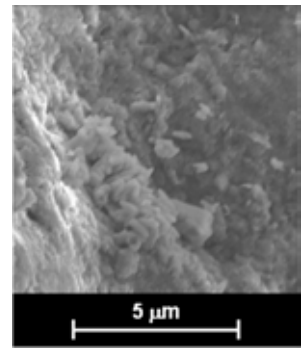

Fig. 5. **New crystals formed in defect**

Artificial scratches are easily recognized and are much deeper than defects normally occurring on the tooth surface (Fig. 4.). Three days after the application of gel with HA particles the defect was filled in by the material and tooth surface looked smoother with homogeneous color (Fig. 4.). Apart deposited particles, newly formed crystals appear in defects (Fig. 5.) supposed to be HA which signify that application of HA gel may enhance further formation of HA from natural environment.

Conclusions

Sample HA was prepared from plaster by microwave-hydrothermal synthesis after 40 minutes of irradiation at 750 W. Characterization techniques showed that non-calcinated sample is composed from fine needle-like particles of Ca-deficient apatite. HA powder was dispersed in methyl cellulose gel and applicated on tooth surface with an artificial defect. Three days after the application defects were filled in by HA gel and newly formed crystals were observed too.

REFERENCES

1. Jenkins G. N.: *The physiology and biochemistry of the mouth*. Blackwell Scientific Publications, Oxford 1978
2. Raynaud S., Champion E., Bernache-Assollant D., Thomas P.: Biomaterials *23*, 1065 (2002).
3. Furuta S., Katsuki H., Komarneni S.: J. Mater. Chem. *8*, 2803 (1998).
4. Suzuki Y., Matsuya S., Udoh K., Nakagawa M., Tsukiyma Y., Koyano K., Ishikawa K.: Dent. Mater. J. *24*, 515 (2005).
5. Yang H., Huang Ch., Tang A., Zhang X., Yang W.: Mater. Res. Bul. *40*, 1690 (2005).
6. Teoreaunu I., Preda M., Melinescu A.: J. Mater. Sci. Mater. Med. *19*, 517 (2008).
7. Katsuki H., Furuta S., Komarneni S.: J. Am. Ceram. Soc. *82*, 2257 (1999).
8. Raynaud S., Champion E., Bernache-Assollant D., Laval J. P.: J. Am. Ceram. Soc. *84*, 359 (2001).

P31 CONVERSION COATINGS ON AMGNESIUM ALLOYS

MARTIN ZMRZLÝ
Faculty of chemistry, Brno University of Technology, Purkynova 118, 612 00 Brno, Czech Republic,
zmrzly@fch.vutbr.cz

Introduction

Magnesium alloys belong to the most perspective metallic construction materials. Besides their good mechanical properties (tensile and yield strength, uniform elongation, hardness) they also dispose by very low density. This fact makes them very popular e.g. in automotive industry, since the lighter is the construction, the lower are service costs (petrol consumption) and consequently environmental damage is diminished.

Unfortunatelly, due to very low electrochemical potential of magnesium, corrosion resistance of these alloys is very poor. In the case of alloys containing lithium is this fact even emphasised.

Typical surface treatment for magnesium alloys are conversion coating. Most effective type of coating, the chromate coating, were excluded from use by EU legislation[1] since they contained a cancerogenic hexavalent chromium. However, in laboratory scale is this type of coating still widely used as a standard of corrosion protection[2].

Goal of this work is to find a chromating solution that will make a continuous coating on the surface of alloy AZ 91. This alloy is most commom magnesium alloy in technical use. The phase structure of this alloy is quite complex, containing α-solid solution of ellements in magnesium, intermetallic compound $Al_{12}Mg_{17}$ and their eutectic mixture, see Fig. 1.

These phases differ a lot in reactivity[3]. Then it is a common result, that α-phase is covered by coating and intermetallic phases remain uncoated.

Experimental

Cast specimens of AZ 91 alloy were used. They were cut to size app. 5 × 20 × 20 mm and grinded by metallographic SiC paper (Struers, No. 320). Composition of alloy is 9 %Al, 1 %Zn and ballance is magnesium.

The starting solution was established according to ref.[4] as 0.35M $K_2Cr_2O_7$ (Lachema, p.a.). Further exeperiments were carried out with solutions 0.12M, 0.035M and 0.0035M. The bath should work at room temperature. Set of solutions that diferred in pH value was also prepared. pH were 3.7; 2.9; 2.1; 1.5; 1.3; 1.2; 1.1; 1.0; 0.9; 0.8; 0.7 and 0.6. Values were set by addition of 1M solution of hydrochloric acid (Lach-Ner, p.a.) and measured by pH-meter Gryf 208

Time of immersion was varied in scale 5; 15; 30 and 60 seconds for each solution.

After the process, the specimen were rinsed by distilled water and ethanol and dried by hot air. The surface was observed on micrsocope Neophot 21 (Zeiss). This way the contiunuity of prepared coating was assessed.

Coating Weight

Coating weight was measured by stripping method[5]. The specimen was weighed (accurancy 0.1 mg) immersed for 60 second in boiling suspension of 2 g Ag_2CrO_4 in 200 ml of solution CrO_3 (15%). After this immersion the specimen was dried as stated above and weighed again.

Corrosion Resistance

Corrosion resistance was measured according to ref.[5]. Weighed specimen was placed into 3.5% solution of NaCl in distilled watter for 1 hour. Than it was rinsed by water and placed in stripping suspension of Ag_2CrO_4 (process described above). Then it was dried and weighed. In the case of coated specimens, the coating weight had to be taken into account.

All the quantitative measurement were done is sets of 3–6 measurement. Q-test for removing of statistical outliers were performed and the average of the results and the stan-

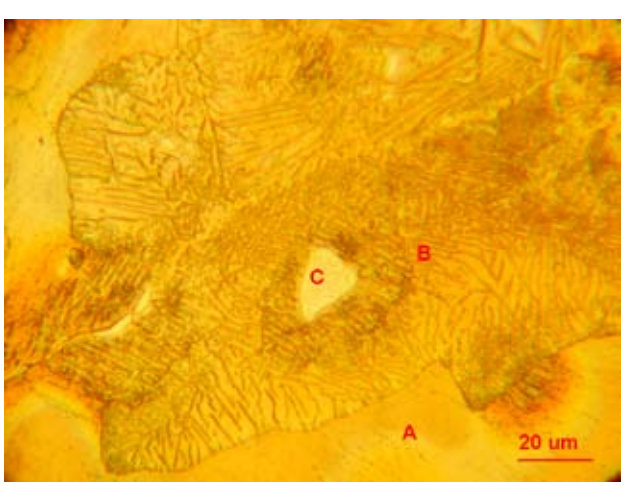

Fig. 1. **Micrograph of alloy AZ 91. Light microscope, mgf.1000 ×. A – solid solution α, B – eutectic of solid solution and intermetalic compound, C – intermetallic compound $Al_{12}Mg_{17}$**

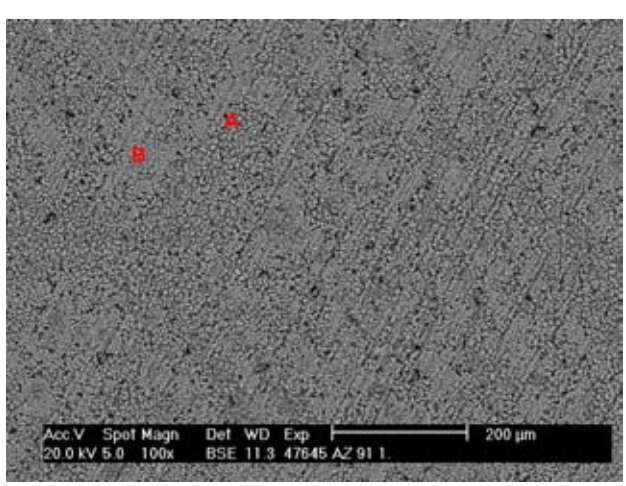

Fig. 2. **SEM Micrograph of chromate coating on alloy AZ 91. A – area, where the substrate is solid solution α, B – area, where the substrate is eutectic or intermetalic compound.**

dard deviation σ were calculated. Absolute error was taken as 2σ.

Results

According to visual assessment (microscopy), the optimal conditions were estimated as: $c_{K2Cr2O7}$ = 0.12M, pH = 0.6 and time of immersion 15 s. At these conditions the specimens were continuously coated, although there were observable differences between grain size at sites of α-phase and grain size at sites ofintermetallic phases (see Fig. 2.).

The coating weight was estimated by stripping method as 660 μm cm^{-2}. Corrosion resistance, estimated by above described method, was obtained at both the coated and uncoated specimen. The corrosion rate of bare AZ 91 alloy was found to be 9 ± 1 mm year^{-1} and rate of alloy with chromate coating was 5 ± 1 mm year^{-1}.

Conclusions

The composition of chromating soultion convenient for prepration of standard AZ91 corrosion specimens was found, besided the optimal immersion time. Possibility of use of the NaCl solution for test of these coatings was proved. Corrosion rate of the coated specimen was approximately half the value of the uncoated AZ 91 alloy.

REFERENCES

1. EU Directive 2002/95/ES, January 27, 2003.
2. Sharma A. K.: Metal Finishing *87,*33 (1989).
3. Gray J. E. Luan H.: J. Alloys Compd. *336*, 88 (2002).
4. Magnesium Electron, Surface treatments for magnesium alloys in aerospace and defence, 2006, http://www.magnesium-elektron.com/products-services.asp?ID=9.
5. Ambat R., Aung N. N., Zhou W., Corros. Sci *42,*1433 (2000).